Additive manufacturing of carbon fiber reinforced thermoplastic polymer composites

Doctoral Dissertation
Doctoral Program in Materials Science and Technology (34th Cycle)

Additive manufacturing of carbon fiber reinforced thermoplastic polymer composites

By

Federico Lupone

******

Supervisor(s):
Prof. Claudio Francesco Badini, Supervisor
Dott.ssa Elisa Padovano, Co-Supervisor

Doctoral Examination Committee:
Prof. Alessandro Pegoretti, Referee, Università di Trento
Prof.ssa Paola Fabbri, Referee, Università di Bologna

Politecnico di Torino
2022

Declaration

I hereby declare that, the contents and organization of this dissertation constitute my own original work and does not compromise in any way the rights of third parties, including those relating to the security of personal data.

Federico Lupone

2022

* This dissertation is presented in partial fulfillment of the requirements for **Ph.D. degree** in the Graduate School of Politecnico di Torino (ScuDo).

If a picture is worth a thousand words, a 3D model is worth a million. This booklet contains plenty of all, it must be worth a gazillion...

Acknowledgment

I would like to express my sincere gratitude to my supervisors Prof. Claudio Francesco Badini and Prof. Elisa Padovano for their guidance and support during this PhD thesis.

I would like to thank all my colleagues and university students at PoliTO both for their collaboration in this research activity and the support, kindness, patience and good time together. A special appreciation to Mario and Francesco for the significant help these years and the interesting discussions on several scientific (and not) topics.

I would also like to thank the referees and the thesis examination committee.

Finally, a special thanks to my parents and all my friends.

Abstract

The objective of the dissertation is to establish a framework for the development of additive manufacturing (AM) technologies toward the fabrication of high-quality of carbon fiber reinforced thermoplastic polymer (CFRP) composites. AM offers valuable advantages with respect to conventional composites fabrication methods, including high design flexibility, near net shape processing of complex geometries with no need of moulds, tools or special equipment (e.g., autoclave), product customization, small material and energy consumption and capability of full automation. In this context, this dissertation analyzed the relation between processing, structure and property across the micro and meso length scales of both short and continuous fiber reinforced polyamide composites fabricated with powder bed fusion (Selective Laser Sintering, SLS) and material extrusion (Fused Filament Fabrication, FFF and Continuous Filament Fabrication, CFF) AM techniques. To this end, a detailed thermo-physical, morphological and mechanical characterization of the materials before and after the printing process was performed. Moreover, a novel approach was developed to rationalize process parameter optimization in SLS, while the ability to control fiber orientation in material extrusion AM methods was used to customize part stiffness and strength and mechanical anisotropy by aligning the fibrous reinforcements layer by layer in multiple ways. Current models used to predict the mechanical behaviour of fiber reinforced composites were also effectively adapted to AM parts by taking into account their peculiar microstructural features into the models. Overall, the results showed that the integration between microstructure control, effective modeling approaches and process optimization could drive the application of AM in the composite industry. The current issues related to the widespread adoption of composite AM, such as difficulties in void suppression, limitations in fiber length and content and other processing defects (interlayer bonding and fiber distribution) were also illustrated by comparing the microstructure and mechanical properties of 3D printed and conventionally manufactured components. Although short fiber reinforcements are preferred due

to ease of AM processing, continuous fiber composites exhibited tremendous enhancement of mechanical properties, with potential to outperform the conventional fabrication methods where complex light-weight structures are needed. Finally, suggestions for possible processing and material improvements were proposed.

Contents

List of Figures

List of Tables

Chapter 1

Introduction

1.1 Motivation

Fiber reinforced polymer composites has attracted enormous interest in the last decades since their properties are otherwise not achievable with traditional materials. Among them, carbon fiber reinforced polymers (CFRP) with short or continuous reinforcements offer relevant advantages over polymers (high mechanical properties, fatigue resistance and temperature stability) and metal alloys (high specific stiffness and strength, corrosion resistance, lightweight and non-energy-intensive manufacturing processes) [1]. In addition, they exhibit high chemical resistance and a low coefficient of thermal expansion. Owing to this unique combination of properties, carbon fiber reinforced polymers has found numerous applications in high-performance industries where mass is a significant design factor, such as automotive, aerospace, wind energy and sport equipment (Figure 1a) [2]. Moreover, the worldwide demand for carbon fiber composites is continuously increasing due to government stimulus package for the development fuel-efficient transportation vehicles and cleaner energy production (e.g., wind, solar) (Figure 1b) [3].

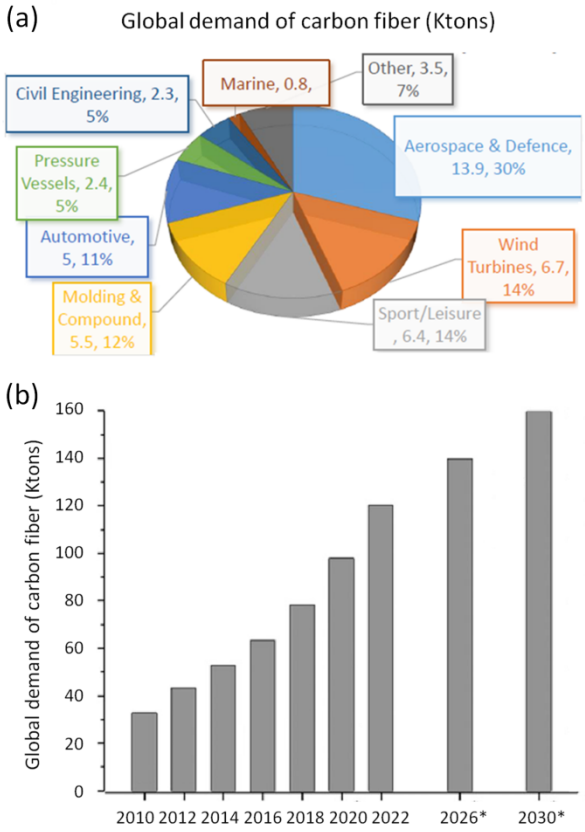

Figure 1: (a) Carbon fiber composite mass consumption by industry in 2016 [2] and (b) global demand and forecast (2010-2030) for carbon fiber composite market [3]

Short fibers are largely employed to enhance the performances of neat thermoplastic polymers by creating composites with improved mechanical and functional properties without changing the production process (e.g. injection or compression moulding) or significantly altering the manufacturing cost and productivity. Short carbon fiber reinforced polymer (SCFRP) composites reach elastic modulus values in the range from 10 to 20 GPa and can withstand up to 200 MPa of applied tensile stress. Moreover, the greatest advantage of using SCFRP composites over thermoset counterparts and metals is represented by a favourable compromise between performances and cost, due to their ease of processing, high volume production output, long shelf life and the potential to recycle scrap [1,4]. Although short fiber reinforced thermoplastics have been continuously improved over the years and have reached a widespread use in different industries, the highest mechanical performances and strength to weight ratio can be obtained by using continuous fibers and thermosetting epoxy matrices. Continuous carbon fiber reinforced polymer (CCFRP) composites has

been used in aerospace and sport car industries for decades and the material characteristics has been fully optimized in terms of fibers sizing techniques and surface treatments and epoxy matrices curing processes. Through these developments high interfacial strength between fiber and polymer, high mechanical performances and fast curing time (from hours to minutes) were achieved [5].

Today, the evolution of processing technologies, combined with customer demands for personalized good and services, are leading to changes in the distribution and scale of manufacturing. Three main drivers are widely acknowledged as key factors for enabling a significant change in the manufacturing landscape: (1) sustainability, (2) automation and (3) product customization. For short fiber thermoplastics this new paradigm mostly results in the necessity of technological improvements to meet an ever increasing demand for customized products. Traditional processes such as injection molding are highly automated and well suited for mass production, but customization of the objects is costly because dedicated and expensive moulds are needed. By contrast, continuous fiber reinforced composites relies on labour intensive and time consuming processing methods (e.g., hand layup, vacuum bag-only), which have a high cost-per-part and are not suited for high volume output automation. Moreover, thermosetting resins show poor end-of-life recyclability and usually require sophisticated cure chemistries or prolonged cure cycles that impedes a translation to more sustainable and efficient production systems. For these reasons, automated processing techniques for continuous fiber reinforced thermoplastic composites parts, such as filament winding (FW), automated fiber placement (AFP) and automated tape layup (ATL), are increasingly popular as alternative to thermosetting resins [5,6].

In this context, additive manufacturing (AM), a direct manufacturing approach that allows the fabrication of 3D objects from a digital design without tooling, could play a significant role in the carbon fiber composite industry. Firstly, additive manufacturing or 3D printing has some potential benefits that stand out to meet the three aforementioned trends for future manufacturing:

1. it is intrinsically less wasteful in terms of material and energy consumption than traditional subtractive production processes [7,8];
2. automation technology in software and production workflow can be easily implemented to AM, thus adding unprecedented abilities to rapid prototyping processes [5,9];

3. the high design flexibility coupled with no need for tooling enables low volume manufacturing capabilities and product customization without additional cost [1,5,6].

Moreover, additive manufacturing can effectively address some of the major limitations of conventional processing methods for fiber reinforced composites. On one side, AM creates complex-shaped and customized composite parts, without the need for mould redesign for every product iteration, thus representing a resource- and cost-efficient solution for small-scale production of short fiber thermoplastics. On the other hand, AM could bridge the gap between CCFRP composites and more sustainable, automated and flexible production approaches. Continuous fiber reinforced thermoplastics can be produced by using relatively simple and affordable AM techniques, able to rapidly translate digital design into finished parts with less human labour, shorter cycle times and less material waste. This will lead to cost savings and greater process efficiency compared to traditional processes [1].

Although AM offers a variety of unique advantages to composite manufacturing, the development of peculiar microstructure, including novel defects, interlayer interfaces, polymer crystalline structure and fiber orientation distributions, also demands additional research. Most significantly, composite parts fabricated by AM exhibit high void content and low polymer crystallinity, that contribute to a reduction of the material performances. The poor interlayer bonding typical of AM parts can result in peculiar failure morphologies. Moreover, the mechanisms underlying the placement and orientation of carbon fibers within the polymer matrix differ from traditional methods and between each additive techniques too. Finally, there still exist insufficient data on the application of mathematical models to predict the mechanical properties of AM composites. Therefore, these aspects are widely examined in this thesis to improve the current knowledge on the relationship between AM process, composite structure and final part property.

1.2 Dissertation overview

The present dissertation aims at addressing the characterization, processing and modeling of additively manufactured carbon fiber thermoplastic composites. Three popular AM techniques for thermoplastic polymers, namely Selective Laser Sintering (SLS), Fused Filament Fabrication (FFF) and Continuous Filament Fabrication (CFF), are chosen for investigation. SLS and FFF are examples of

powder bed fusion and material extrusion AM techniques able to process short fiber thermoplastics. CCF is a patented dual extrusion technology that allows the addition of continuous reinforcements to neat polymers. Polyamide based composites are processed as they are easily accessible and specifically optimized for each additive techniques. In addition, these materials are frequently employed in both academic research and industrial applications. The main objective of the dissertation is to analyse the microstructure and performances of the 3D printed composites and to identify the current limitations of AM techniques through a comparison with traditional manufacturing methods. In fact, owing to the progressive shift of additive manufacturing from prototypes towards end-use parts production, the quality standards required for 3D printed parts are such stringent as those for traditional components. The PhD thesis is arranged as follows:

- chapter 2 will present the state of the art in additive manufacturing of carbon fiber reinforced thermoplastic polymer composites, including both short and continuous fiber reinforcements. This chapter covers relevant previous works on the three different technologies adopted in this thesis. An overview of the main aspects of those technologies and the current knowledge of the influence of carbon fibers on processing, structure and properties of 3D printed thermoplastic polymers will be presented;
- chapter 3 introduces AM processes and materials, including machines and building strategies. The process parameter optimization approach used for SLS is also emphasized. The characterization methods adopted to study the thermal, physical, microstructural and mechanical properties for raw materials and printed parts described along with different models for the prediction of the mechanical properties of the composites;
- chapter 4 is divided in three sections, where the experimental results for SLS, FFF and CFF printed composites are presented and discussed. A detailed analysis of the microstructural defects and fiber orientation induced by the printing processes as well as the related tensile behaviour and failure mechanism is carried out;
- chapter 5 illustrates an in-depth comparison between the microstructure and mechanical performances of short and continuous fiber composites produced by AM and traditional technologies. Suggestions on possible improvements and application spaces for these technologies are also encompassed;
- chapter 6 draws the conclusion of the experimental activity and future research outlooks.

Chapter 2

Additive Manufacturing

2.1 Introduction

Additive manufacturing (AM), also known as 3D printing, has emerged as a group of technologies capable of fabricating a wide range of components and complex geometries directly from computer aided design (CAD) files. This technology has been developed by Charles Hull in 1984 in a process known as stereolitography (SLA), which was followed by subsequent developments such as powder bed fusion (PBF), material extrusion, binder jetting and laminated object manufacturing (LOM) [10].

Figure 2 schematically illustrates the common steps involved in AM processes. Three-dimensional (3D) model of the part is created by using common CAD software. The digitally programmed design is converted to the STL file format, referred as "standard tessellation language", and transferred to the slicing software of the AM printer. By using the software, the layer slicing operation is performed and the whole tool path for the AM printer is created according to user-defined settings. A “gcode” file containing step-by-step instructions of the printing process, is exported and the AM printer can thus produce the designed 3D object according to a layer-by-layer manufacturing strategy. Finally, post-processing is frequently required to remove structures of support and improve part surface finishing or geometrical accuracy [10,11].

Figure 2: Flow chart illustrating all steps involved in AM file preparation and part production [12]

The additive principle offers higher design freedom compared to traditional fabrication methods. This allows the fabrication of complex geometries with high precision without the use of special tools and moulds. Therefore, 3D printing has been initially used by designers to produce aesthetic and functional prototypes due to its fast and cost-effective prototyping capability. The use of 3D printing has reduced the time-to-market and the additional cost that are incurred to develop new products. However, significant improvements in processing methods, materials and equipment over the last years has enabled AM to rapidly moving from the rapid prototyping space to production of end-use working parts [10,13].

The greatest advantages of AM technologies are the possibility to fabricate intricate geometries with high accuracy, unprecedented design flexibility, low material wastage, easy product customization as well as significant savings in manufacturing time and cost for tools and spare parts. Flexibility in design enables engineers to modify the part as many time as required without additional cost. The fabrication of components with complex geometry, otherwise problematic to be obtained with traditional methods, allows a significant improvement of manufacturing and assembly processes by combining multiple components into a single part. Moreover, the shape of the parts can be tailored by topological optimization in order to reduce weight or meet specific functionalities, as frequently happens for airflow or heat dissipation structures. 3D printing is also

intrinsically less wasteful compared to subtractive manufacturing methodologies as material and energy usage can be minimized during manufacturing and product can be more easily repaired. More importantly, personalized products and short production runs can be quickly tailored according to specific needs thus making the technology ideal for product customization and prototyping. In fact, changes in part design can be done using CAD software at negligible extra cost and without modifying manufacturing equipment, such as moulds and dies, for each design iteration. Spare parts production can be modified with the introduction of AM techniques due to the potential of distributed and on-demand manufacturing. In fact, parts are fabricated where and when they are needed, thus reducing operating downtime and cost as well as inventory stock. In addition, the expiry of the first patents has further pushed the development of these technologies by giving university, start-up and industry the way to improve existing processes and equipment or design entirely new ones. Due to these unique advantages, AM has found application in different areas, from biomedical to automotive and aerospace [10,12–16].

However, several disadvantages, related to the intrinsic nature of AM methods, still remains. These drawbacks include high costs of raw materials and some types of printing systems, poor process scalability to mass production, limited part dimensions and material selection, anisotropic properties and geometrical inaccuracies. Entry and production costs are high because specific equipment and expertise are required and raw material are more expensive. The high costs and long fabrication time of AM methods hinder high volume production of any repetitive object (i.e., scalability). Most AM machines have small print area which limits the size of parts that can be fabricated [13,15]. The constraint of working “in-the-box” has inhibited the adoption of these technologies for large structures. The average size of an industrial machine is about 1 m^3, although Oak Ridge National Laboratory has recently developed a 3D printer based on material-extrusion technology (referred as Big Area Additive Manufacturing) with a build volume of 26 m^3 [1]. Moreover, the available selection of materials is not exhaustive since various polymers and metals (e.g., most thermosetting resins, rubber and not weldable metal alloys) cannot withstand the temperature cycles and processing conditions of AM [5,13]. The layer-wise process strategy and the consequent consolidation mechanism also lead to different microstructures compared to conventional methods. Voids between or within layers is one of the major hurdles for AM processes. The residual porosity can be high, thus causing a significant reduction of mechanical characteristics of

the parts. Moreover, the weak bonding between layers induces anisotropic mechanical behavior, expressed by inferior out-of-plane properties [1,5,10,17]. Finally, the geometrical accuracy, resolution and surface finish of AM parts are strictly related to the manufacturing method adopted. The tessellation concept that allows to transform CAD files into 3D printed parts has intrinsic limitations in geometrical accuracy, especially for curved surfaces, as the digital design is approximated by elements with triangular shape. Material extrusion AM techniques, where a filament is deposited through a nozzle with typical diameter greater than 0.4 mm, has lower tolerances and printing accuracy compared to other processes, such a powder-bed or stereolitography (where fine powders or liquid resin are consolidated by a laser beam) [16,17]. For the same reason, the former methods are more prone to produce parts with layer-by-layer appearance [10]. Thermal stresses developed during the printing process can also negatively affect the performance and geometrical accuracy of the final part [10]. Therefore, post-processing (by heat, laser, chemicals or sanding) is usually required to meet the quality requirements, but it is worth noting that these added manufacturing steps increase production time and cost [13,15].

AM involves various processing methods, materials and printer types. Polymers are the most widely used materials in the AM community owing to their limited cost and ease of processing with different methods. Several fabrication techniques are currently available to print polymers and their composites:

- photo-polymerization, also known as stereolitography (SLA);
- material jetting;
- material extrusion, such as fused filament fabrication (FFF) and continuous filament fabrication (CFF) techniques;
- powder bed fusion, including selective laser sintering (SLS) and multi jet fusion (MJF);
- laminated object manufacturing (LOM).

Raw materials are in the form of thermoset resin, reactive monomers, thermoplastic filaments, sheet and powders. Table 1 summarizes the various feedstock form and consolidation mechanisms in polymer AM processes by dividing in different categories as well as the benefit and drawbacks of each method.

Table 1: A summary of raw materials, benefits and drawbacks of the polymer additive manufacturing methods

AM methods	Material	Benefits	Drawbacks	Resolution (μm) [17]
Stereolito-graphy	Liquid photocurable resin	Fine resolution Ability to produce complex parts Smooth surface finish Large build area	Material limitation High cost Poor strength and durability	25-100
Material jetting	Viscous polymer inks	Good surface finish High resolution Full colour parts Multiple material	Low mechanical strength Poor interlayer adhesion Low productivity	25
Material extrusion	Thermoplastic filament	Low cost Simplicity High strength Multi material capability Ability to print continuous fibers	Anisotropy Low productivity Poor surface finish Nozzle clogging High processing temperatures	100-150
Powder bed fusion	Thermoplastic powders	High quality Part complexity No support required	High equipment cost Powder removal	50-100
Laminated object manufac-turing	Sheets	Low material cost High productivity Large build area Ability to process continuous fibers	Poor surface quality and dimensional accuracy Limitation for complex shapes	200-300

Polymeric objects created by AM can feature highly complex and customized geometries, without expensive and time-consuming mould redesign as it would be required for conventional injection molding process. However, the main issue of polymer AM techniques is the lack of materials with good structural and functional capabilities. 3D printed polymeric parts are considered unreliable for several end-user applications due to the intrinsically poor thermal stability, rigidity, strength and functionality of most polymers [18,19]. Therefore, their applications have been limited to conceptual prototypes and spare parts. Owing to these material-specific constraints, the attention has been focused to the development of methods and material feedstock for additively manufacturing polymer composites with high performances. For example, polymer reinforcement with the incorporation of fibers or nanofillers has been proposed with the objective of creating end-use products with improved mechanical of functional properties. In this context, carbon fiber reinforced polymer (CFRP) composites offers a unique combination of mechanical, electrical and thermal properties along with low density and relatively ease of processing. The addition of carbon fiber reinforcements greatly improves the performances of pure polymers produced via AM techniques, thus enabling the fabrication of objects with satisfactory properties for various engineering purposes [1,14,18].

2.2 Additive manufacturing of carbon fiber reinforced polymers

The interest for the development and characterization of carbon fiber reinforced polymer (CFRP) composites has continuously increased in the last years, till it became one of the most popular research topics in both the academic and industrial AM community (Figure 3). This attention can be attributed to the fact that fiber reinforced polymers are particularly suited for this innovative process technique. In fact, most AM methods can process polymers (both thermoplastic and thermosets) usually employed as matrix in composites. Fibers can be inserted into thermoplastic filament for FFF or mixed with plastic powders for SLS, while common pre-pregs sheets can be used in LOM [14,18].

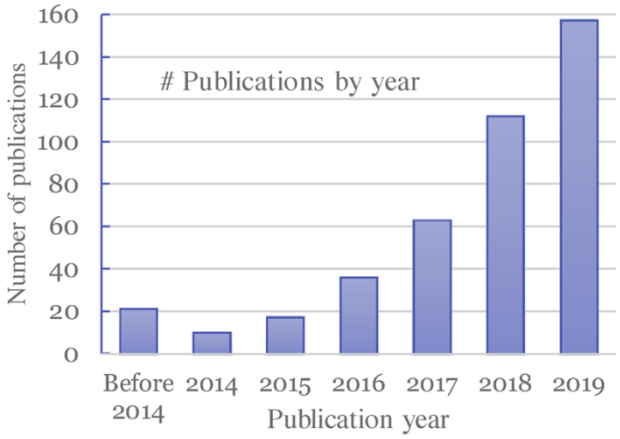

Figure 3: Number of publication per year in carbon fiber composites additive manufacturing or 3D printing (data from Web of Science, 2019) [1]

The integration between carbon fiber reinforced polymers and AM technology offers unique advantages in composite manufacturing compared to conventional methods, such as high precision, complex geometry, customization and less material waste. Additive manufacturing has also the potential to overcome one of the major hurdles of the composite industry, that is fabricating composites parts with high performances in a time and cost effective way. Injection or compression molding are able to produce high quality discontinuous fiber composites but they require expensive moulds and equipment. Moreover, continuous fiber composites are usually manufactured with techniques characterized by high part cost, long processing time and human labour as well as dedicate machines (i.e., autoclave). New automated techniques, such as filament winding and automated fiber/tape placement, can potentially solve these issues, but the high investment cost needed to purchase the specialized equipment has limited their application. By contrast, AM has the potential to quickly realize fully functional composite parts from a digital design without the constraints typical of conventional processing methods in terms of material usage, tools design and production, and time-to-market [5,6].

Nevertheless, current AM methods for CFRP composites have still limitations. The choice of printable material is not wide and processing of high performance polymer matrices such high temperature thermoplastics and epoxy resins is difficult. The speed and repeatability of AM techniques are inferior to conventional ones, especially for short fiber composites. The difficulty in controlling manufacturing defects is also one of the major obstacle of these techniques. For example, voids are common defects in AM polymer composites parts. However, their morphology and amount highly depend on the type of

process adopted. In material extrusion processes filaments are deposited on the build platform one next to the other without applying external pressure. Therefore, voids are always present, resulting in poor mechanical properties [11,14,20] and, in some cases, causing delamination between layers [19–21]. In powder bed fusion methods, voids are formed by partial melting or incomplete coalescence of the powders after exposure to the heat source (i.e., laser for SLS or continuous IR lamps for MJF). However, the amount of pores is lower compared to other techniques and it can be limited by optimizing the process parameters [13,22,23].

In recent years, numerous studies have been conducted to explore the processability and overall performances of additively manufactured CFRP composites [1,14,18,24]. Various aspects have to be taken into account in the development of fiber composites for AM, such as the nature of the matrix and its interfacial interaction with the fibers, the volume fraction, length and orientation distribution of the fibers and the specific AM process and parameters adopted [1,14,18,25]. Similar to conventional composites, carbon fibers enhance modulus and strength at the cost of strain-to-failure (ductility). A relevant increase of viscosity is also foreseen. Moreover, the addition of such fillers alters the thermo-physical properties of the polymer feedstock. In fact, an increase in thermal conductivity and a decrease of the coefficient of thermal expansion (CTE) with increasing fiber loading occurs, as shown in Figure 4 [1].

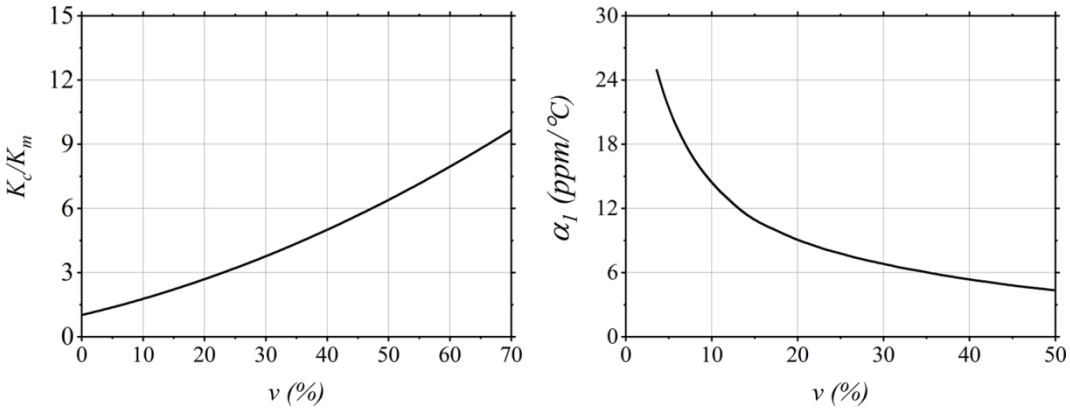

Figure 4: Variation of thermal conductivity (left) and coefficient of thermal expansion (CTE) (right) of a generic carbon fiber reinforced polymer composite as a function of fiber volume fraction (v) [1]. K_c and K_m denotes the thermal conductivity of the composite and neat polymer respectively, while α_l is the CTE in the fiber direction

The former phenomenon promotes heat diffusion in the processed material (i.e., powder bed and deposited bead in powder bed fusion and material extrusion

processes respectively), thus improving part consolidation [26,27]. The decrease of CTE has also been proved to reduce part shrinkage during cooling, thus minimizing residual stresses and improving dimensional accuracy of the final parts. In material extrusion processes this will substantially reduce part distortion, especially in large volume prints [26].

Both short and continuous carbon fibers reinforced polymers can be processed by additive technologies. Thermoplastic-based composites are more frequently used because their melt processability allows easier processing compared to thermosets resins by using well established and accessible AM methods. Short fiber reinforced thermoplastic polymer (SCFRP) composites have been produced using various AM techniques, including fused filament fabrication (FFF) and selective laser sintering (SLS). By contrast, continuous fiber reinforced polymer (CCFRP) composites have been fabricated with fewer techniques so far, mainly based on material extrusion.

The below sections are intended to (1) review the characteristic of the AM methods used in this experimental work and (2) provide insight into the material and processing requirements as well as the composite microstructure and performances typical of each technique. In addition, the main processing defects, such as void formation and anisotropic behaviour are discussed.

2.3 Selective Laser Sintering (SLS)

2.3.1 Technology and materials

Selective laser sintering (SLS) is widely recognized as one of the most consolidated laser powder bed fusion (LPBF) additive manufacturing technologies. It allows the production of plastics and composites parts with unprecedented geometric complexity without the need of supports structures or moulds. Three-dimensional objects can be fabricated from a layer-by-layer fusion of fine powders due to the action of laser beam that selectively scans the powder bed according to a digitally programmed design (Figure 5).

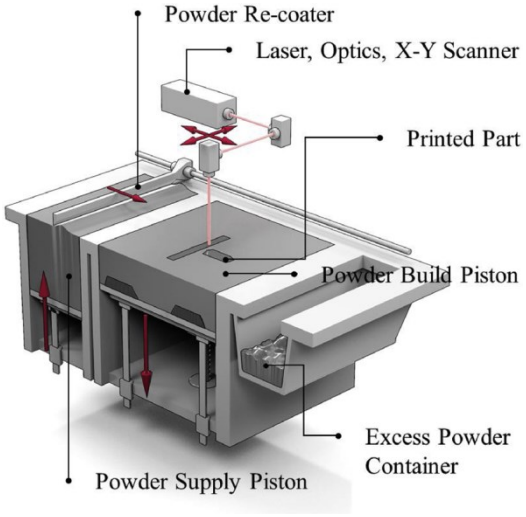

Figure 5: Schematic of selective laser sintering apparatus and operating principle [1]

The laser sintering process consists essentially of three main phases called warm up (A), build (B) and cooling (C) stages, as depicted in Figure 6, where a typical temperature profile during the entire fabrication cycle is reported [28] .

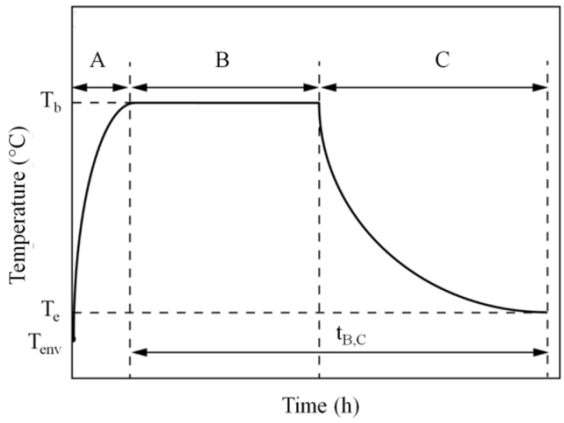

Figure 6: Graphical representation of the typical temperature profile of a standard SLS process. Adapted from [28]

In the warm up stage (A) the build chamber is pre-heated to a temperature in between the polymer crystallization and melting point, referred as powder bed temperature (T_b), by using continuous IR lamps irradiation or resistance heaters. The powder bed is kept at this temperature until the part is finished to avoid out-of-plane distortion. Therefore, isothermal conditions are almost maintained during the entire process. In the build stage (B), the polymeric powders are deposited onto the build platform using a roller or a rake, depending on the SLS machine

adopted, to form a homogenous powder layer. A CO_2 laser beam, placed above the building chamber, moves along the powder bed through scanning mirrors according to a "digitally programmed" pattern in order to melts the powders. Therefore, the laser selectively adds the extra energy required for polymer particles fusion. After laser exposure, the molten powders coalesce at high temperature and slowly solidifies upon cooling to the powder bed temperature. In this way, sufficient bonding between adjacent particles is ensured. A new layer of powder is then spread after the build platform is lowered by the thickness of one layer (i.e., usually between 100 and 200 μm). The layer-wise repetition of powders recoating (1), laser energy input or "powder melting" (2) and material consolidation above polymer melting point (3) allows the production of 3D objects. These three sub-steps take in average between 35 s and 40 s to complete for each layer and are sequentially repeated until part fabrication is finished. Finally, in the cooling stage (C) the entire building chamber is slowly and evenly cooled down under homogeneous conditions to room temperature (T_e) [28].

Great flexibility in terms of part design, high build resolution and high productivity are the main advantages of this technology. SLS has the ability to print complex-shaped structures without using supports because the unsintered powder functions as a support itself. As a result, the difficulties in removing dedicate supporting materials can be surpassed, thus enabling the fabrication of lattice structures, scaffolds for biomedical engineering applications and parts with overhanging features. Moreover, the printed parts show good mechanical performances without significant anisotropy between the different building orientations [28,29]. Owing to these advantages, SLS is an effective alternative to traditional technologies for functional prototypes and spare parts production in different fields, from automotive and aerospace to electronics.

Although SLS has been used from two decades, only few thermoplastic polymers are currently widely adopted. Polyamide based materials represent more than 90% of the SLS production [29,30]. Among them, polyamide 12 (PA12), a semi-crystalline long chain polyamide, is definitely the most widely used both in academia and industry. In fact, most published literature so far has focused on pure or reinforced PA12 powders [23,29,30]. Recently, other semi-crystalline polymers have been developed and commercialized, including polyamide-11 (PA11) [31–33], polyamide-6 (PA6) [34,35], polypropylene (PP) [36–38], high density polyethylene (HDPE) [39,40], polyethylene terephthalate (PET) [41,42], polybutylene terephthalate (PBT) [43–45] and polyoxymethylene (POM) [46]. In addition, high performance polymers such as polyphenylene sulphide (PPS)

[47,48], polyetherketone ketone (PEKK) [49,50] and polyether ether ketone (PEEK) [49,51,52] are entering in the SLS market, although specific machines capable of achieving high building chamber temperatures are necessary for processing [53]. Thermoplastic elastomers such as thermoplastic polyurethane (TPU) have also gained great interest from the beginning of the technologies development due to ease of processing and peculiar mechanical properties [54–58]. Finally, amorphous thermoplastic polymers, such as polycarbonate (PC) [59–61] and polystyrene (PS) [62,63], have been studied. However, their use is limited to aesthetic prototypes and sacrificial molds for casting due to poor sintering quality and high porosity of the final parts [62,64]. An overview of the polymer types used in SLS at commercial or academic research level is presented in Figure 7 [65].

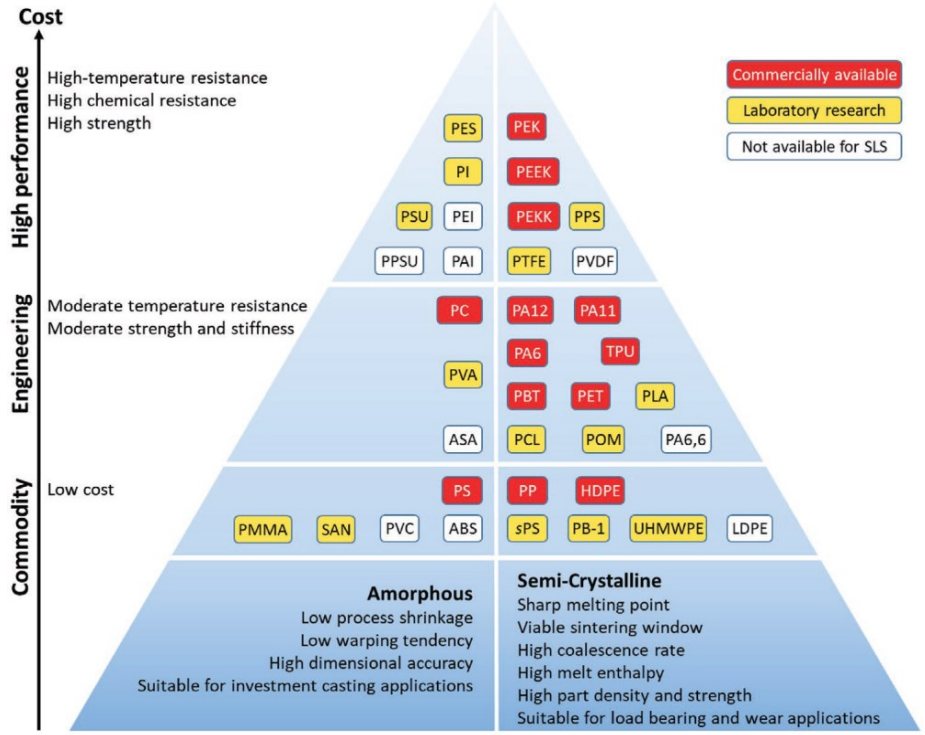

Figure 7: An overview of polymer powders for SLS that are commercially available or have been reported in scientific literature. The materials are classified according to the "polymer pyramid" as commodity, engineering or high-performance amorphous or semi crystalline polymers. The abbreviations listed in this figure that are not used in the text are: low-density polyethylene (LDPE), polybutylene (PB-1), syndiotactic polystyrene (sPS), poly(vinyl chloride) (PVC), styrene-acrylonitrile (SAN), polymethylmethacrylate (PMMA), polycaprolactone (PCL), acrylonitrile styrene acrylate (ASA), poly(vinyl alcohol) (PVA), polytetrafluoroethylene (PTFE), polyamideimide (PAI), polyvinylidene fluoride (PVDF), polyethersulfone (PES), polyimide (PI) and polysulfone (PSU) [65]

Although the apparent simplicity, polymer SLS involves complex multi-physical processes that span over different temporal and spatial scales. Figure 8 graphically illustrates the thermo-physical phenomena involved in the fabrication of three dimensional polymeric parts via SLS. These phenomena, that follows each other in a continuous cycle, are: (1) layer spreading, (2) laser motion and irradiation, (3) thermal diffusion, (4) particle coalescence and (5) solidification / crystallization. This path describes the layer-wise repetition of layer deposition and powder melting and consolidation and it is continuously repeated until job completion by moving down the part bed in z-direction.

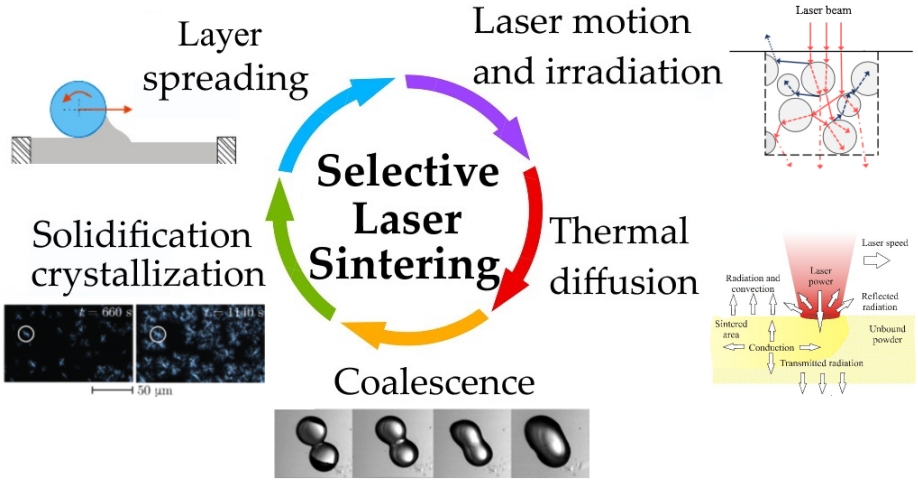

Figure 8: Circle path that describes the different phases and thermo-physical phenomena involved in SLS process of polymers

These thermo-physical phenomena are strictly related to the starting powder properties and the processing parameters adopted and, in turn, affect the quality of the printed objects in terms of material density, microstructure, geometrical accuracy as well as mechanical and functional properties. As it happens for traditional manufacturing technologies, the exact nature and characteristic of a polymer significantly influence the SLS process. It is widely recognized that the processability of polymeric powders and the quality of the printed parts are defined by a stringent combination of intrinsic and extrinsic properties [66]. These material-specific properties are usually summarized in a fishbone diagram, as shown in Figure 9. The morphological and physical properties of the polymeric particles (e.g., particle shape, surface structure, size distribution, etc.) mainly determine the packing density and the flowing behaviour of the powders during layer recoating. The chemical properties are responsible for the ageing behavior of the powders, resulting in variation of molecular weight and part properties.

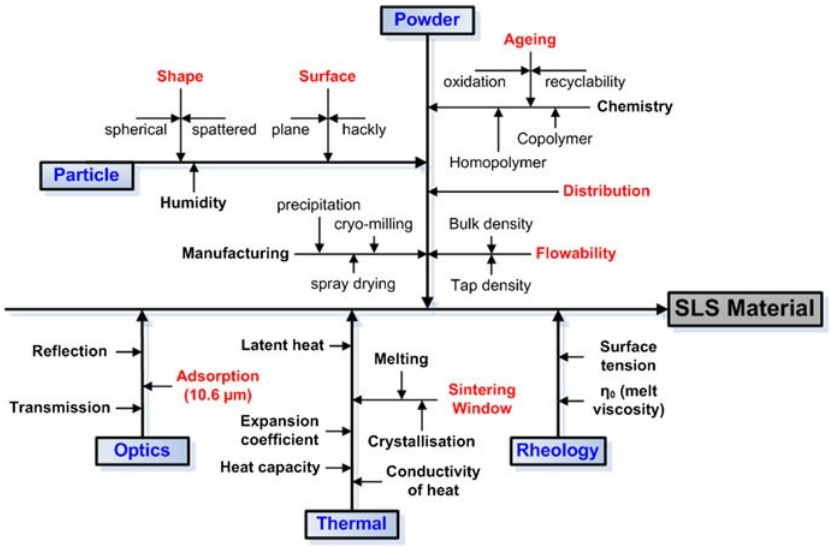

Figure 9: Fish-bone diagram that presents the interdependency of the main intrinsic and extrinsic properties that define the processability of a SLS material and the quality of the printed parts [66]

The optical properties determine how the laser beam interacts with the powder bed as a result of absorption, reflection and transmission phenomena. The thermal and rheological characteristics greatly influence how polymer grains melts, how the temperature distribution and dimensions of the melt pools change over time and how the particles coalesce and solidification proceeds. Most of these properties can be quantitatively measured through different experimental methods. Microscopy observations, calorimetric techniques, thermal degradation analysis and rheometry can be adopted to evaluate these properties for the raw powders. Process parameters such as the nature of the laser source and its diameter, the energy input supplied by the beam and the layer thickness also affect the consolidation mechanism of the material, while powder bed temperature and several machine-specific settings (i.e., powder spreading method via roller or blade, heating system and gas environment of the build chamber) mainly determine the flowing behaviour of the powders, the evolution of polymer crystallization and part shrinkage during cooling and material ageing. However, apart from these qualitative relations, the definition of a general selection criterion to determine if a polymeric powder is suitable for SLS processing is still under debate [22].

2.3.2 Processing defects

The most common defects of polymeric parts produced by SLS are showed in Figure 10. These defects can be closely related to the properties of the starting powders and thermo-physical processes described in Figure 8.

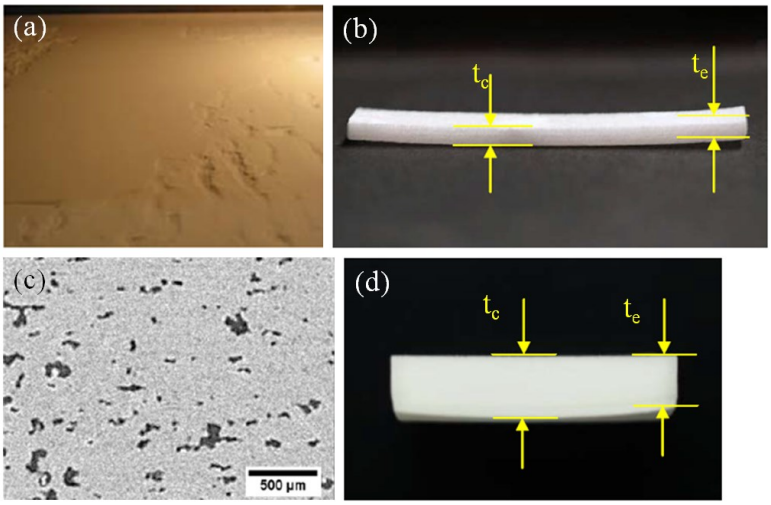

Figure 10: Typical defects observed during laser sintering of polymeric materials related to the physical phenomena of the process and the starting material properties: (a) inhomogeneous powder layer [67] , (b) curling (out-of-plane deformation of the part edges, t_e=t_c) [67], (c) residual porosity [68] and (d) warpage (higher sample thickness in the centre (t_c) compared to the edge (t_e) [67]

Spreading defects

In SLS equipment the powders are deposited onto the part bed by using counter-rotating rollers or translational blades without additional compaction [29]. Since this step is a prerequisite for a successful process, polymeric powders for SLS have to meet certain requirements in terms of particles morphology and flowability in order to be evenly spread in thin layers (usually between 100 and 200 µm) with high packing density on the build platform [66]. Otherwise, inhomogeneous layer spreading and formation of streaks (Figure 10a) could appear [54,69,70]. These defects are responsible for a reduction in density and mechanical properties of the parts and are frequently observed during new material development or when a too high powder bed temperature is set. Similarly to other powder bed fusion AM processes, particles with nearly spherical shape, suitable size distribution (PDS) and surface structure are highly advised for SLS processing. These characteristics favour the occurrence of an almost free flowing behaviour, that is essential to obtain homogeneous and dense layers during

recoating operations. The morphological properties of the particles strictly depend on the powders production method adopted. A number of different approaches are used to obtain polymeric powders, with precipitation and mechanical grinding representing the most widely employed. Figure 11 shows the morphology of commercial SLS powders attained from different manufacturing processes.

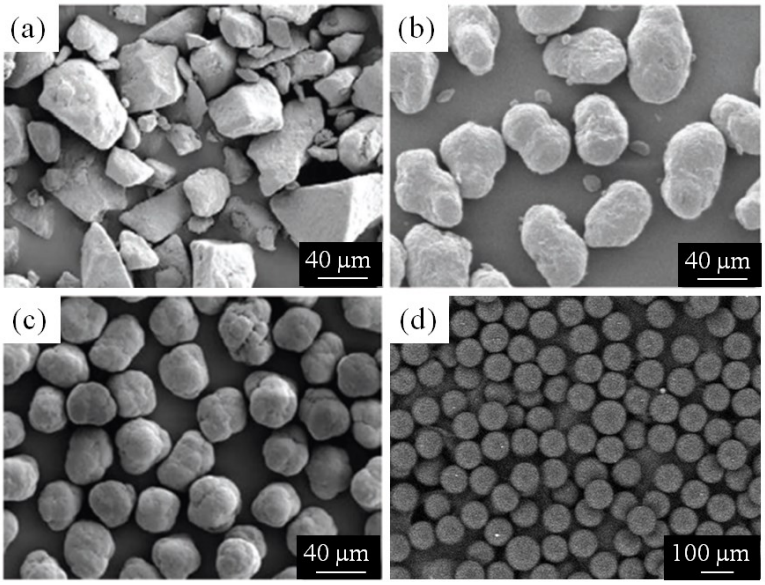

Figure 11: Morphology of polymeric powders prepared with different manufacturing methods: (a) cryogenically ground, rough particles (PA11 powders, PA1101® from EOS GmbH) [65]; (b) potato-shaped particles precipitated from ethanol solution at high temperature (PA12 powders, PA2200® from EOS GmbH) [65]; (c) cauliflower-like particles obtained from direct polymerization of lauryl lactam (Orgasol® PA12 from Arkema) [65] and (d) spherical particles produced by means of emulsion polymerization (PS powders, PrimeCast® 101 from EOS GmbH) [71]

Particles obtained from cryogenic milling process are irregular in shape and size and reveals sharp edges and a smooth surface structure (Figure 11a). As a result, the powders exhibits poor flowing behaviour. This leads to the deposition of layers with poor quality (e.g., low packing density, rough surface and defects) in the building chamber. Therefore, cryogenically milled powders are inadequate in most cases for processing [72]. Potato-shaped particles are usually observed in commercial PA12 powders prepared from precipitation processes (Figure 11b). The typical production cycle consists in dissolving PA12 pellets produced by hydrolytic polymerization in ethanol in a pressurized vessel at temperature up to 150 °C followed by precipitation under controlled conditions and drying. Through this method, powders having tuned particle sizes in the µm range can be obtained

[73]. The precipitation process was first developed by Evonik (Marl, Germany) and the synthesized PA12 powders (brand name Vestosint®) has been adopted in coating technologies for decades [74,75]. As revealed in Figure 11b, these powders show a potato-shaped morphology without sharp edges and a slightly rough surface structure. Most of the particles exhibits sizes between 40 and 80 μm, although fine particles (around 10 μm in diameter) are also present [75]. PA12 powders can also be obtained from anionic ring-opening polymerization of lauryl lactam conducted in suitable solvents (a mixture of ethanol and water) at elevated temperature and pressure. As the temperature or pressure is decreased below a certain threshold, the coagulation and precipitation of the polymer particles occurs. The shape and particle size distribution can be fine-tuned by controlling the process parameters and by adding a low content (about 0.1 wt.%) of SiO_2 or TiO_2 as nucleating agent [76]. This manufacturing process is adopted by the company Arkema (Colombes, France) in the synthesis of Orgasol® Invent Smooth PA12 powders [77] and it generates particles with a cauliflower-like morphology, an almost spherical shape and narrow size distribution around 40 μm (Figure 11c) [68,75]. Spherical particles can be produced either by means of co-extrusion of soluble/insoluble materials (e.g., oils droplets in water) or emulsion polymerization. Polystyrene (PS) powders PrimeCast® 101 commercialized by EOS Gmbh (Krailling, Germany) are an example of the emulsion process (Figure 11d). Polymeric powders usually contain less than 1% of flowing aids, such as nano SiO_2 particles, to improve their flowability [78–82]. In a comparative study on PA12 materials for SLS, Dupin et al. [68] found that the highest packing density (50%) was achieved by using powders produced by direct polymerization (Figure 11c) as they consist of nearly round particles with smaller dimensions and narrower PSD with respect to those obtained by precipitation (Figure 11b). Moreover, Schmidt et al. [72] suggested that a particle size distribution between 20 μm and 80 μm is necessary because flowability issues arises by using powders with a high fraction of fine particles (smaller than 10 μm) due to the increase of inter-particle forces.

Curling

Thermal distortion of the parts, also known as curling, is a common issue associated to SLS technology and it is defined as a local upward deformation of the part edges that appears while the build progresses or during cooling (Figure 10b). This defect can even lead to process failures when the out of plane deformation of the sintered layers exceeds the layer thickness during processing. Curl phenomenon is directly related to the crystallization and shrinkage behaviour

of the polymer [28,67]. In contrast with amorphous materials, semi crystalline polymers experience a significant volumetric change during phase transition upon cooling (Figure 12) [64,83]. This may result in poor geometrical accuracy or even part distortion because the residual stresses created by phase transition cannot be relieved due to the limited chain mobility of the crystalline regions. These stresses are then transferred to the subsequent layers, causing a differential shrinkage between the upper and lower surface of the part so that its edges lift (Figure 10b).

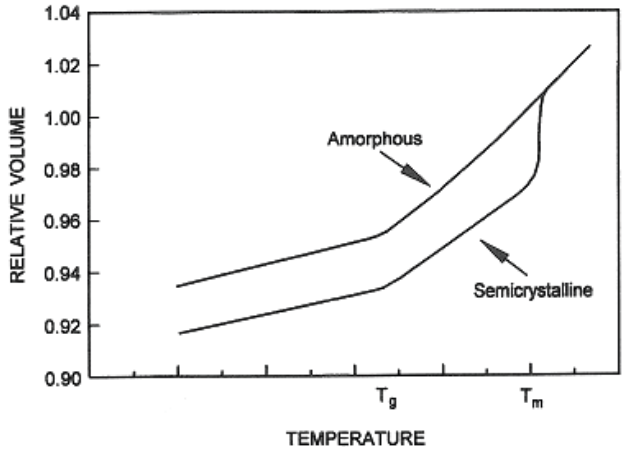

Figure 12: Comparison of relative volume vs temperature curves between amorphous and semicrystalline polymers [83]

Polymer crystallization is thus considered a key aspect to assess its tendency to curl or develop geometrical inaccuracies [28,70,72]. The isothermic laser sintering model proposed by Alsher [84] was firstly used to describe the solidification conditions in the SLS process. According to the model, after laser exposure the polymer melt cools down to the powder bed temperature (T_b), that need to be between melting and crystallization temperatures for processing semi crystalline polymers. At this point both liquid and solid phases, corresponding to the molten material and the surrounding loose powders coexist at the same temperature [84,85]. The polymer remains in the liquid phase until the build step is concluded (Figure 6) and the crystallization take places uniformly during the subsequent cooling stage at low cooling rate (Figure 6). Figure 13 illustrates the thermal conditions in the build stage of the SLS process according to this model through a differential scanning calorimetry (DSC) diagram. The meta-stable region of under-cooled polymer melt marked in Figure 13 is referred as sintering window [23,86].

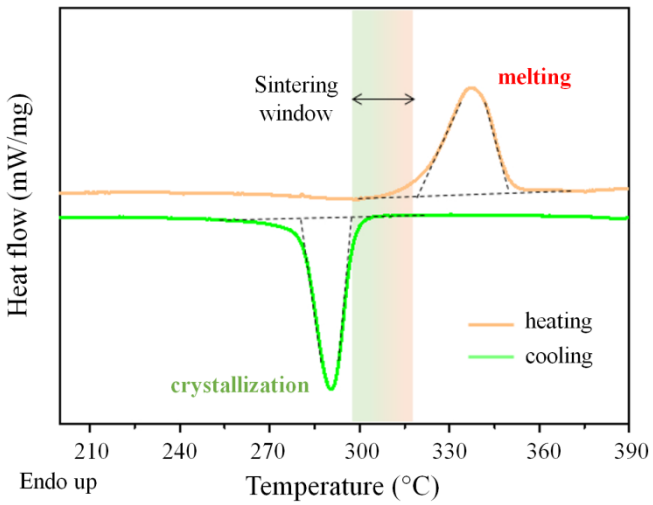

Figure 13: Isothermal crystallization model during the build stage of the SLS process highlighted on a DSC thermogram of PEEK powders. Adapted from [86]

To avoid part distortion, thermoplastic polymers that crystallize slowly upon cooling from the melt are generally preferred [39,83]. Empirical evidence on PA12 indicates that a large sintering window (higher than 20 °C) is advised to inhibit crystallization as long as possible (at least for few layers), thus reducing the amount of residual stresses due to material shrinkage and the probability of curl [22,23,83]. By contrast, a narrow sintering window is unfavourable for SLS processing. In this case, the polymer crystallizes rapidly upon cooling and the sintered layers are prone to residual stress accumulation and distortion, as shown by evaluating the curl height of the final part [67]. However, the validity of this simple criterion has been questioned for high temperature polymers, such as PEEK and PPS, were successfully processed although melting and crystallization events almost overlap in the DSC curves [48,49].

Recent studies put in evidence the limitations of the isothermic laser sintering model to describe the solidification a multilayer polymeric part [28,70,87–89]. Drummer et al. [85] studied isothermal crystallization of different polymeric powders by using DSC analysis. The experiments consists of a heat/cool cycle followed by an isothermal step at different temperatures in the sintering window range (Figure 13) to simulate the SLS process. It was found that crystallization is susceptible to temperature changes with lower rates observed at higher isothermal temperatures. Moreover, the crystallization usually starts during the building process (and not only during the final cooling stage as assumed in the isothermal laser sintering model). Among the investigated materials, PA12 and PP exhibited

the lowest activation energy for crystallization, thus indicating a consistent processability [85]. In a follow up study, Drummer et al. [28] found that PA12 powders achieved a degree of crystallization equal to 50% after 33 layer at T_b. In addition, rheological tests and stick-drop experiments revealed that the phase transition between viscous and solidified material took place about 15 layers after laser exposure [28]. Therefore, polymer crystallization and solidification starts at the build stage as soon as the melt pools cools to T_b and further develops throughout part fabrication in z-direction. Moreover, the analysis of the thermal profile during the build stage demonstrates that a single layer experiences transient temperature fields owing to repeated laser scanning and deposition of new powder layers, followed by a slow cooling (about 0.2 °C/min [70]) as the part bed gradually moves down in the z-direction (Figure 14) [88]. Therefore, the validity of the isothermic model stands for limited building times (10-15 minutes as shown in Figure 14) or, equivalently, to some layers below the surface of the powder bed because the temperatures in z-direction gradually diminish (Figure 14) [28,88].

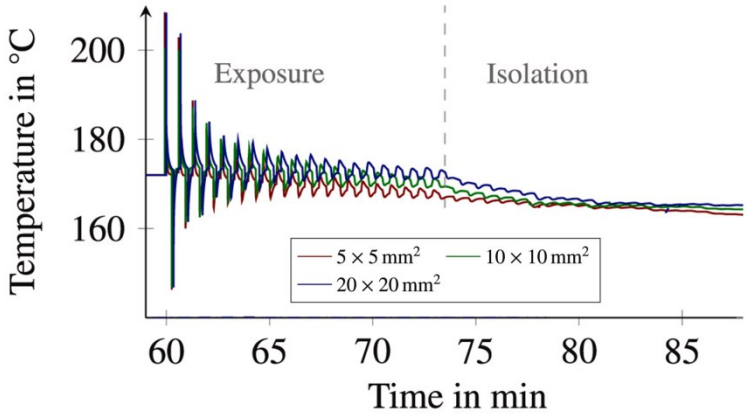

Figure 14: Temperature evolution in the z-direction during the build stage simulated using a FE model validated by IR thermography experiments. The measuring point for the temperature is located at the height of the first layer. After 1h of preheating, 20 layers were melted by the laser (exposure) and 20 further layers were deposited without melting (isolation) while keeping the powder bed temperature at the initial value of 172 °C. The simulations were performed on parts with different cross-section [88]

Other studies [86,88,89] confirmed that crystallization takes place according to a sequence of dynamic non-isothermal steps induced by the contact with a fresh powder layer and quasi-static isothermal steps at T_b, as visible in the exposure region of the temperature profile in Figure 14. Therefore, the crystallization is further promoted by the undercooling effect induced by layer recoating (Figure

14) [28,86,88,89]. Finally, it is worth noting that the thermal history encountered by an individual part is specific because inhomogeneous temperature distributions within the build chamber (both at the powder bed surface and along the z-axis) are common in most SLS systems [89,90].

Porosity

The residual porosity and the quality of the interfaces between layers (Figure 10d), which cannot be completely avoided in the SLS process (but are not involved in conventional ones), depends on powder melting and consolidation. A schematic representation of the physical phenomena involved in the formation of melt pools are depicted in Figure 15 [91,92].

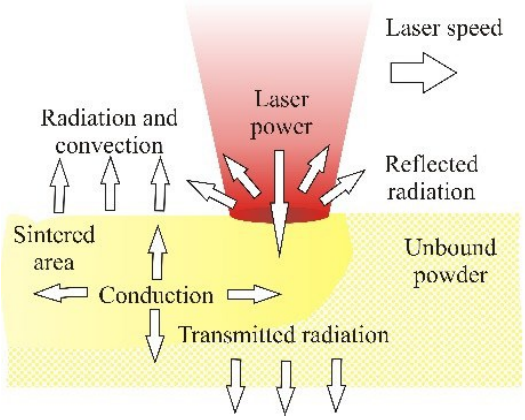

Figure 15: Schematic of energy transfer phenomena occurring in SLS [91]

The laser beam selectively scans the powder bed surface, thus delivering in a very short time interval (in the range of a fraction of milliseconds) the energy required to fuse the crystalline phase of the polymer particles [93,94]. The optical energy of the laser source is mostly converted into heat energy by absorption, while a minor amount is reflected or transmitted (Figure 15). The deposited thermal energy is then transferred inside the powder bed where the polymer particles are melted, thus created a melt pool in the scanned area. Heat transfer within the melted zone take places by conduction, while convection and radiation occur between the surface of the powder bed and the surrounding environment (Figure 15). Heat conduction depends on the thermo-physical properties of the polymeric powders and directly determines the thermal history and temperature distribution of the melted zones. Other heat sources, such resistance heaters and infrared lamps used to warm up the build chamber, are not directly related to the

melt pool formation, although they are responsible for the initial temperature of the unbound powder (Figure 15).

CO_2 lasers showing a wavelength of 10.6 µm are used in standard laser sintering machines because polymers have a high absorption capability in the mid-infrared (mid-IR) region of the electromagnetic spectrum. In fact, the molecular vibrational modes of a polymer are excited by mid-IR lasers, thus allowing to convert the optical energy of the radiation into heat. The granular nature of the powder bed, that consist of particles with similar size compared to the laser wavelength, greatly affects the laser/polymer interaction as well [95]. Diffuse reflection of the radiation caused by multiple scattering events at the particle/air interfaces occurs in the powder bed, in addition to absorption and transmission phenomena [95–97]. Figure 16 showed a simplified representation of these complex interactions according to the model proposed by Laumer et al. [98].

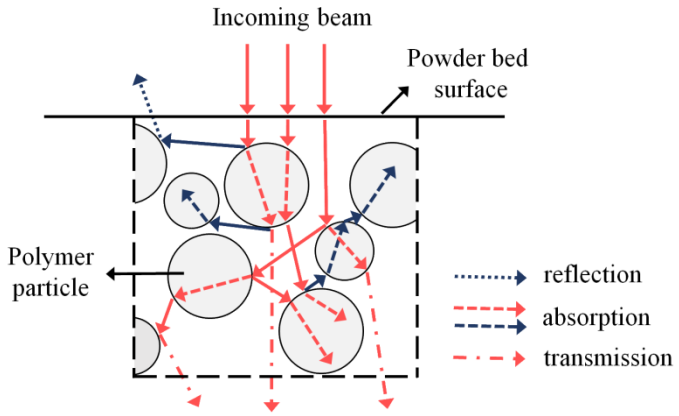

Figure 16: Simplified representation of the interaction between the laser beam and the polymeric powder bed in laser sintering, showing multiple reflections and absorption events as well as transmission through single particles. For ease of drawing ideal round particles are considered. Adapted from [98]

The laser radiation interacts with the powder bed in three different ways: reflection, absorption and transmission. Only a minor part of the incoming radiation is absorbed or reflected at the outer surface of the powder bed. The other photons are either reflected at the particle/environment interface or transmitted through the particle itself. In most cases, these rays repeatedly interact with adjacent powder particles along their ways till they are completely absorbed or reflected back towards the outer surface. The proportion between the radiation absorbed, reflected and transmitted by a single particle is strictly related to the chemical nature of the polymer itself because the absorption depends on the

vibrational motion of the macromolecules. For PA12 strong stretching vibration of the carboxyl groups (O-C=C) ensure high absorption coefficient at CO_2 laser wavelength (10.6 μm). Moreover, it should be noted that the numerous scattering events described in Figure 16 increase the probability of absorption. Owing to this model, Laumer et al. [98] explain why PA12 powders has higher absorption coefficient (0.94) compared to the bulk material (0.75) and to other polymers, such as polyethylene (0.67). Moreover, modeling studies based on ray tracing algorithms [95,99,100] proved that the laser beam propagates into the powder bed (along the z-direction) according to the Beer-Lambert attenuation law:

$$Q(z)=Q_o e^{(-\alpha z)} \tag{1}$$

where Q_0 is the initial intensity (or heat flux) of the radiation at the sample surface (W/m^2). The term $e^{(-\alpha z)}$ represents the exponential decay of laser power as a function of depth, where z denotes the position along the radiation path and α is the attenuation coefficient at CO_2 laser wavelength (m^{-1}). α is defined 1/OPD, where OPD is the optical penetration depth that corresponds to the distance at which the laser intensity is reduced to 1/e compared to its initial value [99]. Different studies [100,101] found that the attenuation coefficient is essential to determine the thermal energy distribution within the powder bed, thus confirming the strong relation between the physical processes sketched in Figure 8.

Conduction phenomena that govern heat diffusion in the powder bed and thus the thermal cycles generated by laser exposure can be physically described using equation (2):

$$\rho C_P \frac{\partial T}{\partial t}=\nabla(k\nabla T)+Q \tag{2}$$

where ρ, C_p and k represents the density, specific heat capacity and thermal conductivity of the polymer respectively and Q is the volumetric heat energy deposited by the laser source (W/m^3). The thermo-physical properties of the powder bed, usually evaluated by thermomechanical and calorimetric techniques, changes in relation to the polymer phase, temperature and porosity [102–104]. Various authors [101–105] reported that heat capacity, conductivity and density are linearly dependent from temperature, although a sharp peak due to the latent heat of melting for C_p and a step-like variation for k and ρ occurs at the solid-molten phase transition. Different literature studies investigated the spatial and temperature evolution of the melt pools as well as the effect of process parameters

through heat transfer models and experimental analysis. Riedlbauer et al. [103] studied the evolution of the melt pool on laser sintered PA12 powders carried out to measure the melt pools size by stereomicroscopy (Figure 17), while the surface temperature distribution was recorded via infrared camera. Numerical simulations based on the resolution of the heat transfer equation (equation (2)) using finite element (FE) method were developed to model the process (Figure 17). Both experimental and numerical analysis revealed that the temperature, width and depth of the melt pools increases when the energy density delivered by the laser is raised (test case 1 to 7) [103]. This corresponds to an increase in laser power and/or a reduction in scan speed.

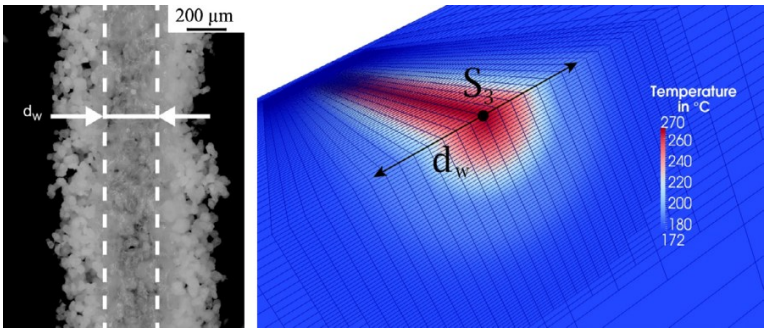

Figure 17: Example of experimental and numerical melting width for PA12 single lines produced with laser power of 3.3 W and scan speed of 1 m/s [103]

A similar behaviour was found for single scan track on polycarbonate [102], PA12 [92,101], PA6 [106] and PEEK [101] polymers as well as by heat transfer modeling of multiple laser tracks on carbon nanotubes (CNT) coated PA12 [104] and polyurethane powders [107]. Quantitative relationship between melt pools characteristics and laser energy density (E_D) were also drawn [94,106,107]. The maximum surface temperature and melting depth are approximately a linear function of E_d, while the melt pool width tends to reach a plateau as E_D increases according to a logarithm function [94,107]. Since melt pool size and temperature distribution affect the densification of the material, constraints conditions were identified for successful processing [104,106,107]. The melting depth should be between one and two times the layer thickness to avoid lack of fusion or excess of the re-melted material respectively. The melting width, related to the spatial distribution of the thermal energy deposited by the beam, should ensure sufficient overlapping between adjacent laser tracks in relation to the hatch spacing adopted (defined as the distance between two adjacent tracks). Moreover, the temperature should stay between polymer melting offset and thermal degradation onset [107]. This temperature interval, referred as “stable sintering region” (SSR) by Vasquez

et al. [108], can be determined by calorimetry and thermogravimetry analysis. Figure 18 graphically shown the stable sintering region for PA12.

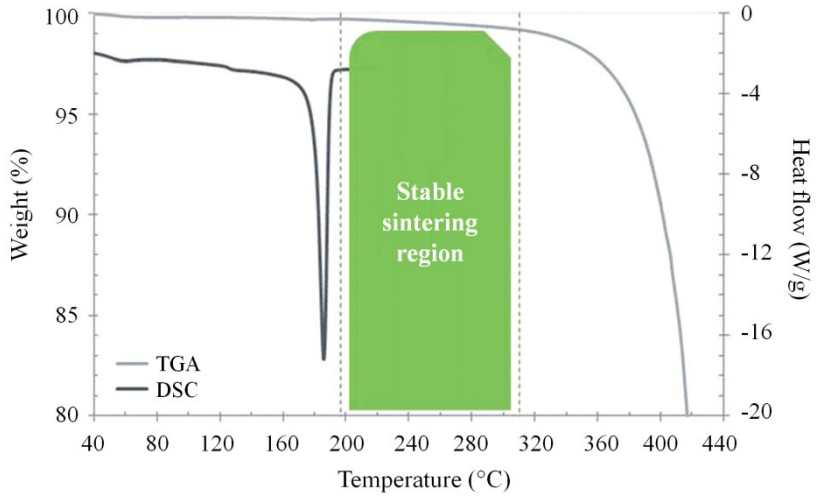

Figure 18: Graphical representation of the "stable sintering region" of polyamide 12 obtained from differential scanning calorimetry (DSC, right vertical axis) and thermogravimetric (TGA, left vertical axis) curves [108]

SLS experiments confirmed that the optimized parameters for CNT/PA12 and TPU parts lie within the energy density range determined by the constraint conditions [104,107]. Moreover, the tensile strength of TPU samples printed in the xy plane and along z direction are found to be proportional to the depth and width of the melt pool respectively [107]. These experimental and modeling results showed that the mechanical properties greatly depends on the laser-induced microstructure and consequently on process parameters, specifically on the energy density supplied by the laser beam to the polymer. This parameter has been used by researchers as a first attempt to optimize SLS processing conditions on PA12 material [109–113]. In fact, the increase in energy supply supports the melting polymer powders and minimizes void content, thus leading to denser parts with better mechanical performances. The amount of energy deposited by the laser beam in the powder bed can be expresses either as area energy density (known as the Andrews Number, J/mm^2) [109–112] or volume energy density (J/mm^3) [113]. The volume energy density is defined as follows:

$$E_D = \frac{P}{vSz} \tag{3}$$

where P is the laser power, v is the laser speed, S is the hatch spacing and h is the layer thickness. This parameter is a more general method of relating process

conditions to microstructure, void content and mechanical properties because it takes account of layer thickness contribution too. However, when the thickness of a powder layer is constant, both energy densities provide comparable positive correlation with mechanical properties of PA12 polymer [113]. Caulfield et al. [111] revealed that porous parts with poor mechanical properties and strong anisotropy were produced by using low E_D value. Solid, stronger and more isotropic samples were instead obtained when E_D is greater than 0.012 J/mm$^{2.}$. Similarly, Dupin et al. [68] reported a strong correlation between open and closed porosity and the energy delivered by the laser radiation due to improved particle melting. However, differences in pore morphology, size and distribution were observed due to the diverse morphologies and chemical structure of precipitated (Duraform PA) or directly polymerized (Innov PA) PA12 powders [68]. Starr et al. [113] found that elastic modulus and yield strength of PA12 parts sharply increased with E_D up to 0.12 J/mm^3 where a plateau is reached. However, the elongation at break still increases because it is more sensitive to small number of defects in the interlayer regions [114]. A similar improvement of mechanical properties with increasing E_D was observed for several polymers, including polyamides [91,115–117], polypropylene [36,37,118], polyurethane [54,55,107], polycarbonate [110] and polystyrene [63]. However, in most studies the process parameter optimization is based on trial and error printing jobs varying one laser parameter at a time. Although various methods, such as design of experiments (DOE) [37,116,117] and response surface methodology (RSM) [119–121], can be applied to explore the relation between process parameter and part performances, this operating way is costly, time and material-consuming and, mostly, neglect the properties of the polymeric powders. The “energy melt ratio” (EMR), defined as the ratio between the energy density applied by the laser (E_D) and theoretical energy required to fuse a single powder layer (E_m), was then proposed in [113] to compare in a more comprehensive way the process parameters, including the effect of build temperature. The material thermo-physical properties as well as powder bed temperature and packing density were considered to calculate E_m. Vasquez et al. [122] extended the use of EMR on the basis of the stable sintering region concept (Figure 18). A convenient processing window was then established between the energy to melt and degrade the polymer respectively. Mechanical testing showed that the tensile strength and elongation at break of PA12 parts gradually improved at increasing E_D values up to the polymer degradation limit. Amado [70] confirmed that high energy density can induce the thermal decomposition of the material, leaving pores generated from gas evolution in the printed sample. Values between 0.20 and 0.25 J/mm^3 were suggested for common

thermoplastic polymers in order to achieve density above 95% [70]. Berretta et al. [49] employed the SSR method proposed in [122] for predicting the process conditions for SLS of high temperature polymer (PEEK) from powders characteristics. As usual, a positive correlation between tensile strength and E_D was reported. However, it seems that the predicted thermal decomposition point does not capture the degradation of the part mechanical performances. The authors suggested that the discrepancies between the fast thermal cycles due to laser scanning and thermogravimetry test (heating rate at 10 °C/min) can explained the results [49]. Yuan et al. [123] improved the method by considering the temperature-depended density and heat capacity of the powders. As shown in Figure 19a, the tensile strength of sintered 0.5 wt.% CNT/PA12 composites tend to saturate above a critical E_D value. This threshold has been related to the material densification as higher strength are reached when the particles are fully coalesced so that no voids or un-molted powders in the interlayer regions appears (Figure 19b and 19c). The author also stated that polymer decomposition is not an issue since the optimized E_D is well before this limit [123].

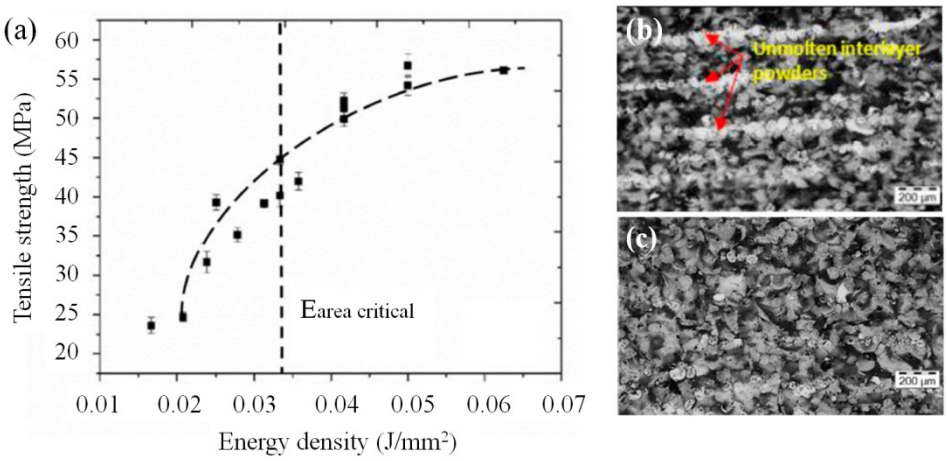

Figure 19: (a) Effect of energy density on tensile strength of CNT/PA12 samples printed in the XY plane and microstructure of parts produced using energy density (b) below (0.271 J/mm^2) and (c) above (0.417 J/mm^2) the threshold value [123]

Apart from polymer melting, full coalescence of the adjacent particles should happen to ensure bonding between them and reduce porosity [83]. Since no external forces, except gravity, are applied to the polymer melt during the process, the driving forces for particle coalescence are the viscous flow of the molten polymer at zero shear conditions and the temperature history of the melt pools. The simplest model to describe the coalescence between two perfectly spherical particles was proposed by Frenkel et al. [124]. The model relates the coalescence

rate dθ/dt at a given temperature to the surface tension and zero shear-rate viscosity of the polymer melt:

$$\frac{d\theta}{dt} = \frac{x}{r} = \left(\frac{3\gamma}{2\eta_0 r}\right)^{1/2} t^{1/2} \quad (4)$$

where x corresponds to the neck radius between the adjacent particles, r is the initial radius of the particles and t is the sintering time. A simple representation of the various step of the coalescence process is displayed in Figure 20 [125].

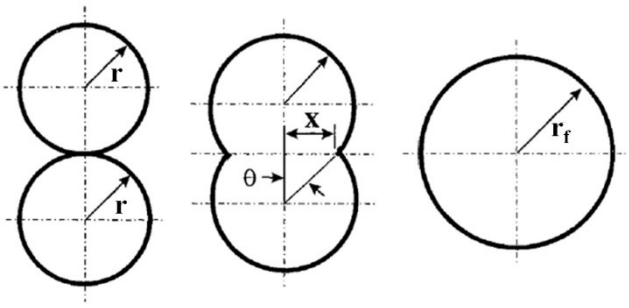

Figure 20: Schematic representation of particle coalescence according to Frenkel's model [125]

The function dθ/dt is proportional to the surface tension (γ) and inversely proportional to the zero shear viscosity in molten phase (η_0) and particle size (r). Surface tension is almost independent from both temperature and polymer nature (35 mN/m for PA12 powders [126]). Therefore, viscosity is the main factor that affect powders coalescence. Since η_0 decreases exponentially with an increase of temperature, the particle neck growth is faster at high temperatures. Conversely, at lower temperatures longer sintering time is needed to achieve the same extent of particle coalescence. Therefore, the degree of polymer densification in the SLS process is mainly affected by the thermal history of the powders in the molten phase, which in turn is influenced by the process conditions (e.g., laser exposure parameters, scanning strategy, etc.) [22,105]. For a better picture of particle neck growth during sintering hot stage microscopy (HSM) is used [55,57,127–130]. Typical images are shown in Figure 21, where the dynamic evolution of powder coalescence at increasing temperature can be observed on a hot stage. The sequence, recorded through time-lapse photography, shows how the contact areas between two distinct particles gradually expands and the neck start to grow up to the creation of a single particle.

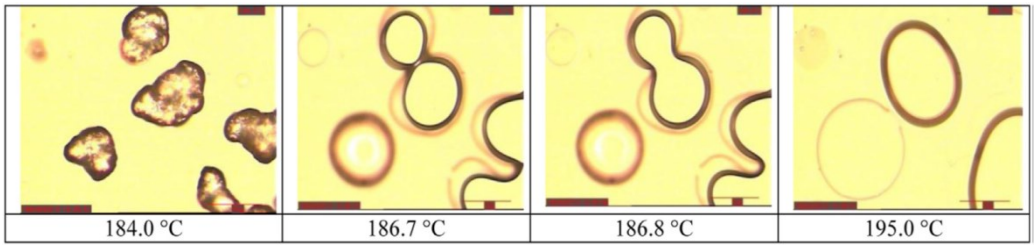

Figure 21: Coalescence of PA12 particles at high temperature observed by Hot Stage Microscopy [55]

Warpage

Another issue concerns the thermal distortion of the parts due to excessive energy inputs. This may reduces the geometric accuracy of the sintered objects and even lead to sever distorsion such as warpage (Figure 10d). Shen et al. [104] proposed from empirical observation an upper temperature limit of 300 °C for CNT/PA12 melt pools, otherwise the particles surrounding the parts may be also melted and the part lose in dimensional accuracy. In some cases, the high thermal stresses induced by overheating of the melt pools has been reported to induce warpage deformation (Figure 10d) and low dimensional accuracy, mainly in the z-direction [75,91,131].

2.3.3 Carbon fiber reinforced polymer composites processed by SLS

Since SLS relies on powder bed technology, short carbon fiber can be easily added to form powder mixtures with a polymer matrix. Goodridge et al. [132] processed carbon nanofibers/PA12 powders, produced by melt mixing and cryogenically fracturing, using EOS P100 Formiga SLS machine. Although uniform fiber dispersion and modest improvement of storage modulus was achieved, the powder production technique adopted was considered not suitable for SLS feedstock. In fact, particle with irregular morphology, leading to a rough powder bed surface, were produced. Therefore, short fibers are usually added to polymeric powders that were previously synthesized (the most widely used is PA12) using simple mechanical mixing by means of powder dry blenders. Before blending fibers are usually chemically treated to modified their surface characteristics in order to achieve improved interfacial adhesion with the matrix. Dry mechanical mixing usually results in fiber average lengths of about one hundred micron or less [1]. The addition of carbon fibers has an important effect on the physical phenomena involved in the SLS process (Figure 8) because their

morphological and thermo-physical properties highly differ from those of the polymer matrix. The geometry of the fibers and their high aspect ratio is expected to lower the flowability of the powders, as it happens by using graphite platelets [133]. However, this effect does not compromise the processability of carbon fiber reinforced polymeric powders as homogeneous and smooth powder layers were observed in literature [134,135].

When a IR radiation, such as CO_2 lasers used in SLS systems, irradiated a fiber polymer composite the optical energy supplied by the radiation is strongly absorbed by the carbon fibers, that are more rapidly heated with respect to the matrix [136]. As a result, the absorption coefficient of fiber reinforced PA12 powders is even higher (0,96 as proposed by Shen et al. [104] for CNT/PA12 powders) compared to the neat polymer. Various studies [27,82,133,137,138] indicated that the addition of absorbing fillers, such as carbon fibers, decreases the penetration depth of the CO_2 laser because the incoming beam is mostly absorbed closed to the powder bed surface, without further propagation into deeper positions along the z-direction. Tian et al. [27] used a modified numerical model of heat transfer integrated by experimental analysis to investigate the laser sintering process of different PA12 composites powders. The variation of the transmitted laser power (P) across a powder layer, performed via the experimental device sketched in Figure 22a, showed that the optical properties and the laser attenuation behaviour with depth for PA12 powders reinforced with 40 wt.% carbon fibers is similar compared to the neat polymer.

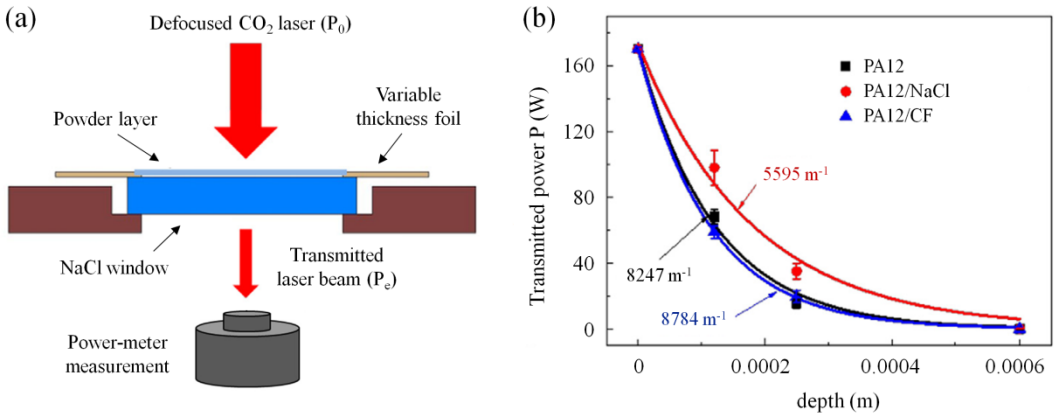

Figure 22: (a) Graphical illustration of the experimental device used by Tian et al. [27] to determine the transmitted laser power across a powder layer with variable thickness; (b) comparison between the laser power transmission of PA12, PA12/CF and PA12/NaCl powder bed. The continuous lines put in evidence the Beer-Lambert law fitting performed to calculate the attenuation coefficient. Adapted from [27]

The exponential decay of the transmitted power along the z-direction, modelled using equation (1), revealed only a small difference in the attenuation coefficient between PA12/CF (8247 m^{-1}) and PA12 (8784 m^{-1}) (Figure 22b). Conversely, the addition of sodium chloride (NaCl) highly impact on the laser energy attenuation since this filler is almost transparent to the laser radiation (Figure 22b) [27]. However, the simulated thermal profile of a single scan track revealed that the melt pool dimensions and maximum temperature (T_{max}) are higher for the fiber reinforced material. For example, melting depth increases from 112.5 μm for neat PA12 to 130 μm for PA12/CF when a laser power of 10 W is used [27]. The lower melting enthalpy and higher thermal conductivity attained of the composite powders were accounted for this difference. Melt pool size and temperature remarkably increase with laser power, thus leading to a better interlayer adhesion and fiber/matrix impregnation, that are key factors to obtain the highest performances for SLS composite parts. The maximum flexural properties were obtained using very high laser power (21 W) with an overall enhancement of modulus and strength of 360% and 100% respectively compared to PA12 parts [27]. Comparable findings were also reported in [139] by modeling heat transfer phenomena during single laser scan in PA12/CNT powder bed. The improved heat conductivity of the material result in higher density. Similarly, Flodberg et al. [140] attributed the reduction in void content (from 4.7% to 0.7%) and their size distribution between pure PA12 and fiber reinforced PA12 parts printed by SLS to the higher laser absorption and heat conductivity of the mixed powders. Consequently, the incorporation of fibers greatly improves the strength of pure nylon 12 samples in both horizontal (x-axis) and vertical (z-axis) printing directions [140].

Apart from flowability, optical and heat transfer properties, the incorporation of fibrous reinforcements to neat polymers causes an increment of the melt viscosity. This phenomenon arises from the interaction between fibers and polymer macromolecules, as the former hamper the motion of the polymer chains. Yan et al. [141] found that adding carbon fiber to polyether ether ketone (PEEK) powders gradually increases the zero-shear viscosity of the polymer. The same numerical model developed in [27,104] was employed to assess the temperature distribution after laser scanning. The authors coupled rheological measurements (η_0 values of the neat and carbon fiber reinforced PEEK powders at different temperatures) with heat transfer simulations to define high and low viscosity regions inside the melt pools (Figure 23a). These regions take into account the different dynamic of coalescence as the higher viscosities slow the coalescence

rate, as described in equation (4). A threshold η_0 value (10^5 Pa s) was chosen to delimit the low viscosity area, also referred as "effective melting zone" since particle coalescence is favoured, because it is considered the upper bound for injection molding of polymer composites [141] (Figure 23a).

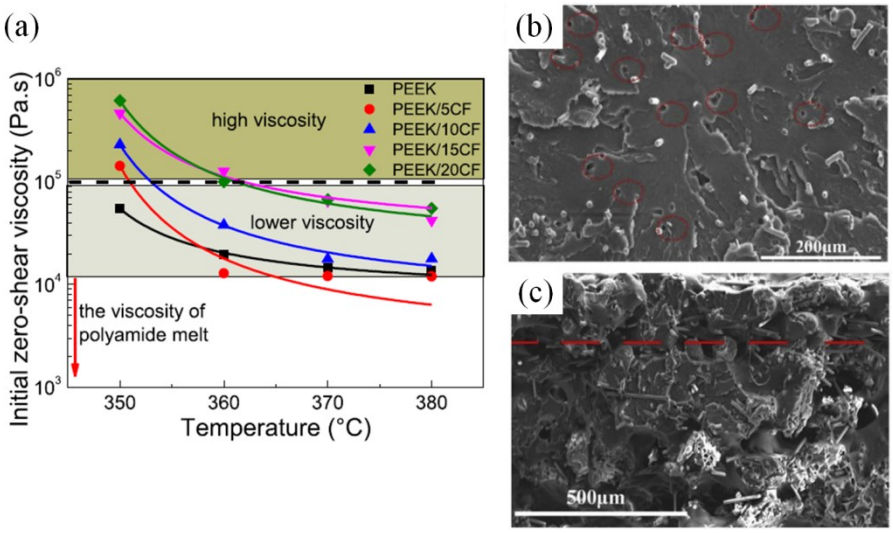

Figure 23: (a) Zero shear viscosity versus temperature of PEEK/CF composites and pure PEEK powders and FESEM images of the fracture surface of the composites with (b) 10 wt.% and (c) 15 wt.% fiber content, showing the different material microstructure. The isoviscous line at 10^5 Pa s, delimiting high and low coalescence rate zones, is outlined in Figure 23a [141]

It was found that the features of the effective melting zone, where the temperature is higher than the isoviscous threshold (Figure 23a), are highly significant for achieving high density and mechanical properties. In particular, a melting depth 20% higher than the layer thickness ensures optimal interlayer bonding because partial re-melting of the previous layer occurs [141]. Since the effective melting zone depth decrease from 200 μm for the neat polymer to 135 μm upon adding 5 wt.% and 10 wt.% of fibers, higher laser energy is required to process PEEK/CF powders. Dense composite parts with elastic modulus and tensile strength equal to 7.36 GPa and of 109 MPa respectively (corresponding to 62% and 22% improvement over neat PEEK) were produced by increasing laser power to 18.5 W and decreasing layer thickness to 100 μm (that is 20% lower than the effective melting zone depth) (Figure 23b). However, higher fiber content yields to parts with large voids and poor interlayer bonding (Figure 23c) [141]. A comparable trend has been reported for 5 wt.% carbon black/PA12 powders, as

the final composite parts displayed lower mechanical properties compared to pure PA12 ones using the same process conditions [138].

Crystallization is the less studied physical aspect of fiber reinforced composites produced by SLS. Although the presence of carbon fibers has been proved to promote polymer crystallization by reducing the energy barrier for nucleation, their effect on the overall crystallization kinetics is still to be understood. Lanzl et al. [142] reported that the crystallization rates of PA12 powders at T_b are increased by adding glass fibers (GF) as the they act as heterogeneous nucleation sites for polymer lamellae. By contrast, Arai et al. [143] found only small differences in crystallization behaviour by adding short GF to polybutylene terephthalate powders. Nevertheless, Yan et al. [134] demonstrated that the processability of PA12/CF composites is still adequate up to 50 wt.% fiber addition as no part distortion and homogeneous powder spreading occur. In this work, uniform fiber distribution as well as proper powder morphology and fiber/matrix interfacial adhesion was obtained using a dissolution–precipitation process where carbon fibers are functionalized with acid surface treatment and then coated with PA12 [134]. PA12/CF samples showed a great improvement of both flexural strength and modulus (44% and 93% respectively for 30 wt.% fibers) with respect to the pure polymer counterpart (Figure 24a). The surface fracture morphology also revealed that dense microstructure (relative density up to 95% for complex structures with 0.6 mm thin walls) and high interfacial shear strength owing to the presence of pulled-out fibers coated with the matrix were achieved (Figure 24b) [134].

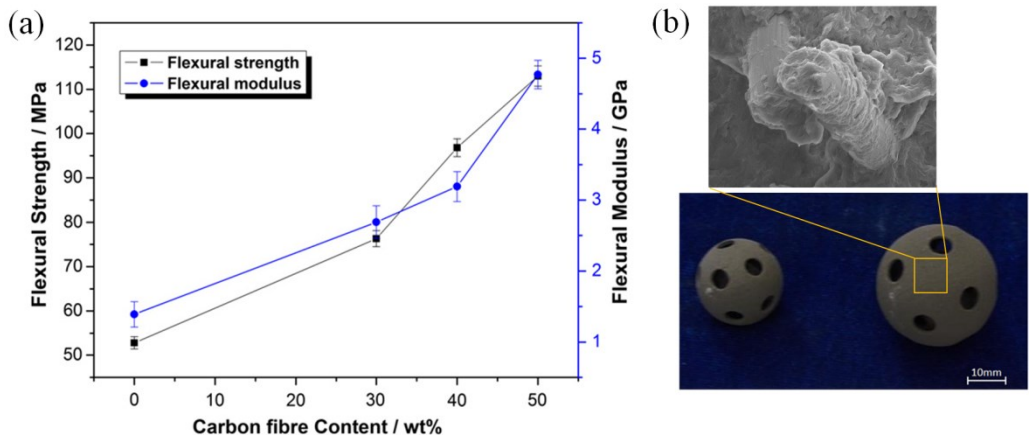

Figure 24: (a) Effect of carbon fiber content on the flexural properties of PA12/CF parts produced by SLS and (b) complex thin walled parts made with 30 wt.% fibers composite with detailed microstructural characteristic [134]

A similar approach was used by Jing et al. [144] to improve the wettability between carbon fibers and polyamide 12 matrix. Nitric acid (HNO_3) treatments were performed to modify the surface of the fibers by adding oxygen groups and causing additional roughness. However, considerable porosity (38%) and low part strength was observed after SLS because these functional groups partly decomposed at the process temperatures. The released gas remains entrapped in the microstructure thus forming large pores. To surpass this drawback, the fibers were further heated to 400 °C for 2 h in N_2 atmosphere before mixing with PA12 particles. In this way, the void content was significantly reduced (4.7%) and the elastic and strength properties were improved by 11% and 5% in both tensile and bending load cases compared to the untreated CF/PA12 composites [144].

It is worth noting that carbon fiber reinforced polymers produced via SLS frequently exhibit high anisotropy in mechanical properties in relation to the build orientation. Jansson and Pejryd [145] analysed the microstructure and tensile behaviour of PA12/CF parts fabricated in six different directions within the build chamber. The highest mechanical properties (66.7 MPa of strength and 6.3 GPa of elastic modulus) were achieved for the sample printed in the x-direction (i.e., moving path of the rake used to spread the powders). In fact, the fibers tend to be oriented along this direction by the interaction with the recoating system. Thus, the fiber alignment is tough to be responsible for the differences in material properties in the build plane, while the pores between the layers negatively affect the properties of the samples in the z-direction [145]. Similar results were reported in other studies on SLS-processed carbon fiber reinforced polyamide 12, where strong anisotropic behaviour was observed in the printed parts due to the fiber orientation and interlayer interfaces characteristic [140,146,147]. In particular, tensile strength and modulus are almost halved in the vertical direction (z-axis) compared to the horizontally printed parts (x-axis) [140,146,147]. Khudiakova et al. [147] further investigated the anisotropy of this material by a comprehensive evaluation of tensile behaviour, microstructure and fiber orientation using microscopy and x-ray computed tomography techniques. A reduction of mechanical properties was observed at increasing divergence from the x-axis (moving direction of the recoating system) and at increasing z-axis components (printing orientation normal to the build plane) (Figure 25). These findings are supported by the preferential fiber alignment along the build plane (and here in the recoater moving direction) captured by the analysis of fiber orientation tensors and the typical failure mechanisms of the samples printed in different spatial directions. The fracture of xz-0° parts (fiber/load alignment) is

controlled by fiber-matrix interfacial shear strength as extensive fiber pull-out was observed. By contrast in xz-90° parts, the load was mainly bore by the matrix since the fibers are perpendicular to the applied stresses and matrix failure favoured by the weak interlayer bonding occurred [147].

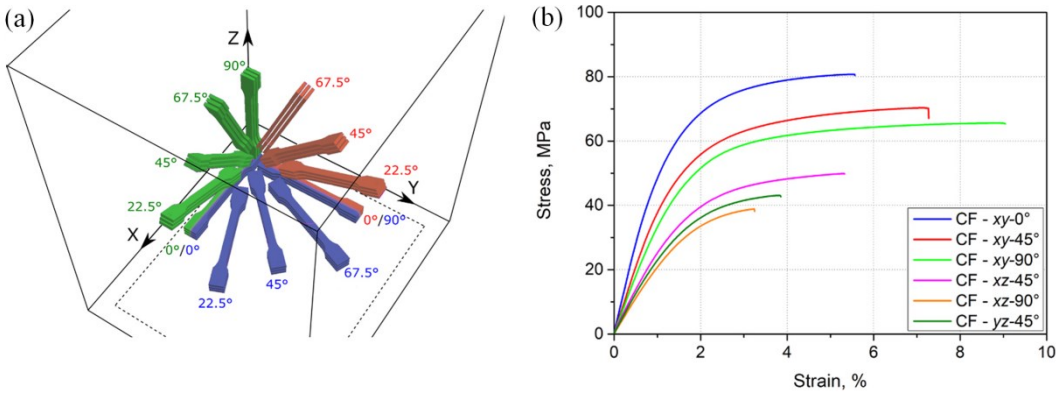

Figure 25: (a) Graphic representation of the spatial orientation of the tensile specimens in the SLS build chamber and (b) resultant stress-strain curves. The recoater moves in the x-direction [147]

The importance of fiber alignment as well as fiber content on the mechanical properties of SLS-processed fiber reinforced polymers was confirmed in [148], where a computational model based on finite element and homogenization methods was developed to characterize the structure-property relationship in PA12/CF parts. The numerical framework, that takes account of fiber orientation and voids and is based on the constitutive models for each composite phase, accurately simulates the mechanical properties and failure processes (i.e., crack propagation) of the printed parts. However, since anisotropy is undesirable in most applications, a novel type of PEEK/CF powders was developed in [149,150] by encapsulating the fibers in the polymer matrix via ball milling. This method granted a homogeneous fiber distribution throughout all spatial directions and improved mechanical isotropy compared to the parts fabricated from commercial dry-mixed powders. Moreover, flowability test revealed that milled powders has good behaviour even when compared to commercial PEEK [149].

The influence of individual process parameters on the quality of carbon fiber reinforced PA12 parts fabricated by SLS was studied in Czelusniak et al.'s work [151]. Design of experiments was applied to systematically investigate the relationship between these factors and selected responses, such as density, mechanical and dimensional properties of the final parts as well as manufacturing

time. Response surface modeling shows a complex interdependency between the process parameters. Dimensional accuracy was found to mainly depends on laser speed and scan spacing. Improved density and mechanical properties were achieved in the direction of higher laser power and lower scan speed and scan spacing. However, if too much energy is transferred to the powders, density and dimensional accuracy are reduced due to polymer thermal decomposition and undesired consolidation of the particles surrounding the scanned region respectively. The author stated that all parameters are important for determining part properties. Moreover, multi-objective optimization showed that the choice of process parameters depends on the criteria adopted. For example, high values of laser power and medium to high scan speed and scan spacing are required to obtain the best trade-off between mechanical performances and dimensional accuracy [151].

2.4 Fused Filament Fabrication (FFF)

2.4.1 Technology and materials

Fused Filament Fabrication (FFF) is one of the most extensively used AM techniques for polymers; it offers many advantages such as low-cost, high speed, convenient and fast operation, and large availability of raw materials (i.e., thermoplastic polymers and polymer-based filaments). Through FFF process, it is possible to manufacture three-dimensional (3D) parts directly from a digitally programmed design via extrusion and deposition of a thermoplastic polymer filament in a layer-wise manner (Figure 26).

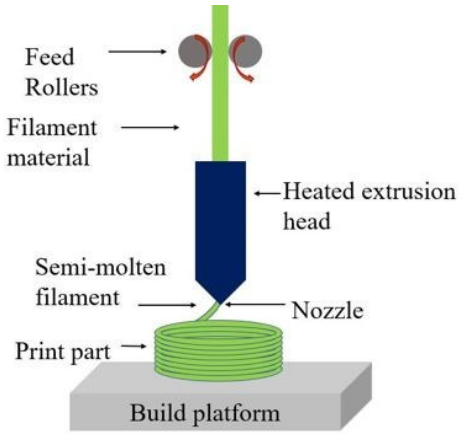

Figure 26: Schematic representation of fused filament fabrication technology. The printing head moves across the build platform to create the part layer-by-layer [152]

The polymeric thread is heated inside the printing head by resistance heaters in order to reach a predefine temperature and then extruded using a steel or brass nozzle. The extrusion temperature is usually set slightly above the polymer melting point to achieve the ideal viscosity for polymer extrusion. The printing head moves along the xy plane to deposit the molten thread onto the build platform in a raster pattern according to the CAD geometry and the "gcode" file settings. In this manner, each layer is created (Figure 26). The build platform then lowers along the z axis by the selected layer thickness, thus allowing the fabrication of the final object one layer at a time [1].

Amorphous and semi crystalline thermoplastic polymers, such as acrylonitrile butadiene styrene (ABS), polycarbonate (PC), acrylonitrile styrene acrylate (ASA), Polylactic Acid (PLA) and polyamides (PA6 and PA12) are the most employed feedstock filaments for FFF technique (Figure 27) [152].

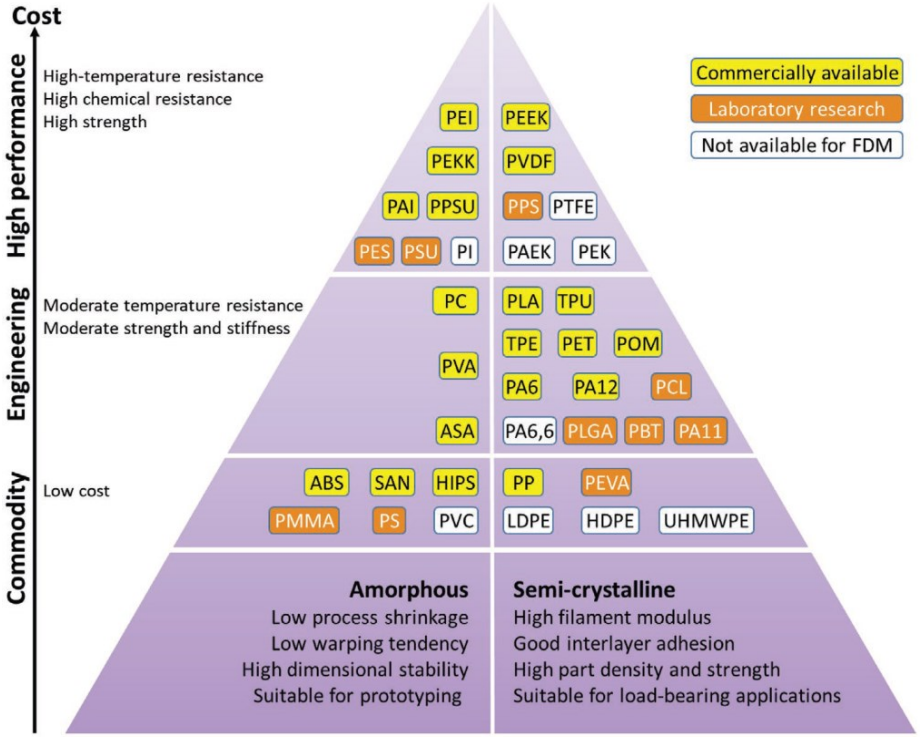

Figure 27: An overview of polymer filaments for FFF that are commercially available or have been reported in scientific literature. The materials are classified according to the "polymer pyramid" as commodity, engineering or high-performance amorphous or semi crystalline polymers. The abbreviations listed in this figure that are not already cited in the text are: polyethylene vinyl acetate (PEVA) and poly(lactic-co-glycolic acid) (PLGA) [65]

Low material and printer cost, simplicity of use and the ability to fabricate parts with good mechanical properties are the main advantages of FFF process. Typical strength values between 40-60 MPa and Young modulus of 1-3 GPa can be obtained by using engineering polymers such as polyamides [152]. On the other hand, strong anisotropic behavior, poor surface quality and relatively low productivity represent the major drawbacks of this technology, whose application is mostly restricted to prototyping and tooling [17,19,20]. In recent years, high performance thermoplastics, such as polyphenylene sulphide (PPS), polyether imide (PEI) and polyether ether ketone (PEEK), were successfully printed via FFF for aerospace and tooling applications, aiming at reducing fabrication costs and times (Figure 27) [18,20]. However, these filaments usually require specific machines, equipped with high temperatures printing heads and enclosed chambers heated at relatively high temperatures (above 100 °C) to be processed [20,53]. FFF technology has the potential for the development of multifunctional parts coming from the deposition of several materials simultaneously through multiple extrusion nozzles [1,18]. Moreover, this technique can be easily employed for the fabrication of thermoplastic polymer composites filled with fiber or particulate reinforcements. Ceramic, metallic or carbon based fillers are added to FFF feedstock by single screw extrusion in order to obtain homogeneous dispersion and distribution into the polymer matrix, thus allowing an enhancement of the overall properties of the printed polymeric parts [14,18,20]

To improve the mechanical and functional properties of the final parts, the influence of the key physical phenomena that characterized the printing process on the part quality need to be explained. Figure 28 illustrates these physical phenomena, from filament feeding and pressure-driven polymer flow inside the liquefier to coalescence between the deposited filaments (also known as beads or roads) and material solidification [26].

Viscosity, surface energy and extrusion temperature are the most important parameters that govern polymer flow inside the liquefier. Generally, polymers with high viscosity at low shear rates (i.e., yield stress characteristics) followed by a shear thinning behaviour, that correspond to a reduction of melt viscosity at increasing applied stresses, are advised for FFF processing [153,154]. On one side, high yield stress values prevent undesired polymer flow by gravity before the pressure is applied, as it happens during print preparation or when the extruder moves across the build platform without printing [153]. On the other hand, shear thinning behaviour will decrease polymer viscosity to ideal values without overly varying the temperature, as typical shear rate values inside the nozzle are about

10^2 and 10^4 s^{-1} [153,155]. Excessive temperatures may degrade the polymer and hamper the formation of beads with stable geometry and supporting abilities for the subsequent layers (inset of Figure 28), while high viscosity values will lead to flow instability due to filament buckling (Figure 28) or even process failure.

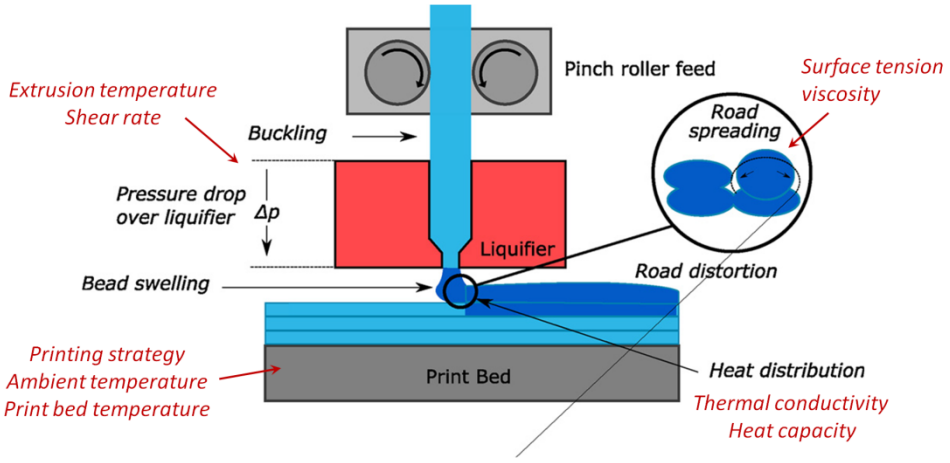

Figure 28: Detailed illustration of the key physical phenomena of the FFF process of polymeric filaments. Material and process parameters influencing these phenomena are also highlighted in red colour. Beads coalescence dynamic is sketched in magnified view to highlight surface contact between beads. Adapted from [156]

The thermo-physical properties of the polymer, such as thermal conductivity (k) and heat capacity (C_p) are also relevant to determine how the coalescence between extruded beads develops. Since filament deposition occurs only for gravity forces, the bond between beads, both side by side and layer by layer, is created solely by thermal-driven viscous flow and molecular diffusion of polymer chains [25,26]. Therefore, surface energy, viscosity at zero shear rate and temperature profile at the inter-bead interface are critical factors for coalescence dynamics. Several studies [157–162] clearly showed that elevated temperature and long exposure time to these temperatures favour wetting and coalescence between the deposited filament and coalescence with the adjacent beads though diffusion of the polymer chains across the interface (inset of Figure 28). High values of k and C_p would enhance heat transfer, thus improving coalescence as the previously laid material is heated up rapidly by the filament that has just exited the nozzle [25,26,156]. Moreover, a low glass transition temperature (T_g) and a large separation between melting and crystallization events (for semi crystalline polymers) are foreseen to enhance the mobility of the macro molecular chains and enhance interlayer adhesion. However, the strong variation of polymer viscosity with temperature and shear rate restricts the temperature and time intervals ideal

for achieving optimal coalescence between beads and successive layers. In fact, the convective heat losses to the surrounding environment (at the build chamber or ambient temperature) promote rapid heat dissipation and high cooling rate during part fabrication [26].

Coefficient of thermal expansion (CTE) and volumetric shrinkage play also a role in the development of residual stresses during solidification, that could eventually alter the shape and dimensional accuracy of the final parts [20,26]. FFF process is particularly prone to the accumulation of thermally-induced residual stress owing to the high CTE of thermoplastic polymers (between 40 and 120 μm/m/°C [154]) and large temperature gradients that develop among layers. In fact, upon cooling the material gradually start shrinking. As a result, internal stresses are generated by the continuous changes in material stiffness upon solidification and the constraint represented by the bonds between the beads. If the value of residual stresses surpasses either the stiffness of the printed layers or the adhesion force between the bottom layer and the build platform, the part bends upward [154,163] as showed by the large scale distortion of neat PP samples in Figure 29a [164]. The high value of CTE and the semi-crystalline structure of PP was deemed as the main driving factors for shrinkage and residual stress accumulation [164–166]. However, the addition of fillers, such as natural fibers, minimizes residual stress built-up by reducing the orientation of the molecular chains and inhibits, up to a certain degree, the polymer shrinking [153,164,166]. This will lead to a significant decrease of part distortion (Figure 29b).

Figure 29: a) Distortion of FFF printed neat polypropylene part and (b) reduction of shrinkage and distortion by adding 30 wt.% hemp fiber to PP [164]

Apart from the previously cited process parameters, a major manufacturing variable is the raster angle, defined as the angle between the deposited bead and the x-axis (Figure 30), which leads to different features on the meso-scale for the printed parts.

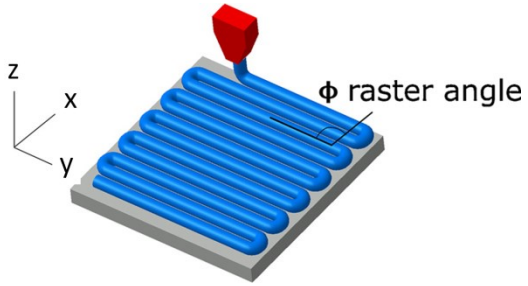

Figure 30: Schematic showing the definition of raster angle, that determine the orientation of the extruded beads in the FFF process [156]

A detailed view of the surface fracture of ABS sample produced using different raster angle values (Figure 31) clearly showed that orientation of the beads have a strong effect on the microstructural features as well as on the mechanical properties and failure morphologies of the fabricated specimens [152,167]. As a result, FFF parts behaves similarly to orthotropic fiber reinforced laminates with significant variation of stiffness and tensile strength in the transverse (y-axis) and out-of-plane (z-axis) direction compared to the bulk polymer. The former direction suffers from poorer performances because the interfaces between layers are weaker [19,20,26,156].

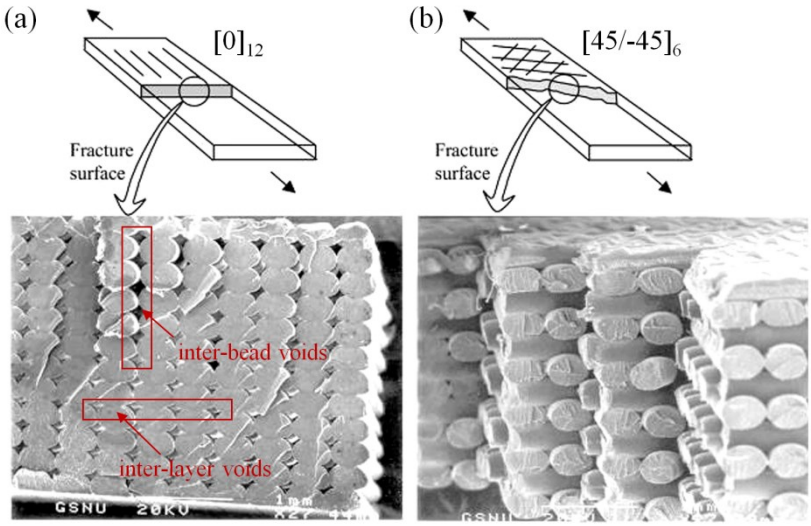

Figure 31: Scanning electron microscopy (SEM) micrograph of the fracture surfaces of ABS specimen printed with different raster angle orientation: (a) [0] and (b) [45/-45]. The images revealed the typical mesostructure of neat polymeric parts manufactured via FFF (inter-beads and inter-layer interfaces) and the effect of raster angle on the microstructure and failure behaviour of the printed parts [167].

Moreover, it is worth noting that several interfaces are present in the fracture surfaces (Figure 31). Inside each layer beads are contiguously laid down, thus creating inter-bead interfaces. Each layer is deposited on top on the previous, forming successive interlayer interfaces. Owing to these interfaces and the consolidation mechanism previously described, voids cannot be avoided (Figure 31). The presence of inter-bead and inter-layer voids is widely recognized as one of the most important defect related to material extrusion AM processes and it ultimately leads to inferior structural performances and anisotropic mechanical behaviour [19,20,26,156].

2.4.2 Carbon fiber reinforced polymer composites processed by FFF

Fused filament fabrication is well suitable for processing short carbon fiber reinforced thermoplastic polymer composites. In fact, reinforced filaments can be manufactured with well-established techniques such as single or twin screw extrusion by mixing chopped or milled fibers with polymer pellets. The composite shreds are then processed in the FFF machine to create 3D components. The printers need only minimal hardware modification such as the usage of hardened steel extrusion nozzles due to abrasiveness of the fibers [168]. Several short carbon fiber reinforced filaments based on thermoplastics matrices including ABS, PLA, PC, PETG, PEI, PEEK and different polyamide grades are today commercially available and printable using both desktop or industrial 3D printers [169].

Discontinuous fiber reinforcements in FFF filaments has been widely investigated since the early years of this century. Shofner et al. [170] fabricated ABS composites with vapour-grown carbon fibers by Banbury mixing, filament extrusion and FFF printing. The authors found that this manufacturing sequence was able to produce parts with an uniform fibers distribution and alignment, low pore content and increased tensile properties, at the expense of flexibility. In the next years, several research works have presented relevant enhancements of the mechanical performances and geometrical accuracy of various polymers produced using FFF technology by adding short carbon fibers into the feedstock filament [11,20,25,26]. In fact, carbon fibers (CF) play an important role not only to enhance the stiffness and strength characteristics of the neat polymer but also to improve the dimensional accuracy of the printed parts, as reported by Duty et al. [171]. For example, an increase between 3 and 4 times of tensile strength and Young's modulus along the printing direction by incorporating 13 wt.% carbon

fibers to an ABS polymer matrix can be achieved [171]. Moreover, the thermal properties of the printed specimens were also altered by the incorporation of the reinforcement. Specifically, the coefficient of thermal expansion of the filament was reduced from 87 μm/m·K of neat ABS to 10 μm/m·K for the composite material [171]. Conversely, a 3-fold increase of thermal conductivity along the printing direction was achieved (0.177 W/m·K and 0.397 W/m·K for neat and reinforced filament respectively) [171]. These differences in the thermo-physical properties of the starting filament could limit the occurrence of dimensional inaccuracies and distortion in the final object and concurrently the risk of print failure. However, Compton et al. [172] found that the temperature of the top layer needs to remain above the polymer glass transition point (T_g) in order to avoid, or at least reduce, distortion in ABS/CF parts processed using BAAM printer. If this temperature approaches or falls below T_g during the deposition of the following layer, the printed part exhibited significant out-of-plane deformation and, in some cases, layer delamination [172].

A detailed review on the FFF process of SCFRP composites was carried out by Brenken et al. [26]. The authors found that most of the published literature is focused on PLA and ABS composites [25,26]. A significant increase of tensile modulus and strength was frequently achieved for these materials compared to the pure polymers**.** Strength at break values usually ranges from 30 to 70 MPa depending on the length and volume fraction of fibers in the feedstock filaments [25,26]. However, typical average lengths of the carbon fibers employed within the feedstock are limited to 100 μm or less because the fibers are broken by the severe shear conditions experienced during filament manufacturing by using common extrusion processes [1]. Moreover, long fibers are not advised as they are more prone to clog the orifice of the extruder during printing [25]. The best mechanical performances were observed for high performance polymer composites based on PEEK and PEI matrices. The highest tensile modulus for short carbon fiber composites (24.5 GPa) was obtained to date by DeNardo [173] by using polyphenylene sulphide (PPS) reinforced with 50 wt.% carbon fibers**.** This weight proportion between reinforcement and matrix, which is the highest reported until now for this technology, is reasonably expected to be responsible for the tremendous increase in modulus with respect to the neat polymer. The highest tensile strength (135 MPa) was instead achieved by Yang et al. [174] by annealing at high temperature (300 °C) a 10 wt.% CF/PEEK composite processed by means of a common FFF printer (without heated chamber). The authors suggested that high crystallinity (35% against 21% of the as-printed material) and

the limited amount of porosity have contributed to these performances. By contrast, the elongation at break suffers from a significant reduction (50x) compared to the unreinforced polymer [174]. Therefore, it can be concluded that the addition of carbon fibers in thermoplastics FFF filament has significantly strengthened the mechanical behaviour of the printed parts at the expense of toughness and ductility [1,11,25,26].

It is well known that the mechanical performances of SCFRP composite parts build via FFF strongly depends on several factors, including fiber-related properties (i.e., length, loading and alignment), process parameters and fiber/matrix interfacial adhesion. Ning et al. [175] studied the influence of carbon fibers content on the mechanical properties of ABS/CF composites produced via FFF technique. Short fibers (100 and 150 μm) were added to the base polymer in different volume fractions, from 3 to 15 wt.%. The highest performances in terms of tensile strength and elastic modulus were reached at 5 wt.% and 7.5 wt.% carbon fiber loadings respectively [175]. However, a further increase in the fiber volume fraction negatively impacted on the mechanical properties of the printed samples because of a higher void content. Moreover, it was found that longer fibers (150 μm) yields higher strength values compared to the shorter ones (100 μm) at the expense of elongation [175].

Tekinalp et al. [176] investigated the mechanical behavior of ABS/CF composites produced via FFF by adding different amount of short carbon fiber to the neat polymer. The effect of porosity as well as that of fiber orientation was also studied. It was found that FFF process yielded very high fiber alignment in the printing direction (i.e., corresponding to the direction of the deposited bead). The analysis of fiber orientation tensor revealed that about 91% of fibers are well aligned due to the high shear stresses encountered in the filament extrusion step. Consequently, an improvement of mechanical properties and a reduction of distortion were reported for the composite parts. Particularly, the addition of 30 wt.% carbon fibers to the polymer matrix enhanced the modulus and strength by 700% and 115% respectively [176]. A comparison between FFF and compression moulded (CM) samples showed that the microstructure of traditionally fabricated composites highly differs from the additively manufactured ones in terms of both fiber orientation as well as void content and distribution (Figure 32) [176]. The adoption of the FFF process causes an increase in the void content for both neat ABS (Figure 32e) and fiber reinforced samples (Figure 32f-h) with respect to compression molded specimens (Figure 32a-d).

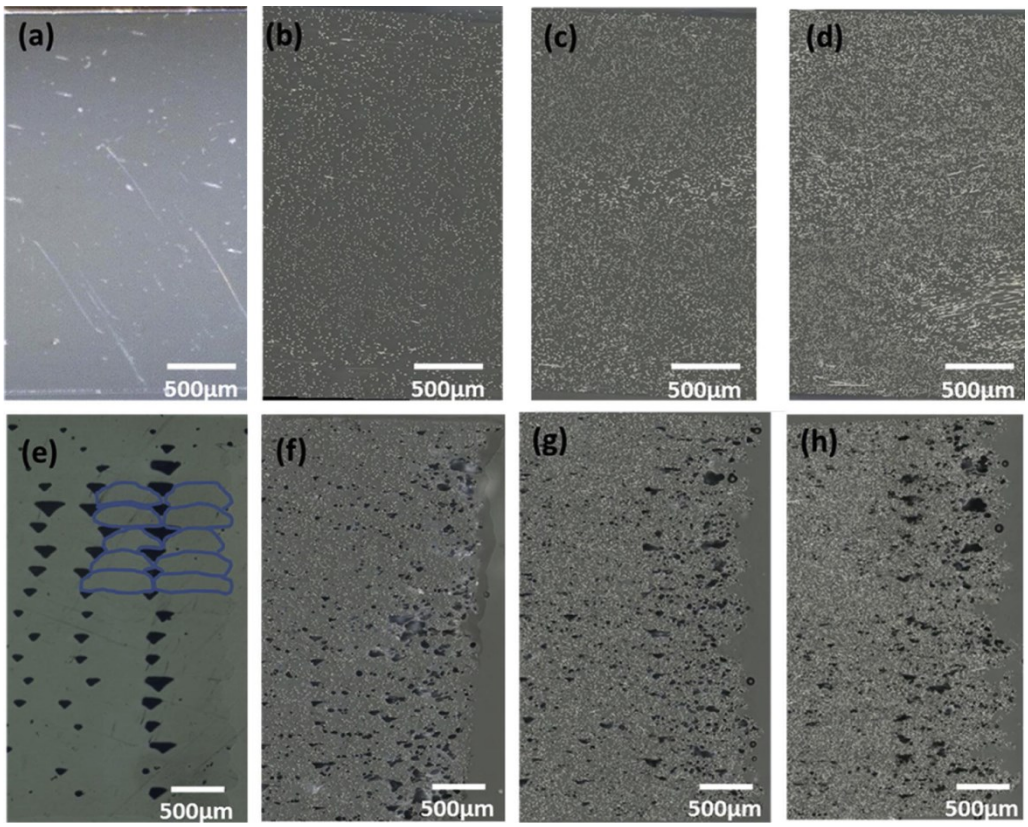

Figure 32: Comparison between the microstructure of short fiber ABS composites produced by compression molding and additively manufactured via FFF. Cross-sectional micrographs of CM samples with (a) 0% carbon fibers (CF), b) 10% CF, c) 20% CF, d) 30% CF and optical images of FFF printed parts with (e) 0% CF, f) 10% CF, g) 20% CF and h) 30% CF [176]

Moreover, the addition of fibers to the polymer filaments modifies the size and distribution of the voids in the printed parts. The triangular pores between the beads present in the neat ABS microstructure (Figure 32e) decrease in size because carbon fibers reduce extrudate swelling and coefficient of thermal expansion, while increasing thermal conductivity (Figure 32f-h). The inclusion of only 10 wt.% CF is sufficient to inhibit filament swelling after nozzle exit, thus leading to smaller inter-beads pores (Figure 32f). Therefore, the authors suggested that the presence of fibers promotes a stronger bonding between adjacent beads [176]. Consequently, the strength values increased with fiber content. However, only a minor improvement was obtained by rising the amount of fibers up to 30 wt.% due to a significant increase in both void content and size (Figure 32h) [176].

It is worth noting that short fiber reinforced composites manufactured by FFF display a strong fiber alignment (Figure 32f-h), that result in a peculiar tendency to have better material properties along the printing direction [25,26,156]. This behaviour was not observed for compression molded parts (Figure 32b-d) [176]. However, the higher strength reported by Tekinalp et al. [176] for compression molded samples suggested that the mechanical behaviour of the composites is more affected by porosity than fiber alignment, thus revealing the main challenge associated with FFF processing of fiber reinforced composites. Hofstätter et al. [177] suggested that a two-step process is responsible for the strong fiber orientation observed trough SEM and computer tomography analysis on PLA/CF composites processed by FFF. The fibers are firstly aligned during the extrusion of the raw filament. This preferential orientation is further strengthened when the filament is forced through the extruder's nozzle of the 3D printer. Brenken et al. [26] deeply investigated how material flow in the printing head affect fiber orientation. Through a detailed review of several modeling studies the authors concluded that the flow fields inside the extruder determines a strong alignment of the fibers in the deposited bead mostly due to the action of shear forces as well as on the convergent geometry typical of the extruder nozzle (Figure 33). Overall, the degree of fiber orientation, that influences the anisotropic characteristics of the printed composites, is defined by the interaction between these flow fields and extrudate swelling, that could slightly reduce fiber alignment when the filament leaves the nozzle [26].

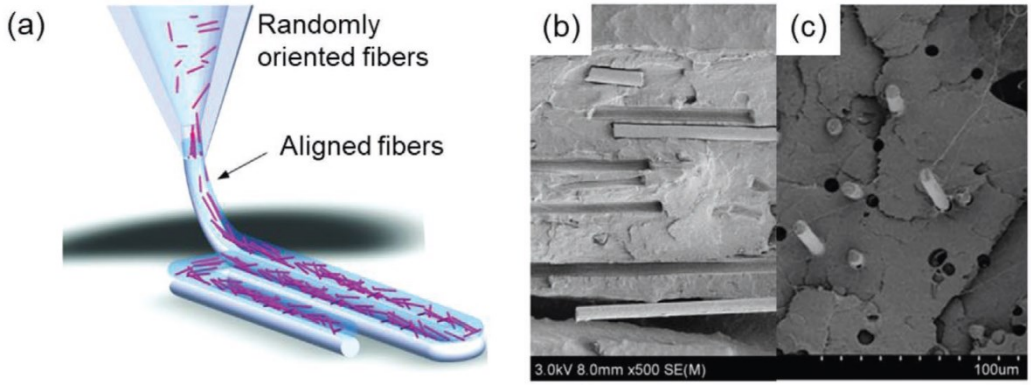

Figure 33: (a) Schematic representation of short fibers alignment due to the shear forces encountered in the nozzle and SEM images of the fracture surfaces of carbon fiber reinforced PLA samples fabricated in different directions: (b) longitudinal (0° raster angle) and (c) transverse (90° raster angle). These images highlighted the high orientation degree of the fibers along the bead deposition direction [65]

Liao et al. [178] studied the mechanical and thermal properties of short carbon fiber polyamide 12 composites fabricated by FFF. Filaments were fabricated by twin screw extrusion at 240 °C from PA12 pellets (trade name Vestamid L1670) and different content of carbon fibers (up to 10 wt.%) with diameter of 7 μm. Calorimetric and rheological analysis of the filament showed that the fibers lower the nucleation barrier for polymer crystallization as well as the melt flow index value. The printed samples revealed a great improvement of tensile and flexural properties as well as impact strength and storage modulus. For example, an enhancement up to 265% and 102% for the elastic modulus and tensile strength respectively for the formulation with 10 wt.% fibers. Similarly, the thermal conductivity of PA12/CF parts also increased up to 278% with respect to the pure polymer. The authors pointed out that this excellent mechanical and thermal behaviour is due to the good dispersion and preferential alignment of the fibers in the bead deposition direction [178].

Owing to the alignment of fibers, the bead orientation, defined by the raster angle parameter (Figure 30), was proved by different authors [179–183] to have a great influence on the overall behaviour of fiber reinforced polymers. In fact, strong anisotropy of properties with higher mechanical performances when the printed beads are parallel to the applied tensile loads is frequently reported [26,179–183]. Jiang et al. [179] investigated the effect of beads orientation on different carbon fibers reinforced polymer composites printed via FFF, including commercially available reinforced filaments based on ABS, PLA, PETG and a copolyester-based polymer with brand name Amphora. The authors reported a significant improvement in stiffness and tensile strength at 0° print orientation at the expense of the elongation at failure. However, all the mechanical properties in the transverse direction (which is perpendicular to the applied load) decreased with the addition of carbon fiber. Ferreira et al. [180] revealed a high degree of carbon fiber alignment in the bead direction by analysing PLA composites with 15 wt.% of fibers through computer tomography. This yielded to the highest improvement of stiffness in the 0° print direction. Zhang et al. [181] compared the microstructure and tensile properties of short carbon fibers ABS composites (fiber content of 14 wt.%) with different bead orientation or architecture (0, ±45° and 90°). It was found that the highest mechanical performances were obtained for 0° printing orientation (where the bead are oriented in the loading direction), followed by ±45° and 90° architectures respectively. Not only the mechanical behaviour but also the microstructure and void content were affected by the bead orientation, with the highest porosity for ±45° architecture. The authors also found

that the interfacial bonding strength of the reinforced samples, obtained by double notch testing, drops with the variation of layer thickness and extrusion speed [181]. In a follow-up work on ABS/CF composites, Ning et al. [182] found higher tensile properties for samples produced with [0/90] raster angle combination compared to [45/-45]. This was attributed to a better translation of the applied tensile load from the polymer to the fibers. Moreover, other printing parameters were found to play a major role on the microstructure of the printed composites. In fact, the inter-beads and inter-layer bond quality was improved by decreasing the printing speed and increasing the extrusion temperature and layer thickness, thus granting for better mechanical properties [182]. Spoerk et al. [183] also found a strong anisotropy in the flexural properties of PP/CF composites as a function of the bead orientation. Figure 34a graphically shows that the flexural stiffness and strength diminishes from 0° to 0°/90°, ±45° and 90° printing orientations, while neat PP samples has an isotropic mechanical behaviour.

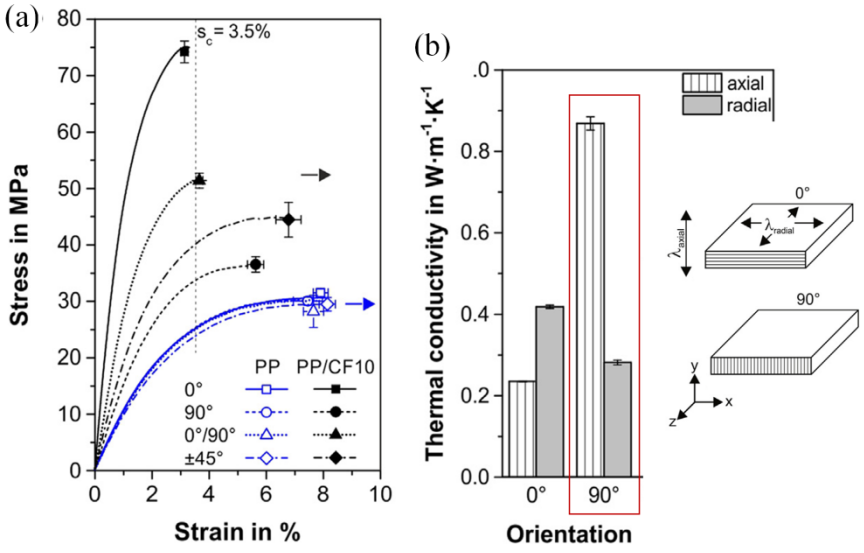

Figure 34: (a) Flexural stress-strain curves and (b) thermal conductivity of neat PP and PP/CF (with 10 wt.% carbon fibers) specimens built by FFF with different printing orientations. The thermal conductivity in the axial (λ_{axial}) and radial (λ_{radial}) direction are measured along the y-axis and in the xz-plane respectively, as displayed in the right part of Figure 34b. Note that the build direction of the specimens corresponds to the z-direction. Adapted from [183]

Besides the widely known effect on mechanical performances, fiber alignment along the bead deposition direction directly influences the thermal properties of the material as well [26]. Generally, the thermal conductivity along the fiber orientation axis is much higher with respect to the transverse direction

[178]. This behaviour is evidenced in Figure 34b by comparing axial and radial thermal conductivity of PP/CF sample fabricated with 90° printing orientation [183]. The shrinkage of the polymer during cooling is constrained by the presence of the fibers, but with a different amount between the bead deposition and the lateral direction [26]. Fiber orientation has also a great effect on the polymer viscosity [184]. In fact, the extensional viscosity increases by orders of magnitude from the transverse to the parallel direction with respect to fiber alignment [26]. In addition, the presence of fibers modifies the flow fields acting on the material during the extrusion step by increasing the viscosity and reducing the flexibility of the molten filament. In some cases, this poor rheological behaviour hinders the coalescence between beads, thus leaving more voids in the final parts (Figure 32h) [176,181]. For example, Ajinjeru et al. [185] found that the addition of carbon fibers to polyphenylene sulfone (PPSU) and ABS matrices, greatly increased the viscosity (about 3 times for 20 wt.% fiber loading).

Apart from void content and mechanical anisotropy, another common issue of fiber reinforced polymers produced by FFF is a weak interfacial adhesion between the polymer matrix and the carbon fibers. This characteristic has a negative impact on the matrix capability to effectively transfer the stresses to the reinforcing fiber, as revealed by the analysis of common failure modes of the printed composites. In fact, high degree of fibers pull-out and interfacial debonding at fiber/matrix interfaces are clearly visible in the SEM micrographs of the fracture surfaces of different short fiber reinforced composites (Figure 35) [180,183]. The pulled out fibers frequently showed clean surfaces with little polymer residue on it (inset of Figure 35a). This indicates a poor interfacial adhesion between thermoplastic matrices and carbon fibers [180,183] .

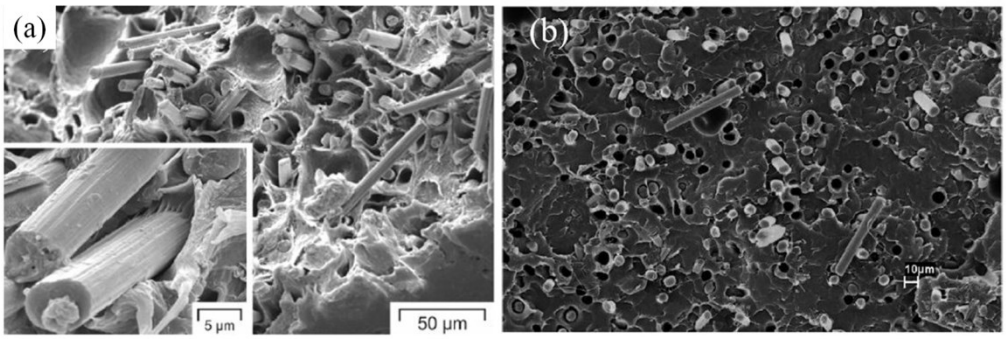

Figure 35: SEM images typical fracture surfaces of carbon fiber reinforced polymer composites printed by FFF: (a) PP/CF (15 wt.%) [183] and (b) PLA/CF (10 wt.%) [180]. In the inset of Figure 35a the fiber surface is magnified

2.5 Continuous Filament Fabrication (CFF)

2.5.1 Technology overview

Although different techniques have been studied in recent years, continuous carbon fiber reinforced polymers are mostly produced with material extrusion technology. In fact, this additive technique is quite similar to well-established processing methods for composite laminates such as automated fiber placement (AFP) or filament winding, albeit the maximum printing size is smaller. In fact, both material extrusion and traditional automated composite technologies are based on the same feedstock (i.e., fibers pre-pregs) and creates laminates with less or more complex layups in a layer-by-layer manner [6,186]. Nonetheless, material extrusion technology was continuously adapted from the initial attempts of continuous fiber printing made in 2001 by Zhong et al. [187] till its maturation in the following decades [21]. This evolution resulted in two different methods for additively manufactured thermoplastic polymers with continuous fibers:

- incorporating the continuous fiber and the thermoplastic filament inside the printing head via a co-extrusion process (also referred as "in-situ fusion" or "in-nozzle impregnation") (Figure 36a) [152,188];
- embedding the continuous fibers directly in the thermoplastic parts using two separate printing heads for the neat polymer filaments and the pre-impregnated fibers strands (also known as "ex-situ prepreg") (Figure 36b) [152,188].

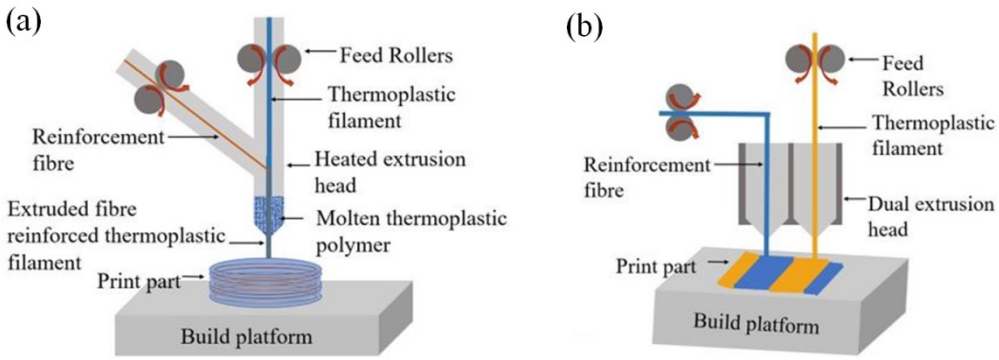

Figure 36: Schematic representation of the methods available for 3D print continuous fiber reinforced polymer (CFRP) composite parts through material extrusion: (a) in-nozzle impregnation process using a co-extrusion 3D printer and (b) ex-situ prepreg process using a dual-extrusion 3D printer for CFRP composites [152]

In-nozzle impregnation process

Figure 36a shows a schematic illustration of in-nozzle impregnation process where a traditional FFF system is updated with a specific printing head to allow for continuous fibers deposition. The system uses two distinct printing spools, for polymer matrix and reinforcement respectively. The technological approach relies on directly embedding the fibers inside the printing head. The matrix is supplied in the liquefiers as filament at a selected temperature chosen as a function of the thermal and rheological properties of the polymer itself. The fibrous reinforcement (usually fiber bundles with more than one thousand individual fibers) is then pushed through the core of heated nozzle to be continuously impregnated by the molten polymer. As soon as the composite filament is laid down, it quickly solidifies and adheres to the previously deposited layers (Figure 36a) [152]. Although this method provides high flexibility in terms of fiber/matrix proportion and even though a great enhancement of tensile and flexural properties compared to unreinforced thermoplastics has been reported in various studies [189–192], some problems were found. Proper wetting and impregnation of carbon fibers with a thermoplastic polymer is difficult to achieve and defects may arise in the printed material, including voids between layers, poor fiber/matrix bonding and incomplete fiber impregnation [191]. This is an inherent problem of in-nozzle impregnation since the pressure applied by the system is not as high as in other processes, such as pultrusion. Another issue is related to fiber feeding, which can either be broken in the extrusion head owing to their low compression strength or clog the orifice [168].

Ex-situ prepreg process

A major stride for CFRP composites 3D printing has been perceived with the development of a patented ex situ prepreg process by the company MarkForged Inc. (Massachusetts, USA), that was the first manufacturer of a commercial desktop 3D printer for continuous fiber reinforced materials in 2014 [1,21]. This technology, named Continuous Filament Fabrication (CFF) [193], utilizes a printing head equipped with two separate extruders, for the plastic matrix and continuous fiber filaments respectively, and a motor to feed them inside the printing head (Figure 36b and Figure 37a). The materials are laid down at different times during single layer fabrication and a fiber cutting mechanism is adopted to stop fiber feeding before starting the deposition of the following layer. The printers can process neat polyamide (PA) or short carbon fiber reinforced PA conventional filaments (diameter of 1.75 mm) as "matrix materials" and a continuous fiber filled polyamide tow (diameter of 0.36 mm) as "reinforcement"

(Figure 37a). The reinforcing filaments can be Kevlar, glass or carbon fibers (about 35% volume fraction) pre-impregnated in a thermoplastic resin. Owing to the use of pre-impregnated filament, the problems related to fiber/matrix adhesion that accompany in-nozzle impregnation processes are thus surpassed [194].

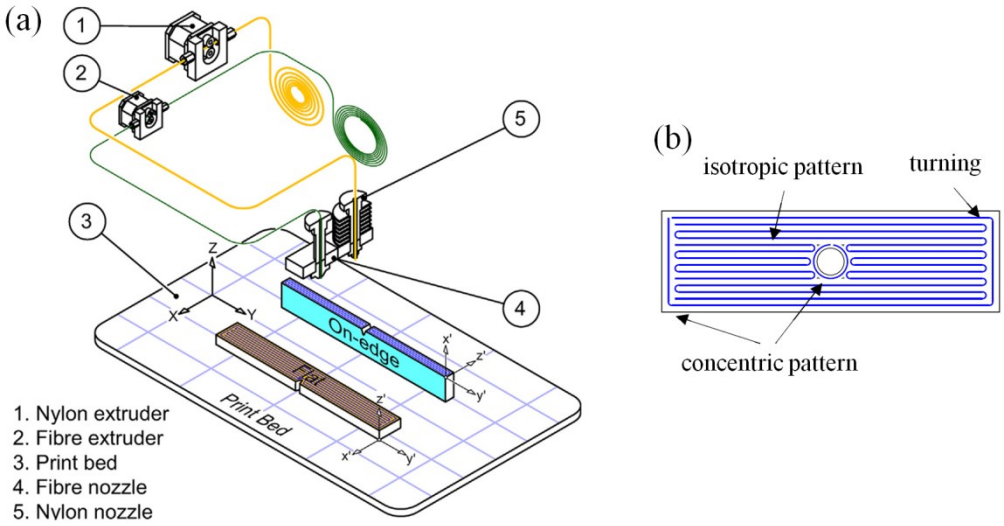

Figure 37: (a) Simplified representation of the working principle of MarkForged CCF printers [194] and (b) sketch of possible fibre path design (isotropic and concentric) where the blue lines represent possible fiber paths [186]

This technology allows more flexibility in terms of part design compared to co-extrusion systems, because the reinforcement can be placed using isotropic or concentric fill pattern, as showed by the blue lines in Figure 37b. In the former case, the fibers are deposited unidirectionally until the part edges are reached, where sharp turning is done to complete layer filling (Figure 37b). The latter enables the deposition of the fibers in concentric ring following the outer perimeter or inner geometrical features (such as holes or fillet) of the part (Figure 37b) [186]. Moreover, only individual layers or some regions inside a layer can be produced using the pre-impregnated fiber reinforced filament, thus allowing reinforcement in selected areas to obtain specific performances whilst minimizing cost [186]. The mechanical performances achievable are significantly higher with respect to AM parts made of neat polymers or short fibers reinforcement. The company declares tensile strength of 700 MPa and elastic modulus 54 GPa for its continuous carbon fiber reinforced parts [195]. Anisoprint LLC (Moscow, Russia) has developed a similar printing system, called Prom IS 500 [196]. Differently from MarkForged, the printer uses a continuous carbon fiber filament coated by thermosets in order to enhance the adhesion to different polymer matrices [197]

and an open source software allowing more control in fibre deposition paths. Moreover, the machine is featured with a high temperature extrusion head (up to 410 °C nozzle temperature) to print high performance thermoplastics such as PEEK and PEI. A wide choice of polymer matrices (e.g., PC, PA, PEEK, PEI, PSU) and fiber reinforcement (glass or carbon) is available [196]. However, little data are available to date on the mechanical properties of the printed parts [1]. Another system for CCFRP composites printing was developed by CEAD company [198]. The system consists of an industrial size machine (build volume 4x2x1.5 m) based on a gantry system capable of extruding polymer matrix and reinforcing filaments (40% fiber weight fraction) simultaneously [198].

The ex-situ prepreg technology relies on the production of pre-impregnated filaments with continuous fibers. An example of this process is given by Hu et al. [199] that designed a specific extrusion device for manufacturing continuous carbon fiber filaments pre-impregnated with PLA (Figure 38a). The filaments were obtained by single screw extrusion using a coaxial extrusion mould with a special nozzle for preventing fiber clogging. The 1K carbon fiber bundle (Toray T-300) was passed into a heated pipe before entering the single screw extruder. The thermoplastic polymer pellets (NatureWorks 4043 PLA) were then fed into the extruded. The action of the screw is able to properly impregnate the fibers, thus creating a good interfacial adhesion. The extruded filaments were then cooled down into a water bath at a controlled cooling rate and dried (Figure 38a).

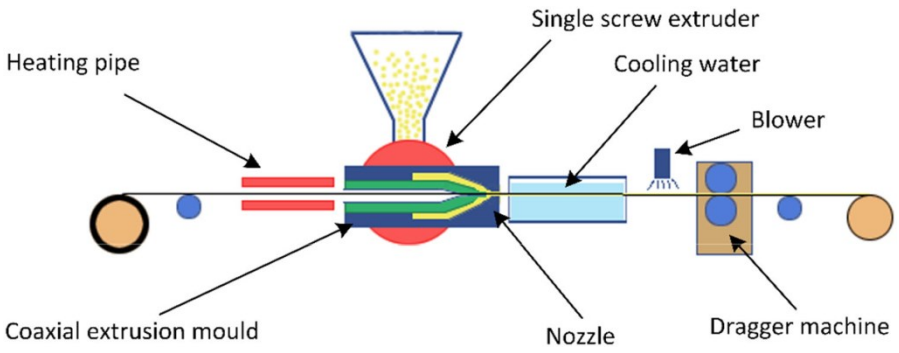

Figure 38: Schematic illustration of the manufacturing process 3D printable CCF prepreg filament [199]

Printing tests using an home-made FFF printer show that the PLA/CCF samples achieved a higher strength (541.6 MPa) similar composites produced by solution casting and hot pressing (248 MPa) when fabricated using optimized extrusion temperature, speed and layer thickness are used [199]. In this way, the

drawbacks of in-situ processes (i.e., poor interfacial bonding between fiber and polymer matrix) are surpassed.

The physical phenomena involved in CCF process resembles traditional material extrusion AM technology for polymers (Figure 28). However, the shear conditions and nozzle temperature are adjusted to achieve a viscosity range that allows the pre-impregnated filament to pass through the extruder without clogging the nozzle or leading to flow inconsistency [199]**.** Amorphous or semi crystalline polymers showing low crystallinity are used to embed the continuous fibers as it helps in improving bead shape stability and printing accuracy [21,196,200]. For example, pre-preg filaments manufactured by MarkForged has amorphous semi aromatic polyamides as matrix materials [193]. Finally, the coalescence between adjacent beads and the adhesion between layers is hindered owing to the absence of compaction forces and the marked differences in the thermo-physical properties of the reinforced filament between the longitudinal and transverse directions. Thus, the printed parts usually exhibit considerable void contents [1].

2.5.2 Carbon fiber reinforced polymer composites processed by CFF

As already mentioned in the previous paragraph, polyamides are the preferred matrix system for 3D printing continuous carbon fiber reinforced polymer (CCFRP) composites. The achievement of high modulus and strength components is the main objective of AM continuous fiber reinforced polymers. In fact, this type of reinforcement is specifically used to obtain mechanical performances far beyond the limits of standard 3D printed polymers. In this context, extensive studies have been carried out in recent years to characterize the microstructure and mechanical performances of polyamide composites reinforced with continuous carbon fiber (PA/CCF) produced using CFF via MarkForged® printing systems [1,21,186]. Several studies [156,202–206] examined the morphology of the pre-impregnated carbon fiber filament, revealing that it consists of 1k fiber bundles (meaning that each bundle contains about 1000 fibres) coated with an amorphous polyamide resin. The fiber content was estimated to be between 33% and 36% using different techniques, such as pyrolysis, thermo gravimetric analysis in air environment, optical microscopy image analysis or matrix acid digestion [203–206]. Moreover, some morphological defects were also highlighted, such as voids due to incomplete impregnation and a sub-optimal fiber distribution (Figure 39).

In fact, the reinforcing phase is arranged into separate bundles surrounded by large areas filled by the polymer matrix only (Figure 39a) [156,204–206].

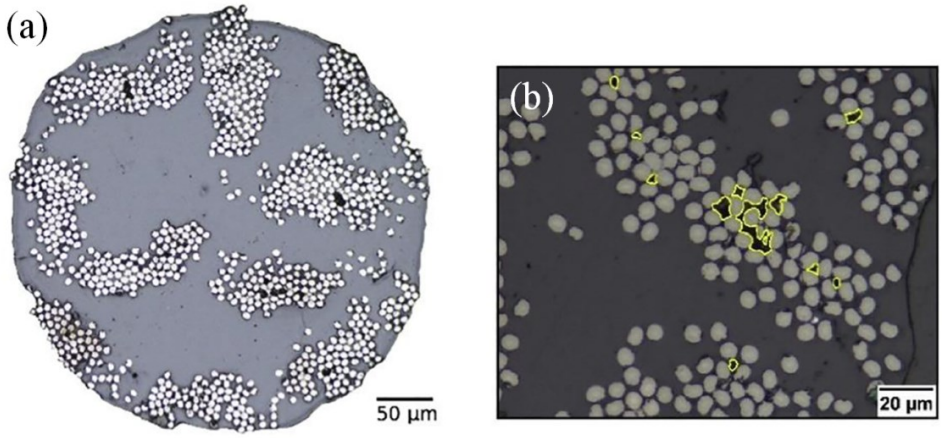

Figure 39: (a) Cross-sectional optical images of as received carbon fiber filaments (average diameter of 380 µm) and (b) magnified view of poorly impregnated areas [204]

Van Der Klift et al. [202] produced PA/CCF composites with the Mark One printer by adding concentric rings of carbon fibers in the middle region of printed specimens. The tensile tests evidenced a significant improvement of strength at break up to 464.4 MPa by increasing the fiber content. From the results obtained by using the inverse rule of mixture (RoM), the authors suggested that Toray T300 standard modulus carbon fibers bundles are used in the pre-impregnated filaments supplied by Markforged [202]. Dickson et al. [207] noticed that the increase in tensile strength was gradually diluted upon a continued increment of fiber loading. This behaviour was attributed to a meagre bonding between fiber and pure nylon layers and, more importantly, to the increased amount of voids at high fiber loading. Blok et al. [156] performed different experiments to evaluate the printing quality and mechanical properties of PA/CCF composites fabricated using MarkOne printer in comparison with a short fiber reinforced counterpart. Albeit continuous fibers grant a 10-fold improvement of tensile properties (e.g. strength at break equal to 726 MPa and 83.5 MPa for long and short fiber 3D printed part), the printing method has inherent limitation in design flexibility. In fact, the stiff fiber reinforced filament cannot fill small turning radii as well as sharp angles, thus creating fibreless areas (Figure 40a) [156]. Moreover, optical microscopy analyses of the XY cross-section of a longitudinal part (i.e., fibers unidirectionally oriented at 0°) unveiled the presence of other manufacturing defects, such as voids between beads and inhomogeneous distribution of matrix and fibers (Figure 40b and 40c) [156]. The formation mechanisms of the porosity

were related to both processing conditions and continuous fibers. In fact, the rapid cooling of the deposited bead below polymer matrix glass transition impedes the growth of contact interfaces and the extent of molecular diffusion between layers [208]. In addition, the high anisotropic viscosity typical of continuous fiber prepregs limits filament squeeze flow in the transverse direction, thus leaving air gaps between beads [206]. These defects are deemed to be responsible for a poor shear response of the material.

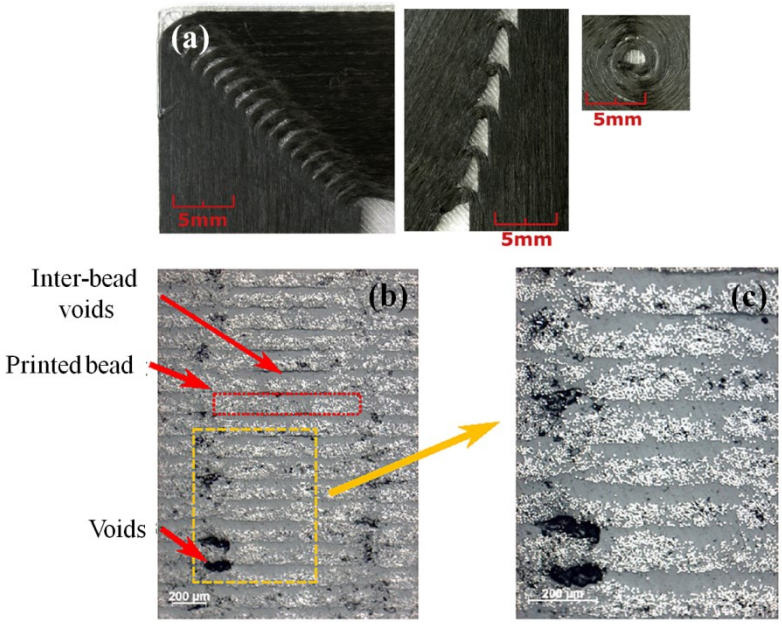

Figure 40: (a) Geometrical details (corner radii, sharp edges) of benchmark parts obtained using MarkOne printer and (b, c) optical micrographs of the cross section of the printed part revealing the typical layered structure and distribution of voids [156]

Justo et al. [209] characterized the plane mechanical properties of fully reinforced PA/CCF coupons in both tensile and compression mode. The coupons were extracted from the printed samples to overcome the design limitations of Mark One printer. A detailed comparison between the experimental data and the properties of a conventional epoxy laminates (AS4 carbon fiber/epoxy) clearly showed that the mechanical performances of AM parts are far inferior in all load conditions (i.e., tension, compression, in-plane shear in both longitudinal and transverse direction) [209]. This is due to the presence of defects, such as pores (~12%) and region with high matrix concentration), the low amount of fibers (about half compared to traditional laminates) and weaker mechanical strength of polyamides compared to epoxy resins [209]. Goh et al. [203] systematically studied the fracture modes of longitudinal PA/CCF samples under tension and

bending loadings. The failure mechanism of the tensile samples was controlled by fiber breakage (tensile rupture) and delamination between layers (shear rupture), giving rise to a step-like fracture surface (Figure 41a and 41b). Differently, in the flexural sample the failure starts in the top surface due to compressive stresses and propagates till final rupture due to fiber breakage at the opposite side that is subjected to a tensile stress state (Figure 41c and 41d) [203].

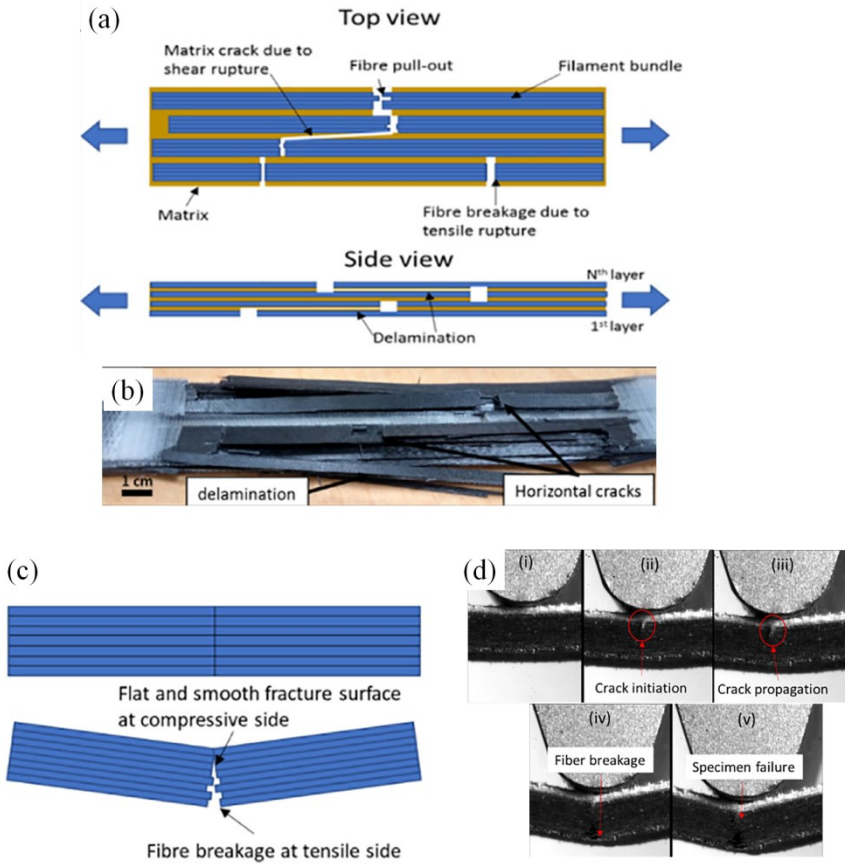

Figure 41: Schematic illustration of fracture mechanism of additively manufactured PA/CCF samples under (a) tension and (c) bending load case; (b) visual observation of the fracture mode of a tensile specimen showing cracking and delamination and (d) image sequence of the three point bending test captured using high speed camera [203]

The influence of build orientation, fiber volume percentage and infill pattern (isotropic or concentric, as shown in Figure 37b) on the mechanical performances of longitudinal composites were also investigated [204,207,210–212]. It was found that flat samples exhibited higher performances due to a lower amount of layer-to-layer interfaces compared to on-edge counterparts [210]. As expected, tensile and flexural properties showed significant improvements by increasing the

fiber loading for both isotropic [204] and concentric infill [211,212]. However, the elastic modulus varies almost linearly with fiber content, while the increase in strength drops at high reinforcement volume fraction (Figure 42a) due to the occurrence of mixed fiber breakage/delamination failure [212]. Values as high as 436 MPa for tensile and 423.5 MPa for three point bending tests were reported for a fiber volume fraction of 27% [210]. Insufficient fiber/matrix bonding due to poor interfacial adhesion, revealed by extensive fiber pull-out the fracture surfaces (Figure 42b), uneven fiber distribution and a large amount of voids were considered the reasons for the lower values of mechanical properties compared to those expected for composites produced using conventional fabrication methods [204,210–212]. Moreover, the initial deposition point of the fiber reinforced filament in a layer and fiber curvatures at the part edges lead to additional stress concentration and multi-axial stress state that will ultimately result in premature failure [211,212].

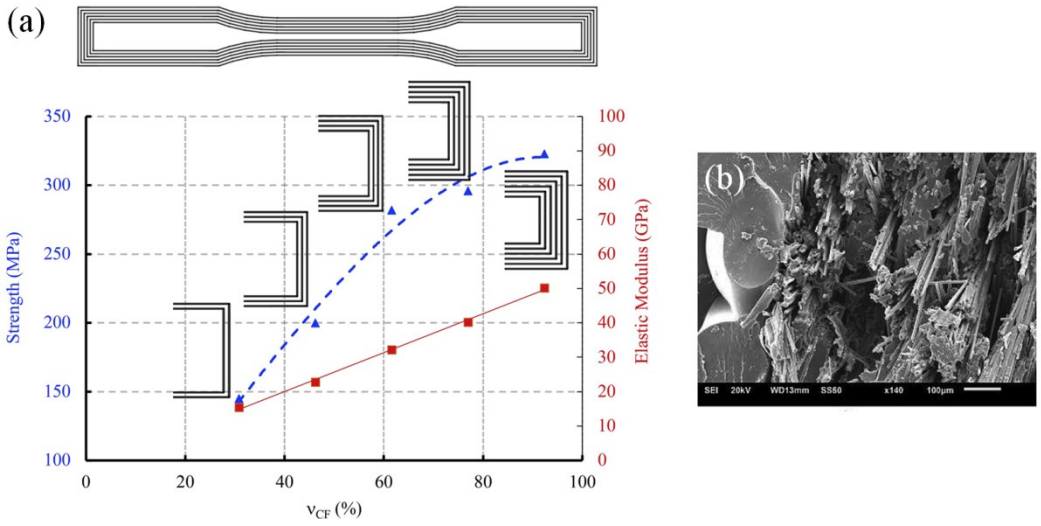

Figure 42: (a) Tensile strength and Young modulus of PA/CCF samples printed with a concentric infill pattern as a function of υ_{CF} (% of the sample cross-section reinforced with carbon fiber filaments). Printing pattern for each specimen is schematically sketched in inset figures to indicate the differences in fiber reinforced filaments arrangement. Please note that the real carbon fiber volume fraction is lower than υ_{CF} since the raw filament has 34% of fibers [212]; (b) SEM image of a typical fracture surface showing fiber pull-out [210]

Several authors focused on the characterization of the intra-laminar and inter-laminar properties of PA/CCF composites by analyzing the tensile response in the principal material direction, including longitudinal (0°), transverse (90°) and in-plane shear (±45°) as well as interlaminar shear strength and fracture toughness

[206,208,213–215]. These comprehensive characterizations aimed at determining the elastic constant and strength features of the individual ply, interfaces strength and fracture mechanisms that are needed to design continuous fiber laminates for structural applications. It was reported that elastic modulus and strength changed up to an order of magnitude from [0] to [±45] and [90] layup [206,208,213–215]. Moreover, Caminero et al. [216] showed that the interlaminar shear strength (ILSS) of 3D printed composites reinforced with continuous carbon fibers are higher compared to those obtained by using glass and Kevlar fibers. As already observed for tensile and flexural strength, the increase in ILSS was limited at high fiber loading [216]. However, both ILSS and fracture toughness under mode I (G_{IC}) and mode II (G_{IIC}) interlaminar fracture tests were found to be 50% lower compared to hot compression molded polyamides composites with identical fiber content [206,208,216]. The authors agreed that the transverse and interlaminar properties represent a major limiting factor for the development of continuous fiber composites by AM techniques. In fact, 3D printed parts are more prone to delamination and matrix cracking under mechanical loading owing to the defects induced by the printing process [206,208,216]. These observations pointed out that AM parts display highly different mechanical responses in relation to the orientation of stresses due to the anisotropic characteristics of the printing process and continuous reinforcement. Therefore, a careful optimization of the laminae stacking sequence is required to 3D print continuous fiber composites with good structural capabilities. Saeed et al. [215] reported that a quasi-isotropic layup, such as $[0/45/90]_s$, has an intermediate behaviour between the longitudinal and transverse ply properties. A reduction by one third in elastic modulus and by half in strength with respect to the longitudinal composites was observed. Mei et al. [217] examined the mechanical behaviour of 3D printed PA/CCF with different quasi-isotropic layups. It was reported that $[0/45/90]_2$ laminate has higher tensile strength at break, stiffness and ductility compared to $[30/45/60]_2$, $[15/45/75]_2$ because the fibers in [0] plies bear the tensile load more effectively. In addition, the study showed that a post-treatment by hot pressing improved the mechanical properties of the laminates. In particular, strongest interface bonding are created by enhancing the fiber/matrix interface wettability and by removing the air gaps induced during printing as a result of higher treatment temperature and time respectively [217]. Apart from structural performances, fiber orientation was also found to influence the thermal conductivity [218] as well as the temperature profiles during the printing process [219].

Overall, several processing issues such as weak adhesion between stacked layers, high pores content and poor fiber distribution in the printable filament, were identified in literature [203,204,206–212,216]. To address these challenges and improve the mechanical properties of AM composite parts, Peng et al. [220,221] suggested that a careful design of the laminate structures, by alternating continuous and short fiber reinforced plies (referred as "separate distribution" in the papers) helps to improve the tensile strength (but not the stiffness) of the 3D printed components. This synergistic reinforcement effect was attributed to an improved interfacial strength and better interface quality between layers, that hamper crack propagation during mechanical loading [220,221]. Moreover, the introduction of plies oriented at 45° into the 3D printed parts almost doubled its energy absorption during flexural tests, up to 1613 MJ/mm [221]. He et al. [206] demonstrated the adverse effects of porosity (≃12%) on PA/CCF performances by analyzing the effect of post-processing the printed samples using compression molding (CM). A reduction of porosity down to 5% and an improvement of the interfacial bonding between matrix and fiber was obtained by compression molding, leading to a substantial improvement of mechanical properties (up to 78% for transverse tensile strength and 90% for flexural strength and interlaminar fracture toughness) and failure modes [206]. This study indicated the importance of reducing the void percentage in the printed parts. In this context, the company 9T Labs (Zurich, Switzerland) has recently designed and commercialized a novel two-step process, named Additive Fusion Technology (AFT) [222], to produce continuous fiber composites based on PA12 or PEEK matrix. The feedstock material is firstly 3D printed using a material extrusion-based system and then a compression molding treatments inside a heated oven is performed. This post-processing step is able to reduce the void content to 2-3% and improve the interlayer bonding [222]. Due to this hybrid method and the high fiber content in the raw filaments (60 vol.%), the company claimed that the final parts display elastic and strength properties similar to those of conventional laminates [222].

2.6 Modeling and analytical techniques

Fiber reinforced polymers are traditionally modelled to predict their mechanical response to tensile loading using different analytical approaches based at the micro and macro-mechanical level. The former is based on the properties of individual composite constituent (fiber and matrix) and includes rule of mixture (RoM), shear lag model, Halpin-Tsai equations, Mori-Tanaka model and many others [14,20]. The latter is based on the properties of individual plies within a

laminated composites and include classical laminate theory (CLT) and volume averaging method [14,20]. These modeling approaches can be applied to both short and continuous reinforcement, although macro-mechanical models are more suitable for analyzing the behaviour of long fiber reinforced material.

2.6.1 Short fiber composites

As already mentioned, several theories have been proposed to estimate the mechanical properties of short carbon fiber reinforced polymer (SCFRP) composites. The modified rule of mixture and the Halpin-Tsai model are the simplest analytical approaches to estimate the elastic modulus of SCFRP composites. Both models assume a perfect fiber/matrix interfacial bonding and takes into account fiber geometry effect in terms of length and aspect ratio. The formulation of the modified rule of mixture is expressed in equation (5) [14,20]:

$$E=\chi_1\chi_2 E_f V_f+E_m V_m \tag{5}$$

where E is the elastic modulus of the composite, χ_1 and χ_2 are factors that describe the effect of fiber orientation, length and aspect ratio and, finally, V_f, E_f, V_m and E_m denote the volume fraction and elastic modulus of the fiber and matrix respectively. Alternatively, Halpin-Tsai equations, originally developed for unidirectional composites, derived the longitudinal and transverse elastic moduli, E_{11} and E_{22}, from the general expression of equation (6) [14,20]:

$$\frac{E}{E_m}=\frac{1+\varsigma\eta V_f}{1-\eta V_f} \tag{6}$$

where the shape parameter ς depends on fiber aspect ratio while η is determined by fiber geometry as well as fiber and matrix moduli, that in turn depends on loading conditions. Lanzl et al. [142] applied the Halpin-Tsai model to predict the elastic modulus of short glass fiber reinforced PA12 composites fabricated by SLS. A good agreement was found up to 10% fiber loading by volume. At higher fiber percentage the discrepancy between the theoretical tensile moduli and those obtained experimentally for SLS composites greatly increased owing to the presence of voids in the printed samples [142]. The contribution of voids is usually modelled in conventional composites by adding a correction factor for porosity as follow [223]:

$$E_c=E(1-\varphi)^n \tag{7}$$

where E_c is the elastic modulus of a void-containing composite and φ is the void content. The void efficiency exponent n described how voids induces stress concentrations during mechanical loading [223]. As 3D printing processes are frequently associated with large void formation, Rodriguez et al. [224] proposed to treat additively manufactured parts (in this case neat ABS part processed by FFF) as a material-void composites using the simple rule of mixture, implying a porosity exponent equal to 1 for longitudinal properties and 0.5 for transverse properties. More complex models, such as Mori-Tanaka theory for non-diluted composites and classical laminate theory [225–227], are also used in short fiber composites stiffness predictions. Both approaches were proved to be valid for 3D printed parts too, as the estimation of elastic modulus for short fiber composites fabricated by FFF with different values of layer thickness [227] or different bead orientation [225,226] was found to match the theoretical values with an average error between 5% and 10%. The modified rule of mixture is also applied to predict the tensile strength of SCFRP composites. Zhu et al. [228] reported modeling error lower than 10% by using this approach in ternary carbon fiber/polyamide 12/epoxy composites produced by SLS and post-infiltration of the thermoset resin.

A comprehensive model based on the modified rule of mixture and a laminate analogy approach was developed by Van de Werken et al. [1] to predict tensile strength and stiffness respectively of a general SCFRP composites processed by AM technologies. The model was validated against the experimental data of ABS/CF composites from [176]. The variation of tensile properties with fiber aspect ratio is shown in Figure 43. Strength and stiffness values were normalized with respect to the respective properties predicted for a composite material with fibers with infinite length and perfect alignment in the loading direction. In the calculations, fibers were considered as mostly aligned to determine the highest bound for mechanical properties. Moreover, this assumption is quite realistic for some AM techniques, for example FFF, that are able to produce a selective alignment of fibers in the printed components [26]. Moreover, a typical critical fiber length for a short fiber thermoplastic composites (0.5 mm) was used to simulate the effective reinforcing effect of fibers [1].

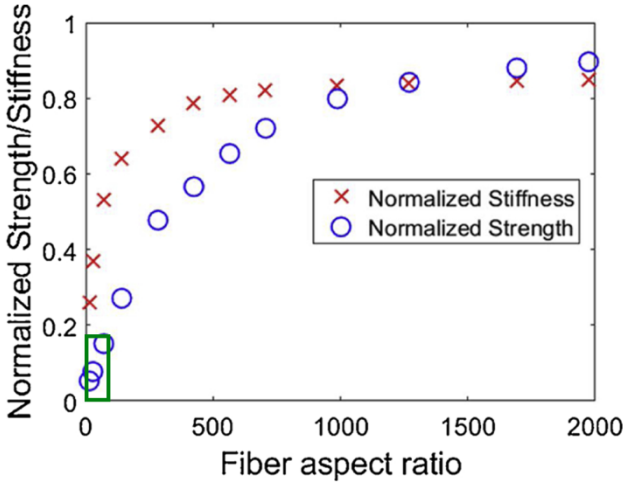

Figure 43: Effect of fiber aspect ratio (diameter of carbon fibers equal to 7μm) on AM short fiber composite tensile strength and elastic modulus. The green rectangle defines the region of the normalized strength/stiffness vs fiber aspect ratio graph covered by AM short fiber composites [1]

The trend reported in Figure 43 display that high performance short fiber composites, with strength and Young's modulus higher than 80% of their maximum theoretical values can be obtained when the aspect ratio of the fibers is at least 1000. Considering the typical diameter of carbon fibers (7 μm), the average fiber length is required to be 7 mm [1]. However, the length of the carbon fibers commonly used in AM feedstock is well below this value (i.e., usually lower than 200 μm) due to processing constraints and an increment of defects content [1]. It is also important to stress out that the model proposed by Van de Werken et al. [1] neglects fiber end effects, thus leading to an overestimation of strength values by almost 20 %. Therefore, it can be concluded that the potential increase of mechanical performances using short fiber reinforcement is restricted to a small region of the graph (green rectangle in Figure 43).

2.6.2 Continuous fiber composites

The prediction of tensile properties of continuous carbon fiber reinforced polymer (CCFRP) covers high significance in the composite industry since these materials were specifically developed for structural applications. Moreover, their properties can be easily optimized without modifying material composition in view of the orthotropic mechanical behaviour of individual plies and the infinite layups (i.e., sequence of ply orientations) that can be chosen to form a laminate. At this purpose, both micromechanical and laminate based models were used for both

conventionally manufactured parts, although classical laminate theory (CLT) has the largest accuracy and flexibility.

The modified rule of mixture (MRoM) was also employed in numerous studies [204,206,211,212,220] to forecast the tensile properties of additively manufactured PA/CCF composite printed with longitudinal fiber orientation. However, a good consistency between modeling and experimental results were only found for fiber content below 11% [211]. Conversely, at high fiber volume fraction MRoM predictions significantly deviate from the experimental values, with failure strengths between 30 and 50% lower than those theoretically predicted [204,206,211,212,220]. These relevant discrepancies were attributed to the adverse contribution of voids, poor interlayer and fiber/matrix interfacial adhesion and non-homogenous fiber distribution [204,206,212]**.** Melenka et al. [229] firstly proposed the Volume Average Stiffness (VAS) method to estimate the elastic properties of continuous Kevlar fibers reinforced composites produced using CCF technique. The printed composite is considered as made of different regions, namely solid, infill e shell, each showing specific elastic properties as a function of the filament material and toolpath adopted (Figure 44).

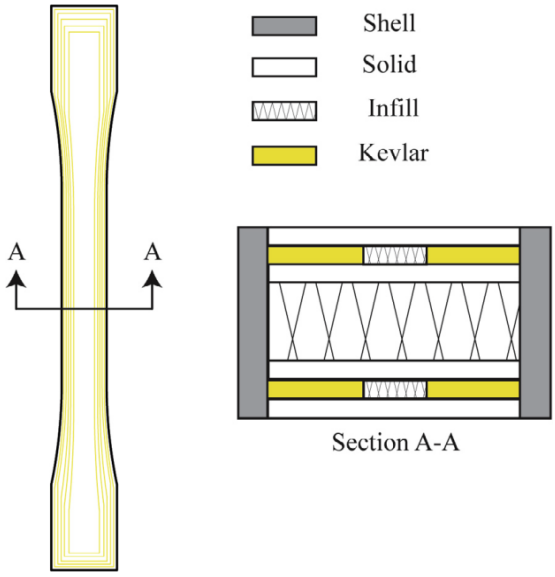

Figure 44: Schematic illustration of the structure of the Kevlar fiber reinforced tensile dog-bone produced by using CFF technique: top view (left) and cross-sectional view (Section A-A) (right) of the printed samples. Solid regions are sketched as solid white rectangles, infill regions are represented a hatch pattern and Kevlar reinforced regions are sketched in yellow colour [229]

The method involves a volume averaging of the stiffness matrices of these regions. The volume of each region can be simply estimated from geometrical observations. The void model developed by Rodriguez et al. [224] was used the determine the micromechanical properties of solid, infill e shell regions. The method offered accurate predictions of the elastic modulus with an error of 6.2% and 0.1% for composites containing 8% and 10% of Kevlar fibers respectively [229]. The VAS method was also adopted by Al Abadi et al. [230] and Yu et al. [231] for modeling PA/CCF parts. The results revealed that the elastic properties (elastic modulus and Poisson's ratio) can be estimated with good correspondence for different laminate characteristics in terms of fiber content, fiber infill pattern and ply orientation as well as load scenario. Modeling errors lower than 10% and 20% were reported for tensile and flexural moduli respectively [231]. These discrepancies were explained by considering that the fiber deposition path embedded in material extrusion AM process (e.g., sharp turn at the part edges shown in Figure 40a) significantly affects the failure mechanism, mainly for complex loading conditions such as those caused by three-point bending tests [231]. Classical Laminate Theory (CLT), whose detailed formulation is described in the following (section 3.3.2), was used by Saeed et al. [215] to predict the mechanical properties of PA/CCF composites. CLT predictions were found to accurately evaluate longitudinal and transverse moduli, while a higher error was reported for shear modulus. Moreover, Polyzos et al. [232] found that the prediction of the elastic modulus of 3D printed composite reinforced with carbon, glass and Kevlar fibers by using CLT coupled with different micromechanical and void models results in low modeling error (less than 10%). Therefore, this study confirmed the potential of CLT to simulate the properties of CCFRP composites produced by AM. However, it is important to note that most modelling studies are focused on elastic properties [215,230–232] and longitudinal parts were mainly characterized [230,231].

Chapter 3

Materials and method

3.1 Material processing

3.1.1 Selective Laser Sintering

Polyamide 12 powders reinforced with 20 wt.% carbon fibers (PA12/CF) were purchased from Advand3D Materials GmbH (Hamburg, Germany). The powders were processed using Sharebot SnowWhite direct laser sintering machine (Sharebot S.r.l., Nibionno, Italy) for microstructural and mechanical properties characterization. Neat polyamide 12 (PA12) purchased from the same supplier was also processed for sake of comparison. Sharebot SnowWhite printer (Figure 45) uses a continuous wave CO_2 laser with an emitting wavelength of 10.6 μm to selectively fuse the polymeric powders. The laser diameter is equal to 200 μm while the maximum power is 14 W. The build chamber consists of a build plate, two powder tanks and two overflow bins for material recycling. The build area (10x10x10 cm) is significantly smaller compared to standard industrial SLS machines (Figure 45). The heating system is composed by four halogen lamps (Haloline, Osram, LEDVANCE GmbH, Augsburg, Germany) placed on top of the build plate in the shape of a square. The power of the lamps is 120 W or 230 W depending on their position. The temperature of the powder bed is measured through an IR sensor. The machine operates in air environment and it is equipped with a translational recoating blade to spread a layer of powders over the build plate (Figure 45b) [233].

Figure 45: Sharebot SnowWhite SLS machine: external view (left image) and internal view of the build chamber (right image)

As discussed in Chapter 2, the optimization of process parameters is of great concern for improving the properties of the SLS parts. In this thesis, a new approach based on the isothermal crystallization kinetics was adopted to choose the appropriate powder bed temperature (T_b) while the laser exposure parameters (e.g. laser power, scan speed) were optimized according to the stable sintering region (SSR) approach proposed by Vasquez et al. [122].

Optimization of powder bed temperature

According to literature, the powder bed temperature (T_b) has to be selected between the melting and crystallization onsets of the material obtained using a standard heat/cool DSC cycle (sintering window in Figure 13) to avoid out of plane deformation of the part or curling [28,72,108]. This curl deformation is usually evaluated experimentally by measuring the degree of curvature of the bottom surface (curl angle) or the height of the upward edges (curl height) of a benchmark part [234–238]. Soe [238] demonstrated that the curl phenomenon is highly dependent on temperature, sample geometry and position in the part bed, with T_b having the highest impact. In fact, experiments with cross-shaped parts on EOS P700 machine showed that a variation of powder bed temperature of 1/2 °C has a relevant influence on the curl height [238]. Therefore, the author suggested to print cross-shape samples and set a T_b value 2/3 °C higher than temperature at which the parts stop curling. However, the proposed approach is time consuming and does not consider the quasi-isothermal solidification conditions typical of the SLS process (Figure 6).

A new criteria based on the analysis of the isothermal crystallization kinetics obtained through DSC is then proposed. The DSC program consists of a rapid

heating up to a temperature 30 °C higher than polymer melting peak to completely fuse the powders, followed a rapid cooling down to a temperature selected in between the sintering window. This temperature (T_{iso}) is hold isothermally for 120 min to measure the heat flow variation induced by the crystallization process. A set of 13 different isothermal temperatures chosen within the sintering window (from 160 to 172°C) were used. Details about the test procedures are given in the "Experimental techniques" section of this chapter. The experimental data, that describes the crystallization kinetics, were compared to the amount of curl measured on SLS parts produced using powder bed temperature values equal to T_{iso}. This comparison is useful to understand how phase transition influence curl development and select the optimal processing condition. To this end, four rectangular flat plates (80x10x1 mm) were printed for each T_b value. This geometry was already adopted as a benchmark by previous studies [234–237] to measure the amount of curl in SLS parts. The deformation of the plates is described by measuring the curl height from the bottom length of the curled samples from stereomicroscopy images taken at low magnification (8x). Figure 46 shows a sketch and some images of the out of plane deformation of a printed part as well as the measuring principle adopted for the evaluation of the curl height. Table 2 summarizes the experimental and validation protocol used for powder bed temperature optimization.

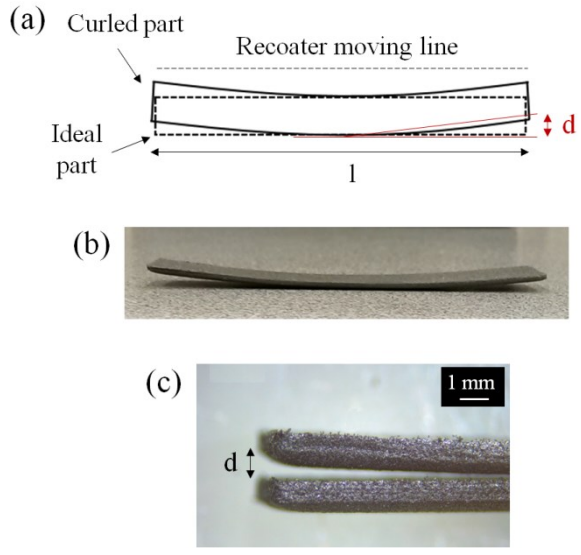

Figure 46: (a) Sketch of the out of plane deformation of a curled rectangular plate produced by SLS showing the method adopted for the evaluation of the curl height, (b) photographic image of a curled samples and (c) example of a typical stereomicroscopy image used to measure the curl height

Table 2: Summary of the experimental approach used in the optimization of the powder bed temperature. The strategy combines isothermal DSC tests and curl height measurements at different temperatures within the sintering window

Experimental test	Temperature (°C)	Output parameters
Isothermal crystallization kinetics	from 160 °C to 172 °C, every 1 °C	Crystallization halftime ($t_{1/2}$)
Curl experiments		Curl height

Optimization of laser exposure parameters

Laser exposure process parameters were optimized with the aim of obtaining the highest possible density and mechanical properties of the printed parts. To this purpose the SSR method proposed in Vasquez et al. [122] was adopted. This method is based on the hypothesis that the laser beam should heat the powder bed to a temperature sufficiently high to fully melt the polymer without leading to thermal degradation. This condition is met when the temperature of the melt pool remains between the offset of the melting peak and the onset of thermal degradation of the powders, obtained by DSC and TGA experiments. This temperature interval is referred as Stable Sintering Region (SSR). However, for simplicity of use the SSR is usually expressed in terms of energy density rather than temperature [122].

The energy required to melt a powder layer (E_m) and the energy needed for thermal degradation (E_{deg}) could be quantitatively determined from the thermal and physical properties of the raw powders evaluated with common experimental techniques (DSC, TGA, tap density test, etc.). E_m (J/mm^3) is defined as the sum between the energy required to preheat the material from T_b up to its melting point and to fully melt the polymer grains themselves:

$$E_m=\left[C_p^{powder}(T_m - T_b)+h_f\right]\rho\Phi \quad (8)$$

where C_p ^{powder} is the specific heat capacity at the bed temperature, T_m is the melting peak temperature, h_f corresponds to the melting enthalpy, ρ and Φ denotes the true density and the packing factor of the powders respectively. E_{deg} (J/mm^3) is

calculated from the energy needed to heat the powders to the degradation onset and plus the energy needed to exceed the energy activation barrier as follow:

$$E_{deg} = E_m + \left[C_p^{melt}\left(T_{deg} - T_m\right) + \frac{E_A}{M_W}\right]\rho \quad (9)$$

where C_p^{melt} is the specific heat capacity of the powder melt (i.e., mean value from 190 °C and 260 °C), T_{deg} and E_A are the onset degradation temperature and activation energy respectively and M_w denotes the molecular weight of the polymer. All parameters were evaluated experimentally by thermal and physical characterization of the PA12/CF powders, except M_w. As Sharebot SnowWhite machine does not operates in inert environments, thermal degradation of the powders in air was studied. The energy density supplied by the laser per unit volume is defined as:

$$E_D = \frac{P}{vSz} \quad (10)$$

where P is the laser power, v is the scan speed, S denotes the hatch spacing, corresponding to the distance between two consecutive laser scans and z is the layer height. The Energy Melt Ratio (EMR) parameter is then introduced as a metric to correlate powder properties (E_m) and machine setting (i.e., the volumetric laser energy density that summarizes the effect of laser powder, scan speed, hatch spacing and layer height):

$$EMR = \frac{E_D}{E_m} \quad (11)$$

Therefore, an energy-based processing window can be defined to predict the laser parameters that could induce sufficient energy for melting whilst keeping the temperature within the stable sintering region defined from powder properties.

To evaluate the accuracy of the method a series of specimens were printed using different values of laser energy density chosen in between the limits of the SSR. For this purpose, laser power and scan speed were varied one at a time. Table 3 listed the experimental design adopted. Flat dog-bones with dimensions complying geometry 1BA of ISO 527-2 standard were manufactured to evaluate the tensile properties of the composite material, while cuboid samples (10x5x5 mm in size) were used to characterize the microstructure induced by the SLS process as well as the density and dimensional accuracy of the parts. Four dog-bone and two cuboid samples were produced for each set of parameters (Table 3).

Table 3: Summary of the process parameter combinations used to produce PA12/CF samples by exploring the SSR region as these parameters leads to different laser energy density values. Layer height and hatch spacing were always set at 100 μm. T_b was set at 170 °C according the results of the optimization process previously described

Laser power P (W)	**Scan speed s (mm/s)**	**Volume energy density E_D (J/mm^3)**
2.8	2400	0.117
2.8	1440	0.194
2.8	960	0.292
3.5	2400	0.146
3.5	1140	0.243
3.5	960	0.365
4.2	2400	0.175
4.9	3000	0.163
4.9	2400	0.204
4.9	2600	0.314
5.6	3120	0.179
5.6	2400	0.233
5.6	1680	0.333
6.3	2400	0.263
7	2400	0.292

All samples were built in the xy plane using a flat orientation (Figure 47a). A bidirectional scanning strategy with 90° rotation of the laser scans between layers was employed (Figure 47b). A shrinkage correction factor equal to 3.5% was used to compensate the volume contraction of the parts resulting from cooling and crystallization.

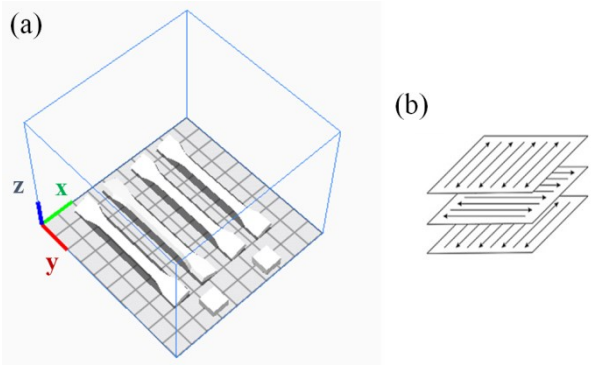

Figure 47: Schematic representation of (a) building orientation and (b) scanning strategy adopted for printing dog-bone and cuboid samples by SLS. The building plate is on xy plane and the recoater moves along the x-axis. The laser rotates 90° every layer

3.1.2 Fused Filament Fabrication

A short carbon fibers reinforced polyamide 6 filament (PA6/CF) with trade name "Carbon PA" was purchased from Roboze SpA (Bari, Italy). The filament has a diameter of 1.75 mm and it was processed through a Roboze One FFF machine, also supplied by Roboze SpA (Bari, Italy) (Figure 48).

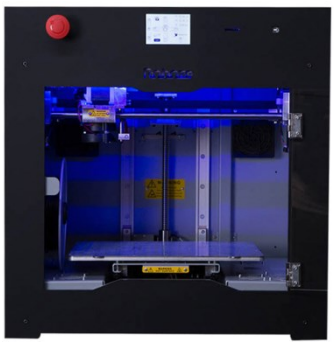

Figure 48: Roboze One FFF printer

The printer is equipped with a heated build plate with dimensions 280x220x200 mm and a print head able to reach temperature as high as 300 °C. A beltless system is adopted to control the print head movements, thus enabling

higher precision and tolerances in the order of microns. The standard brass nozzle was replaced by a stainless steel one (diameter of 0.6 mm) to avoid damage due to the abrasive action of the carbon fibers [239]. A schematic representation of the FFF process is illustrated in Figure 49a. A stepper motor equipped with two toothed gears feeds the thermoplastic filament directly through the print head ("direct drive extrusion system"). The filament then passes into the heated nozzle to deposit on the build platform according to the desired pattern. The orientation of the deposited bead with respect to the x axis of the build platform is referred as raster angle.

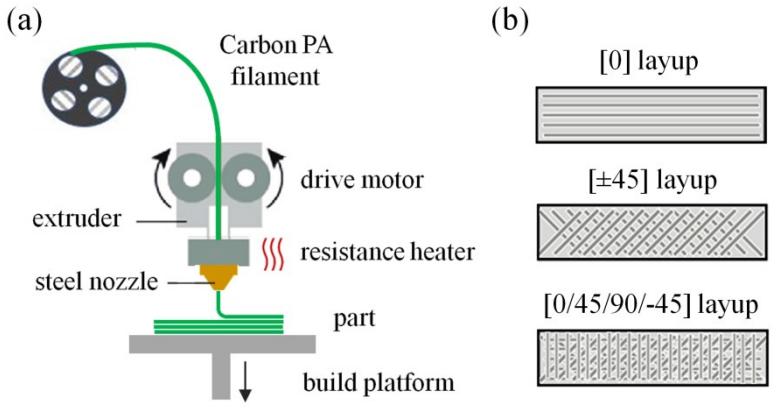

Figure 49: a) Conceptual sketch of the FFF printing process of PA6/CF using Roboze One and (b) schematic representation of the different layup adopted

Flat dog-bone samples were built in the xy plane in compliance with ISO 527-4 standard (specimens of type 1B). Three printing architectures (also referred as layup) with different bead orientation along the sequence of the stacked layers, namely [0], [±45] and [0/45/90/-45], were adopted to investigate the effect of fiber orientation on the microstructure and mechanical properties of the printed parts (Figure 49b). The specimens were fabricated with two perimeter contours using the process parameters recommended by the filament supplier (Table 4).

Table 4: Summary of the process parameters used for FFF printing of PA6/CF specimens

T_{bed} (°C)	$T_{extrusion}$ (°C)	Infill speed (mm/min)	Layer height (mm)	Infill density (%)	Printing architecture or layup
45	300	3000	0.2	100	[0], [±45], [0/45/90/-45]

A raft was always employed to improve the adhesion between the part and the build platform and facilitate part removal. Rectangular samples (10x10x10 mm) were also produced to assess the density of the parts. Since PA6 is susceptible to humidity, the filament was dried in oven before printing for 8 hours. Otherwise, the absorbed moisture could drive the formation of defects which negatively impact on the mechanical performances of the samples [152].

3.1.3 Continuous Filament Fabrication

Neat polyamide (referred as PA filament) with brand name "Nylon W" and pre-impregnated continuous carbon fibers filaments (referred as CCF filament or tow) were supplied by CMF Marelli Srl (Cinisello Balsamo, MI, Italy), official reseller of the company MarkForged Inc. (Cambridge, MA, USA) in Italy. According to the supplier, PA filament is made of a "specially tuned polyamide 6 copolymer" [193]. In contrast, CCF filament consists of continuous fibers strands (Toray® T300 standard modulus carbon fibers) impregnated with a partially aromatic polyamide [193,205]. The filaments were processed through Mark Two® desktop 3D printer supplied by MarkForged Inc. (Figure 50) to produce polyamide composites reinforced with continuous carbon fibers (PA/CCF).

Figure 50: MarkForged Mark Two® desktop 3D printer and filament spools of neat PA polymer and pre-impregnated continuous carbon fibers

This system uses a dual extrusion printing technology named Continuous Filament Fabrication (CFF) [193]. A conceptual sketch of the CFF process is displayed in Figure 51a. The Mark Two® is equipped with two printing heads granting the use of two different spools, one of unreinforced polymer matrix (PA filament) and one of pre-impregnated continuous fibers reinforcement (CCF filament) (Figure 51a). The filament feeding mechanism is based on a Bowden-type extruder system, where the raw material is pushed through a long and flexible Teflon tube from the extruder assembly to the hot end.

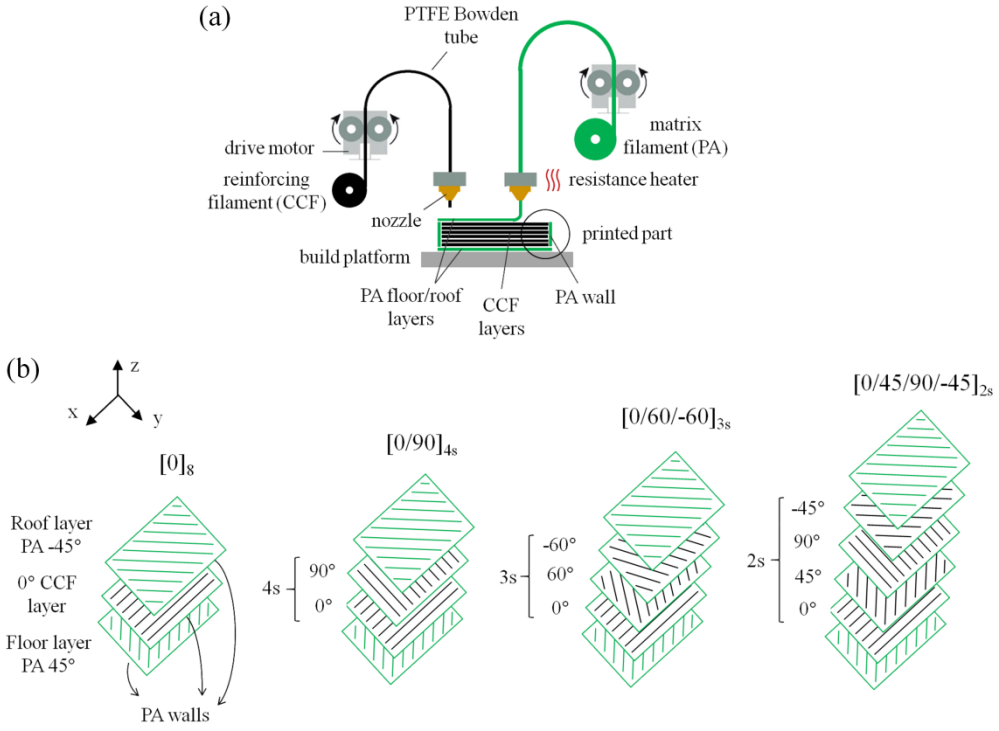

Figure 51: (a) Schematic representation of MarkForged® CFF printing process and (b) internal structure of the PA/CCF composites comprising PA roof/top layers, CCF reinforced intermediate layers showing fibers infill with different orientations (0°, 90°, 45°, 60°) according to the layup adopted and a PA wall for each layer

To fabricate PA/CCF composites the PA filament is firstly deposited along the perimeter of the part. Secondly, the pre-impregnated CCF filament is extruded through a second heated nozzle to fill the internal region of the part with continuous fibers strands. The extruder moves in the build plane in accordance with the tool path designed using the slicing software of the 3D printer (Eiger™) specifically developed by MarkForged for their printing systems. The build platform is lowered along the z axis by a layer thickness and the two steps previously described are repeated layer by layer until the completion of the part. The design of the entire system (i.e., 3D printer and software) allows to lay down the reinforcing filament as required by the user. In this way, the orientation of the continuous carbon fibers can be tailored by modifying the raster angle settings of each layer via the slicing software. Other printing parameters, such as infill density, number of floor/roof layers as well as perimeter walls, can be manually set up. As a result, the printed parts are conforming with the shape designed by means of a 3D graphics software and the specific layout of matrix and reinforcing filament for each layer (Figure 51a). However, the extrusion temperature and

speed are fixed. In fact, PA and CCF filaments are extruded at 273 °C and 252 °C respectively, while the printing speed was estimated to be 15 mm/s for the reinforced filaments in previous works [194,208]. The layer thickness is also fixed at 125 μm. The build platform is not preheated, but it is recommended to apply a glue (Elmer's Washable School Glue stick) on it to help the adhesion of the first layers.

Different types of PA/CCF composites were fabricated to investigate the influence of the continuous fiber orientation, expressed in terms of laminate layup, on the microstructure and mechanical response of the 3D printed parts. To this end, PA/CCF composites with longitudinal (referred as [0]), cross-ply (referred as $[0,90]_s$) and quasi-isotropic $[0/\pm60]_s$ and $[0/45/90/-45]_s$ layups were produced. Only balanced and symmetric laminates were chosen to simplify the modeling effort and to study layups of interest for the composite industry. In particular, $[0/\pm60]_s$ and $[0/45/90/-45]_s$ were selected as examples of quasi-isotropic composites with three-layer and four-layer symmetry respectively. The printing patterns and layups adopted are schematically represented in Figure 51b. It can be seen that the internal structure of the 3D printed parts is made of two distinct regions: outer shell, consisting of solid floor/roof layers and perimeter walls, and internal infill. Neat PA filament was used to print the first (i.e., floor) and last (i.e., roof) layer of the samples (Figure 51b) as well as the perimeter of each layer (named as wall in Figure 51b). The floor layer improves the adhesion between the printed part and the build platform and it is advised to avoid fibers rupture during part removal. The roof layer was used for symmetrical reason. The perimeter wall was printed to guarantee good dimensional accuracy and surface finish. The CCF filament was instead adopted for the infill region of the samples using isotropic pattern where the continuous fiber beads are laid unidirectionally throughout the layer. The 3D printer software was used to modify the orientation of the beads in each ply according to the different laminate layups (Figure 51b).

PA/CCF rectangular samples were fabricated in compliance with ASTM D3039 standard to characterize the tensile properties of the laminates. In fact, this geometry with constant cross-sectional shape guarantees that the continuous fibers are perfectly aligned without discontinuity. Table 5 reports the dimensions of the samples. Aluminum end tabs with thickness of 1.5 mm and length of 56 mm were bonded to the specimens by means of an epoxy glue (3M™ Scotch-Weld™ Epoxy Adhesive DP420) to avoid gripping damage during testing. The surface of both the aluminum end tabs and gripping areas of the samples were roughened

with silicon carbide abrasive paper (180 grit) to enhance bonding. Four specimens for each laminate layups were produced.

Table 5: Summary of the process parameters used for FFF printing of PA6/CF specimens

Sample notation	ASTM standard	Laminate layup	Dimensions (mm)
$[0]_s$	D3039	[45], $[0]_8$, [-45]	250 x 15 x 1.25
$[0/90]_s$	D3039	[45], $[0/90]_{4s}$, [-45]	250 x 25 x 2.25
$[0/45/90/-45]_s$	D3039	[45], $[0/45/90/-45]_{2s}$, [-45]	250 x 25 x 2.25
$[0/\pm60]_s$	D3039	[45], $[0//\pm60]_{3s}$, [-45]	250 x 25 x 2.5

The volume fractions of neat PA and CCF filaments (referred as V_{PA} and V_{CCF} respectively) in each laminate layup can be determined dividing the volume of the filament consumed to print a sample (in cm^3) by the total volume of the sample ($V_{composite}$). These data, reported in Table 6, will be employed to determine the theoretical density of the composite (see Section 3.2.4) as well as the carbon fiber content of each composite layup (see Section 4.4.2).

Table 6: Printing volumes and volume fractions of neat PA and CCF regions obtained from Eiger software for each laminate layup

Laminate layup	Sample volume $V_{composite}$ (cm^3)	Volume of printing filament (cm^3)		PA volume fraction V_{PA} (cm^3)	CCF volume fraction V_{CCF} (cm^3)
		PA	CCF		
$[0]_s$	4.42	1.26	3.16	28.5	71.5
$[0/90]_s$	13.27	2.66	10.61	20.0	80.0
$[0/45/90/-45]_s$	13.19	2.51	10.68	19.0	81.0
$[0/\pm60]_s$	14.67	2.69	11.98	18.3	81.7

Necked dog-bone samples with rectangular pattern (filaments at ±45° with respect to load direction) according to ISO 527-2 standard were also printed to test the tensile properties of the neat PA matrix. In this case, the printing process resembles conventional FFF technology. Only the plastic matrix nozzle is used (Figure 51a). To avoid the negative influence of absorbed moisture on the CFF process, PA filament was dried at 80 °C for 8h. Moreover, it was stored in a Pelican moisture-proof dry box during printing.

3.2 Characterization methods

3.2.1 Differential Scanning Calorimetry (DSC)

The thermal transitions and the crystalline fraction of the raw materials were investigated by differential scanning calorimetry (DCS) experiments through a PerkinElmer Pyris 1 instrument (PerkinElmer Inc., Waltham, MA, USA). Samples of powders or filament with a mass of 10 ± 1 mg were tested according to a standard temperature cycle consisted of heating–cooling cycle from 25 °C to 300 °C at a rate of 10 °C/min in inert atmosphere (N_2 flow at 20 ml/min). Characteristic temperatures and enthalpies for melting and crystallization events were calculated from the DSC curves using Pyris software. The glass transition temperature was estimated as the midpoint of the inflectional tangent of the measured curve, as suggested in ASTM E-1356 standard. The crystalline fraction (X_c) of the polymer matrix was obtained using equation (12):

$$X_c = \frac{\Delta H_m}{\Delta H_m^0 (1-f)} 100\% \quad (12)$$

where ΔH_m is the enthalpy of fusion, corresponding to the area under the melting peak, ΔH_m^0 is the enthalpy of fusion for a fully crystalline polymer (reference value found in literature for PA12 and PA6 are 209 J/g [134] and 240 J/g [240] respectively) and f denotes the weight fraction of fibers, if present. A reheating step at 10 °C/min was also carried out to provide more information on the thermal transitions of the investigated materials.

The same instrument was used to determine the specific heat capacity of PA12/CF and PA12 powders for SLS technology at the solid and liquid phase. For this purpose, a temperature modulated step-scan DSC experiment was performed as described in ASTM E1269–11 standards. The samples were heated from 30 °C

to 240 °C by continuously repeating dynamic (at 10 °C/min heating rate) and isothermal segments (1 min) every 5 °C.

Isothermal crystallization experiments were also performed on the PA12/CF powders. A specific DSC program was used to simulate the thermal conditions inside the SLS building chamber. A graphical representation of the temperature cycle used is depicted in Figure 52. The cycle consisted of an initial heating from room temperature to 210°C (about 30°C higher than the melting point of PA12) at 20°C/min. This temperature was held isothermally for 2 min to fully melt the polymer crystals. The samples were rapidly cooled (60°C/min) to simulate what happens after laser exposure until a constant temperature T_{iso} is reached and then held isothermally for 120 min at this temperature to record the heat flow variations due to polymer crystallization. Different T_{iso} between 160 and 172 °C were considered (see Table 2). After the isothermal step, the sample was heated to 220°C at 10°C/min to melt the polymer grains again. This last step was performed to compare the melting behaviour and the degree of crystallization of the powders treated with the isothermal DSC cycles and the samples printed by SLS**.**

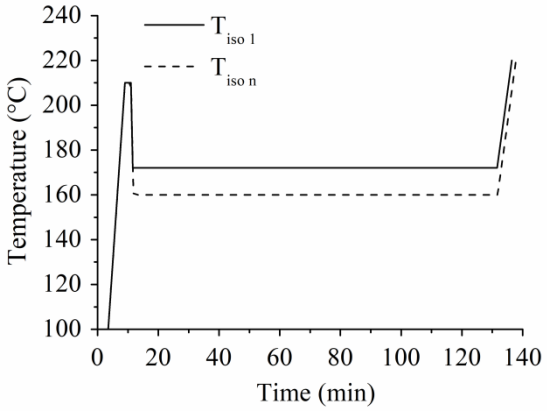

Figure 52: Temperature cycle used for the DSC isothermal crystallization tests

3.2.2 Thermo gravimetric Analysis (TGA)

The thermal stability and composition of the materials were studied by thermal gravimetric analysis (TGA)using a Mettler Toledo TGA/SDTA851^{e} instrument (Mettler Toledo, Columbus, OH, USA) equipped with of a gas control station to switch from inert to air atmosphere analysis. Samples of powders or filament having a mass of 35 ± 5 mg were heated in alumina crucibles from 25 °C to 1000°C. The tests were conducted in inert atmosphere (argon flow at 50 ml/min)

at a heating rate of 10 °C/min. Weight loss against temperature curve and weigh loss derivative curve were used to evaluate the temperatures corresponding to the onset degradation (T_{onset}) and the maximum weight loss rate (T_p). Moreover, the weight fraction of fibers was calculated from the difference between the weight of final residues of the reinforced and neat polymer.

For PA12/CF and PA12 powder for SLS technology, TGA tests at different heating rates (i.e., 5, 10 and 20 °C/min) were performed in air atmosphere to investigate the thermo-oxidative degradation process that could happen during the printing using Sharebot SnowWhite (see Section 3.1.1). The onset degradation temperature was calculated when a 1% weight loss is obtained in the TGA signal recorded at 10 °C/min. The integral isoconversional method was instead employed to determine the activation energy for thermo-oxidative degradation (E_A) using the Kissinger–Akahira–Sunose equation [241]:

$$\ln\left(\frac{\beta}{T_\alpha^2}\right) = -\frac{E_A}{R}\left(\frac{1}{T_\alpha}\right) + \ln\left(\frac{A \cdot R}{E_A}\right) \tag{13}$$

where β corresponds to the heating rate of the TGA experiment, T_α is the temperature at which the degree of conversion α is reached (in this case α=50% was considered by analyzing polymer degradation step), A is a pre-exponential factor and R denotes the universal gas constant (8.314 J/mol °K). By plotting the values of $\ln(\beta/T_\alpha^2)$ against $1/T_\alpha$ a linear regression of the experimental data could be carried out. The activation energy is then calculated from the slope of the linear fit multiplied by R.

3.2.3 X-Ray Diffraction (XRD)

The crystalline structure of the raw materials and 3D printed samples was evaluated by x-ray diffraction (XRD) experiments using a Panalytical PW3040/60 X'Pert PRO diffractometer. The instrument is equipped with a Cu-Kαx-ray source emitting at a wavelength of 1.5418 A°. All measurements were carried out using a 2θ angular range of 10°–60° with a step size of 0.013°.

3.2.4 Density measurements

The density of the raw materials was evaluated using Ultrapyc 5000 helium gas pycnometer (Anton Paar QuantaTec, Boynton Beach, FL, USA) according to ASTM B923-20 standard. The density of the 3D printed parts were obtained with the buoyancy method by using the Archimede or hydrostatic balance (ASTM

B962-17). Ethanol was adopted as immersion liquid to fill the pores of the samples. The void content (φ) of the printed composites was calculated using equation (14):

$$\varphi = \left(1 - \frac{\rho_{printed}}{\rho}\right) 100\% \quad (14)$$

where is $\rho_{printed}$ and ρ are the density of the 3D printed parts and raw materials respectively (i.e., powders for SLS and filaments for FFF/CFF technologies). In the case of PA/CCF composites produced by CFF, the raw material is a composite that consists of both neat PA and reinforced CCF filaments. Therefore, the theoretical density of the material was calculated in turn using the rule of mixture:

$$\rho = \rho_{CCF} V_{CCF} + \rho_{PA}(1 - V_{CFF}) \quad (15)$$

where are ρ_{PA} and ρ_{CCF} are the density of as received filaments obtained from pycnometry and V_{CCF} is the volume fractions of CCF filament for each layup adopted (Table 6).

3.2.5 Powder layer density and flowability

The characterization of the powder layer density and flowability of the powders during layer recoating is difficult to be accomplished and indirect measurements are normally performed. The bulk/tap density test was employed to assess the packing efficienct of neat PA12 and PA12/CF powders. The apparent density (ρ_{bulk}) was evaluated by filling a cylindrical container of standard volume (25 cm^3) with the test powder. The tap density (ρ_{tap}) was then measured by using a manual tapping procedure based on ASTM D7481 without any external pressure applied on the powder surface [242]. In this way, two parameters usually adopted to describe the powder layer density and flowability in powder bed AM techniques, namely packing factor (ϕ) and Hausner ratio (HR) , can be determined according to equations (16) and (17) respectively [69]:

$$\phi = \frac{\rho_{bulk}}{\rho} \quad (16)$$

$$HR = \frac{\rho_{tap}}{\rho_{bulk}} \quad (17)$$

where ρ is the true density of the powders obtained by gas pycnometry. The flowability of the powders was also evaluated through the Hall flowmeter funnel in compliance with ASTM B213–17 standards.

3.2.6 Optical microscopy

Optical microscope

Optical microscopy was used to study the morphology and microstructure of the raw materials (filaments for FFF and CFF technology only) and 3D printed parts. For this purpose, YZ cross sections (i.e. perpendicular to the build plane) of the filaments and printed parts (one for each different processing condition adopted for samples production) were cut through a metallographic precision cut-off saw (Brilliant 220, QATM Gmbh, Mammelzen, Germany). The cross sectioned samples were mounted at room temperature in acrylic or epoxy resin and manually polished using standard metallographic preparation methods (grinding with abrasive SiC papers from 600 grid up to 4000 grid and polishing with 1 μm diamond paste on a napped cloth). The polished samples were then studied by means of a Leica DMI 5000 M microscope (Leica Microsystems GmbH, Wetzlar, Germany). Optical micrographs were collected at different magnification level from 50x to 500x to observe the quality of the composites and to identify microstructural features and defects related to processing, such as voids, interlayer interfaces and fiber orientation and distribution in the polymer matrix. Image J® software was used to analyze the images by measuring relevant features (e.g., void content, filament diameter, fiber diameter, beads dimensions and so on). In particular, high resolution micrographs of the entire YZ cross section of the additively manufactured parts, constructed by stitching several consecutive optical images collected at 50x magnification, were analyzed to calculate the void fraction. To this end, a thresholding with isodata algorithm was carried out.

The optical microscope was also employed to assess the orientation of the carbon fibers in PA12/CF parts obtained by SLS. XY cross sections (i.e., parallel to the build plane) of the sample were cut, mounted and polished for microscopy observations. Different micrographs were captured at 100x magnification to be analyzed by using the aforementioned image processing software. The optical images were processed according to a procedure described by Jansson and Pejryd in [145]. In detail, the orientation of more than 1600 fibers was evaluated by measuring the angle formed the fiber itself and the movement direction of the recoating blade. Finally, the length distribution of the short carbon fiber used in the PA6/CF filament was evaluated by image analysis. To this purpose, a laboratory furnace (Elite Thermal System Limited BSF 11/22, Italy) was used to heat some filament fragments up to 800 °C in N_2 atmosphere for 30 minutes in order to decompose the polyamide matrix by pyrolysis. A small quantity of fibers

was put onto a microscope slide. Several micrographs were then collected at 100x magnification and 200 fibers were measured to gain reliable length distribution data.

Stereomicroscope

A Leica EZ4W stereo microscope (Leica Microsystems Gmbh, Wetzlar, Germany) was used to observe the tensile fractured surfaces of the 3D printed composites as well as to evaluate the curl height of the rectangular flat plates produced by SLS.

3.2.7 Field Emission Scanning Electron Microscopy (FESEM)

The morphology of the fracture surfaces of the 3D printed tensile specimens and the fiber/matrix interfacial bonding were investigated by means of a ZEISS Merlin® field emission scanning electron microscopy (FESEM) from Carl Zeiss Microscopy GmbH (Jena, Germany). FESEM analyses were also carried out to study the morphology of the feedstock materials before printing (i.e., as-received SLS powders and cryo-fractured surface of the filaments). The images were recorded using a wide magnification range (from 50x to 10000 kx) at an accelerating beam voltage between 3 (at high magnification) and 15 kV (at low magnification). The dimensional characteristics of the raw powders were determined by examining different FESEM images at 500x magnification through Image J® processing software. At least 300 particles or fibers collected from 20 micrographs were measured to obtain an accurate statistical evaluation of the particle size distribution of PA12 particles and the length distribution of the short carbon fibers respectively. A thin film of platinum was always applied on the samples by sputter coating to reduce charging effects and improve imaging quality.

3.2.8 Tensile tests

The mechanical properties of the additively manufactured parts were characterized by means of uniaxial tensile tests. For this purpose, MTS Criterion Model 43 universal testing machine (MTS Systems Corporation, Eden Prairie, MN, USA) equipped with a 5 kN load cell was used. The tests were performed at room temperature at a quasi-static cross-head velocity of 1 mm/min for the composite samples and 2 mm/min for the neat polymers. The international reference standards adopted for testing were ISO 527-4 and ASTM D3039 for short and continuous fiber reinforced composites respectively. An extensometer

with a gauge length equal to 25 mm was utilized to record elongation data. To improve the statistical significance of the results, four samples were tested for each combination of process parameter for SLS as well as each layup configuration for FFF and CFF. The elastic modulus, strength and elongation at break were obtained from the recorded stress-strain curves.

The tensile properties of the raw materials used to print PA/CCF composites through CFF were also determined by uniaxial tensile testing of single PA and CCF filaments to put in evidence the differences between neat and continuous fiber reinforced polymers. Filament fragments with 75 mm length were cut from the spools. Tensile tests of single PA filaments were performed according to ASTM D638-14 without using tabs. A specific set of grips was placed in the machine to avoid sample slippage. The cross-head velocity was set to 10 mm/min. However, in the first part of the test this value was reduced to 1 mm/min to precisely evaluate the Young modulus of the material. In contrast, the CCF filament samples were tested with mounting tabs according to ASTM D4018-17. Both ends of the sample were bonded via a high strength epoxy resin adhesive to a cardboard support having a hole with 15 mm diameter. The mounted test specimens were then placed carefully in the machine grips and the lateral side were cut away. A cross-head velocity of 1 mm/min was used for testing. The area of the PA and CCF filament cross sections were determined by measuring their diameters at distinct points along the filament length through a digital caliper. Five samples were tested for each filament type.

2.3.9 Dimensional accuracy

The dimensional accuracy of the 3D printed parts was evaluated by quantifying the deviations from the nominal dimensions obtained from the CAD geometry by using a digital caliper. For SLS parts the deviation per unit length, that corresponds to the average value of the dimensional errors (d_{error}) along the three sample axis (i.e., length, width and thickness), was used to assess the influence of the laser energy density on the geometrical accuracy of the printed objects according to equation (18)

$$d_{error} = \frac{d_{measured} - d_{nominal}}{d_{nominal}} 100\% \quad (18)$$

where $d_{measured}$ and $d_{nominal}$ are the dimensions (length, width or thickness) of the printed parts and CAD design respectively.

3.3 Models for the prediction of mechanical properties

In the composite material community, the prediction of the mechanical properties of fiber reinforced polymers has been investigated for decades. The elastic modulus and tensile strength of conventional composites can be calculated by well-known and widely used micro-mechanical models (i.e., fiber/matrix level). Moreover, macro-mechanical models (i.e., lamina level) were also developed to determine the elastic properties and the stress response of continuous fiber reinforced laminates under different load conditions. In both approaches the volume fraction and orientation of fibers are the main indicators used to evaluate the properties of the composites. These existing micro and macro mechanical theories can also be applied to analytically predict the tensile properties of AM composite reinforced with short or continuous fibers. However, slight modifications can be required to take into account the microstructural differences that often exists between the composite parts produced by AM and traditional processing techniques, particularly the void content [14,20].

3.3.1 Short fiber composite theories

Several methods have been proposed to predict the elastic modulus and strength of short fiber reinforced polymer composites [14,20]. The theories based on the rule of mixture (RoM) are the most popular due to their simplicity and physical appeal. The RoM is based on the assumptions that the property of a composite is the volume weighed average of the properties of its constituent phases (i.e., matrix and reinforcing fibers) and that a perfect fiber/matrix interfacial bonding exists. It is also assumed that fiber and matrix are equally strained and the fiber distribution is perfectly isotropic. However, most composites do not meet these ideal conditions. As a result, different factors have been implemented into the RoM equations to take into account the effect of fiber orientation, length and diameter as well as the the interfacial shear strength between fiber and polymer matrix in the modeling [14,20].

Elastic modulus

For stiffness prediction the shear lag model proposed by Cox and Krenchel [243] was adopted. The model predicts the longitudinal modulus of short fiber reinforced composites by adding to the simple rule of mixture two parameters that describe the contribution of fiber length and orientation. Since 3D printed composites usually exhibit a considerable amount of voids, the Cox-Krenchel

model was further modified by adding a porosity correction factor. Therefore, the elastic modulus of the composite E_c can be determined from equation (19):

$$E_c=(\eta_\theta \eta_l E_f V_f+E_m V_m)(1-\varphi) \quad (19)$$

where η_θ and η_l are the fiber length and fiber orientation efficiency factor respectively, E_f, V_f, E_m and V_m are the elastic modulus and volume fractions of fiber and matrix respectively and φ is the void content of the 3D printed part.

The fiber orientation efficiency factor η_θ can be calculated using the formulation introduced by Krenchel with the assumption of negligible fiber transverse deformation and flexural stiffness [243]:

$$\eta_\theta=\sum a_n \cos^4 \theta_n \quad (20)$$

where a_n is the fraction of fibers oriented at an angle θ_n with respect to the loading direction. The orientation distribution of the fiber depends on the processing conditions (e.g., shear forces or flow pattern). Typically, η_θ is equal to 1 when the fibers are aligned in the direction of the applied stresses, 0.375 for in-plane randomly distributed fibers and 0.2 for three dimensional randomly distributed fibers [243].

The fiber length efficiency factor η_l can be obtained by using Cox's model [244], derived by analyzing the load transfer between a single fiber and the surrounding polymer matrix with zero stress at the fiber ends:

$$\eta_l=1-\frac{\tanh(\beta l_f/2)}{(\beta l_f/2)} \quad (21)$$

where l_f is the average fiber length while (l_f/β) is a characteristic length for fiber/matrix stress transfer. β can be expressed as [243]:

$$\beta=\left(\frac{2G_m}{E_f r^2 \ln(R/r)}\right)^{1/2} \quad (22)$$

where G_m is the shear modulus of the polymer matrix, r is to the fiber radius and R corresponds to the distance between the centers of two nearest neighbor fibers. This parameter can be obtained by using the concentric cylinder model proposed by Rosen [245]:

$$R=r\sqrt{\left(\frac{1}{V_f}\right)} \tag{23}$$

The term (1-φ) is used to quantify the influence of voids on the mechanical properties of the composites according to the model developed by Rodriguez et al. [224], where 3D printed parts are treated a material-void composite.

Tensile strength

For strength prediction the modified Kelly-Tyson model was employed [246,247]. In this model the rule of mixture is modified by considering the effect of non-uniform fiber length (i.e., shorter and longer than the critical fiber length l_c) and orientation. The model puts forward that the external load is transferred from the matrix to the fibers through shear forces in the interfacial regions. For a ductile matrix, this means that a linear variation of the stress in a single fiber with respect to the distance x from its end can be assumed. Therefore, the tensile strength of the composite σ_c can be evaluated as follows [247]:

$$\sigma_c=\left\{\eta_\theta\left[\sum_{l_i=0}^{l_i=l_c}\frac{V_i\tau_y l_i}{2r}+\sum_{l_j=l_c}^{l_j=l_{max}}V_f\sigma_f\left(1-\frac{l_c}{2l_j}\right)\right]+V_m\sigma_m\right\}(1-\varphi) \tag{24}$$

where V_i corresponds to the volume fraction of fibers with length l_i, τ_y is the fiber/matrix interfacial shear strength, σ_f denotes the ultimate tensile strength of the fiber, σ_m represents the average matrix stress at the composite failure and V_m is the volume fraction of the matrix. The critical length of a fiber in a polymer matrix (l_c) represents the minimum length required for effective transfer of stress from matrix to the fiber and it can be expressed using equation (25):

$$l_c=\frac{\sigma_f r}{\tau_y} \tag{25}$$

where r is the fiber radius. Kelly and Tyson [246] refers to ½l_c as the load transfer length and l_c/d as the critical aspect ratio of the fiber. It is worth noting that the terms η_θ, obtained from equation (20), and (1-φ) are also present in equation (24) to correct for the effects of fiber orientation and void content.

3.3.2 Classical Laminate Theory (CLT)

Classical Laminate Theory (CLT) is a mathematical method widely used to analyse the mechanical behaviour of continuous fiber reinforced composites. It

allows to determine the displacements, curvatures an strains of orthotropic laminates subjected to different mechanical (i.e., forces and moments) and thermal loads. CLT was developed in the 1960s as a direct extension of the Kirchhoff–Love plate theory proposed for thin, isotropic and homogeneous materials. However, some adjustments have been implemented to take account of the inhomogeneity in the thickness direction typical of orthotropic material, that results in the adoption of more complex stress-strain relationships for each lamina. CLT is based on different assumptions, whose details are given in [243]. In short, each laminate ply is treated as a homogeneous thin plate with known orthotropic properties subjected to a plane state of stress. Moreover, a perfect bonding between plies, that corresponds to continuity of displacements thorough the laminate thickness, is considered. CLT was used to predict the mechanical properties of 3D printed continuous fiber reinforced laminates (PA/CCF) as they show orthogonal behavior. Moreover, the assumption of continuity of displacements appears to be reasonable from a mechanical viewpoint because the 3D printed parts are highly non homogeneous due to the presence of neat PA roof and floor layer, regions with high fiber or matrix concentration and voids. As already mentioned, CLT provides the ability to analyse the mechanical response of orthotropic laminates to mechanical loadings. The laminates can be made of multiple unidirectional or woven plies stacked in different directions according to the layup adopted. The CLT formulation used to predict the tensile properties of PA/CCF laminates are presented below [243].

The basic requirement for CLT analysis is the characterization of the five constants governing the elastic behaviour of the materials adopted to produce PA/CCF laminates at the ply level (see Section 4.3.4). These constants are the longitudinal (E_{11}), transverse (E_{22}) and shear modulus (G_{12}) as well as the Poisson's ratios (v_{12} and v_{21}). The stiffness matrix $[Q]_k$ of each *k* ply can therefore be created for both neat PA and CCF reinforced materials (Q_{PA} and Q_{CCF} respectively):

$$Q_{PA}=\begin{bmatrix} E/(1-\upsilon^2) & \upsilon E/(1-\upsilon^2) & 0 \\ \upsilon E/(1-\upsilon^2) & E/(1-\upsilon^2) & 0 \\ 0 & 0 & G \end{bmatrix} \tag{26}$$

$$Q_{CCF}=\begin{bmatrix} E_{11}/(1-\upsilon_{12}\upsilon_{21}) & \upsilon_{21}E_{11}/(1-\upsilon_{12}\upsilon_{21}) & 0 \\ \upsilon_{12}E_{22}/(1-\upsilon_{12}\upsilon_{21}) & E_{22}/(1-\upsilon_{12}\upsilon_{21}) & 0 \\ 0 & 0 & G_{12} \end{bmatrix} \tag{27}$$

where E, G and v correspond to the elastic moduli and Poisson's ratio of the PA lamina (no distinction was made between longitudinal and transverse direction because the neat polymer is perfectly isotropic) and E_{11}, E_{22}, G_{12}, v_{12} and v_{21} denote the elastic moduli and Poisson's ratios of the CCF lamina (Table 27). The transformation matrix, that describes a coordinate system transformation between the local or principal material axes (1-2) and the global or laminate axes (x-y), is applied to calculate the transformed reduced stiffness matrix of the CCF laminae ($\overline{Q}_{CCF}$) for different fiber/ply orientations:

$$\overline{Q}_{CCF}=TQ_{CCF}T^{-1} \tag{28}$$

where $\overline{Q}_{CCF}$ and Q_{CCF} correspond to the stiffness matrix of the CCF reinforced plies in the global and local coordinate system respectively. The transformation matrix T is computed as a function of the angle θ formed between each fiber reinforced ply and the x-axis as follow:

$$T=\begin{bmatrix} \cos^2\theta & \sin^2\theta & 2\sin\theta\cos\theta \\ \sin^2\theta & \cos^2\theta & -2\sin\theta\cos\theta \\ -\sin\theta\cos\theta & \sin\theta\cos\theta & \cos^2\theta-\sin^2\theta \end{bmatrix} \tag{29}$$

The coordinate system transformation described in equation (29) is not required for neat PA laminae since the material is perfectly isotropic. As a result, $\overline{Q}_{PA}= Q_{PA}$. The extensional [A], bending-extension coupling [B] and bending [D] stiffness matrices are calculated by taking into account the position of each lamina in the layup using equations from (30) to (32):

$$A_{ij}=\sum_{k=1}^{n}\overline{Q}_k(z_k-z_{k-1}) \tag{30}$$

$$B_{ij}=\frac{1}{2}\sum_{k=1}^{n}\overline{Q}_k(z_k^2-z_{k-1}^2) \tag{31}$$

$$D_{ij}=\frac{1}{3}\sum_{k=1}^{n}\overline{Q}_k(z_k^3-z_{k-1}^3) \tag{32}$$

where z_{k-1} and z_k correspond to the distance, or in other word the vertical position, of the bottom and top surface of the ply *k* from the midplane of the laminate respectively. Thereafter, a relationship between the applied loads (i.e., moments M and normal stresses N) and the related strains (i.e., curvatures κ and midplane strains ε_0) can be written as follow:

$$\begin{Bmatrix}\varepsilon_0\\ \kappa\end{Bmatrix}=\begin{bmatrix}A & B\\ B & D\end{bmatrix}^{-1}\begin{Bmatrix}N\\ M\end{Bmatrix} \tag{33}$$

It is worth noting that in the case of symmetric and balanced laminates no coupling between extension and bending (i.e., [B]=0) as well as between extension and shear (i.e., the terms A_{16}, A_{26}, A_{61},A_{62} of the extensional matrix are zero) occurs. In addition, the laminate is subjected to normal stresses only during uniaxial tensile tests. Therefore, equation (33) can be simplified to:

$$\{\varepsilon_0\}=[A]^{-1}\{N\} \tag{34}$$

The strain along the laminate thickness can be calculated from:

$$\begin{Bmatrix}\varepsilon_x\\ \varepsilon_y\\ \gamma_{xy}\end{Bmatrix}_k=\begin{Bmatrix}\varepsilon_x^0\\ \varepsilon_y^0\\ \gamma_{xy}^0\end{Bmatrix} \tag{35}$$

Finally, for each *k* ply the strains in the principal material axes (1-2) are determined from the strains in the laminate axes, obtained from equation (35), by applying a coordinate system transformation, while the related stresses can be computed by considering the stiffness matrix $[Q]_k$:

$$\begin{Bmatrix}\varepsilon_1\\ \varepsilon_2\\ \frac{1}{2}\gamma_{12}\end{Bmatrix}_k=[T]\begin{Bmatrix}\varepsilon_x\\ \varepsilon_y\\ \frac{1}{2}\gamma_{xy}\end{Bmatrix}_k \tag{36}$$

$$\begin{Bmatrix}\sigma_1\\ \sigma_2\\ \tau_{12}\end{Bmatrix}_k=\begin{bmatrix}Q_{11} & Q_{12} & 0\\ Q_{12} & Q_{22} & 0\\ 0 & 0 & Q_{66}\end{bmatrix}_k\begin{Bmatrix}\varepsilon_1\\ \varepsilon_2\\ \gamma_{12}\end{Bmatrix}_k \tag{37}$$

The CLT calculations were exploited by using a laminate failure analysis simulation tool [248] available from “cdmHUB” website. The longitudinal elastic modulus of the laminate was computed by using the extensional stiffness matrix according to equation (38) [243]:

$$E_{11}^{lam}=\frac{A_{11}A_{22}-A_{12}^2}{A_{22}t} \tag{38}$$

where t represents the laminate thickness (Table 5). The tensile strength at break (σ_{lam}) was instead estimated by performing a progressive ply failure analysis according to the simple ply discount method [243]. The progressive failure analysis starts by applying an axial tensile load N_x to the laminate and determining the stresses in each *k* ply through the CLT formulation described above. In fact, the strain tensor components of each lamina are equal owing to the assumption of continuity of displacement of Classical Laminate Theory, while the stress distribution highly differs because each *k* ply has distinct elastic properties in relation to the orientation of the fibers. When the calculated stresses are equal or higher than the ply strength defined by using the Tsai-Hill failure criterion, the ply breaks. If none of the laminate layers fails, the applied load is gradually raised, until the first ply failure (FPF) is determined. Once a ply has failed the five elastic constants of the material are fully degraded and the stiffness matrices are recalculated. As a result, the damaged ply or plies are not able to bear the applied loads, that are consequently redistributed among the remaining layers of the laminate. This hypothesis corresponds to the stiffness reduction method referred as "full reduction/ply removal" in the simulation tool [248]. The previous procedure is then repeated until all the plies of the laminate have failed, thus leading to the estimation of the last ply failure (LPF) load. Generally, for quasi isotropic laminates the transverse plies fail firstly, followed by angled plies (e.g., oriented at 45° or 60°) and longitudinal ones respectively due to an increase of the applied load. The strength at break can be determined dividing the LPF load by the nominal thickness of the laminate. For cross-ply layup, only the transverse (E_2) and shear (G_{12}) moduli were set to 0 after first ply failure. This assumption, corresponding to stiffness reduction method referred as "2 mode" in the simulation tool [248], is widely acknowledged as more suitable to describe the progressive damage in $[0/90]_s$ laminates due to transverse matrix cracking [243,249,250]. In fact, the damaged plies can still carry part of the applied load, at least in tension, due to the contribution of the fibers [249,250].

Since the internal structure of the printed laminates consists of wall and infill regions (Figure 51), each ply can be considered as a two part-system, as proposed by Choi et al. [226] for short fiber composites processed using FFF. In fact, CLT is employed to model the infill region of the laminates, constituted by CCF strands only (or ±45° neat PA in the outer layers). A simple rule of mixture (RoM) approach is then used to take account of the contribution of the neat PA wall surrounding each layer. Therefore, the elastic modulus and strength at break of the PA/CCF parts were calculated as follows:

$$E_c=E_{11}^{lam}(1-V_{walls})+E_{11}^{PA}V_{walls} \quad (39)$$

$$\sigma_c=\sigma_{lam}(1-V_{walls})+\sigma_{1t}^{PA}V_{walls} \quad (40)$$

where $E_{11}^{lam}$and σ_{lam} corresponds to the elastic modulus and strength of the infill region of the PA/CCF laminate computed by using CLT analysis and $E_{11}^{PA}$and σ_{1t}^{PA} are the tensile properties of the nylon material (Table 27). The volume fraction of the neat PA wall region V_{walls} was estimated by considering the samples geometry using equation (41):

$$V_{walls}=\frac{PW_{wall}N_{walls}t_{layer}N}{V_{composite}} \quad (41)$$

where P is the sample perimeter, N_{walls} is the number of PA perimeters, t_{layer} denotes the layer thickness and N is the number of layers. The width of the PA wall (W_{wall}) was estimated by optical microscopy (Figure 94) and it is equal to 0.75 mm. The total volume of the composite ($V_{composite}$) was obtained from the 3D printer software (Table 6). The geometrical parameters used in the calculations are listed in Table 7 for each laminate layup.

Table 7: Geometrical details of the 3D printed samples structure

Sample notation	Sample perimeter P (cm)	Number of layer N	Layer thickness T_{layer} (mm)	Number of walls N_{walls}
$[0]_s$	53	8	0.125	1
$[0/90]_s$	55	16	0.125	1
$[0/45/90/-45]_s$	55	16	0.125	1
$[0/\pm60]_s$	55	18	0.125	1

Chapter 4

Results and discussion

4.1 Selective Laser Sintering

4.1.1 Powders characterization

Morphological and physical properties

The morphology and surface structure of PA12/CF powders is displayed in Figure 53 at different magnification levels. The powders are a homogeneous mixture of PA12 particles and discontinuous carbon fibers (Figure 53a). The polymeric particles show a cauliflower-like shape with a slightly undulating surface structure (Figure 53b). FESEM images also suggest that PA12 particles exhibit a nearly regular and narrow particle size distribution (PDS), which will be addressed during the experimental characterization. By comparing these morphological properties with a detailed literature and patent investigation [17,65,68,75,76] it is reasonable to assume that the polymeric particles correspond to Orgasol® family PA12 powders, produced by the chemical company Arkema with a direct anionic polymerization process. The high magnification FESEM image (Figure 53c) clearly shows the lamellar structure of the polymer crystalline phase, which consists of stacks of parallel crystal lamellae with an almost flat orientation. Moreover, it can be observed that the PA12 powders surface is partially coated with perfectly round particles with nanometre size (Figure 53c). In fact, inorganic additives such nano-SiO_2 or carbon black are commonly added to SLS powders by mechanical mixing or dry-coating processes in order to improve their flowing

behaviour during powders spreading stage [78–82]. These fillers are referred as flow agents or flowing aids [23,29,81,82].

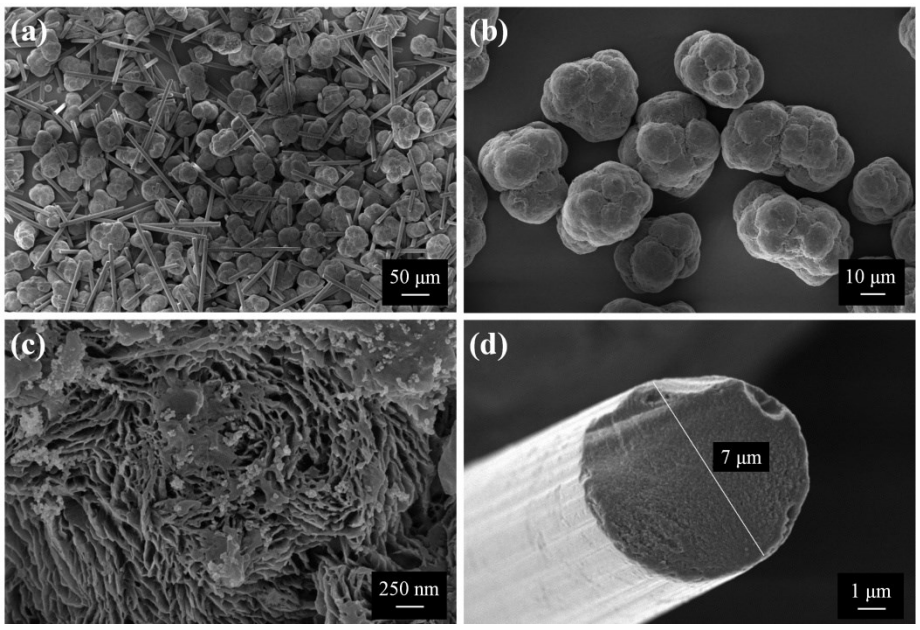

Figure 53: Scanning electron microscope images of PA12/CF powders: (a) low magnification image and details on (b) polymer particles, (c) polymeric particle surface and (d) carbon fibers

Figure 53d depicts an individual carbon fibers showing a diameter of 7 µm. The fiber surface is clean and relatively smooth with few parallel grooves along its axial direction owing to the typical structure of PAN-precursors used in the fibers manufacturing process (i.e., wet spinning) [251,252].

Figure 54 depicts the dimensional distribution of the PA12/CF powders carried out by image analysis of FESEM micrographs. Polymer particles exhibit a very narrow particle size distribution (PSD), typical of Orgasol® powders, ranging between 30 µm and 60 µm with a average particle size of 42 µm. By contrast, carbon fibers shows a wide length distribution with an average value of 91 µm (Figure 54). The dimensional characteristics of PA12/CF powders are summarized in Table 8. The parameters d_{10}, d_{50}, d_{90}, corresponding to the particle sizes/lengths equal to which the 10%, 50% and 90% respectively of the PSD is confined, are reported in the table.

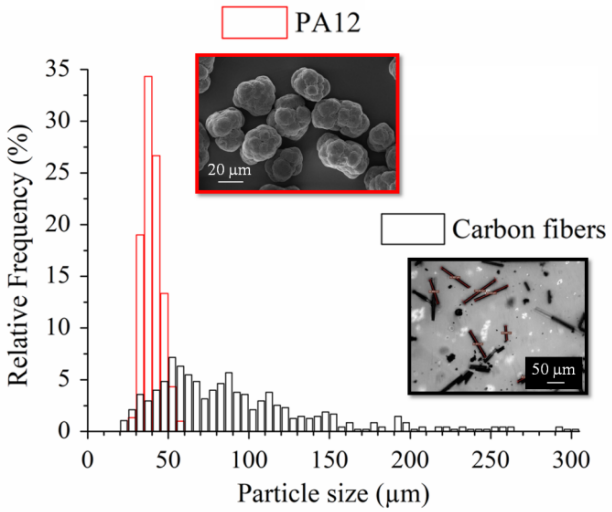

Figure 54: PA12/CF powders size/length distribution obtained with ImageJ® software: polyamide particles and carbon fibers

Table 8: Dimensional properties of PA12 particles and carbon fibers

	d_{10} (µm)	d_{50} (µm)	d_{90} (µm)
PA12 particles	33	39	47
Carbon fibers	40	81	157

The particle morphology and the characteristics of the PDS curve do not allow to effectively define the flow properties of the SLS powders. Therefore, true density, packing factor, Hausner ratio and Hall flow rate of PA12/CF powders were analyzed by tap density tests and volumetric flow rate measurements with Hall flowmeter funnel. Unreinforced PA12 powders were also studied for sake of comparison. The experimental results are reported in Table 9. Particularly, the packing factor (Φ) denotes the ability of a powder to freely occupy a confined volume without mechanical action and the Hausner ratio can be adopted to rank the flowability of the powders according to [253]. Pure polyamide powders present excellent flowability and packing efficiency (Table 9). In fact, it is widely acknowledged that polymeric powders with almost spherical shape and narrow PSD (in the dimensional interval from 20 to 80 µm) are particularly suitable to be processed through SLS [66].

Table 9: True density, packing factor, Hausner ratio and Hall flow rate of PA12/CF and neat PA12 powders

Material	True density ρ (g/cm^3)	Packing factor Φ	Hausner ratio HR [1]	Hall flow rate ($s/10cm^3$)
PA12/CF	1.140 ± 0.001	0.39	1.28 (fair)	fail
PA12	1.045 ± 0.001	0.47	1.16 (good)	14.5

The addition of carbon fibers worsened the packing efficiency and flowing behaviour of the neat PA12 powders due to the high aspect ratio typical of fibrous reinforcement and the wide fiber length distribution. This is further confirmed by the Hausner ratio and Hall flow test results (Table 9). However, experimental runs on the SLS machine demonstrate that the lower packing efficiency and flowability of the reinforced powders does not significantly hinder the production of fully-dense components (Section 4.1.2).

Thermal properties

The DSC curves of neat PA12 and PA12/CF powders are shown in Figure 55.

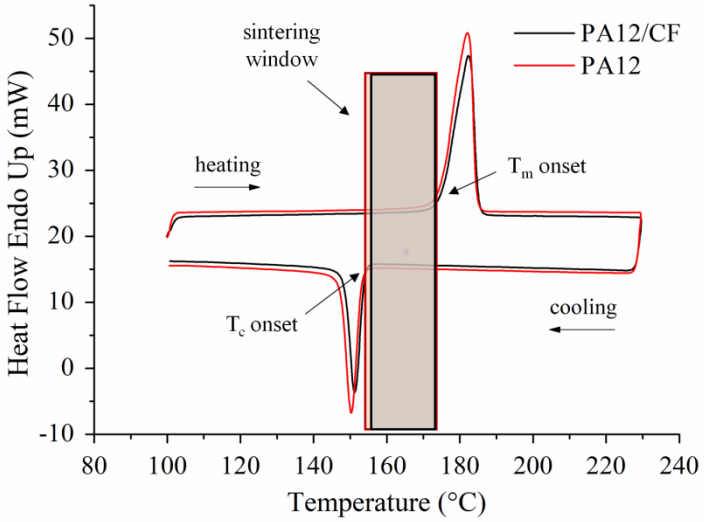

Figure 55: DSC curves of PA12 and PA12/CF raw powders. The "sintering window" of PA12 and PA12/CF are indicated in the figure by red and grey colour respectively

[1] Classification according to [253].

The heating-cooling traces of both materials reveals distinct melting and crystallization events with a wide temperature interval between the onset of polymer fusion and crystallization (Figure 55). The existence of this interval ("sintering window"), is highly favourable for processing in SLS machines [22,23,28,29,72,108]. Moreover, the melting peaks are sharp and show a high enthalpy of fusion (Figure 55) owing to the high crystallinity (48%) and crystallite perfection of PA12 particles [75]. This behaviour suggests that the advantage of using lasers, that is supplying a lot of energy in a very short time, is well exploited. Moreover, a high melting enthalpy is advised to avoid the partial melting of the particles in the vicinity of the printed part [55,72]. A slight shift in the crystallization events (~1 °C) can also be observed for PA12/CF (Figure 55). In fact, carbon fibers promotes the formation of polymer crystals, as often reported in literature for various polymer composites [134,254,255]. The nucleation effect of carbon fibers is further highlighted by DSC cooling runs performed on PA12 powders with different CF contents (from 5 to 20 wt.%), as shown in Figure 56. This could lead to a higher tendency to curling during processing. However, Yan et al. [134] suggested that the lower volumetric shrinkage during cooling typical of carbon fiber reinforced composites compared to the neat polyamide matrix improves the accuracy of the printed parts.

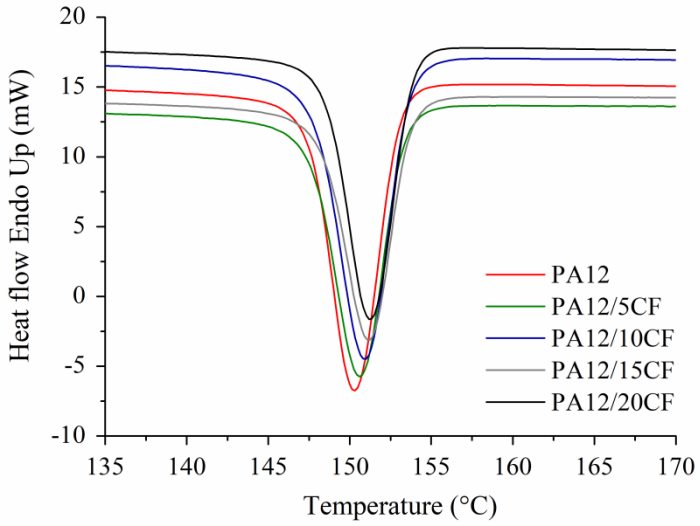

Figure 56: DSC cooling curves of PA12 and PA12/CF powders reinforced with 5, 10, 15 and 20 wt.% of carbon fibers

Since SLS can be considered as a quasi-isothermal process taking place at the powder bed temperature (T_b) [28], isothermal crystallization kinetics were also

studied. In fact, this analysis could be very effective to gain detailed information on the evolution of polymer crystallization during the entire SLS building process. Figure 57 shows the heat flow curves recorded during the isothermal step of DSC tests performed at different crystallization temperatures (T_{iso}) according to the procedure described in Section 3.2.1.

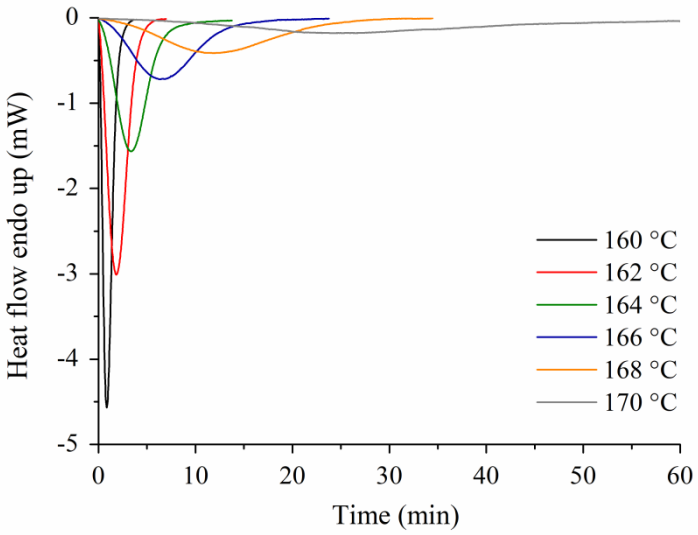

Figure 57: Heat flow versus time DSC thermograms of PA12/CF powders at different isothermal crystallization temperatures

The crystallization peaks are progressively delayed in time and the corresponding maximum heat flow values decline with the increase of the temperature T_{iso} (Figure 57). Accordingly, a longer time is needed for the polymer to crystallize. This aspect is highly relevant for SLS processing of PA12/CF powders because the slower the crystallization take places, the lower is the risk of out-of-plane deformation of the sintered layers due to residual stress build up and crystallization shrinkage [28,70]. Moreover, it can be observed that very low heat flow (i.e., < 0.05 mw/mg) was recorded when the temperature approaches 168 °C (Figure 57). At higher temperatures the DSC signal became gradually weaker, indicating that crystallization is further delayed until no phase transition occurs at all above 170 °C. A similar behaviour was found for PA12 and PEEK powders [86,87]. In fact, polymer crystallization is a thermally-activated process and the phase transition at low undercooling (i.e., when the temperature is near the melting onset) is thermodynamically hindered by the nucleation barrier.

The degree of crystallization X(t) can be calculated by time integration of the heat flow curves of Figure 57 using equation (42) [256]:

$$X(t)=\frac{\int_{t_0}^{t}\frac{dH_c(t)}{dt}dt}{\int_{t_0}^{t_\infty}\frac{dH_c(t)}{dt}dt} \quad (42)$$

where H_c is the heat flow measured during the isothermal crystallization tests. The evolution of the degree of crystallization with time at different T_{iso} is depicted in Figure 58. The X(t) versus time curve corresponding to 172 °C is not reported as no crystallization occurs.

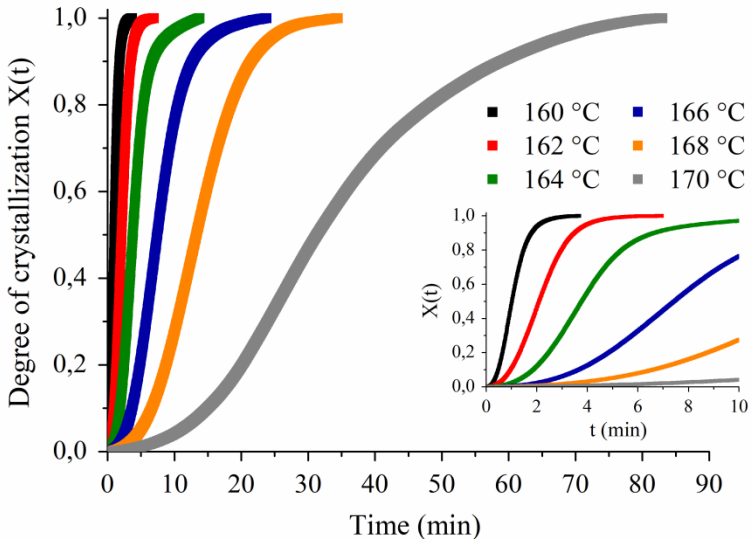

Figure 58: Evolution of the degree of crystallization during isothermal crystallization of PA12/CF powders at 6 different T_{iso}. Inset: magnified view of the initial part of the crystallization kinetics curves

It can be seen that polymer crystallization always progresses following a similar sigmoidal path (Figure 58). More precisely, the turnover speed, that is the speed at which the conversion between melted and solidified polymer crystals proceeds, lowers at increasing T_{iso}. As a result, the crystallization process occurs more slowly. The experimental crystallization halftime $t_{1/2}^{M}$ (i.e., time at which 50% of the total crystalline phase of the polymer is formed) can be easily obtained from the above mentioned curves (Figure 58). The crystallization kinetics were further analyzed using the Avrami theory [87,256]:

$$X(t)=1-e^{(-k(T)t^n)} \quad (43)$$

where n is the Avrami exponent, related to the mechanisms of crystallization such as the nucleation mode and the dimensionality of the crystal growth [256] and

k(T) is the crystallization growth rate. This parameter is temperature dependent. To calculate the Avrami exponent and the crystallization growth rate from the slope and y axis intersection of a straight line, equation (44) is reformulated in its logarithmic form [87,256]:

$$\ln(-\ln(1-X(t))) = \ln k(T) - n \ln t \tag{44}$$

Figure 59 depicts the double logarithmic plots of ln(-ln(1-X(t))) against lnt for different T_{iso}, useful for evaluating the Avrami exponent n and crystallization rate k by linear fitting (dashed lines in Figure 59). The linearization was performed within a specific interval of crystallization degree values (from 3% to 80%) in order to obtain the highest modeling accuracy (i.e., coefficient of determination R^2 of the linear fit higher than 0.99).

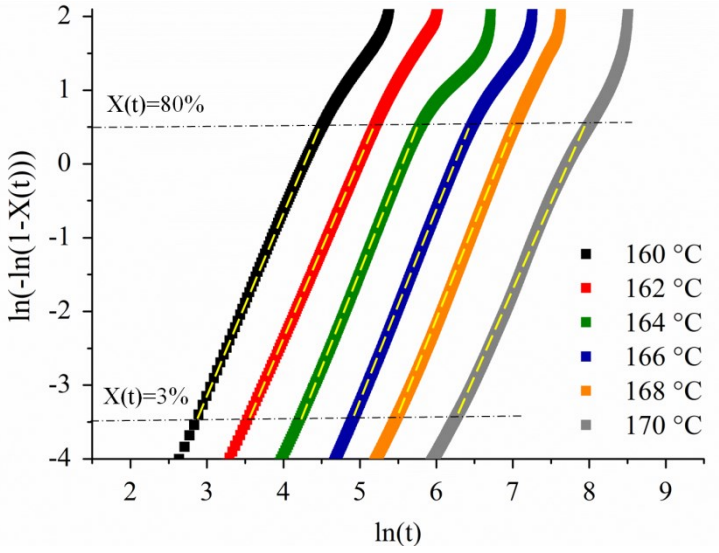

Figure 59: Plots of ln(-ln(1-X(t))) - lnt for different T_{iso} showing the linear fit (yellow dashed lines) obtained from the Avrami model for X(t) between 3% and 80%

The crystallization kinetic parameters obtained experimentally and calculated using the Avrami model are listed in Table 10. It can be seen that a substantial positive correlation exists between $t_{1/2}$ and temperature (Figure 59 and Table 10). This is also reflected by the reduction of the crystallization growth rate k at increasing T_{iso} (Table 10). This behavior is typical for thermoplastic polymers [86,87,257]. A negligible deviation (<±1%) between the modeling result and the experimental data can be seen for $X(t) \leq 80\%$ (Figure 59 and Table 10).

Table 10: Crystallization kinetic parameters for PA12/CF powders isothermally crystallized at different temperatures. n denotes the Avrami exponent, k is the growth rate of crystallization. R^2 is the coefficient of determination for the Avrami fit, the $t_{1/2}^E$ and $t_{1/2}^A$ are the crystallization halftimes from the experiments and Avrami model respectively and t_{peak} is the time at which the heat flow reaches the maximum value

T_{iso} (°C)	n	k (s^{-1})	R^2	$t_{1/2}^E$ (s)	$t_{1/2}^A$ (s)	t_{peak} (s)
160	2.46	2.77×10^{-5}	1.00	61.0	61.3	51.0
161	2.89	1.84×10^{-6}	1.00	84.3	84.7	73.0
162	2.42	5.68×10^{-6}	1.00	125.5	125.5	109.0
163	2.98	2.01×10^{-7}	1.00	155.2	156.9	137.6
164	2.59	5.44×10^{-7}	1.00	226.5	227.9	201.0
165	2.87	4.73×10^{-8}	1.00	314.5	315.5	290.0
166	2.61	8.52×10^{-8}	1.00	445.8	447.5	380.0
167	2.92	5.93×10^{-9}	1.00	580.0	581.8	546.0
168	2.62	1.68×10^{-9}	1.00	797.3	801.8	718.0
169	2.89	7.72×10^{-10}	0.99	1240.0	1249.3	1180.0
170	2.53	3.56×10^{-10}	1.00	1878.5	1881.0	1451.0
171	2.81	1.62×10^{-10}	0.99	2661.3	2675.5	2368.0
172	-	-	-	-	-	-

The values of the Avrami exponent range from 2.4 to 3 and do not show a clear temperature dependence. This means that crystallization probably follows a mixed bi-dimensional and three-dimensional growth with formation of lamellar

and spherulitic crystals [86,87]. Moreover, the results of the isothermal crystallization tests show that PA12/CF would reach half crystallization after 18 min at 168 °C. Since the exposure time of a single layer is 45 s in average, it can be inferred that the crystallization starts just after few layers are sintered (inset of Figure 58) and reaches 50% crystallization after 20 layers (Table 10). Therefore, the validity of the isothermic sintering model (i.e., the polymer powders fused by the laser remain in the molten phase until the entire building step is finished) is restricted to the early stage of printing and consequently build height. Similar findings were also achieved by other research groups on neat PA12 and PEEK powders [86,87]. The activation energy for crystallization E_A was calculated through the Arrhenius method by using equation (45) [85]:

$$\ln(t_{peak}) = -\frac{E_A}{R}\left(\frac{1}{T_{iso}}\right) + \ln\left(\frac{AR}{E_A}\right) \tag{45}$$

where t_{peak} is the maximum heat flow time and R is the ideal gas constant. The experimental data of $\ln(t_{peak})$ vs. $1000/T_{iso}$ obtained from isothermal crystallization kinetics were plotted in Figure 60 and fitted by linear regression. The activation energy E_A is evaluated to be 544 kJ/mol, which is slightly higher compared to the neat PA12 value (501 kJ/mol) extrapolated from [87].

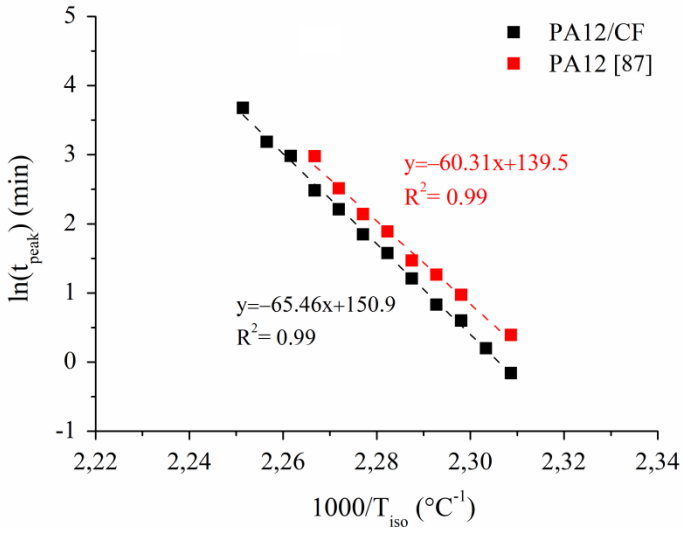

Figure 60: Arrhenius-type plot showing the temperature dependency of t_{peak} described by the activation energy for polymer crystallization. Neat PA12 data obtained from [87] are also reported for comparison

These results indicate that carbon fibers slightly affect the crystallization of PA12 matrix. In fact, higher is the activation energy, more severe is the effect of a

temperature change near T_{iso} (i.e., supercooling) for the nucleation and growth of polymer crystallites. Therefore, this parameter could be adopted as a guideline for material screening in SLS [87].

Figure 61 show the thermo-gravimetrical curves in inert environment of neat PA12 and PA12/CF powders. The powders exhibit a single-step degradation at 400 °C, corresponding to the pyrolysis of the polymer chain backbone. The thermal stability slightly increases with the addition of carbon fibers in the matrix, as observed from a slight shift to higher temperature of the derivative curves describing polymer degradation (inset of Figure 61). The fiber content of PA12/CF powders (19.2 wt.%) was also determined from TGA outcomes (Figure 61) by subtracting the final residues of unreinforced PA12 (i.e., carbonaceous char) and PA12/CF curves.

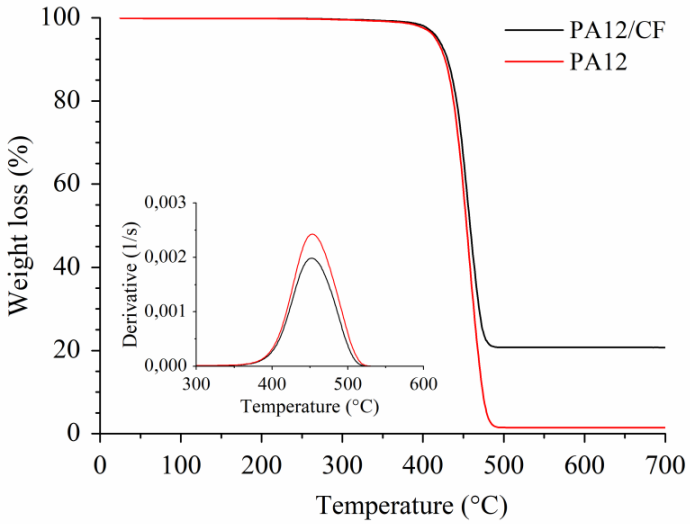

Figure 61: TGA curves of neat PA12 and PA12/CF in argon atmosphere. Inset: derivative curves showing the maximum rate degradation temperature

TGA experiments in air atmosphere were also conducted to evaluate the onset degradation temperature (T_{deg}) and the activation energy for thermo-oxidative degradation ($E_{A\ deg}$) for PA12/CF powders. In fact, the SLS printer used in this research activity operates in air environment. The onset degradation temperature, corresponding to 1% weight loss in the TGA curve obtained using a heating rate equal to 10 °C/min, was observed at 369 °C (Figure 62a). The activation energy was estimated to be 330.6 kJ/mol (with a coefficient of determination R^2 of 0.99) using the integral isoconversional method described in Section 3.3.2. A slightly lower value was obtained for neat PA12 (296.5 kJ/mol), thus confirming that

carbon fibers enhance the thermal stability of the PA12 matrix [134,255]. Isoconversional plots for α=50%, that correspond to a weight loss of 60% in the TGA curves (Figure 62a), are showed in Figure 62b.

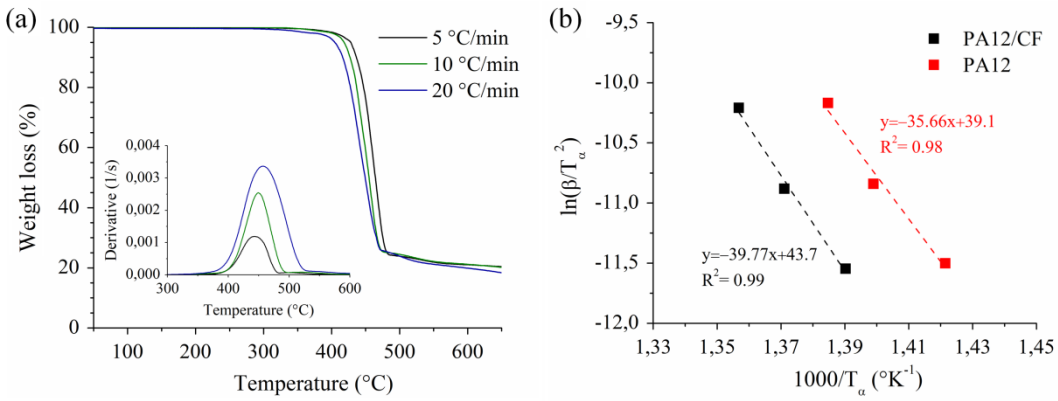

Figure 62: (a) TGA and weight loss derivative curves (inset) of PA12/CF at different heating rate; (b) isoconversional plot of $\ln(\beta/T_\alpha^2)$ versus $1000/T_\alpha$ obtained from TGA curves. Experimental data collected by thermogravimetric analysis of neat PA12 powders in air are also reported for comparison

The stable sintering region (SSR), introduced by Vasquez et al. [108] to identify the optimum temperature interval for successful SLS processing, can be evaluated by bringing together DSC and TGA experiments (Figure 63).

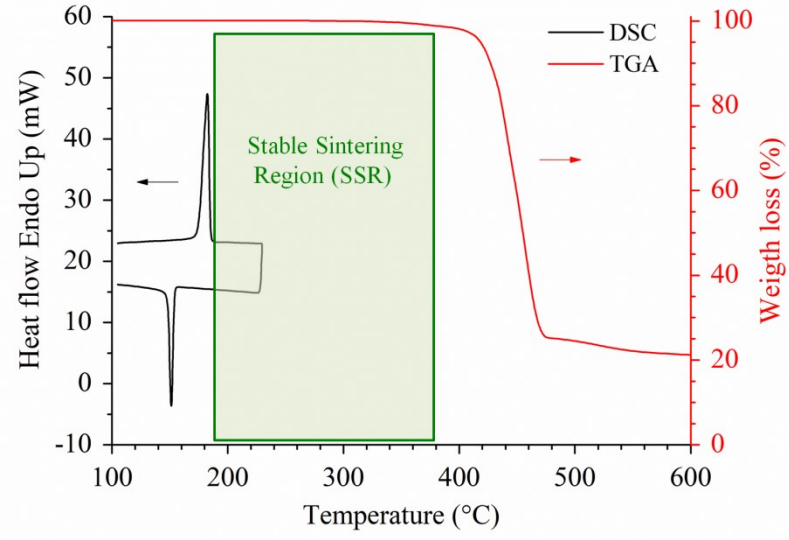

Figure 63: Graphical representation of the stable sintering region for PA12/CF powders. DSC thermogram (left axis) and TGA curve in air atmosphere (right axis) are reported in the graph

PA12/CF powders display a broad temperature range between the melting offset and the start of polymer decomposition in air (Figure 63). This is crucial because a wide SSR is widely accepted as one of the most important material requirement for laser sintering [22,49,108,123].

The variation of heat capacity with temperature was measured experimentally through a modulated DSC experiment. The specific heat of neat PA and PA12/CF powders linearly increased with temperature in the solid phase. Sharp peaks related to the latent heat of fusion of the polymer can also be seen followed by a minor increase of the heat capacity at higher temperature (Figure 64).

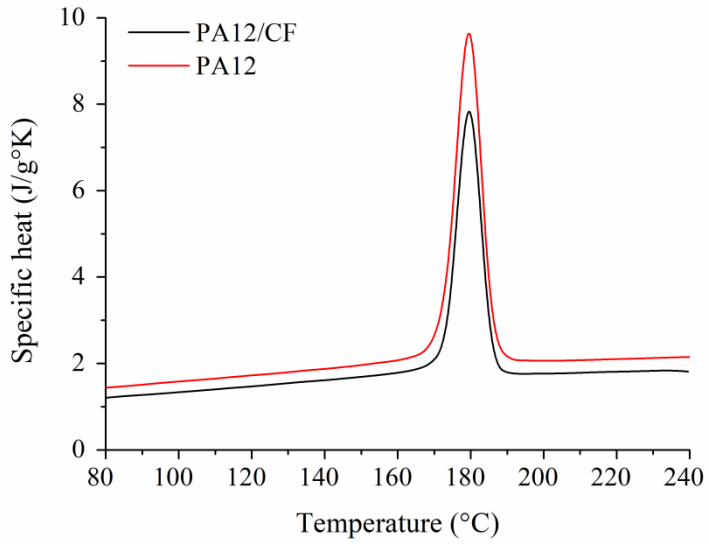

Figure 64: Specific heat capacity of neat PA12 and PA12/CF powders as a function of temperature from solid to molten phase

The thermal and physical properties of PA12/CF powders are summarized in Table 11. The molecular weight of the polymer was obtained from literature [68]. These properties are used to evaluate melting and degradation energy according to equations (8) and (9) (see section 3.3.1). The specific heat value at the powder bed temperature (T_b=170 °C) and the heat capacity of the polymer melt, determined as average value between the melting offset and 240 °C (see Figure 64), are reported Table 11, while the true density and packing factor of the powders were listed in Table 9. The extent of the sintering window and stable sintering region are also reported in Table 11.

Table 11: Thermal properties of PA12/CF powders needed for the calculations of melting and degradation energy. Sintering window and SSR are also reported

Properties	Value
Onset melting temperature $T_{m\ onset}$ (°C)	174.7
Melting peak T_m (°C)	182.3
Endset melting temperature $T_{m\ endset}$ (°C)	184.9
Enthalpy of melting h_f (J/g)	81.41
Onset crystallization temperature $T_{c\ onset}$ (°C)	153.9
Enthalpy of crystallization h_c (J/g)	39.2
Powder specific heat $C_p^{\ powder}$ (J/g °K)	1.99
Melt specific heat $C_p^{\ melt}$ (J/g °K)	1.81
Onset degradation temperature in air T_{deg} (°C)	369
Activation energy $E_{A\ deg}$ (kJ/mol)	330.6
Weight average molecular weight M_W (g/mol) [2]	18080
Sintering window (°C)	21
Stable Sintering Region (°C)	184

[2] Molecular weight was derived from [68].

4.1.2 Process window of PA12/CF composite: defects optimization

Powder bed temperature

It is largely acknowledged that during the SLS processing of semicrystalline polymers and their composites the powder bed temperature is selected in-between the onsets of melting and crystallization, in agreement with the isothermic laser sintering model [22,28,29,72,108]. This region, that correspond to the under-cooled polymer melt, is usually known as "sintering window" and was evaluated for PA12/CF powders using with a standard DSC measurement (Figure 55). According to literature [22,29,39,72,108], the powder bed must be pre-heated to a temperature higher than the crystallization onset ($T_{c\ onset}$ in Table 11) to prevent polymer crystallization that leads to shrinkage, residual stresses build-up and distortion in the final part. At the same time, T_b need to be lower that the melting onset ($T_{m\ onset}$ in Table 11) to avoid that the particles around the part begin to melt. Literature suggests that the sintering window should be sufficiently large to circumvent these obstacles [22,29,39,72,108]. The DSC curve of Figure 55 showed that PA12/CF exhibits a wide sintering window (22 °C). However, it must be pointed out that this scheme is just an idealized representation of the thermal reality as it is acquired using a fixed heating and cooling rate (10 °C/min) that never exists during SLS processing. In fact, empirical evidences clearly show that if a too low building temperature is selected, crystallization may start during the first layers, which typically reveals in the part contour bending upwards (i.e., curling) [28,39,72,238].

A quantitative analysis of part curling resulting from SLS processing of PA12/CF powders at different pre-heating temperatures (T_b) inside the sintering window was carried out using rectangular flat plates as benchmark samples (see Figure 46). Figure 65 shows the relationship between temperature, curl height and inverse of crystallization halftime. It is possible to notice that the amount of upward deformation of the part progressively increased from 168 °C to 163 °C. At lower temperature no data points are reported in Figure 65. In fact, the upward deformation of the plates developed to such an extent that the parts are dragged along by the recoater movement during the spreading of a new layer of powders. Therefore, it can be stated that curl development is very sensitive to small changes in the powder bed temperature.

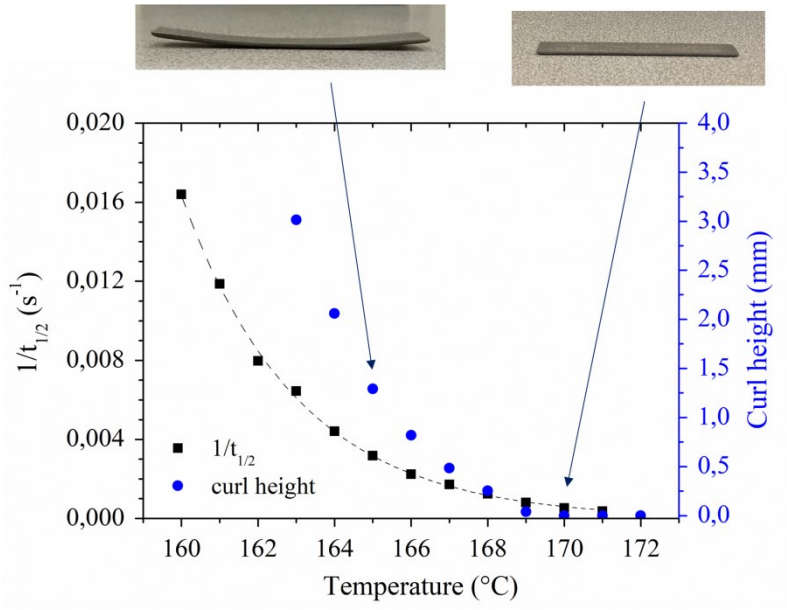

Figure 65: Inverse of crystallization halftime $1/t_{1/2}$ (left axis) and measured curl height (right axis) at different T_b for PA12/CF powders. Photographic images of rectangular samples printed at 165 °C and 170 °C are also shown

The experimental results of the curling analysis can be explained by considering the crystallization behaviour of PA12/CF powders studied by more realistic isothermal DSC measurements. As depicted in Figure 57, polymer matrix crystallization takes place in isothermal condition during processing (above $T_{c\ onset}$) and this phase transition is time and temperature-dependent. The plot of the inverse crystallization halftime $1/t_{1/2}$ versus temperature graphically depicts this behaviour (Figure 65).

As revealed in the graph, a fairly good agreement between $1/t_{1/2}$ and curl height was found. This indicates that a strong relationship between powder bed temperature, crystallization kinetics and curl development in the sintered parts exists and the polymer phase transition induces this out of plane deformation. In fact, in semi crystalline polymers the crystallized regions formed upon cooling experiences a sudden reduction of volume, usually known as crystallization shrinkage (see Figure 12) [64,83,127,258]. This phase transition between molten and solidified states almost freezes the polymeric chains into highly ordered crystals with lamellar or spherulitic morphologies and creates internal stresses. By contrast, the amorphous regions gradually and uniformly shrink upon cooling. Moreover, although a viscosity increase occurs due to the temperature change, these regions maintain high molecular mobility until glass transition (T_g=40°C for

PA12/CF powders [259]). If the crystallization is slow enough ($t_{1/2}$ > 20 min, see Figure 65 and Table 10), the residual stresses and the volume contraction developed due to crystallization shrinkage are accommodated by the motion of the polymeric chains of the amorphous regions. Otherwise, if the crystallization is too quick ($t_{1/2}$ < 20 min, see Figure 65 and Table 10) the amorphous areas do not have sufficient time to relieve the internal stresses, that are transferred to the subsequent layers, causing an upward deformation of the part. As a result, crystallization should be inhibited during processing at least for several sintered layers. The halftimes analysis show that $1/t_{1/2}$ approaches zero at about 170 °C (Figure 65), where the crystallization rate k is as low as 10^{-10} s (Table 10) and the maximum heat flow is significantly below 0.05 mw/mg (Figure 57). This means that the driving force for crystallization is low enough that the crystallization-induced stresses can be minimized during the building process. Therefore, T_b can be theoretically estimated nearby this temperature for PA12/CF. In this work T_b was set at 170 °C because no part deformation occurs and the powders can be easily spread onto the build platform by the recoater at the same time. At temperature higher than 172 °C it was observed that the particles placed in the direct neighbourhood of the area exposed to the laser beam partially melt and stick on the part surfaces leading to spreading defects and poor definition of the final objects [39,44,67,70,72].

Accordingly, to set the powder bed temperature right, it is not sufficient to determine with a standard DSC heat/cool cycle the range of possible temperatures defined by the sintering window. By contrast, the crystallization kinetic parameters including k and $t_{1/2}$ quantitatively describes how the polymer phase transition proceeds and directly affects the development of part curling. In this way, the isothermic laser sintering model and the consequent “sintering window concept” can be surpassed, as depicted in Figure 66. The halftimes analysis indicates that practical T_b value need to be set where the curve depicting the temperature evolution of $1/t_{1/2}$ approaches zero (Figure 66). However, T_b values near the melting onset are not advisable. Visual inspections of the powder bed are usually carried out to avoid spreading issues. However, flowability experiments performed at high temperature by using rotating drum or shear cell equipment are suggested to obtain a thorough understanding of powder agglomeration in the SLS chamber (known as bed caking) [69,260,261].

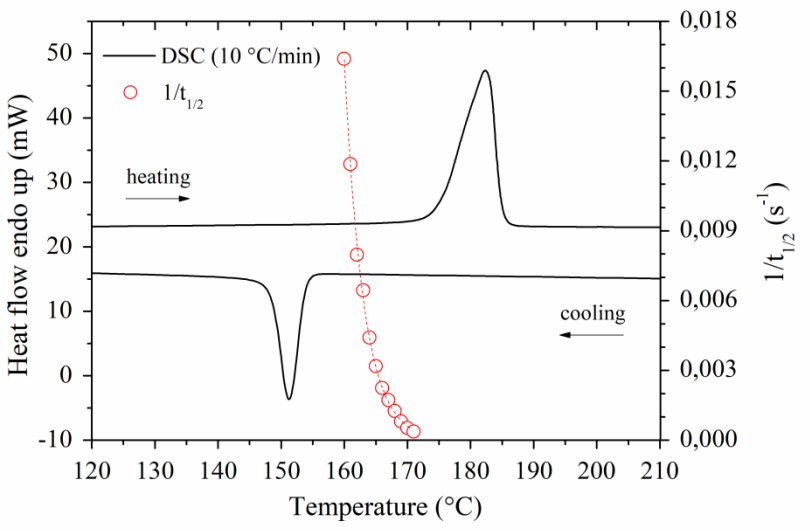

Figure 66: Overlap between the sintering window obtained from standard DSC measurement (heat/cool cycle at 10 °C/min) and the plot of $1/t_{1/2}$ (min^{-1}) over temperature

A 2nd heating step was also performed to compare the melting behaviour of the powder sample pan after isothermal crystallization at different temperatures for 120 min in the DSC measuring cell and the part printed by SLS (Figure 67). The curves show that the melting peak shape (corresponding to the enthalpy of fusion) and temperature of PA12/CF powders isothermally crystallized at 168 °C fairly resembles those obtained by analyzing a typical SLS part.

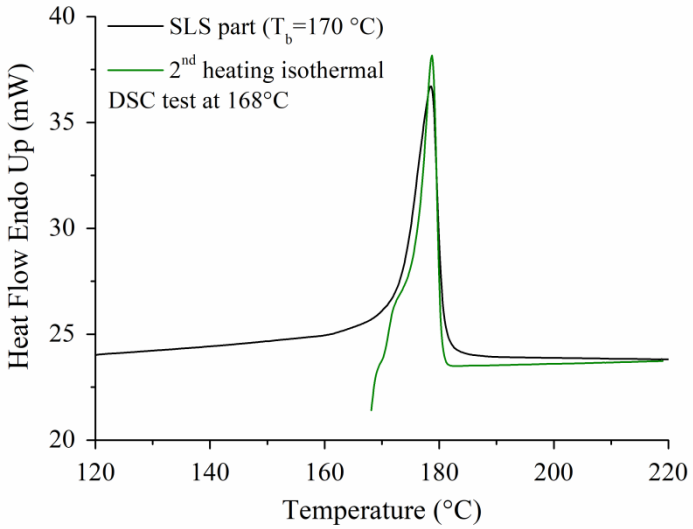

Figure 67: Comparison between the 2nd heating of the isothermal crystallization DSC experiment perfumed at 168 °C and the 1st heating of a SLS part printed using T_b=170 °C

The DSC traces of the samples treated using other isothermal temperatures were not reported in Figure 67 because the melting curves displayed much lower similarity compared to the printed sample. This means that the typical thermal history of the laser sintering process at T_b=170 °C can be approximated through an isothermal crystallization test at 168 °C. This difference in temperature could be explained by the slight temperature decrease occurring when a new layer of powders is spread and the slow cooling gradient (0.2 °C/min [70]) that exists due to the movement of the build plane along the z-direction. The first phenomena, referred as cold powder coating, causes a higher supercooling of the polymer melt, which promote the nucleation of crystallites. Therefore, the temperature of the powders in the feeding pistons should be kept near T_b, otherwise it contributes to rapid crystallization and curling [86,101].

It can be concluded that, aside from these slight physical discrepancies, the proposed approach based on isothermal crystallization is accurate to describe how crystallization development influences the dimensional accuracy (Figure 65) as well as the final crystal structure of the printed samples (Figure 67). Moreover, by measuring the temperature profile of a layer as the build progresses, an accurate prediction of the local crystallization behaviour of the polymer as a function of the position along the z axis could be carried out [88,89,105].

Laser energy density

The laser exposure parameters also play a relevant role in determining the final properties of the components. The temperature range defined by the SSR depicted in Figure 63 can be expressed quantitatively in terms of energy density needed for powders melting and degradation using equations (8) and (9). The thermo-physical properties of the PA12/CF powders listed in Table 11 were used for calculations. The values of the energy to melt a layer (E_m) and the energy required for polymer degradation (E_{deg}) in J/mm^3 are reported in Table 12.

Table 12: Volumetric energy density required for melting (E_m) and degradation (E_{deg}) of PA12/CF powders and corresponding EMR values

Parameter	E_D (J/mm^3)	EMR
Energy required for melting E_m	0.047	1
Energy required for degradation E_{deg}	0.431	9.2

The Energy Melt Ratio parameter was then introduced to correlate powder properties (E_m) and machine settings, expresses as volumetric laser energy density (E_D). This parameter summarizes the effect of laser powder, scan speed, hatch spacing and layer height. EMR values between 1 and 9.2, corresponding to energy density of 0.047 and 0.431 J/mm^3, were estimated for successful sintering process (Table 12). A processing window was thus defined to predict the laser energy density values able to induce polymer melting whilst maintaining the temperature of the melt pool below the degradation onset.

Figure 68 shows the effect of laser energy density on the tensile strength, void content and dimensional accuracy of PA12/CF samples. The energy density is expressed as Energy Melt Ratio (EMR) according to equation (11) while the dimensional accuracy was calculated as deviation per unit length from CAD design (i.e., average value of the dimensional error along the sample width, length and thickness) according to equation (18) (see section 3.2.9).

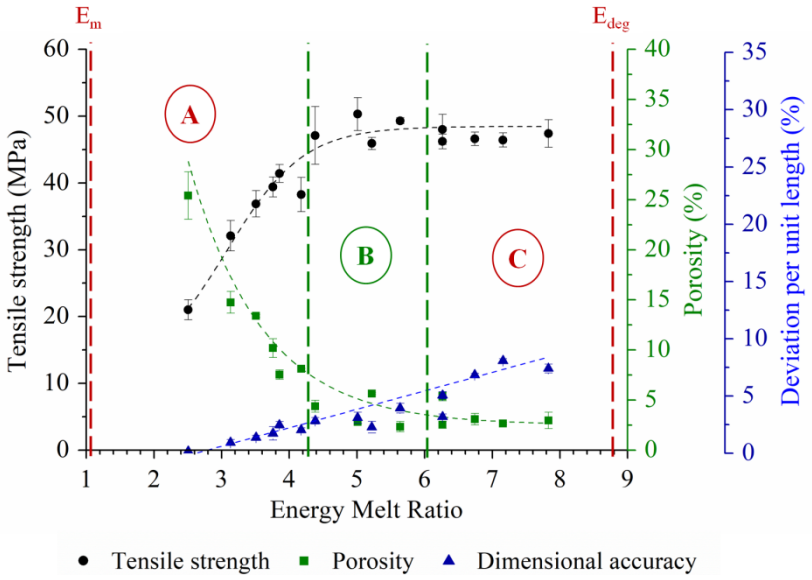

Figure 68: Tensile strength, porosity and dimensional accuracy (in terms of deviation per unit length) of PA12/CF samples produced with different laser energy density values expressed using EMR parameter

A significant enhancement of the tensile strength of PA12/CF parts at rising laser energy densities up to the SSR midst can be seen. An average strength at break of 50.3 ± 2.5 MPa was achieved using an EMR value of 5, that correspond to E_D=0.233 J/mm^3 (Figure 68). However, this property remains nearly stable or even slightly diminishes when the energy supplied by the CO_2 laser further raised

(Figure 68). The onset of this mechanical property plateau coincides with a change in the consolidation level of the material. In fact, the void content of the printed samples gradually decreases with increasing EMR, reaching low values (between 2.5 and 3%) when EMR is greater than 4.4 (that is $E_v > 0.2$ J/mm^3). By contrast, the geometrical accuracy of the parts progressively worsened, reaching inacceptable values when EMR approaches the predicted polymer degradation point (Figure 68). As a consequence, it is possible to define different areas in the stable sintering region, named as A, B and C in Figure 68. The microstructure and geometrical accuracy of the YZ cross section of PA12/CF samples fabricated with different E_D values inside these areas are showed in Figure 69.

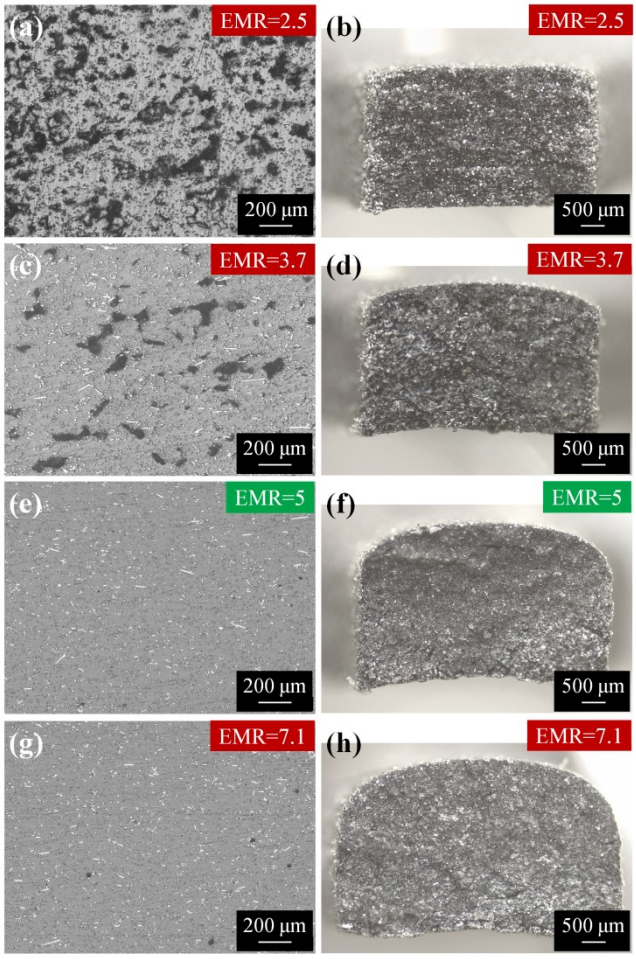

Figure 69: Optical micrographs of YZ cross section of PA12/CF parts produced with energy density values corresponding to defined areas of the SSR region: (a) 0.117 J/mm^3 (EMR=2.5), (c) 0.175 J/mm^3 (EMR=3.7), (e) 0.233 J/mm^3 (EMR=5) and (g) 0.333 J/mm^3 (EMR=7.1). Stereomicroscopy images of the respective surface fractures are displayed to illustrate the variation of dimensional accuracy of the printed parts with E_D

The variations in void size, content and distribution are clearly visible in the cross-sectional optical micrographs by moving from top (low EMR) to bottom (high EMR) in Figure 69. The stereomicroscopy images of the fractured surfaces of dog-bones specimens after tensile tests outlines the differences in part dimension and geometry owing to the energy density applied during SLS process (Figure 69). In this way, it is possible to describe the evolution of the sintering state and processing defects of the SLS printed PA12/CF samples in relation to the laser exposure parameters.

According to the stable sintering region approach [122], laser energy inputs higher than the predicted energy to melt a layer E_m (left dashed line in Figure 68, that defines the lower limit of the stable sintering region) can be successfully adopted for printing. However, parts with high void content and poor mechanical performances were produced using laser energy density values approaching this limit (region "A" in Figure 68). Although the porosity gradually decreases from 25% to 9% by rising the value of EMR from 2.5 to 3.7 (Figure 68), the optical micrographs clearly reveal that partial melting and coalescence of the powders occur in both cases (Figure 69a and 69c). The low tensile strengths observed in region "A" are then caused by the high porosity level of the samples (Figure 68). However, the high dimensional accuracy of the printed parts (Figure 69b and 69d) could allow their use in specific applications where porosity is required, such as thermal insulation [262], filtration [263] or various biomedical applications such as scaffolds for bone regeneration [264,265] and cell encapsulation [266].

The optimal processing conditions lie within a small area (referred as "B" in Figure 68) around the center portion of the stable sintering region. In this area the best compromise between strength at break, part densification and dimensional accuracy was reached (Figure 68). Optical microscopy observations confirm that the samples display a low pore content without visible defects at the fiber/matrix interfaces (Figure 69e). Therefore, a critical value of E_D nearby 0.23 J/mm^3 (that is 5 times greater than the predicted E_m) could be defined by considering the experimental results reported in Figure 68 as the critical amount of laser energy needed to successfully processed PA12/CF powders. In fact, the Young modulus and the elongation at break of the parts attained the higher values of 3.25 GPa and 4.7% respectively by using E_D=0.233 J/mm^3 and the dimensional accuracy (3%) can be considered acceptable too (Figure 68 and Figure 69f). Therefore, it would appear convenient to set large energy input for processing PA12/CF powders in order to print almost fully dense components (with pore content near 2%) and at the same time avoid polymer thermal decomposition. Unfortunately, although the

porosity of the samples remains low (Figure 69g), the printing accuracy gets significantly worse by using energy density values approaching the upper limit of the processing window (right dashed red line in Figure 68 corresponding to the beginning of polyamide thermal degradation). This can be clearly observed from the data reported in Figure 68 (region "C") and from the stereomicroscopy image (Figure 69h). The high divergence between the actual sample dimensions and the CAD design (up to 8% in the worst case scenario, as shown in Figure 68) can be most likely attributed to an excessive amount of energy delivered by the laser beam. The overheating of the melt pools causes partial melting of the particles in close proximity to the scanned area, that can thus adhere to the printed part surfaces. This lead to poor geometrical accuracy (i.e., round edges), incorrect dimensions or even distortion of the parts, as observed in Figure 69h. In fact, in some cases the melt pool is overheated to such an extent that the thermally induced stresses developed during the build process lead to warping of the final 3D objects (Figure 69h). Warping is probably caused by an excessive melt pool fusion depth, also referred as extra sintering, during the construction of a layer resulting from a too high power or too slow scan speed [115]. Different studies [104,106,107] showed that the depth of the melt pools should be lower than two times the layer thickness, otherwise an excess of re-melted material will take place. Owing to both the high thermal stresses and shrinkage, the parts printed with such parameters reveals significant deviations from the expected dimensions, mainly in the z-direction [131]. It can be concluded that the thermal degradation of the polymer is not a concern in this particular additive technology, because the SSR approach avoids it. On the contrary, incomplete sintering of the powders at low energy input, which lead to large residual porosity, and poor dimensional accuracy at high energy level are more relevant for the overall characteristics of the printed products in view of possible engineering applications in several industries. Therefore, the optimal choice for laser exposure parameters falls, at least for the investigated material, in a processing window that is quite smaller than the stable sintering region assessed by thermo-physical analysis of the powders.

Theoretically, an EMR value equal to one is sufficient to completely melt a layer of polymeric powders. However, PA12/CF parts having good mechanical strength, a minor amount of defects and limited deviation from the expected dimensions can be produced applying EMR between 4.5 and 6. These values are significantly higher with respect to the minimum energy predicted by the model. Comparable results were found in previous studies on polyamide 12 and carbon

nanotubes filled polyamide 12 composites (PA12/CNT) carried out by Vasquez et al. [122] and Yuan et al. [123] respectively. In both cases a 4 to 5 times increase in the energy density compared to the predicted energy required to fully melt the polymer was necessary to obtain samples with very low pore content and good mechanical performances. Similarly, Chatham et al. [48] found evidence that also for a high performance polymer, such as polyphenylene sulphide, the optimal process parameters to print high quality parts with complex geometries result in an energy density 5.2 times greater than E_m. In another study, Berretta et al. [49] observed a similar processing trend (i.e., large difference between the optimized applied energy density and the needed predicted one) in high temperature laser sintering of polyether ether ketone (PEEK) powders. The explanations of this considerable divergence between the predictions and the experimental results are in the following.

The Energy Melt Ratio parameter takes account of the thermal transitions only (i.e., melting of the powders in a calorimetric apparatus) and does not consider other physical phenomena relevant for material consolidation in the SLS process. As a result, although an EMR value equal to 1 leads to polymer melting, additional energy is needed for full densification due to:

- a partial energy loss during laser scanning as a result of the optical interaction between the beam and the powder bed (i.e., absorption and attenuation of the radiation);
- the need for the particles to fully coalesce.

Yuan et al. [123] pointed out that only 22% of the energy supplied by the CO_2 laser is effectively absorbed by PA12/CNT powders, thus attributing the aforementioned discrepancy solely to the optical properties of the powder bed, that lead to a not entirely efficient heat absorption. However, detailed studies carried out by a research group of the Institute of Photonic Technologies at the Friedrich-Alexander-Universität Erlangen-Nürnberg [98,267,268] showed that polyamide 12 powders efficiently absorb the incident CO_2 laser radiation. The results of various experiments performed using a double-integrating sphere measurement setup clearly indicated that the absorptance of PA12 powders surpass 90% at the wavelength of CO_2 lasers (i.e., 10.6 μm) [98,267,268]. Moreover, it was also found that the absorption coefficient is almost independent from the layer thickness [98,268] and the temperature (up to the polymer melting point) [267]. This behaviour can be explained by considering the chemical nature of the polymer (i.e., strong absorptance of PA12 at 10.6 μm due to stretching

vibration between the OC–C groups) and the numerous reflections and scattering events that occurs when the beam penetrates in a granular media (Figure 16) [98]. It can be expected that polyamide 12 powders absorbed most of the energy delivered during laser exposure in SLS machines. The absorptance of the powders is likely enhanced by adding carbon based material to the neat polyamide because these fillers typically exhibit high absorptance in the infrared radiation wavelength [22,27,82,133,137,138]. Therefore, other optical phenomena need to be considered for explaining the energy inputs required to print a fully dense object. Bierwisch et al. [94] recently proposed a new method, based on the Attenuated Melt Ratio (AMR) parameter, to take account of the attenuation of the laser radiation in the powder bed. This parameter represents an improvement over the Energy Melt Ratio (EMR) from a physical point of view. In fact, the optical properties of the powders are also considered by substituting the layer thickness arbitrarily set by the operator ('d' in equation (11)) with the length scale of attenuation of the laser energy within the powder bed ('$1/(\phi\ a)$', where ϕ denotes the packing factor and a is the attenuation coefficient of the powders). AMR was derived from a detailed theoretical analysis of the spatial distribution of the thermal energy delivered by the laser beam supported by numerical simulation at the particle scale and measurements of surface temperature for single layers via IR thermography. The analytical models proposed in this work allow to evaluate the depth and temperatures of the melt pool as a function of the laser energy density (i.e., logarithmic and linear relationship respectively). In this way, a process window for optimum sintering conditions can be established between a lower boundary (i.e., melt pool depth $\geq$ layer thickness) and an upper boundary (i.e., melt pool temperature $\leq$ polymer degradation temperature). The authors proved the validity of this process window by using stiffness, strength and density data of PA12 [68,122] and PEEK [49] printed parts found in literature [94].

Apart from the laser/powder interaction, a cluster of particles should have sufficient time to coalesce, thus closing the pores in-between. However, the particles experience fast heating and cooling cycles due to the fact that the laser-powder bed interaction occurs in a very short timeframe (10^2 μs). These thermal conditions could hinder the coalescence process because the melt pool remains in a low viscosity state ($<10^3$ Pa s for neat PA12, as referred by [127]) for a limited amount of time. Therefore, the laser energy input should be increased. As a result, the temperature of the melt pool can be significantly raised, thus leading to a convenient reduction of the viscosity of the polymer melt [104,141]. Wegner et al. [269] found that the maximum melt pool temperature during laser sintering of

PA12 powders should remain far above the melting peak (between 250 °C and 280 °C) to achieve high density and elongation at break values, good interlayer bonding and process consistency. Based on these observations a process theory (named “Theory on the Continuation of Melting Processes”) was proposed [269]. This indicates that elevated temperatures and times in the molten state, induced by energy inputs higher than the theoretical melting one, are required to reduce the viscosity of the polymer and give sufficient time for the particle to coalesce, as experimentally observed in [107] for polyurethane parts. Alternatively, by using lower scan speed, the rate of energy delivery and consequently the interaction time between the radiation and the powder bed can be increased [104,270]. The fusion of the powders could be also improved by properly changing the hatch spacing value [107] or by adopting a double scanning strategy [271]. Both these methods are effective to boost the coalescence between particles, thus reducing the void content in the printed parts. In this context, Chatham et al. [272] recently suggested the introduction of the Critical Coalescence Ratio (CCR) parameter to take account of the coalescence between a pair of spherical particles, governed by the competing effect of the polymer melt viscosity at zero shear rate (η_0) and the crystallization process. CCR was defined as the ratio between the dimensionless neck radius (‘x/t’ defined in equation (4) and Figure 20) at the point of physical gelation (equal to 10% relative crystallinity) and the dimensionless neck radius corresponding to a critical degree of material densification (i.e., relative density ρ/ρ_T=0.94) [272]. This value was chosen because it defines the transition between two different physical mechanisms of powders densification during sintering, namely open pore suppression due to viscous flow coalescence and closed pore suppression due to bubble diffusion, as suggested by Scherer et al. [273]. The model for CCR calculation takes into account the quick variations of temperature during the printing process, that greatly alter the coalescence and crystallization dynamics. In fact, the temperature profiles for single layers sintered with several combinations of laser exposure parameters were measured via IR thermography. These data were used to simulate coalescence and crystallization kinetics using the upper-convected Maxwell (UCM) model proposed by Bellehumeur [125] to describe densification in rotational molding and the Hoffman-Lauritzen model respectively. UCM is an evolution of the Frenkel theory described in equation (4) that consider the effect of polymer viscoelasticity on coalescence. The authors found that the highest mechanical properties of PA12 parts, corresponding to a plateau similar to that observed for PA12/CF powders in region "B" of Figure 68, can be accurately predicted by using this parameter [272].

Upon this literature survey, the divergence between E_m and the critical energy experimentally measured to print fully dense components can be attributed to two physical aspects of the SLS process (laser attenuation and particles coalescence) that are absent in the EMR equation. The related material characteristics (i.e., attenuation coefficient, rheological properties and crystallization behaviour of the powders) can be added in the process parameters selection process, as suggested in [94,272]. In this way, not only melting but also full consolidation of the polymer powders can be considered.

4.1.3 Microstructural characterization and fiber orientation

As discussed in the previous section, high quality composite parts were obtained by an accurate optimization of the process parameters. The microstructural characteristics of PA12/CF samples fabricated by choosing the best processing condition (T_b=170 °C, P=5.6 W, v=2400 mm/s) are depicted in Figure 70, where optical micrographs of the YZ cross section of the sintered specimens at different magnification are displayed.

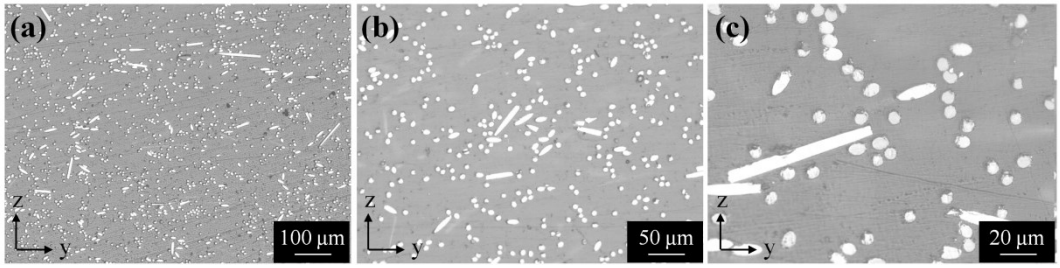

Figure 70: Optical micrographs of YZ cross section of PA12/CF parts sintered with energy density of 0.233 J/mm^3: (a) low magnification image, (b) detailed view of the distribution of carbon fibers in the polymer matrix and (c) high magnification image showing the fiber/matrix interfaces

Figure 71 shows the XY cross-section of the PA12/CF composites, that is parallel to the part bed (and the building platform). From these micrographs it can be noticed that the fibers are aligned in the x-y plane, that coincides with the part bed of the printer (Figure 71a and 71b). More precisely, the degree of orientation of the carbon fibers with respect to x axis can be evaluated by measuring the angle that exists between each fiber and the x axis by using an image analysis software (Figure 71c).

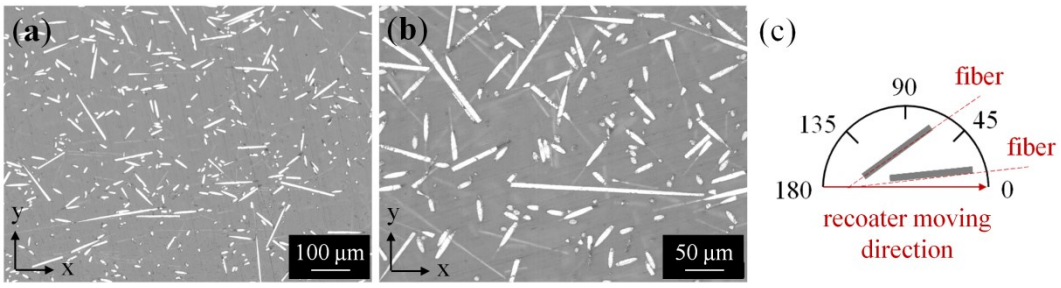

Figure 71: (a, b) Optical micrographs of the XY cross section of a PA12/CF part at different magnification level. The white elongated objects correspond to the carbon fibers while the gray region denotes the polymer matrix. (c) Orientation chart showing the measuring principle for fiber orientation evaluation (recoater moving direction)

Figure 72 displays the relative frequency distribution of the fiber orientation in PA12/CF samples with respect to the translation movement of the blade, that correspond to the x-axis direction. The data were obtained through a statistical analysis of more than 1600 fibers according to the measuring principle schematically depicted in Figure 71c. It can be seen that a preferential alignment of the carbon fibers along the blade movement direction occurs. In fact, 57% of carbon fibers are included in the 0-40° range (Figure 72).

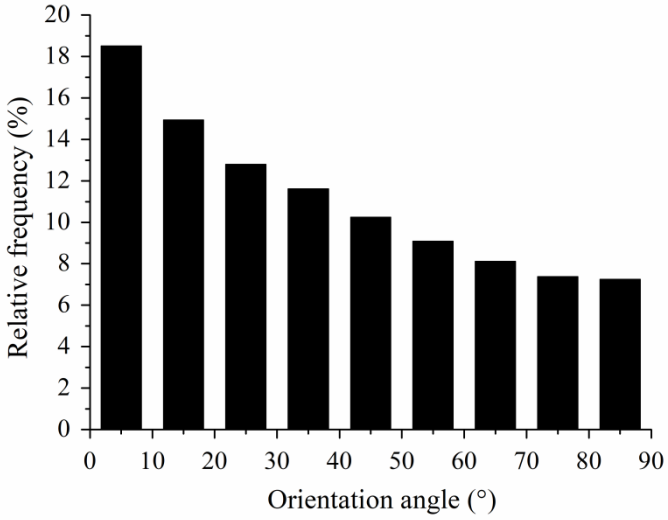

Figure 72: Relative frequency distribution of carbon fiber orientation in a printed sample: 0° correspond to the x-axis of the part bed and it is parallel to the recoater movement direction, while 90° is perpendicular

The physical mechanism underlying the in-plane alignment of fibers along the part bed and here, the preferential fiber orientation in the x direction (Figure 71a and 71b) was described by Jansson and Pejryd [145] for a short carbon fibers

polyamide composites (CarbonMide® PA12-CF powders supplied by EOS Gmbh). This preferential orientation of fibers is caused by the mechanical action of the recoating system (i.e., in Jansson and Pejryd's work [145] a translational blade similar to the one designed for the Sharebot SnowWhite machine used in this thesis) during the deposition of a new powder layer. As sketched in Figure 73, the blade hits the fibers during layer spreading, thus aligning them in the x-y plane.

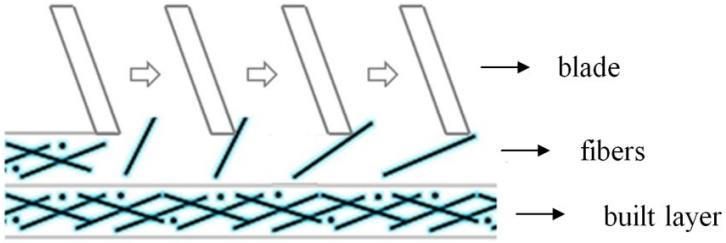

Figure 73: Diagram that presents the interdependency of the main intrinsic and extrinsic properties

The optical micrographs of both YZ and XY cross-sections of PA12/CF samples (Figure 70 and Figure 71) corroborates this observation because no fibers are aligned along the z-axis direction (i.e., perpendicular to the part bed). Moreover, most fibers (57%) are aligned along the x-axis direction, while others maintain a random orientation in the x-y plane (Figure 71a and 71b and Figure 72). These results are in good agreement with those reported in [145] and can be explained by taking into account that longer fibers (i.e., length equal or higher with respect to the layer thickness) are more probably aligned by the blade movement (Figure 73). The flow of the polymeric particles along the direction of the recoater movement also drag the alignment of short fibers in this direction.

Similar fiber orientation ratios were found in other studies through high resolution computer tomography (μCT) analysis on short carbon fibers polyamide 12 [147] and short glass fibers poly-butylene terephthalate and polyamide 6 composites [35,271] manufactured by using roller-type SLS machines. The fibers analysed in this studies have an average length between 90 and 100 μm, which is almost equal to that of the carbon fibers used in PA12/CF powders. The authors agreed that the fibers are in-plane aligned within a layer (50-60% in the roller movement direction and 30-40% perpendicular to the roller movement, which correspond to the x and y-axis respectively). Only a minor amount of fibers (5-15%) are aligned along the z-axis, which denotes out-of-plane orientation in the building direction [35,147,271]. It was also found that the orientation of fibers is

not affected by changes in most processing parameters including recoating speed and laser energy density [35,271]. By contrast, a reduction in layer thickness results in a higher degree of alignment because additional fibers directly interact with the printer's recoating system [35]. Owing to these experimental results and the underlying theory (Figure 73), it can be concluded that short fiber reinforced composites processed by SLS display similar fiber arrangement regardless of the SLS machine and process parameters adopted. However, it is possible that fiber length and layer thickness could somehow affects the degree of orientation in the x-direction.

The crystalline structure of the polymer matrix in PA12/CF part was studied by X-ray diffraction and calorimetric techniques. Figure 74 shows both XRD patterns and DSC melting curves of the raw powders and 3D printed samples produced with energy density values that are representative of the three regions identified in Figure 68.

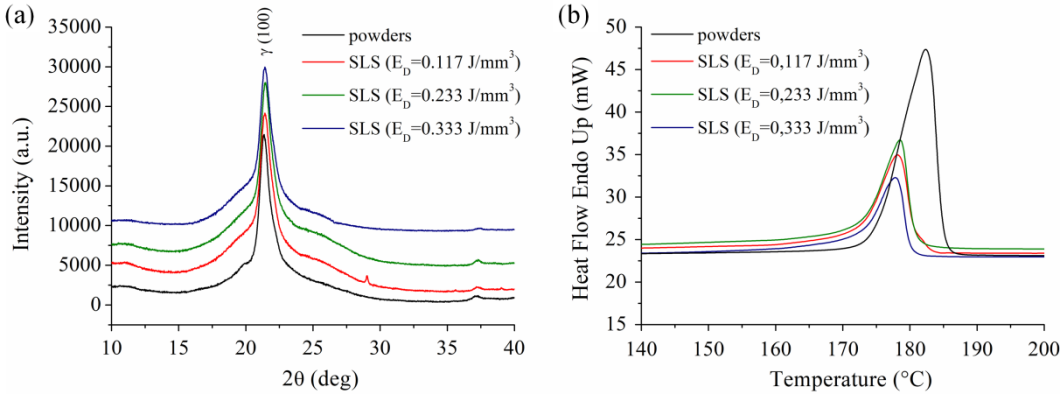

Figure 74: (a) X-ray diffraction patterns and (b) DSC curves of raw powders and 3D printed PA12/CF samples produced with different energy density values within the SSR region. A limited temperature interval is magnified in the DSC curves in Figure 74b to highlight the melting behaviour of the material

The spectra of the raw powder display a broad halo, typical of an amorphous phase, with a sharp peak emerging at 2θ = 21.4° (Figure 74a), which belongs to the (100) Miller index of γ crystalline phase of polyamide 12 [274]. PA12/CF samples manufactured using SLS exhibit almost identical patterns compared to that of raw powders irrespective of the laser exposure parameters adopted, as revealed by the peak shape and position (Figure 74a). A single melting peak, that denotes the fusion of the γ crystalline structure of the polyamide 12, was recorded for both raw powders and SLS samples in the DSC curves (Figure 74b). However,

a higher melting temperature and enthalpy can be observed for the powdered material (Figure 74b). These properties were summarized in Table 13.

Table 13: Diffraction peak (2θ°), melting temperature (T_m), enthalpy of fusion (h_f) and crystalline fraction (X_C) of raw PA12/CF powders and SLS parts built by using different energy density values, as obtained from X-ray diffraction and calorimetric experiments

Sample	$(100)_\gamma$ (2θ°)	T_m (°C)	h_f (J/g)	X_C (%)
Powder	21.4	182.3	81.4	48.1
SLS (E_D=0.117 J/mm^3)	21.3	178.1	45.1	26.6
SLS (E_D=0.233 J/mm^3)	21.4	177.8	45.4	26.8
SLS (E_D=0.333 J/mm^3)	21.3	178.6	46.8	27.6

The crystalline fraction of the polymer matrix after laser sintering, calculated using equation (12), is significantly lower compared to that of the raw powders (27 and 48% respectively) for every laser energy input considered (Table 13). This difference is likely due to the substantial discrepancy between the thermal histories resulting from SLS processing and powders manufacturing. In fact, the typical thermal condition of the SLS process consists in repeated heating/cooling cycles during laser scanning prior to a slow cooling from T_b to room temperature [89,275]. By contrast, during powders production anionic polymerization and crystallization take place simultaneously in a stirred reactor at high temperature, between 100 and 120 °C [76]. This particular process leads to the preparation of PA12 powders with higher melting temperature and enthalpy compared to those of standard grade used in injection molding [75,76].

4.1.4 Mechanical properties

The mechanical properties of neat PA12 and PA12/CF parts produced by SLS using the same energy density input (E_d=0.233 J/mm^3) are illustrated in Figure 75 as tensile stress-strain curves. From the graph it can be observed that the carbon fibers strengthened the polymer, as revealed by a significant enhancement of the

elastic modulus (+117%). A moderate increase of the strength at break (+12.4%) was also found at the expense of the elongation at break (-77%) (Figure 75).

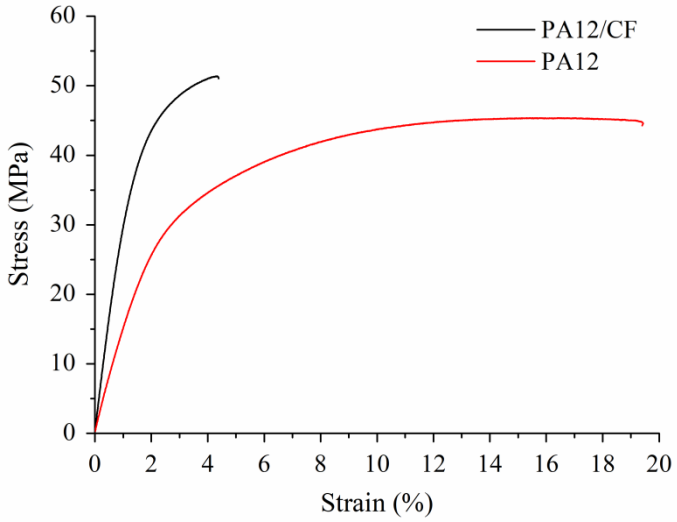

Figure 75: Stress-strain curves of neat PA12 and PA12/CF samples produced by SLS using the same combination of process parameters: laser powder of 5.6 W, scan speed of 2400 mm/s, hatch spacing of 100 µm and layer height of 100 µm (corresponding to E_D=0.23 J/mm^3)

The limited increase of the tensile strength can be explained by taking into account that the reinforcing effect of carbon fibers strictly depends on their lengths. In fact, high strength composites can be obtained only when the fibers length exceeds the critical length (l_c) for a particular fiber/polymer matrix system. By using equation (25) the critical length of a carbon fiber in a PA12 matrix can be estimated at 400 µm. Nevertheless, the fibers used in PA12/CF powders, and more broadly in SLS composites, could not own such lengths, otherwise they would negatively interfere with the laser sintering processability of the material (e.g., reduced flowability and high melt viscosity) [134,228].

The failure morphology of a printed PA12/CF part was studied by examining FESEM images of the surface fracture after tensile test (Figure 76). The lower magnification SEM micrograph (Figure 76a) clearly indicates that the PA12/CF powders are well consolidated in an almost fully dense microstructure and only very few void can be seen. An incomplete bonding between individual PA12/CF particles is only visible in the sides of the part because the outer perimeter was printed with a lower laser powder (P=2.8 W) to improve the dimensional accuracy and the surface finish (Figure 76b). This is a typical feature of the surface of both pure and reinforced polymer parts manufactured by SLS [147].

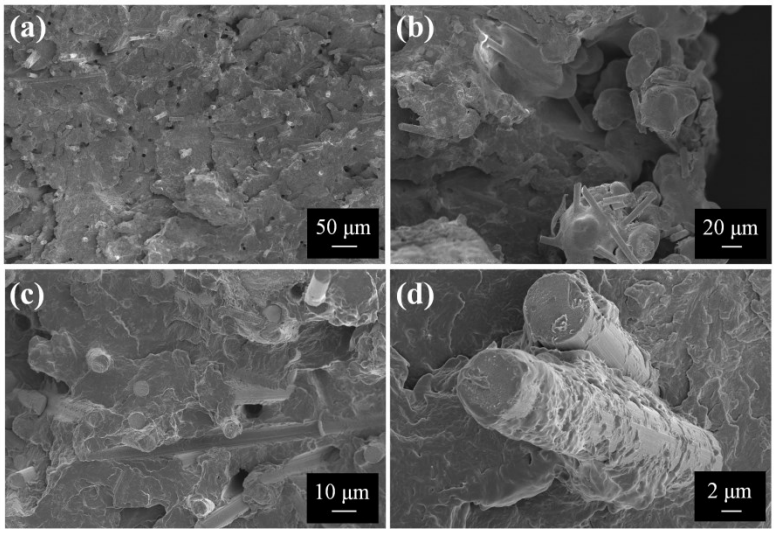

Figure 76: FESEM micrograph of the tensile surface fracture of PA12/CF samples produced by SLS: (a,c,d) fracture surface morphology at different magnification level highlighting the failure mechanism of the composite and (b) magnified view of the outer perimeter of the part (produced with lower laser power to improve printing accuracy)

Although the fracture surface exhibits a slightly rough morphology, the sintered composite shows a brittle failure behaviour (Figure 76a), as suggested by tensile testing as well (Figure 75). The failure mechanisms that can be highlighted in the FESEM images include fiber pull-out, interfacial debonding between fibers and matrix and polymer shear failure. All these mechanisms can be observed in Figure 76c where small round holes and fiber imprints caused by matrix/fiber debonding as well as matrix shear deformation are clearly visible. Some fiber pull-outs can also be observed in Figure 76c. A magnification of two protruded fibers (Figure 76d) reveals that the surface of the fibers is coarse and mostly coated by a thin layer of matrix material. This means that a suitable interfacial adhesion between carbon fibers and PA12 matrix has been developed through laser sintering [134,144]. Fiber rupture, that is another typical fracture mechanism of short fiber composites, is not common in this material. This can be explained by considering that the stresses transferred from the polyamide matrix to the carbon fibers is low because the length of all fibers is significantly lower than l_c.

4.1.5 Prediction of mechanical properties

Table 14 summarize the mechanical and physical properties of PA12 and carbon fibers (CF) needed for predicting the elastic modulus and tensile strength of the 3D printed composites though the modified RoM approach described in Section

3.3.1. Experimental tests were carried out to determine the mechanical properties of neat PA12 using ASTM standards. Typical values reported in literature [276,277] were used for short CF (Table 14). In this table, 1 and 2 correspond to the direction parallel and perpendicular to the applied tensile loads and 12 denotes in-plane shear. Fibers diameter and mean length were obtained from raw powders characterization (see Section 4.1.1). Fibers volume fraction was calculated using equation (46):

$$V_f = \frac{W_f \rho_f}{W_f \rho_m + W_m \rho_f} \quad (46)$$

where ρ_m and ρ_f are the density of the PA12 matrix (see Table 9) and carbon fibers (1.76 g/cm^3) [276,277] respectively and W_f is the weight fraction of fibers derived from TGA curve.

Table 14: Material properties of neat PA12 and carbon fibers adopted for the prediction of Young modulus and ultimate tensile strength of PA12/CF composite printed by SLS using a modified RoM approach

Material properties	PA12	CF
Longitudinal elastic modulus E_1 (GPa)	1.49	230
Transverse elastic modulus E_2 (GPa)	1.49	15
In-plane shear modulus G_{12} (GPa)	0.40	15
Poisson's ratio ν_{12}	0.39	0.2
Axial tensile strength σ_1 (MPa)	44.8	3500
Volume fraction (%)	87.6	12.4
Fiber diameter 2r (µm)	-	7
Mean fiber length l_f (µm)	-	91.9

The Young modulus of PA12/CF composite parts was obtained according to equation (19). The fiber length efficiency factor η_l is 0.2, which is a typical value for polymer composites reinforced with short CF with similar length to those employed in this study [245]**.** The fiber orientation efficiency factor η_θ was found to be 0.489 by using equation (20) based on the fibers orientation distribution determined experimentally (Figure 72). The voids content φ of the PA12/CF composites was obtained by gas pycnometry (2.37%). The critical fiber length l_C for the PA12/CF system was estimated to be 404 μm by taking into account the fiber/matrix interfacial shear strength τ_y=30.3 MPa, obtained by Tanaka et al. [278] through single fiber pull-out tests at room temperature. Since the fibers exhibit much lower lengths than l_c, equation (24) can be simplified as follows:

$$\sigma_c = \left(\eta_\theta \frac{V_f \tau_y l_f}{2r} + \sigma_m V_m\right)(1-\varphi) \tag{47}$$

where σ_c is the ultimate tensile strength of the composite, l is the average fiber length, r is the fiber radius, V_f and V_m are the volume fraction of fiber and matrix respectively and σ_m denotes the tensile strength of neat PA12.

Comparison of modeling results with experimental data

Table 15 shows the values of the mechanical properties thereby predicted. The relative error in percentage of the modeling results is determined as:

$$\text{error} = \frac{\text{prediction-experimental value}}{\text{prediction}} 100\% \tag{48}$$

Table 15: Predicted Young modulus and tensile strength values of PA12/CF composite produced by SLS and relative error between models and experimental data

PA12/CF	Experimental values	Predicted values	Relative error (%)
E (GPa)	3.25	3.39	+4.1
σ (MPa)	50.3	61.8	+18.6

Although its simplicity, the prediction of the modified rule of mixture is in good agreement with the experimental elastic modulus, with an error of 4.1%. This value is lower compared to that obtained by Lanzl et al. [142] on short glass fiber reinforced PA12 parts produced by SLS using the Halpin-Tsai model. However, the strength at break is overestimated by a factor of ⅕ (Table 15). The higher modeling error for strength can be attributed to the fact that this micromechanical modeling approach contemplates a perfect bonding between fiber and matrix, which is not the case in this composite. Moreover, the tensile strength is more affected by the presence of voids, and it is very difficult to take account of their effect on the fracture mechanism. In fact, a lower error value (9.5%) was reported by Zhu et al. [228] in the prediction of ultimate tensile strength of PA12/epoxy/CF ternary composites processed using a two-step approach where SLS is followed by resin infiltration. This difference can be attributed to the low pore size and improved interfacial bonding between fibers and matrix achieved by infiltrating the SLS parts with a high strength epoxy polymer [228].

4.2 Fused Filament Fabrication

4.2.1 Filament characterization

Morphological and physical properties

Figure 77 shows optical and electron microscopy images of the cross section of PA6/CF filament. As frequently observed in FDM feedstock materials, the PA6/CF filament exhibit a circular cross section with a nominal diameter of 1.75 mm (Figure 77a and 77c). The fibers are evenly distributed within the filament, with no differences between the core and the edges. A high amount of voids with round or irregular shape and different dimensions are also clearly visible in Figure 77a. A detailed investigation though image analysis of several optical images of polished cross sections detected a mean void content of 4.8 ± 0.2 %. Moreover, the porosity is not homogeneously distributed in the feedstock filament. In fact, a high quantity of large voids located in the middle part of the composite thread coexists with fewer smaller pores in the edges (Figure 77a). The formation of these voids can be attributed to the evolution of entrapped gas during fiber reinforced filament manufacturing using single screw extrusion [175,176,279].

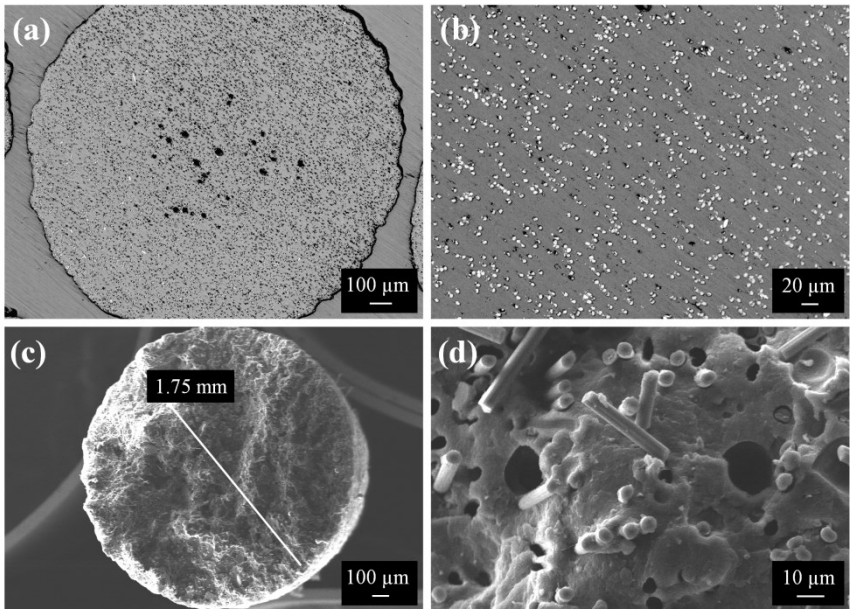

Figure 77: (a,b) Optical images of the polished PA6/CF filament cross-section at various magnification and (c,d) FESEM micrographs of the cryogenically fractured filament, highlighting the voids shape and the alignment of carbon fibers in the extrusion direction

At higher magnification it can be noticed that the carbon fibers are fairly good aligned to the filament length, that corresponds to the extrusion direction of the composite thread (Figure 77b). This is further confirmed by FESEM images of the filament cross section obtained by means of cryogenic fracture in liquid nitrogen, where the fibers appear well oriented along the sample axis (Figure 77d). The preferential alignment of carbon fibers is created by the shear stress and pressure imposed during the filament extrusion process and it is likely further enhanced after 3D printing [26,177]. In addition, large voids attributed to gas evolution and small round holes generated by fibers pull-out can be seen in the filament cross section (Figure 77d). Some broken fibers fragments that lies on the fracture surface as a result of the rupture of the pulled out fibers are also visible (Figure 77d).

A typical optical image of the carbon fibers after polymer removal through pyrolysis is displayed in Figure 78a. The dimensions of the fibers were evaluated by analyzing several micrographs using ImageJ® software. An average diameter of 6.5 µm was found by measuring 100 individual fibers (Figure 78a), while estimated length distribution histogram is displayed in Figure 78b.

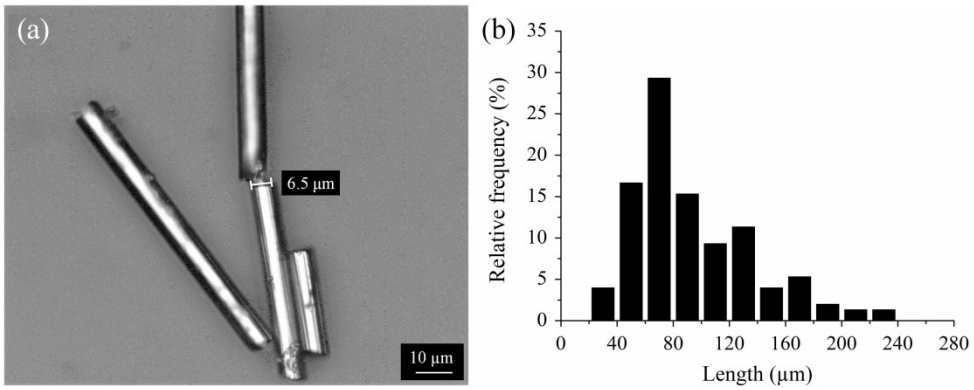

Figure 78: (a) Optical microscope image of the carbon fibers after polymer matrix pyrolysis and (b) fiber length distribution plot obtained by using ImageJ® software.

The results reveal a slightly asymmetric distribution of fiber lengths with an average value of 94 µm (Figure 78b). It is important to point out that the carbon fibers employed in various polymeric FFF feedstock filaments exhibited similar length distribution. In fact, milled fibers with average length of 80-100 µm are frequently used to improve the properties of FFF polymeric parts [26,176,179]. Otherwise, it has been reported that when chopped fibers with length of a few mm are added as reinforcing phase, substantial fiber breakage happens during compounding/high-shear mixing with the thermoplastic polymer. The reduction of the fiber length can be attributed to the interactions between fibers and equipment surfaces (i.e., barrel and screw), polymer matrix and other fibers [176].

Figure 79a shows the X-ray diffraction pattern of the PA6/CF filament. The intense peak at $2\Theta = 21.5°$ corresponds to γ-crystalline phase of the polyamide-6 matrix. In addition, the two broad shoulders at 2Θ of approximately 20° and 23.7° can be assigned to the planes (200) and (202/002) of the α-crystal of the same polymer respectively (Figure 79a) [240,255]. Narrow peaks arising from the large bump belonging to the polymer amorphous phase also appears in the XRD pattern of the filament. These peaks, at 2Θ of 18.3°, 30.1°, 35.5°, 43.1°, 57.0° and 62.6°, are attributed from X'Pert Highscore Plus software to magnetite (i.e., ICDD card 01-088-0866). Backscattered FESEM images of the feedstock filament indicates that micron-size particles (about 1 µm) are distributed in the polymer matrix (Figure 79b). The semi-quantitative EDS spectra carried out at different spots (referred as Sp. 3 and Sp. 2 in Figure 79b) revealed that these particles are mainly composed by oxygen and iron (O = 24 wt.% and Fe = 31 wt.%).

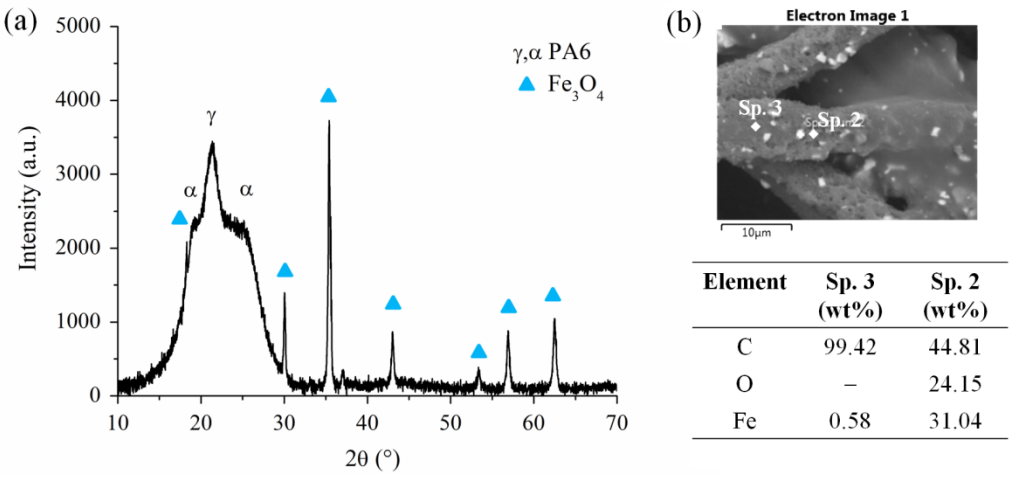

Element	Sp. 3 (wt%)	Sp. 2 (wt%)
C	99.42	44.81
O	–	24.15
Fe	0.58	31.04

Figure 79: (a) XRD spectra of PA6/CF filament and (b) SEM/EDS analysis of the filament cross-section revealing the presence of magnetite (i.e., micron-size white particles in the SEM back-scattered image of Figure 79b)

Therefore, XRD and SEM-EDS results outlined the presence of magnetite, Fe_3O_4, as second filler in the PA6/CF filament. This compound is not frequently used in polymeric composite materials. However, the unusual combination of properties of magnetite has promoted its adoption as multi-functional filler in thermoplastic polymers and rubber for various applications (e.g., sound dampening) since the early 2000s [280,281]. In fact, the addition of Fe_3O_4 increases the density and modulus of plastics, thus providing sound and vibration dampening and a *"quality feel"* to products. Moreover, the electrical, thermal and radiation shielding characteristics can also be improved [280,282]. The density of both filaments was obtained by gas pycnometry and values of 1.01 g/cm^3 and 1.27 g/cm^3 were obtained for neat PA6 and PA6/CF filaments respectively.

Thermal properties

The DSC curves of PA6 and PA6/CF filaments are displayed in Figure 80. The 1st heating-cooling cycle revealed that both materials exhibits distinct melting and crystallization peaks at about 233 °C and 185 °C (Figure 80a). A slight shift to higher temperatures of these thermal transitions was detected for neat PA6 filament compared to PA6/CF (Figure 80a). The shift of the melting event can be attributed to the high thermal conductivity of the carbon fibers, that promotes heat transfer during polymer fusion [134,254,255]. On the other hand, the high content of fibers influence the crystallization behaviour of the composite filament by preventing the mobility of the polymer chains, thus decreasing the temperature for crystal nucleation and growth [254,255].

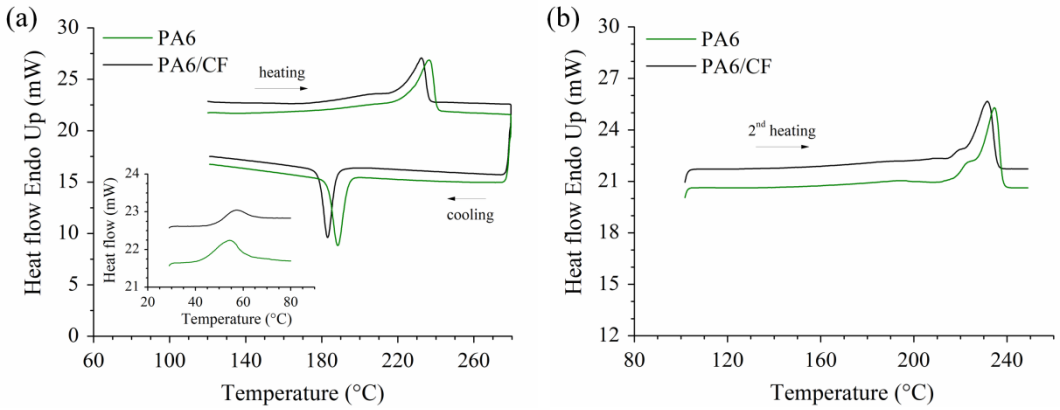

Figure 80: (a) Heating/cooling DSC curves of neat PA6 and PA6/CF filaments and (b) 2nd heating thermograms of the same materials. Inset of Figure 80a: glass transition behaviour of PA6 and PA6/CF filaments

The glass transition behavior of the filaments is shown in the inset of Figure 80a, where the first part of the DSC thermograms is magnified. In both curves an enthalpy relaxation peak is clearly visible. Neat PA6 exhibits a glass transition temperature (T_g) of 50 °C, as commonly reported in literature [254,283,284]. A slightly higher T_g was recorded for PA6/CF (52 °C) because the fibers slow the motion and rearrangement of the polymer structure [254,255,285]. The transition temperatures and the crystalline degree derived from DSC curves of neat PA6 and PA6/CF are summarized in Table 16.

Table 16: Thermal and physical properties of the neat PA6 and PA6/CF filaments. Glass transition (T_g), melting (T_m) and crystallization (T_c) temperatures and and polymer crystalline fraction (X_c) were determined by DSC. Degradation temperatures ($T_{d\ onset}$ and $T_{d\ peak}$) and fiber weight fraction (W_f) were evaluated from TGA curves in inert environment

Filament	T_g (°C)	T_m (°C)	T_c (°C)	X_c (%)	$T_{deg\ onset}$ (°C)	$T_{deg\ peak}$ (°C)	W_f (%)
PA6	49.6	236.5	188.4	22.4	374.4	415.3	-
PA6/CF	52.3	232.9	183.1	22.6	363.2	410.5	15.5

During the 2nd heating step, the melting behaviour of the filaments changes by the occurrence of a broad shoulder before the endothermic peak (Figure 80b). This behaviour has been reported for polyamides and other semicrystalline

polymers and can be assigned either to the melting of imperfect crystallites (usually referred as melting–recrystallization–remelting phenomena) or different crystal morphologies [134,286].

The thermal stability of neat PA6 and PA6/CF filaments in inert environment was investigated by thermal gravimetric analysis. The weight loss and derivative curves are illustrated in Figure 81. A single degradation step, corresponding to the pyrolysis of the polyamide matrix, is observed in both thermograms. The onset degradation temperature ($T_{deg\ onset}$) and the temperature at which the maximum rate of weight loss occurs ($T_{deg\ peak}$) are reported in Table 16. The carbon fibers content (15.5 wt.%) of the reinforced filament was also obtained from the TGA curves by subtracting the final residues of the PA6/CF and neat PA6 samples.

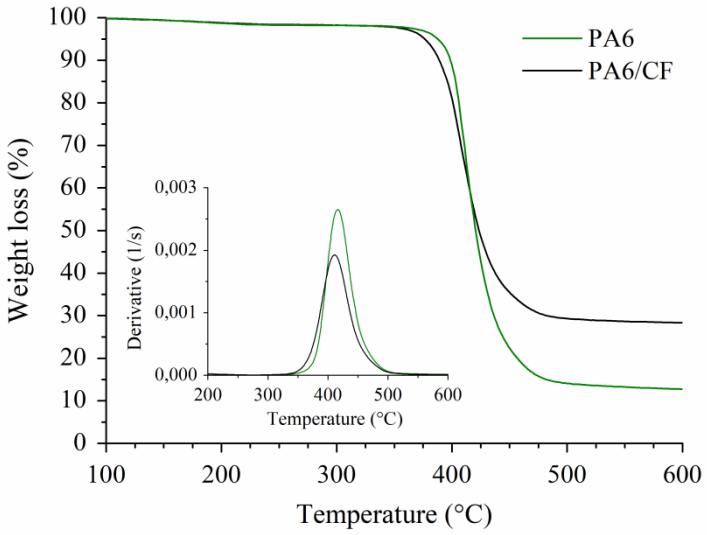

Figure 81: TGA curves of neat PA6 and PA6/CF in argon atmosphere. Inset: derivative curves showing the maximum weight loss rate temperatures

A thermogravimetric analysis in air atmosphere (Figure 82) was also performed to assess the amount of magnetite particles in the PA6/CF filament, already observed in XRD and EDS spectra (Figure 79). Multiple degradation stages can be clearly observed from the TGA and derivative curves of neat PA6 and PA6/CF filaments (Figure 82). The thermo-oxidative decomposition of the PA6 takes place between 350 °C and 450°C with the breakdown of the polymer main-chain bonds, followed by the oxidation of the carbonaceous char previously formed at temperatures above 500 °C [287,288]. This degradation behavior is observed for both printing filaments (Figure 82). The last step of the PA6/CF curve is associated to the burn out of the carbon fibers between 600 °C and 800

°C (Figure 82). By evaluating the weight loss after the 2nd and 3th degradation steps it is possible to calculate the fibers and magnetite content in the filament (15.5 and 4% by weight respectively).

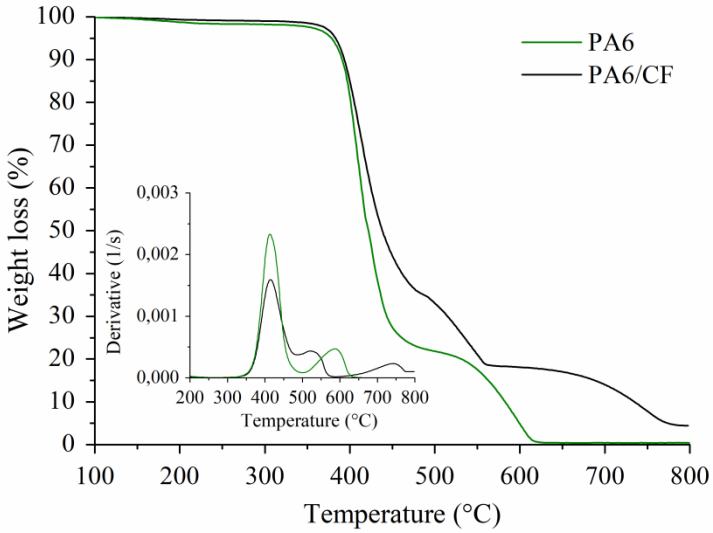

Figure 82: TGA curves of PA6/CF in air atmosphere. Inset: weigh loss derivative curves revealing the different degradation steps of the composite filaments

The thermal properties of the PA6/CF filament indicate that an extrusion temperature between polymer melting and degradation has to be set to obtain a suitable melt viscosity without reaching PA6 decomposition. Moreover, a bed temperature just below T_g is recommended to prevent the thermal distortion of the printed parts at the end of the process. Therefore, the process parameters suggested by the filament and machine manufacturer (Table 4) were adopted for printing PA6/CF samples.

4.2.2 Microstructural characterization and fiber orientation

Polymeric and composite objects produced by FFF are composed by two regions, namely outer shell, consisting of roof and floor layers and perimeters, and internal rasters usually referred as infill. In fact, during printing of each layer the filament is firstly deposited along the perimeter of the part, referred as wall [226,289]. Then, the printing head moves alternatively upward and downward to lay down the extruded beads in the infill region according the raster angle settings adopted.

A schematic representation of the structure resulting from the FFF process is sketched in Figure 83a. The wall and infill regions as well as the layered structure

arising from the additive process can be easily recognized in the FESEM micrograph of the entire cross-section of a PA6/CF samples produced with [±45°] architecture (Figure 83b). The wall region consisted of two adjacent beads following the perimeter of the specimen, while filaments deposited alternatively at plus or minus 45 degrees are used in the infill.

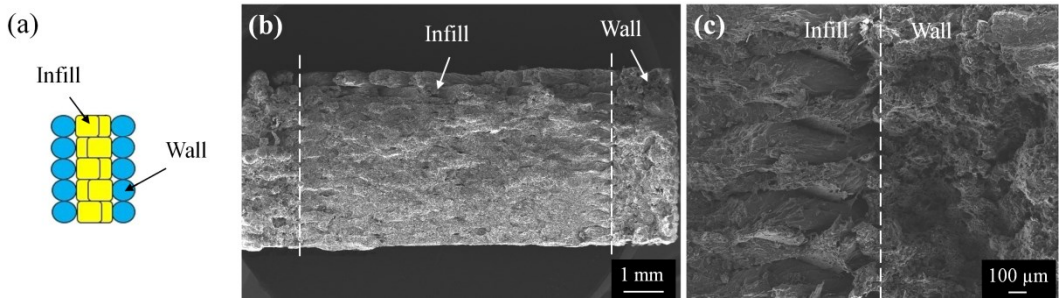

Figure 83: (a) Sketch of the typical mesostructure of polymer-based parts produced with FFF, (b) FESEM image of the cross-section of [±45] PA6/CF sample showing the layered structure with two walls and the infill region and (c) high-magnification FESEM micrograph of the interface between walls and rastered beads

The interface area between these regions is magnified in Figure 83c, where the 45° rastered beads are clearly visible. Some irregularly-shaped voids can be observed in the wall/infill interfacial region due to a non-complete overlapping of the adjacent extruded filaments. Other voids with elongated form are also located between the stacked layers (Figure 83c).

The mesostructure (that is the material structure at a sub-millimetre level), void distribution and fibers orientation of PA6/CF printed composites was further studied by using both optical and electron microscopy. The microstructural features and defects of FFF build samples are mainly controlled by the process parameters and filament deposition path, such as extrusion temperature, beads dimensions (width and thickness), beads overlap and orientation [20,289,290]. Figure 84 shows optical and FESEM images of the typical mesostructure of PA6/CF parts. The extruded beads profile (sketched in red in Figure 84a), is limited by the presence of a significant amount of voids between layer and adjacent rasters (Figure 84a). The dimensions of the printed beads strictly resemble the extruder nozzle diameter (600 µm) and the layer thickness (200 µm). A porosity content of about 10% was calculated from the several micrographs of polished cross-sections of the FFF printed dog bones samples for tensile tests using a greyscale threshold on ImageJ software. Similar values were obtained by using Archimede method (see Section 3.2.4): 10.8%, 9.5% and 9.8% for [0],

[±45] and [0/45/90/-45] samples respectively. The small variation in void content between the printing architectures can be probably ascribed to minor differences in inter-layer and inter-beads void distribution [181,291]. However, the author suggests that their influence on the mechanical properties of the final parts should be negligible compared to the beads / fibers orientation.

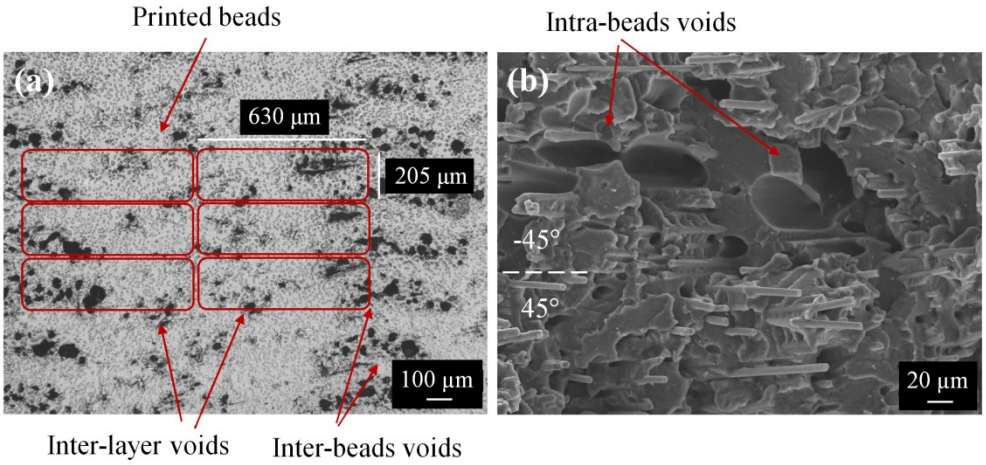

Figure 84: (a) Optical micrograph of a polished YZ cross-section of PA6/CF composite part produced by FFF and (b) FESEM image of the tensile fracture surface of [±45] printed sample. Beads profile and dimensions as well as various type of voids (i.e., inter-layer and inter-beads voids) are outlined in the optical image, while intra-layer pores and inter-beads voids caused by gas bubbles entrapped in the filament are visible in the FESEM images

Voids are inherent defects in FFF printed parts as a result of the absence of pressure and the thermal cycles involved in the layer-wise printing process [289]. Different types of voids can be easily distinguished in the optical and FESEM micrographs in Figure 84. Inter-layer voids consist of small gaps in the interlayer areas caused by a partial bonding between layers (Figure 84a). Large inter-beads pores with irregular shape are located at the beads as a result of an incomplete coalescence between adjacent beads (Figure 84b). In unreinforced polymer parts these types of voids usually stand for the major part of the porosity fraction and exhibited a regular pattern of triangular gaps due to polymer die swelling and incomplete filament sintering [175,176]. However, the addition of carbon fibers increases the thermal conductivity and decreases die swell of the polymer matrix, thus modifying the shape and distribution of inter-beads voids (Figure 84a). In addition, smaller intra-beads voids with almost round shape were observed in the FESEM micrograph (Figure 84b). These pores resemble gas bubbles and show the same morphological characteristics in terms of shape and size as the voids

observed in the filament before printing (Figure 77). Therefore, it can be assumed that gas escaping during the filament manufacturing process is the most probable formation mechanism [175]. Various authors already described these types of voids in 3D printed fiber reinforced polymer composites parts produced by FFF. Partial bonding between layers and adjacent beads, gas escaping and independent movement of polymer and fibers during processing were proposed as mechanisms behind pores evolution [175,176,180].

Figure 85 depicts the optical images of the polished YZ cross sections of PA6/CF specimens produced using different [0/45/90/-45], [0] and [±45] architectures. The micrograph of the quasi-isotropic specimen clearly reveals how the raster angle settings affect the composite microstructure and the orientation of the carbon fibers. In fact, it is possible to notice the layered structure of the composite part alternating 0°, 45°, 90° and -45° oriented beads and the resulting fibers cross section (Figure 85a).

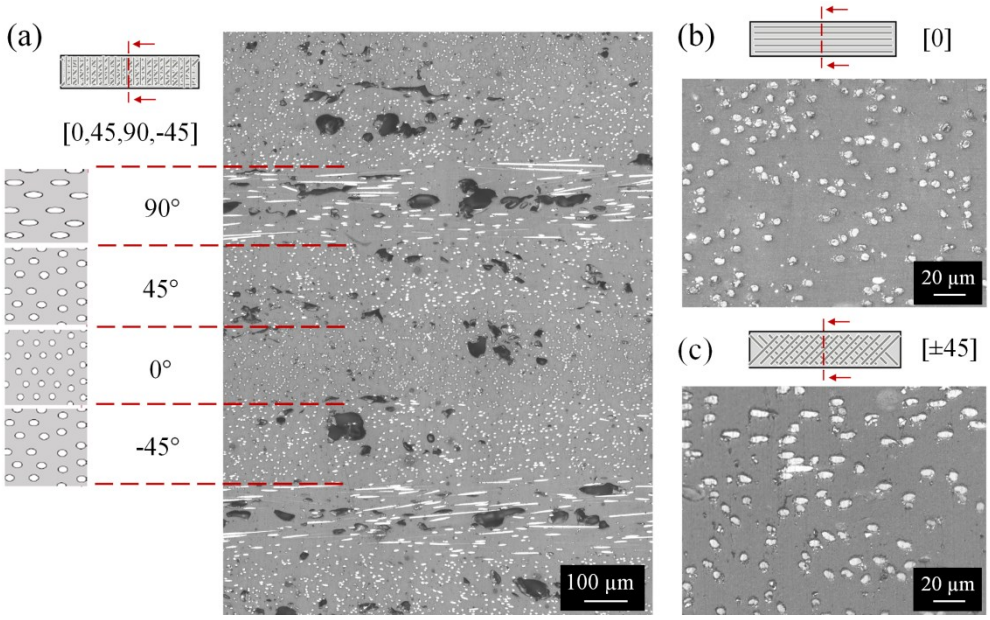

Figure 85: Optical micrographs of the polished YZ cross sections of PA6/CF samples printed with various architectures: (a) [0/45/90/-45], (b) [0] and (c) [±45]. In figure (a) the cross sectional shapes of the fibers observed in the stacked layers are schematically sketched

It is widely accepted that the orientation of short or continuous fibers in composite materials can be qualitatively and quantitatively evaluated by analysing the elliptical or circular footprints left by the fibers on a polished surface observed

with an optical microscope [292–294]. In fact, in transverse layers (i.e., with beads deposited at 90° with respect to the sample axis) the fibers exhibit a nearly rectangular or elongated cross sectional shape, that changes into elliptical, circular and again elliptical ones in layer oriented at -45°, 0° and 45° respectively (Figure 85a). As a result, it is possible to assume that the orientation of carbon fibers in quasi-isotropic PA6/CF samples differs from one layer to the successive ones in a regular fashion according to the [0/45/90/-45] layup sequence adopted, as schematically sketched in right side of Figure 85a. The examination of the cross sections of [0] and [±45] PA6/CF samples further demonstrates the preferential orientation of fibers along the printed beads direction (Figure 85b and 85c). This specific microstructure was observed in various fibers reinforced polymer composites processed through material extrusion AM technologies [176–183]. In particular, the FFF process enhances the alignment of fibers in the printing direction, in addition to that obtained in the feedstock filament manufacturing process. During the building process the thermoplastic polymer matrix melts down in the printing head. The shear stresses and velocity gradients occurring when the melted filament passes through the extruder nozzle underpin the strong alignment of the fibers along the extrusion direction [26]. This alignment method or "*flow-induced orientation"* has been described also by numerical simulations of the extrusion process of fiber reinforced filaments [26]. These studies showed that fibers alignment significantly increased as a result of the elongation flow that occurs at the converging section of the nozzle, although polymer swell could slightly alter the degree of orientation after nozzle exit [26].

The described microstructural characteristics reveals that FFF allows to tailor the stiffness and strength of 3D printed carbon fiber reinforced polymer composites by changing layer by layer the filament deposition paths. In this way, fibers orientation and thus material properties can be precisely adjusted according to specific applications and loading conditions. The greater reinforcing effect can be obtained by printing composite parts with beads oriented along the sample axis (i.e., 0° raster angle) because the carbon fibers are preferentially aligned along the applied tensile loads. The mechanical properties of the parts gradually deteriorate in relation to the angle formed between the deposited beads and the externally applied loads. This design flexibility of 3D printed short CFRPs in terms of material properties is not obtainable with conventional manufacturing techniques such as compression or injection moulding. Therefore, these characteristics brings FFF products closer to fibers reinforced laminates.

The DSC thermographs of PA6/CF composites before and after the printing process are illustrated in Figure 86. The melting and crystallization behaviour of the raw filament and 3D printed part is fairly good comparable (Figure 86). In detail, the melting curves shape and peak temperature (Figure 86a) as well as the polyamide crystalline fractions calculated using equation (12) are almost equal (22.6% and 22.2% for the filament and printed samples respectively). This may indicate that the cooling conditions experienced during filament manufacturing and FFF printing are quite similar, thus leading to the same crystalline structure of the polyamide matrix in terms of both phase and degree of crystallinity.

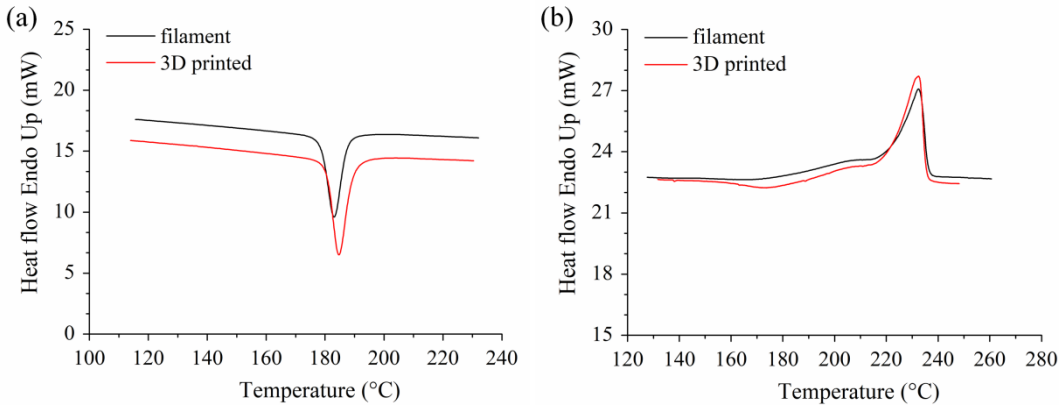

Figure 86: DSC traces of PA6/CF raw filament and 3D printed samples: (a) melting and (b) crystallization curves

4.2.3 Mechanical properties

Figure 87 depicts the stress versus strain curves of 3D printed neat PA6 and PA6/CF specimens resulting from uniaxial tensile test at room temperature. The fiber reinforced samples were manufactured with [0], [±45] and [0/45/90/-45] architectures. The stress-strain curves of the printed PA6/CF specimens reveal similar characteristics with a linear elastic behaviour until brittle rupture (Figure 87). By contrast, neat PA6 samples display a ductile curve with low modulus and high elongation at break (Figure 87). The addition of carbon fibers to the polymer leads to a significant improvement of elastic modulus, between 3 and 4.5 times depending on the architecture adopted. The tensile strength increases, but at a lesser amount due to the higher porosity content of the fiber reinforced samples compared to the neat polymer (Figure 87). Both stiffness and strength at break of the PA6/CF parts highly differs from one architecture to the others (inset of Figure 87).

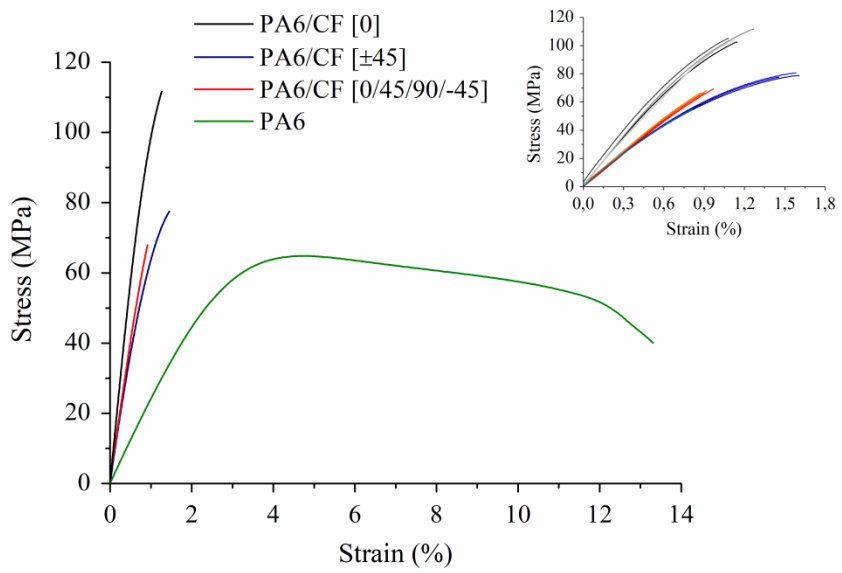

Figure 87: Stress-strain curves of neat PA6 and PA6/CF specimens. Inset: magnified view of the tensile curves of PA6/CF samples with different architectures only

Table 17 summarizes the mechanical properties of the tested specimens, including Young modulus, ultimate tensile strength and elongation at break, and the pore contents. The highest mechanical properties (E=11.7 GPa and σ=105.8 MPa) were found in the [0] specimens. In fact, as already shown in Figure 85b, when the raster angle is 0° for all layers the short fibers are well aligned along the tensile load direction, thus effectively carrying the applied stress.

Table 17: Tensile properties and voids content of neat PA6 and PA6/CF samples produced with different printing architectures

Material - layup	Elastic modulus (GPa)	Tensile strength (MPa)	Strain at break (%)	Porosity (%)
PA6/CF - [0]	11.71 ± 0.55	105.8 ± 4.0	1.2 ± 0.1	10.8 ± 0.4
PA6/CF - [±45]	7.48 ± 0.56	72.9 ± 12.2	1.3 ± 0.4	9.8 ± 0.5
PA6/CF - [0/45/90/-45]	7.98 ± 0.07	67.6 ± 1.3	0.9 ± 0.1	9.5 ± 0.2
PA6 - [±45]	2.54 ± 0.08	64.0 ± 1.3	14.0 ± 5.9	1.3 ± 0.1

The mechanical performances decrease by using more complex architectures, such as [±45] and [0/45/90/-45] because the orientation of fibers resemble the specific layups adopted for printing. Particularly, the elastic modulus and tensile strength are lowered by 34% and 31% respectively for [±45] samples and 32% and 36% respectively for [0/45/90/-45] ones (Table 17). The strain at break of PA6/CF composites is severely limited by the negative effect of voids as well as the high content of carbon fibers incorporated in the feedstock filaments (Table 17). In fact, adding a rigid fiber in a polymer matrix induces stress concentration around fiber edges and restricts the mobility of the polymer molecular chains. This favours the formation of cracks in the matrix, thus negatively affecting the ductility of the material [175,183,254,255]. The lower elongation values of [0/45/90/-45] samples (Table 17) can be attributed to the presence of 90° layers, where the fibers are oriented transversely with respect to the applied load. These results indicate that the mechanical behaviour of the printed composites are highly affected by the amount, length and orientation of the carbon fibers. Although the highest performances are obtained for longitudinal samples, [±45] and [0/45/90/-45] architectures should be used for applications where strong anisotropy in the mechanical behaviour of the printed composites has to be avoided. Table 18 lists the tensile properties of several short CFRPs based on polyamide matrices manufactured by FFF to compare the performances of PA6/CF samples produced in this study with existing literature.

Table 18: Summary of the Young modulus and tensile strength values reported to date for short carbon fibers reinforced polyamide composites printed through FFF with [0] and [±45] architecture

Material	Filler loading (%)	Printing layup	Elastic modulus (GPa)	Tensile strength (MPa)	Ref.
PA12/CF	10	[0]	3.6	93.8	[178]
PA6/CF	10	[0] / [±45]	4.0 / 2.4	128.0 / 97.5	[295]
PA6/CF	14	[0] / [±45]	7.6 / 5.1	92.0 / 63.3	[296]
PA66/CF	15	[±45]	7.9	95.7	[297]
PA6/CF	15	[0]	9.9	97.7	[146]

PA6/CF	20	[0]	6.2	52.0	[298]
PA12/CF	23	[0]	8.8	89.0	[225]

It can be seen that PA6/CF parts exhibit comparable mechanical properties (or even higher for elastic modulus) with respect to literature data (Table 18). Higher tensile strength was reported in Peng et al. [295], where a surface treatment using a silane coupling agent was carried out on the carbon fibers to enhance the adhesion with the matrix.

Figure 88 illustrates macroscopic images of the surface fracture of the PA6/CF tensile specimens obtained by stereomicroscopy. These micrographs clearly reveal the mesostructural differences between the architectures adopted as well as the brittle failure typical of the carbon fiber composites.

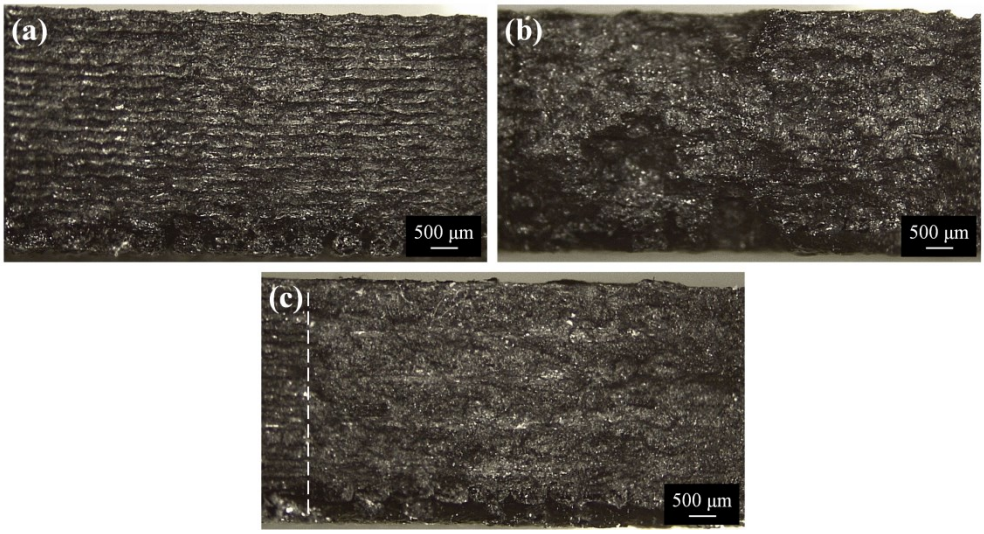

Figure 88: Stereomicroscopy images of the surface fractures of PA6/CF dog-bone samples after tensile tests: (a) [0], (b) [±45] and (c) 0/45/90/-45] architecture. The interface between wall and infill regions in Figure 88c is marked by a dashed line

The specimen printed with [0] architecture exhibits a regular surface fracture where the typical mesostructure induced by the unidirectional layup (i.e., parallel beads aligned in the printing direction) and the interfaces between layers are clearly visible (Figure 88a). By contrast, tensile testing of [±45] and [0/45/90/-45] samples lead to more irregular surface fractures, where the multiple stacked layers are not easily distinguishable. The middle part of the fracture surface of the [±45]

sample shows some step-like features with inclination at 45° (Figure 88b). Moreover, in the quasi-isotropic architecture the rupture of the beads in the infill and wall regions can be identified (Figure 88c). A more detailed analysis of the failure morphology of the PA6/CF composites at a micro-scale level was performed by using FESEM (Figure 89). The tensile fracture surface of specimens produced with [±45] architecture exhibits fiber breakage inside each layer, thus indicating the major role plays by carbon fibers in the composite strengthening. Moreover, little delamination between stacked layers, outlined by large voids occurred in the interlaminar regions (Figure 89a). The preferred orientation of the carbon fibers in the bead direction can also be clearly observed in the micrograph (Figure 89a).

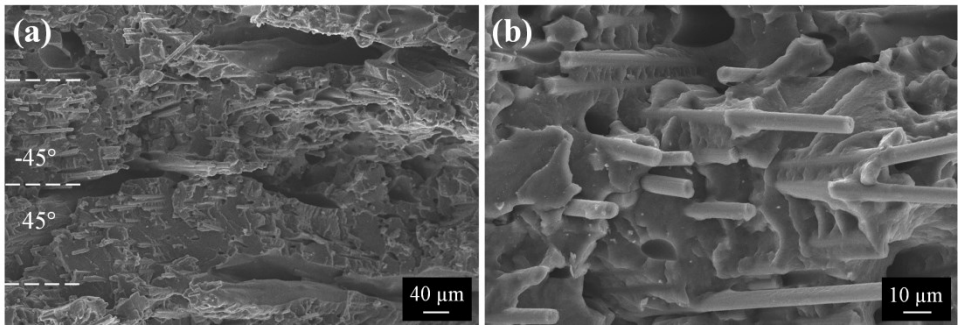

Figure 89: FESEM micrographs of the tensile fractured surface of [±45] PA6/CF sample: (a) low magnification image revealing interlayer delamination and fiber rupture and (b) high magnification image showing fiber/matrix interface and fiber pull-out

At higher magnification (Figure 89b), additional details on the favourable fiber/matrix interface properties can be detected. The surface of the broken carbon fibers is coated with polymeric residues to some extent, thus revealing that mechanical interlocking and good interfacial adhesion was created between fibers and matrix inside the printed beads (Figure 89b). This suggests that an adequate stress transfer from the polymer to the carbon fibers is expected when loads are applied to the composite samples. Finally, fibers pull-out also happens to a small extent, as revealed also by the presence of small round cavity in the fracture surface (Figure 89b).

4.2.4 Prediction of mechanical properties

Table 19 reports the elastic constants, strength and other physical properties of the composite material constituents needed for applying the modified RoM described in Section 3.3.1. The mechanical properties of the PA6 matrix, carbon fibers and

Fe_3O_4 particles were measured using ASTM standards or provided by literature [276,299]. The tensile strength of Fe_3O_4 was extrapolated from the results of tensile tests at high temperatures reported in [300]. Other important physical parameters (i.e., filler content, fiber diameter and average length) were collected by experimental analysis of the raw filament (see Section 4.2.1). In particular, the volume fractions of fillers were calculated by adapting equation (46) for a ternary composite.

Table 19: Material properties of the PA6/CF composite constituents adopted for the calculation of elastic modulus and tensile strength using the modified RoM

Material properties	PA6	CF	Fe_3O_4
Longitudinal elastic modulus – E_1 (GPa)	2.54	230	211
Transverse elastic modulus – E_2 (GPa)	2.54	15	-
In-plane shear modulus – G_{12} (GPa)	1.22	15	-
Poisson's ratio – ν_{12}	0.39	0.2	0.4
Axial tensile strength – σ_1 (MPa)	64.0	3500	76
Volume fraction (%)	86.6	10.5	2.9
Fiber diameter 2r (μm)	-	6.5	-
Mean fiber length l_f (μm)	-	94.2	-

The elastic modulus of the PA6/CF composites was obtained by using equation (19) modified for predicting the properties of ternary composites:

$$E_c=\left(\eta_\theta \eta_l E_f V_f+\eta_{\theta\ oxide} E_{oxide} V_{oxide}+E_m V_m\right)(1-\varphi) \quad (49)$$

where E_C, E_f, E_{oxide} and E_m are the elastic modulus of the composite, fibers, magnetite and matrix respectively and $\eta_{\theta\ oxide}$ is the orientation factor for Fe_3O_4, that was considered equal to 1/5 as the filler particles have a randomly 3D

arrangement in the polymer matrix. Finally, V_f, V_{oxide} and V_m are the volume fractions of fibers, magnetite and matrix respectively. A fiber length efficiency factor η_l of 0.39 was determined by using equations from (21) to (23). The fiber orientation efficiency factor η_θ was calculated according the Krenchel formulation by taking account of the typical mesostructure of the samples printed by FFF (Figure 83) and the fiber alignment within the extruded beads:

$$\eta_\theta = \eta_{\theta\ infill} V_{f\ infill} + \eta_{\theta\ walls} V_{f\ walls} \tag{50}$$

where $\eta_{0\ infill}$, $V_{f\ infill}$, $\eta_{\theta\ wall}$ and $V_{f\ wall}$ are the fiber orientation efficiency factors and the volume fractions of infill and perimeters regions respectively. In fact, two different regions, namely wall and internal infill, showing distinct mechanical behaviour due the printing tool path adopted can be distinguished in Figure 83. The volume of each region of the printed parts can be estimated from simple geometrical observations. The volume fraction of the contour and infill regions was obtained using equations (51) and (52):

$$V_{f\ walls} = \frac{V_{walls}}{V_{composite}} = \frac{2 l_1 N t_{layer} W_{walls}}{l_1 b_1 h} \tag{51}$$

$$V_{f\ infill} = 1 - V_{f\ walls} \tag{52}$$

where V_{walls} denotes the volumes of the wall regions, N is the overall number of layers, t_{layer} is the layer thickness. The width of walls (W_{walls}) was evaluated using electron microscopy (Figure 83) and it is equal to 1.4 mm. The total volume of the printed part $V_{composite}$ was determined by considering the dimensions (length l_1, width b_1 and thickness h) of narrow parallel-sided portion of the tensile dog-bones. For each layup the walls are always printed with 0° raster angle while the infill is related to the specific layers stacking sequence adopted. The microstructural analysis has revealed a strong alignment of short carbon fibers in the printed bead direction due to the nature of the FFF process. Therefore, the fiber orientation efficiency factor of the wall region is $\eta_{\theta\ wall}=1$. For the infill region, $\eta_{\theta\ infill}$ can be calculated using the Krenchel approach (equation (20)) for each layup adopted. Table 20 summarizes the parameters used to compute the volume fractions of the wall and infill regions of PA6/CF composites with different printing architectures as well as the $\eta_{\theta\ infill}$ values. An Excel template was adopted to perform the calculations. Using this approach, η_θ is equal to 1, 0.43 and 0.525 for [0], [45] and [0/45/90/-45] layups respectively.

Table 20: Geometrical features of the structure of 3D printed samples produced with different architectures

Parameters	[0]	[±45]	[0/45/90/-45]
Length l_1 (mm)	60	60	60
Width b_1 (mm)	10	10	10
Thickness h (mm)	4	4	4
Number of layers N	20	20	20
Layer thickness t_{layer} (mm)	0.2	0.2	0.2
Width of walls W_{walls} (mm)	1.4	1.4	1.4
Fiber orientation efficiency factor $\eta_{\theta\ infill}$	1	0.25	0.375

The porosity content φ of the printed PA6/CF composites was determined experimentally by using the Archimede method (Table 17). The critical fiber length l_C for the PA6/CF system, was calculated using the fiber/matrix interfacial shear strength τ_y of 43.2 MPa measured experimentally by Tanaka et al. [278]. The obtained values (i.e., 263 μm) is higher than the maximum length recorded from fiber length distribution analysis (Figure 78). Therefore, the tensile strength of the composite σ_c can be once again obtained according to the simplified Kelly-Tyson model of equation (47), although adapted for ternary composites:

$$\sigma_c = \left(\eta_\theta \frac{V_f \tau_y l_f}{2r} + \sigma_{oxide} V_{oxide} + \sigma_m V_m\right)(1-\varphi) \quad (53)$$

where l_f is the average fiber length, r is the fiber radius and σ_{oxide} and σ_m are the tensile strength of the neat PA6 polymer and Fe_3O_4 respectively.

Comparison of modeling results with experimental data

The elastic modulus and ultimate tensile strength calculated using the above mentioned models for each architecture are summarized in Table 21, where the

relative error (%) between the predictions and the experimental values is also reported.

Table 21: Young modulus and tensile strength of PA6/CF composites produced by FFF obtained using the modified RoM models for ternary composites and relative error (in brackets) against experimental results

Layup	Experimental		Predicted	
	E (GPa)	σ (MPa)	E (GPa)	σ (MPa)
[0]	11.71	105.8	11.38 *(-2.9)*	111.8 *(+5.4)*
[±45]	7.48	72.9	7.00 *(-6.9)*	80.2 *(+12.7)*
[0/45/90/-45]	7.98	67.6	7.74 *(-3.1)*	85.5 *(+20.9)*

It can be seen that the modified RoM approach, adapted by adding the porosity correction factor (1-φ), is accurate to predict the elastic modulus of 3D printed ternary composites reinforced with short carbon fibers. In fact, relative errors lie between -2.9% for longitudinal layup and -6.9 for [±45] layup (Table 21). A comparable underestimation (between 5% and 10%) of the elastic modulus of short fiber polymer composites printed by FFF was obtained by using CLT analysis, adjusted with RoM to take into account the effect of perimeter walls [226], as well as Mori-Tanaka homogenization theory [225]. In the former model a lower bound estimate for the effective elastic properties of PA12/CF composites was predicted by considering the fiber orientation distribution and aspect ratio measured experimentally. The author suggests that the high degree of molecular orientation of the polymer chains derived from the FFF processing conditions [224] could partially explain the underestimation of the Young modulus obtained both in this thesis and in literature [225,226] using different modeling approaches. The RoM model shows a lower predictive accuracy for tensile strength (Table 21). As already mentioned for SLS composites, the high void content in the 3D printed parts and the hypothesis of perfect fiber/matrix adhesion in RoM are responsible for the discrepancies between experimental and modeling results. Moreover, it is worth noting that the error is higher for [±45] and [0/45/90/-45] composites compared to longitudinal parts (Table 21). This is probably related to the fact that the failure of these complex architectures occurs both by fibers/matrix

interfacial debonding and interlayer delamination (Figure 89a). As expected, the contribution of Fe_3O_4 particles on the composite strength is negligible compared to stiffness [280,281]. In fact, magnetite behaves similarly to other low aspect ratio fillers commonly used in plastics such as glass beads, barium sulphate (Ba_2TiO_4) and calcium carbonate ($CaCO_3$), that increase polymer rigidity and slightly lower strength.

4.3 Continuous Filament Fabrication

4.3.1 Filament characterization

Morphological and physical properties

Figure 90 shows the morphology and microstructure of the printing filaments (i.e., neat PA and CCF) through a collection of optical and FESEM images.

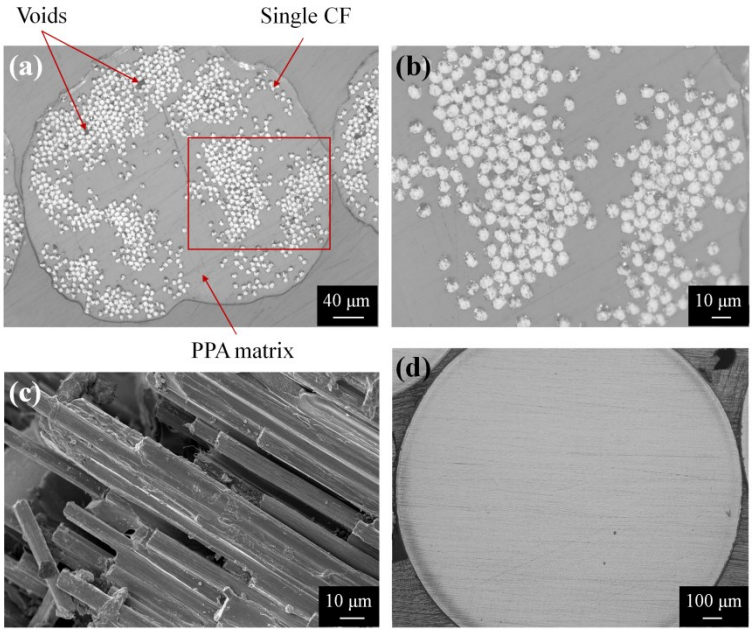

Figure 90: Optical images of the polished cross-section of (a) CCF and (d) neat PA feedstock filament. (b) Magnified view of a high fibers concentration region within the CCF tow. (c) FESEM image of the cryo-fractured surface of the CCF filament

CCF filaments exhibit the typical structure of a pre-impregnated material, also known as “pre-pregs” in the composite industry. A single filament (380 µm in diameter) consists of a continuous carbon fibers bundle containing around 1000 fibers fully impregnated with a polymer matrix (Figure 90a). However, it is worth noting that the distribution of fibers in the polymer matrix is hardly homogeneous

and regions with high concentration of fibers are alternated to matrix rich areas (Figure 90a). This morphological feature can be quantitatively studied by measuring the discrepancy between the average fiber content (V_f) for the entire filament (35%) and the local V_f in a fiber rich region (magnified in Figure 90b). These values are reported in Table 22 together with other relevant morphological properties of the printable filaments.

Table 22: Morphological properties obtained from image analysis of several optical images of PA and CCF filament. Cross-sectional area, number and volume fraction of fibers were measured for the overall CCF filament as well as for a local region showing high fiber content, marked in red on Figure 90a. The filament diameters stated by Markforged® are reported in bracket.

Region	Parameter	PA	CCF
Filament	Measured area (10^3 µm^2)	2402 ± 6	115 ± 1
	Diameter (µm)	1747 ± 4 *(1750)*	381 ± 5 *(380)*
	Porosity (%)	< 0.1	1.3 ± 0.2
	Fibers diameter (µm)	-	7.1 ± 0.2
	Number of fibers	-	1032 ± 2
	Fibers volume fraction (%)	-	34.8
Local	Measured area (10^3 µm^2)	-	4.65
	Number of fibers	-	104
	Fibers volume fraction (%)	-	87.3

Few tiny voids can also be noticed in the CCF filament cross section (Figure 90a). These voids are considered inherent manufacturing defects of thermoplastic pre-pregs because the high amount of fibers and the high melt viscosity of the resin could prevent a complete impregnation of the fibers [193,301–303]. Therefore, a lower fiber/matrix bonding can be expected in these regions.

A lateral view of the CCF filament after cryogenic fracturing was also analysed by FESEM (Figure 90c). Numerous aligned continuous fibers partly coated with the matrix material can be noticed (Figure 90c). The average diameter of the fibers (7.1 μm) was measured by image analysis (Table 22). Differently, neat PA filaments exhibit the morphology of a classical polymeric feedstock for FFF technique. The cross section has a diameter of about 1.75 mm and no voids can be seen (Figure 90d). A smooth outer coating is also visible in the cross sections of both filaments (Figure 90a and 90d).

Thermal properties

The thermal transition of neat PA and CCF filaments were investigated by calorimetric techniques. The DSC traces of both materials are showed in Figure 91. In the 1st heating-cooling cycle at 10 °C/min the curve depicting the PA filament clearly reveals distinct endothermic and exothermic peaks at 201 °C and 167 °C (Figure 91a), that correspond to the melting and crystallization of the α crystalline structure of PA6 respectively [205]. A double melting peak appears in the curve depicting the 2nd heating step of the neat PA filament (Figure 91b). Moreover, the melting event occurs at slightly higher temperatures (205 °C) with respect to the 1st heat cycle (Figure 91a).

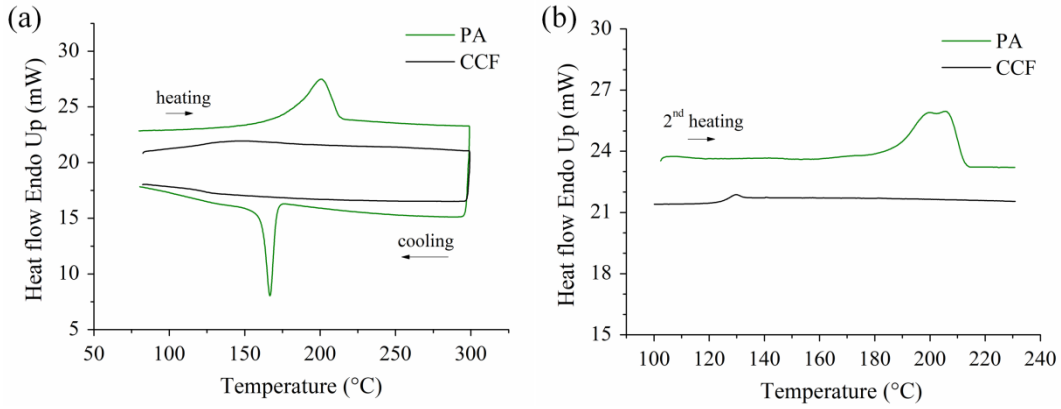

Figure 91: a) DSC 1st heating-cooling curves, (b) DSC 2nd heating curves of PA and CCF filaments. The glass transition of CCF tow can be clearly observed in the 2nd heating step

A literature survey [134,286] suggests that the previously described thermal behaviour can be assigned to the melting-crystallization-remelting of crystallites with distinct morphological features (e.g., thickness and distribution of lamellae) or the occurrence of distinct crystalline phases. By contrast, the CFF filament does not present any melting or crystallization peak (Figure 91a), as typical of

amorphous thermoplastic polymers. The glass transition occurs at 127 °C and it can be observed in the 2nd heating step upon erasing the thermal history of the polymer (Figure 91b).

Similar glass transition temperature (i.e., 125-127 °C) are usually reported for PA6I/6T, a semi-aromatic polyamide belonging to the polyphthalamide (PPA) family [284]. This polymer type or similar blends of linear and semi-aromatic polyamides from EMS-Grivory (EMS-CHEMIE AG, Domat/Ems, Switzerland) including Grivory G and Grivory HT grades are mentioned in a patent dealing with the manufacturing of composite filament by MarkForged [193]. These polymers exhibit higher mechanical properties (E=3 GPa and σ=85 MPa), long-term temperature stability (up to 120 °C) and fiber wettability compared to linear polyamides, such as PA6 [284,304]. Therefore, the authors suggest that PA6I/6T is likely the amorphous matrix embedding the continuous fibers in the CCF filament, differently from what has been proposed by a previous work (i.e., PA6/3T) [205]. This hypothesis is supported by the results obtained by Dutra et al. [213] using asymptotic homogenization technique to predict the elastic properties of individual PA/CFF plies from those of the printed parts. The model revealed that the composition of the thermoplastic matrix embedding the continuous fiber is not the same for the neat PA and fiber reinforced filaments. A polymer with Young's modulus ≥ 3 GPa is necessary to obtain accurate prediction of both transverse and in-plane shear moduli of the reinforced plies [213]. This information could be useful to interpret the thermo-mechanical properties of PA/CCF composite parts produced using MarkForged® printers.

The thermal stability of PA and CCF filaments was studied by TGA experiments carried out in inert atmosphere. The resultant weigh loss (%) and weight loss derivative (1/s) curves are displayed in Figure 92. The printing tows shows a slight weight loss (about 2%) between 100 and 200 °C (Figure 92). The author suggests that the degradation of the outer coating of the CCF (Figure 90a) and PA filaments (Figure 90d) or the evaporation of residual moisture is likely related to these events. The thermal decomposition of the polyamide backbone chain takes place in a single step at higher temperatures (Figure 92). However, it can be seen that CCF tow exhibits a better thermal stability with respect to neat PA filament (Figure 92). This behaviour can be easily explained by taking into account that the reinforcing tow is made of a plurality of carbon fibers embedded in a semi-aromatic polyamide matrix (Figure 90a and Figure 91) showing higher thermal stability compared to PA6 [205].

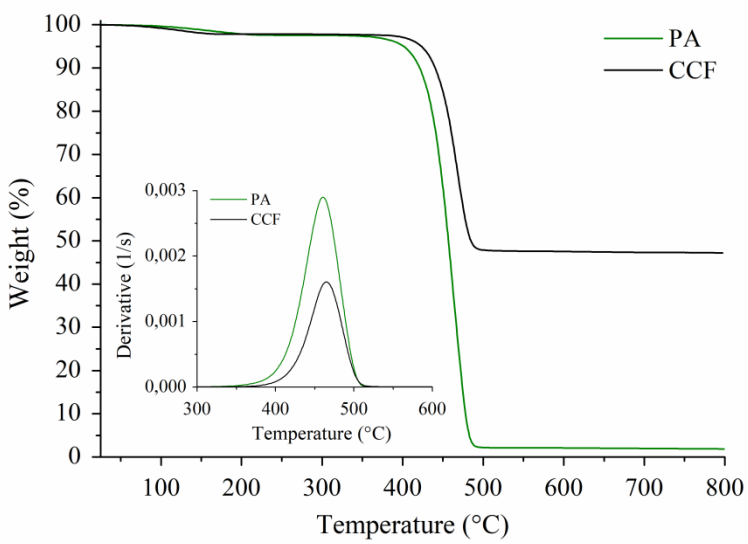

Figure 92: Weight loss curves of neat PA and CCF filaments in inert environment revealing the degradation mechanism and the onset ($T_{d\ onset}$). Inset: weight loss derivative showing the maximum degradation rate ($T_{d\ peak}$) temperatures of the filaments

As in an inert atmosphere the polymer matrix suffers pyrolysis without the carbon fibers are being decomposed, the thermo gravimetrical analysis was used to evaluate the weight fraction of continuous fibers embedded in the CCF filament (46.6 wt.%), defined by subtracting the polymer char residue to the weight loss at 800 °C (Figure 92a). Table 23 summarizes the thermal and physical properties of the neat PA and CCF filaments.

Table 23: Thermal and physical properties of the printable filaments. Melting, crystallization and glass transition temperatures (T_m, T_c and T_g respectively) were obtained from DSC analysis, apart from the T_g of the neat PA filament (derived from [205]). The onset and peak degradation temperatures ($T_{d\ onset}$ and $T_{d\ peak}$ respectively) and the volume fraction of fibers (V_f^{CCF}) were calculated from TGA experiments

Filament	T_m (°C)	T_c (°C)	T_g (°C)	$T_{d\ onset}$ (°C)	$T_{d\ peak}$ (°C)	V_f^{CCF} (%)	ρ (g/cm³)
PA	200.8	166.8	22.0	403.7	460.2	-	1.11
CCF	-	-	127.5	420.7	465.2	36.9	1.39

The volume fraction of carbon fibers (V_f) of the reinforcing tow, useful for predicting the mechanical properties of the printed parts, was determined using equation (46), taking into account the density of the PA6I/6T matrix (ρ_m=1.18 g/cm^3) [304], the density of Toray T300 standard modulus carbon fibers (ρ_f=1.76 g/cm^3) [276] and the fibers weight fraction obtained from TGA (W_f=46.6%). Finally, the density of the printing filaments was assessed by gas pycnometry. The values of all the properties reported in Table 23 are comparable to those obtained in other studies on MarkForged® materials [205,206,210,220].

Mechanical properties

Figure 93 shows the stress-strain response of single PA after uniaxial tensile tests. The ductile behaviour and the high elongation of the pure polymeric filament can be clearly distinguished from the shape of the stress-strain curve depicted in Figure 93a. An initial linear elastic response in the low stress region (up to approximately 30 MPa) is followed by a shoulder that defines a transition between linear elastic and nonlinear plastic behaviour (Figure 93a). At higher stress strain hardening possibly occurs due to the alignment of polymer macromolecules in the loading direction until final rupture (Figure 93a). The appearance of the surface fracture of the filament clearly reveals a ductile failure morphology with a high amount of plastic deformation undergone by the material before fracture (inset of Figure 93a). Moreover, it can be observed that the failure occurs along a surface that creates a 45° angle with respect to the loading direction (inset of Figure 93a).

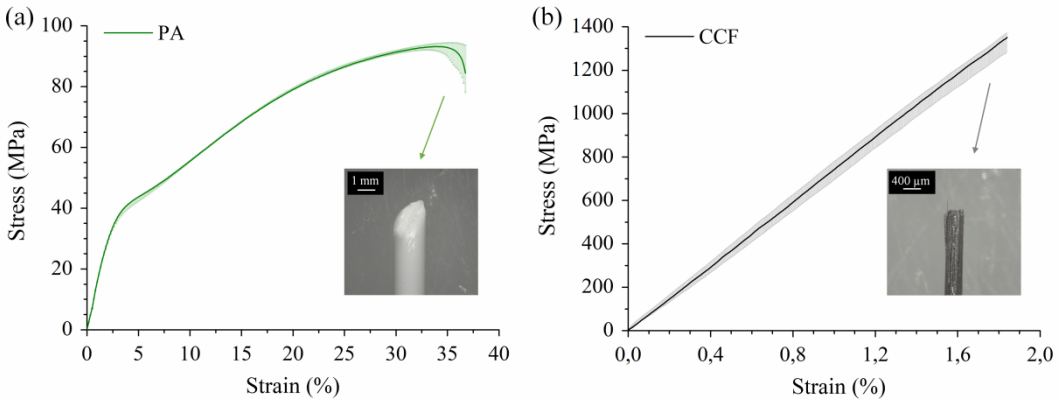

Figure 93: Tensile stress-strain curves of (a) PA and (b) CCF filaments. The macroscopic failure morphology of the filaments is illustrated in the inset figures

On the other hand, the stress-strain response of CCF filament resembles a typical brittle material with a linear elastic behaviour until catastrophic fracture

that occurs at low elongation (1.9%). The presence of a plurality of continuous carbon fibers aligned in the direction of the applied stress is responsible for the significantly higher elastic modulus and strength at break of the CCF filament compared to the neat PA one. The tensile properties of both materials are summarized in Table 24. Finally, it is worth noting that the macroscopic failure morphology and the overall mechanical behaviour of the CCF filaments is comparable to those obtained in another study [220].

Table 24: Tensile properties of pure PA and CCF filaments. An accurate evaluation of the elastic modulus of the CCF filament was not possible because standard extensometer cannot be used on filaments with very low cross-section (diameter of 380 μm). The value reported in the table was derived from [220]

Printing filament	Elastic modulus (GPa)	Tensile strength (MPa)	Elongation at break (%)
PA	1.50 ± 0.99	93.9 ± 1.6	38.4 ± 3.02
CCF	74.43 ± 2.50	1344.0 ± 37.3	1.9 ± 0.13

4.2.3 Microstructural characterization and fiber orientation

The mechanical properties and structural integrity of the composite parts are directly related to the microstructure and defects induced by the CFF printing process. The microstructural characterization of the printed PA/CCF composites was carried out by optical microscopy. Figure 94 displays a collection of micrographs of the polished YZ cross section of longitudinal PA/CCF composites (i.e., [0] layup) at different magnification level. The entire PA/CCF cross section obtained by stitching consecutive low magnification images is illustrated in Figure 94a. A 0.75 mm wide wall composed by pure PA and the infill region of CCF filaments with a clear and defect-free interface can be easily distinguished in the micrograph (Figure 94a). Moreover, the typical layered microstructure of additively manufactured parts as well as the appearance of a large amount of voids with different sizes and shapes can be observed (Figure 94a). The void content was estimated through image analysis and it is equal to 11.1%. Comparable values were obtained in other studies for longitudinal reinforced composites processed using Mark Two printer by using image analysis of optical micrographs [156,203,209] and micro-computer tomography (micro-CT) [206].

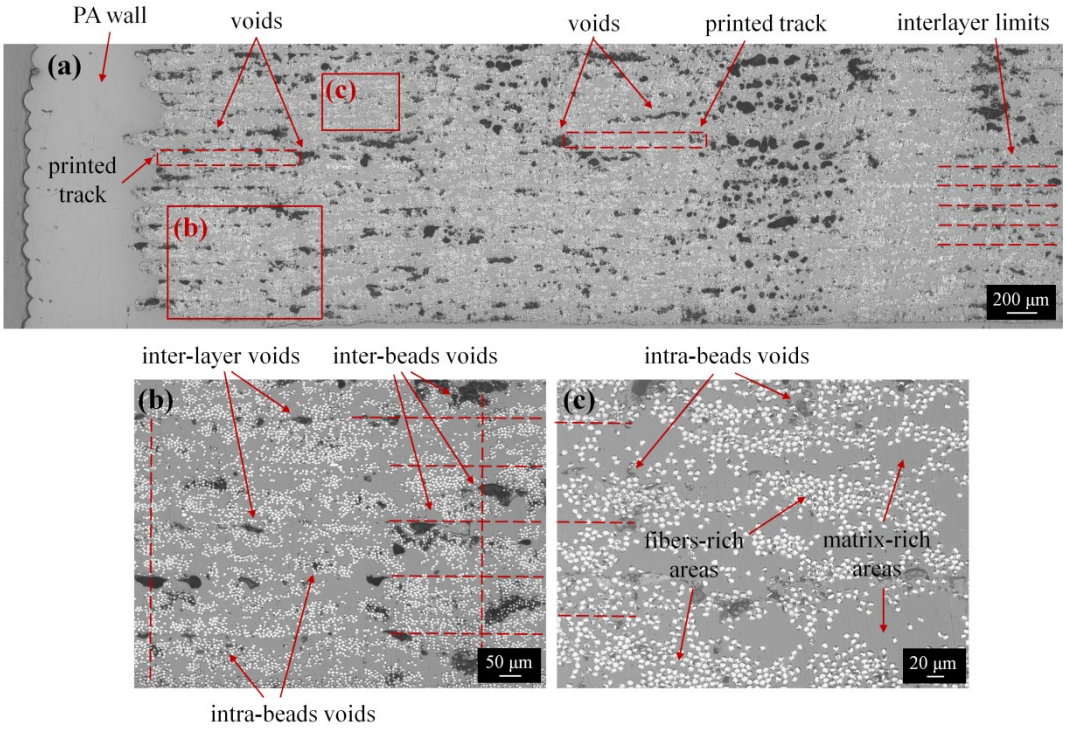

Figure 94: Optical micrographs of the YZ cross section of longitudinal PA/CCF composite samples at various magnification: (a) panoramic view, (b) magnified view showing bead interfaces (vertical dashed lines), interlayer limits (horizontal dashed lines) and different types of voids and (c) magnified view showing an intra bead region with matrix and fibers-rich areas along with small inter-beads voids.

The printed beads dimensions were estimated to be about 125 µm in height and 900 µm in width (Figure 94a). These values are comparable to the layer thickness adopted for printing and the diameter of the nozzle designed for extruding the CCF filament respectively. As the initial diameter of the printing tow is equal to 380 µm, as shown in Table 22 and Figure 94a, it can be deduced that the CCF filament is significantly flattened during printing.

The previously described micrograph is magnified in Figure 94b. In this image, the limits between layers and between adjacent beads are highlighted with horizontal and vertical red dashed lines respectively. Different types of voids can be distinguished in the printed part as a function of their morphology and formation mechanism. Elongated voids located in the interlayer regions (“inter-layer voids”) can be seen in Figure 94b. Large and irregularly shaped voids are frequently observed in the interfaces between adjacent beads (Figure 94b) and thus are referred as "inter-bead voids". These types of voids are the consequence of an incomplete joint between layers and adjacent beads respectively. Image

analysis reveals that inter-beads voids count for about ⅘ of the total amount of porosity in the printed composite. However, it can be noticed their distribution is not homogeneous because the amount of voids varies from one interface between two beads to the other (Figure 94a and 94b). Tiny voids with nearly circular shape are also visible in a magnified image detailing the microstructure of each printed bead (Figure 94c). The origin of these pores, named as "intra-bead voids" in Figure 94c, is still under debate in the literature [204,206,208]. By the author knowledge, the incomplete matrix impregnation in fibers rich areas of the as received filament likely explains the creation of these small voids [204,208]. Otherwise, the relaxation of CF bundles immediately after filament extrusion has also been proposed as formation mechanism [206]. The microstructure of each printed bead resembles that of the raw filament (Figure 90a). In fact, regions with high fiber concentration are alternated to areas where polymer is largely prevalent (Figure 94c), thus leading to a non-homogeneous fiber distribution in the printed part. Comparable morphological characteristic of the longitudinal PA/CCF composites in terms of beads dimensions, appearance of poor interfaces between layers and adjacent beads as well as voids content and distribution were also found in literature [156,204,206,208]. Moreover, although some hardware differences exist between FFF printing of short and continuous fibers composites (e.g., filament nature, shape of the extrusion nozzles, printing strategy), the microstructural features of the printed parts and the processing defects (including wall and infill region, layer-by-layer appearance, filament flattening upon printing and voids types and distribution) are quite similar.

The comparison between the morphology of the CCF filament before printing, where the only relevant defect corresponds to an uneven distribution of the fibers in the polymer resin (Figure 90a), and the final composite microstructure (Figure 94) indicates that the voids content is significantly higher for the printed samples. A closer look into the consolidation mechanism typical of material extrusion AM processes is needed to explain why these voids are considered an intrinsic defect of continuous carbon fiber composites produced by CFF. In this AM process, material consolidation occurs by the creation, softening and growth of the contact surface between contiguous beads. This phenomenon, schematically depicted in Figure 95a, fairly resembles the welding process between polymer interfaces [26]. The filament that has just exited the nozzle reheats or even re-melts the material that was previously deposited. At this moment, a contact area between adjacent beads is created by wetting (1 in Figure 95a). The contact surface softens due to heat diffusion, thus promoting the growth of a neck at the interface (2 in Figure

95a). During neck growth, the polymer chains starts to diffuse from one bead to the other, until they randomize thus creating a strong interfacial bond (3 in Figure 95a) [25,26]. However, the lack of pressure and the high temperature variations that occur when the filament is laid down on the previously deposited material increase polymer viscosity. This reduce molecular mobility, thus preventing the coalescence of the contact surfaces with consequent creation of voids (Figure 95a). This trait highly differentiates AM from conventional processing methods of continuous fiber laminates, where temperature, pressure and time are precisely controlled to enhance material consolidation and minimize porosity content between 0.1 and 1% [201] [305–308].

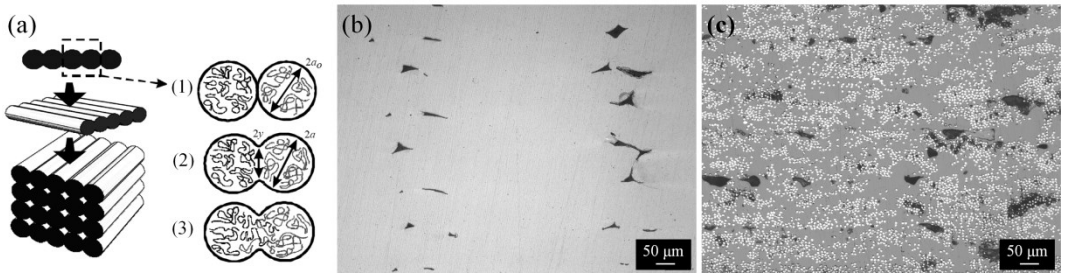

Figure 95: (a) Graphical illustration of the consolidation mechanism between adjacent filaments in FFF/CFF printing: (1) initial contact surface between contiguous beads, (2) neck growth and (3) chain diffusion and randomization. Optical micrographs of (b) neat PA and (c) longitudinal PA/CCF composites samples. Figure 95a was adapted from [26]

Moreover, significant differences can be noticed between neat polymer and continuous fiber reinforced composite parts produced with the same printing system (Figure 95b and 95c). Neat PA reveals triangularly shaped voids between contiguous beads (Figure 95b). These triangular gaps are created because the bottom part of the deposited beads flattens upon contact with the previous layers, while the top part cools in air shaping round edges. No other voids are present in the printed part and the interlayer limits are not visible (Figure 95b). In PA/CCF composites triangular gaps disappears due to a decrease in die-swell and increase in thermal conductivity of the reinforced filament (Figure 95c). However, the overall porosity is significantly higher (≃11%) and exhibits irregular shape and size (Figure 95c). In fact, the consolidation between beads is hindered by the high T_g of the amorphous polymer matrix embedding the fibers and the anisotropic properties of the fibers themselves. In fact, different studies on the thermal history during the CFF printing process of carbon fiber polyamide composites proved that the extruded beads are rapidly cooled below the glass transition of the polymer

(Table 23) [208,219]. Only three layers underneath the newly deposited filament experiences heating above this temperature [208]. This means that the diffusion of the polymer chains is quickly stopped, thus negatively affecting the degree of consolidation between beads and layers. Moreover, the highly anisotropic heat conduction properties of the fibers impedes that the heat flows into the layup and transverse direction, thus promoting the formation of pores. In fact, the thermal conductivity of a single fiber is much higher along its axis (13 W/m·K) compared to the radial direction (1.5 W/m·K) [309–311].

Figure 96 displays typical optical micrographs showing the microstructure of $[0/90]_s$ and $[0/45/90/-45]_s$ samples on the YZ cross section. Panoramic images, obtained by stitching about 50 micrographs, are shown in Figure 96a and 96d. Numerous voids (approximately 11% as estimated by image analysis) are present in both composites, although pore size, shape and distribution differs from the longitudinal samples. It is worth noting that similar porosity values were found for every laminate layup from the density measurements based on the Archimede principle (buoyancy method) and by using equations (14) and (15). Table 25 summarizes the results for the PA/CCF composites and the neat PA samples.

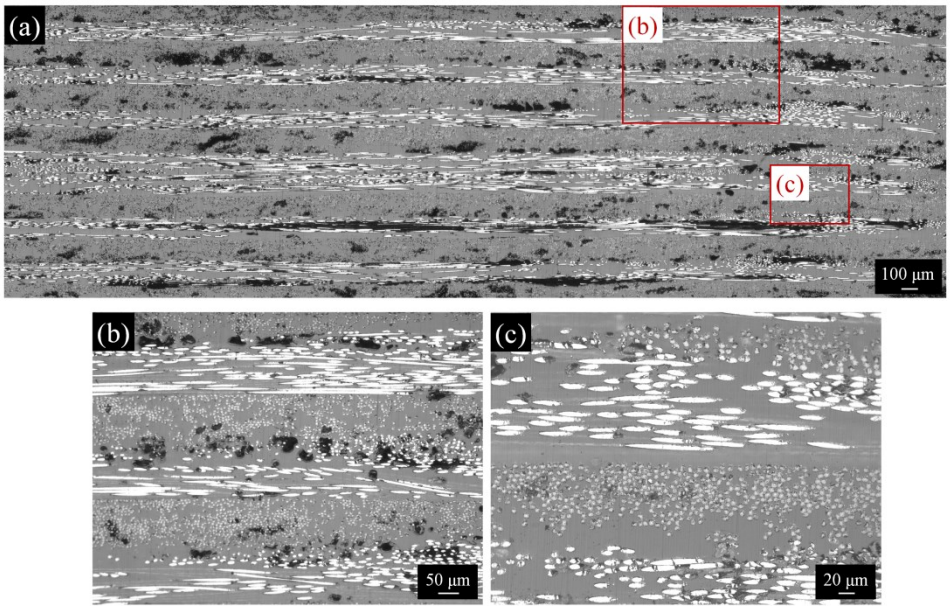

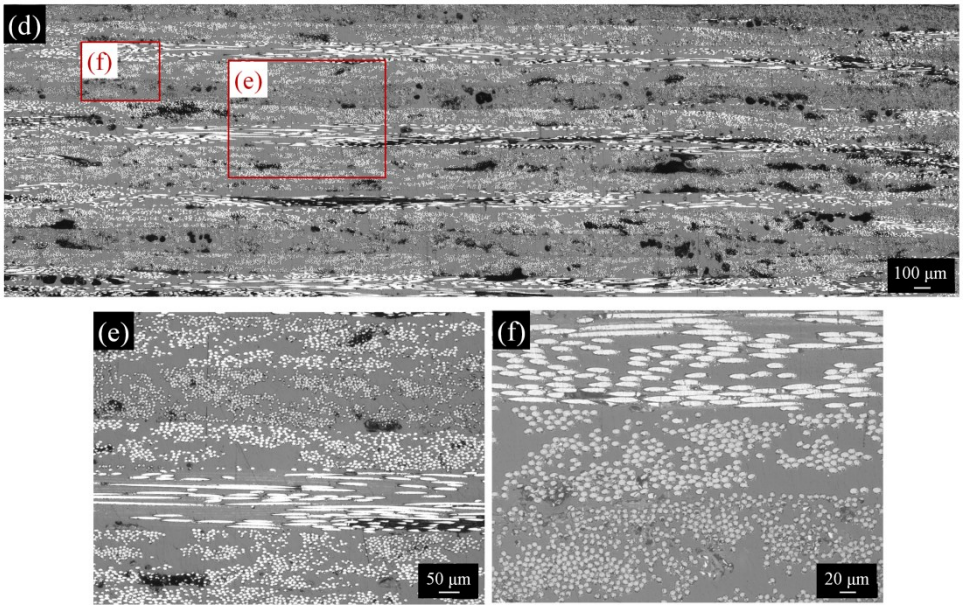

Figure 96: Optical micrographs of the YZ cross-section of (a) cross-ply and (d) quasi isotropic $[0/45/90/-45]_s$ printed parts. Images of the laminate stacking sequence and interlayer voids for (b) $[0/90]_s$ and (e) $[0/45/90/-45]_s$ samples and magnified views in areas inside the extruded beads for (c) $[0/90]_s$ and (f) $[0/45/90/-45]_s$ composites showing irregular fibers distribution and large matrix dominated regions

Table 25: Void content of PA/CCF composites and neat PA samples obtained by image analysis of polished optical micrographs and buoyancy method (density measurements using Archimede balance)

Sample notation	Void (%) image analysis	Void (%) buoyancy
neat PA	1.0	1.1
PA/CCF [0]	11.1	10.4
PA/CCF $[0/90]_s$	11.1	10.9
PA/CCF $[0/\pm60]_s$	11.6	11.4
PA/CCF $[0/45/90/-45]_s$	11.3	11.5

The ply stacking sequence typical of the different layups adopted are easily distinguished from the magnified micrographs of the YZ cross section for $[0/90]_s$ (Figure 96b) and $[0/45/90/-45]_s$ (Figure 96e). The fibers are oriented according to the layup sequence, as shown by the variation of the shape of the cross section in each layer. Interlayer voids can also be seen in the microstructure (Figure 96b and 96e). Higher magnification images in areas inside the printed beads for $[0/90]_s$ and $[0/45/90/-45]_s$ laminates (Figure 96c and 96f) indicate that the microstructure is not homogeneous due to the appearance of regions with high content of carbon fibers or polymer matrix, as already seen in the longitudinal composite (Figure 94c). Finally, few voids arising the intrinsic porosity of the CCF filament are visible inside each layer.

As already mentioned, the shape and distribution of the voids are strongly affected by the laminate layup (Figure 94 and Figure 96). The irregularly shaped voids located mainly between adjacent beads in the [0] composite (Figure 94) are replaced by elongated pores in the interlayer limits in the other layups (Figure 96). The difference in the morphology and distribution of voids can be attributed to the fact that the temperature profiles and residual strains generated during the CFF process highly depend on the laminate layup, as measured by Kousiatza et al. [219] through fiber Bragg grafting sensors and thermocouples embedded in the middle plane of PA/CCF composites produced with the same printer used in this thesis. The authors observed "in-situ" the temperature history of the building process of unidirectional (continuous carbon fibers oriented at 0°) and biaxial layups (±45°), reported in Figure 97 [219].

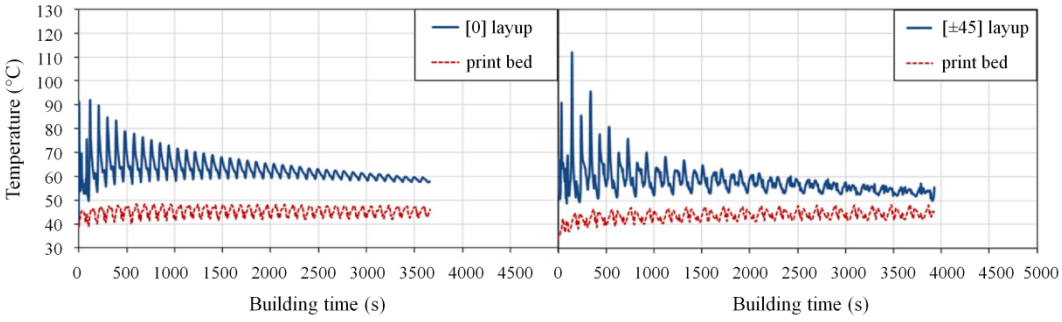

Figure 97: Temperature profiles of the middle plane of continuous carbon fiber reinforced polyamide composite samples with [0] and [±45] layups developed in the CCF process [219]

By comparing the temperature histories of the two laminates it is clear that the smooth and gradually declining temperature profile typical of the longitudinal part

give way for high temperature fluctuations in [±45] layup (Figure 97) [219]. Specifically, the rapid drop of temperature that occurs during biaxial composite printing indicates that complex laminates, including [0/90] and quasi-isotropic layups, likely undergo different thermal conditions during processing (i.e., lower temperatures for longer time periods) with respect to longitudinal laminates (Figure 97) [219]. Therefore, the neck growth and the diffusion of PA chains between layer interfaces are reduced, thus leading to the creation of large interlayer voids (Figure 96). Au contraire, [±45] parts exhibit higher temperature in the first printed layers (Figure 97) [219]. In fact, the distance travelled by the extruders to repeatedly deposit adjacent reinforced beads with an angle of 90°, 60° or 45° with respect to 0° is shorter due to the sample geometry. The higher initial temperatures help the contiguous bead to again soften by joining with the last extruded filament. This in turn result in enhanced bonding and less voids in the interbeads regions (Figure 96) with respect to [0] laminates (Figure 94).

4.3.3 Mechanical properties

The different tensile behaviour of PA/CCF composites and neat PA samples are evidenced by examining the stress-strain graphs reported in Figure 98a.

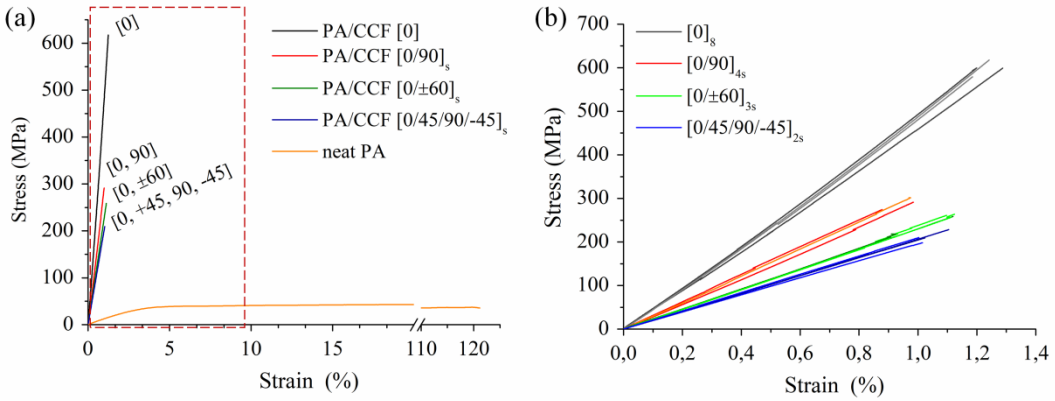

Figure 98: (a) Typical strain-stress curves of PA/CCF laminates with various layup and neat PA sample and (b) magnified graph showing the tensile curves of the PA/CCF printed samples only

Pure polyamide exhibits a typical ductile behaviour with very high elongation at break (≃120%), but poor stiffness and strength characteristics. Conversely, the stress-strain curves of PA/CCF composites show linear elasticity until brittle failure at low strain values irrespectively of the layup adopted, as highlighted in Figure 98b. This mechanical response is similar compared to single CCF tow

(Figure 93b). Moreover, PA/CCF composites display a slight increase in elastic modulus at increasing applied load because the fibers tend to straighten in the loading direction during the tensile test. This phenomenon is commonly observed in continuous fiber laminates processed both by additive and conventional technologies [208,312]. The measured mechanical properties and standard deviations are listed in Table 26. Since the volume fraction of fibers (V_f) is an important indicator to evaluate the properties of composites, these values are also reported in Table 26. For each laminate layup, V_f can be determined by using equation (54):

$$V_f = \left(\frac{V_{CCF}}{V_{composite}}\right) V_f^{CCF} \quad (54)$$

where $V_{composite}$ is the total volume of the printed sample, V_{CCF} is the volume (in cm^3) of CCF filament used for printing the sample (Table 6) and V_f^{CCF} is the volume fraction of fibers of the CCF filament itself derived by using equation (46).

Table 26: Tensile properties of neat PA and PA/CCF composites with various layups. The volume fraction of carbon fibers (V_f) for each layup is also reported. The slight deviation in fiber content between longitudinal and other layups is related to the different thickness of the tensile samples recommended by ASTM D3039 standard

Sample notation	Elastic modulus (GPa)	Tensile strength (MPa)	Elongation at break (%)	V_f (%)
Neat PA	1.64 ± 0.11	43.3 ± 0.3	115.5 ± 36.8	-
PA/CCF [0]	48.34 ± 2.11	597.8 ± 16.4	1.2 ± 0.05	26.4
PA/CCF $[0/90]_s$	29.82 ± 4.79	294.4 ± 15.4	1.0 ± 0.13	29.5
PA/CCF $[0/\pm60]_s$	23.09 ± 0.16	250.4 ± 21.7	1.0 ± 0.04	29.9
PA/CCF $[0/45/90/-45]_s$	20.60 ± 0.80	211.6 ± 12.5	1.1 ± 0.10	30.1

As shown in Table 26, the longitudinal composite has the highest mechanical properties (E=48.3 GPa and σ=597.8 MPa). In fact, the fibers are oriented in the loading direction and can effectively bear the applied stresses. The stiffness and strength at break values are highly improved compared to the neat polymer (29-fold and 13-fold enhancement respectively, Table 26) and are similar to those disclosed in several literature studies for PA/CCF composites with similar fibers V_f and internal structure (i.e., presence of roof/floor layers and walls of pure PA) [202–204,210,213,313]. As observed in conventional laminates, the mechanical properties decline for $[0/90]_s$ and quasi-isotropic layups (Figure 98b and Table 26). In fact, the tensile response of the composites strongly depends on the laminate stacking sequence because the angled plies could not effectively bear the stresses applied during uniaxial tensile tests. Specifically, a reduction in stiffness equal to 38% and 57% for $[0/90]_s$ and $[0/45/90/-45]_s$ composites respectively with respect to [0] parts was reported (Table 26). A slightly higher decrease of strength at break (50% and 64% for the same layups) was observed (Table 26) as a result of the poor transverse and interlaminar strength of the printed parts [206,208,216].

The macroscopic characteristics of the tensile fractured surface of PA/CCF composites and their failure mechanisms were studied by stereomicroscopy analysis (Figure 99). The micrographs were obtained by stitching 4 different images with 8x magnification. Distinct failure modes can be easily distinguished by examining the micrographs. The longitudinal composite exhibits a step-like fracture with the appearance of horizontal and vertical cracks resulting from tensile stresses. The main failure mechanisms identified are fibers rupture and pull-out (Figure 99a). These features are typical of laminated composites with longitudinal fibers manufactured either by additive or traditional methods [203,214,312]. The $[0/90]_s$ laminate displays the smoothest fracture surface, that is perfectly perpendicular to the loading direction (Figure 99b). The failure likely starts due to transverse matrix cracking in 90° plies and layers delamination between 0° and 90° plies (Figure 99b). Afterwards, at higher applied loads cracks develop also in 0° plies until ultimate fracture by fibers breakage and pull-out (Figure 99b). This failure mechanism affects the surface fracture morphology, that presents a slight stair-like facet visible in the lower portion of the sample (Figure 99b).

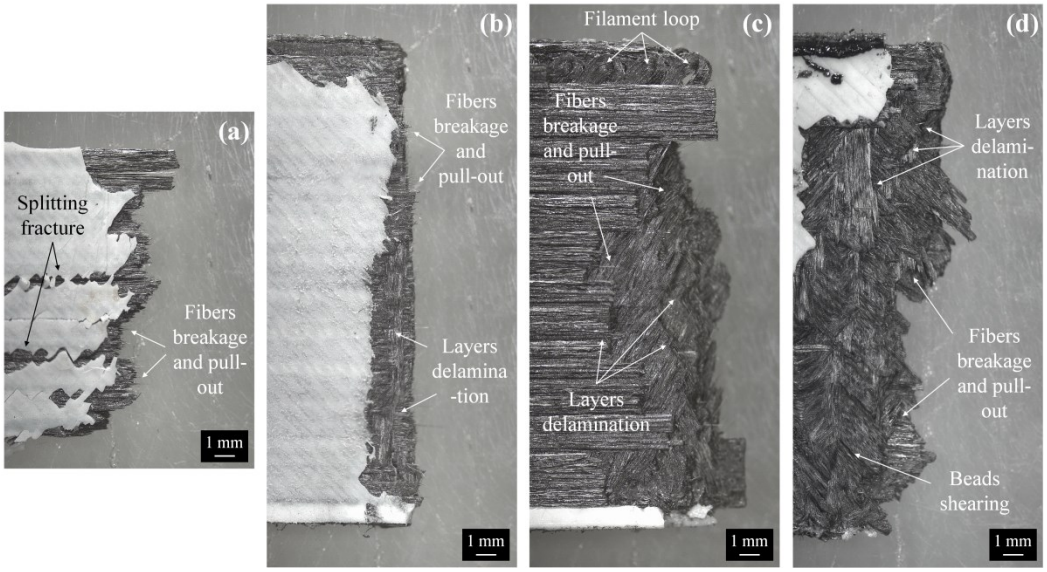

Figure 99: Macroscopic images of the fractured surfaces of PA/CCF laminates: (a) $[0]$, (b) $[0/90]_s$, (c) $[0/\pm60]_s$ and (d) $[0/45/90/-45]_s$. Different failure mechanisms including fibre breakage and pull-out, beads shearing and interlayer delamination are outlined in the figure

Differently, the fracture surfaces of the quasi-isotropic laminates are highly irregular (Figure 99c and 99d). The failure modes abruptly change from fibers to interlaminar rupture due to poor interlayer bonding and the complex layup of these laminates. The main failure mechanisms identified are shear rupture at bead-bead interface, delamination between layers and fibers pull-out (Figure 99c and 99d). Finally, filament loops on the upper perimeter of the $[0/\pm60]_s$ part can be observed in Figure 99c). These loops are created by the sharp turn of the extruder head at the part edges and can be considered intrinsic defects of the additive process [156,204].

A detailed view of the surface fracture PA/CCF composites was obtained by FESEM analysis (Figure 100). The micro-scale failure morphology of the longitudinal laminates is characterized by extensive fiber breakage and pull-out (Figure 100a). The applied stresses are efficiently transferred from the polymer to the reinforcement phase so that the failure is mainly controlled by fibers and higher mechanical strength could be achieved. The surface of the pulled out fibers is partly coated with polymer residues, suggesting a good interfacial bonding (Figure 100a). Polymer fracture is also visible in the FESEM micrograph (Figure 100a).

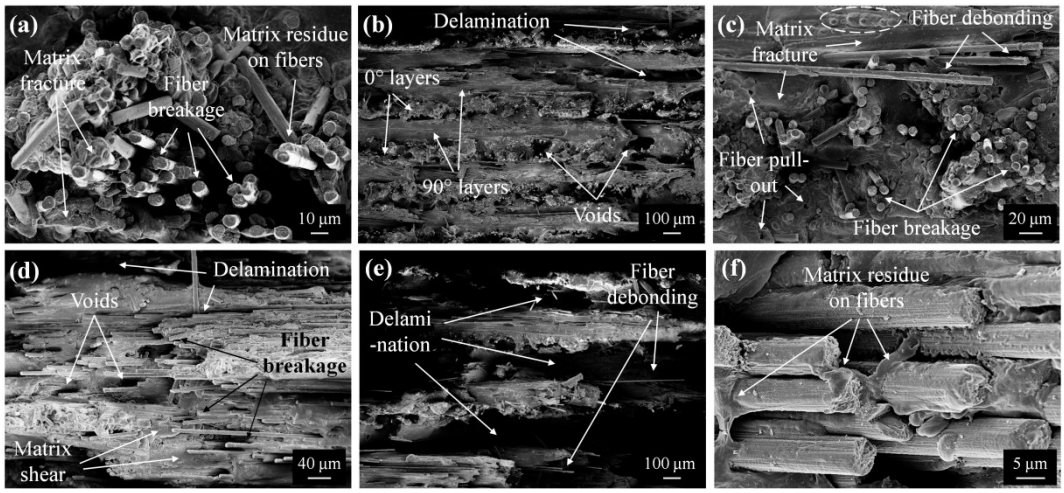

Figure 100: FESEM images the surface fracture of PA/CCF laminates: (a) [0], (b,c) $[0/90]_s$, (d) $[0/45/90/-45]_s$ and (e,f) $[0/\pm60]_s$ $[0/45/90/-45]_s$. Fibers breakage and pull-out, fibers debonding, polymer matrix deformation and failure as well as layers delamination are highlighted in the micrographs

The fracture surface of the cross-ply laminates is defined by a periodic structure consisting of 0° and 90° layers which are repeatedly alternated, as typical of $[0/90]_s$ layups (Figure 100b). As already observed from macroscopic analysis (Figure 100b), the fracture surface is rather regular with few voids and delamination zones mainly located in the interlaminar areas. It is worth noting that the failure morphology of 0° and 90° plies highly differs, as highlighted by the high magnification FESEM image in Figure 100c. The transverse plies, where the fibers are oriented at 90° with respect to the loading direction, reveals a smooth fracture surface with localised matrix failure regions and extensive fibers debonding (Figure 100c). The surface of the debonded fibers has only few polymer residues on it. Some micro-hills, indicating the plastic deformation of the polymer, are also visible in the fractured surface in the regions with higher polymer content (dashed circle in Figure 100c). This suggest that matrix failure along with fiber/matrix detachment are the failure mechanisms that occurs of 90° layers. Differently, the fracture surface of the longitudinal plies is more irregular. The carbon fibers are either embedded in the polymer matrix, broken by tensile loading or pulled-out from the fracture surface (Figure 100c). Therefore, 0° layers fail by fibers rupture and pull-out, thus suggesting higher load bearing capability.

The fracture surfaces of the quasi-isotropic laminates (Figure 100d and 100e) are characterized by large delamination regions at the interface between layers, matrix shear deformation and fibers debonding. These microscopic fracture

morphologies are behind the macroscopic interlaminar failure mode of these composites observed in Figure 99c and 99d. However, it seems that a good fiber/matrix interfacial adhesion exists also in off axis plies, as revealed by the presence of polymer residues attached to the fibers surfaces (Figure 100e).

4.3.4 Prediction of mechanical properties

Table 27 summarizes the elastic and strength properties of neat PA matrix and CCF reinforced plies, that were adopted for applying the Classical Laminate Theory (CLT) approach described in Section 3.3.2. These material constant were derived from literature for both the neat PA [212] and CCF reinforced lamina [208]. In the table, the subscript T and C defines tensile and compressive load cases respectively.

Table 27: Material properties of neat PA and CCF reinforced plies adopted for CLT modeling [208,212]

Material properties	**PA lamina** [212]	**CCF lamina** [208]
Longitudinal elastic modulus – E_1 (GPa)	0.94	69.4
Transverse elastic modulus – E_2 (GPa)	0.94	3.5
In-plane shear modulus – G_{12} , G_{23} (GPa)	0.34	1.9
Poisson's ratio – ν_{12}	0.4	0.41
Axial strength in tension – σ_{1T} (MPa)	54	905.3
Axial strength in compression – σ_{1C} (MPa)	44.1	426
Transverse strength in tension – σ_{2T} (MPa)	10.8	17.9
Transverse strength in compression – σ_{2C} (MPa)	44.1	66
Shear strength in tension – σ_{1S} (MPa)	48	43.4

Since the printed parts consists of PA wall and CCF infill regions (Figure 51), the elastic modulus and strength of the laminates was calculated by combining CLT results with the rule of mixture to model the contribution of the nylon perimeter surrounding each layer by using equations (39) and (40) respectively.

Comparison of modeling results with experimental data

The values of the mechanical properties of the PA/CCF composites calculated using the CLT analysis and the relative modeling errors (%) are reported in Table 28 along the experimental results of the tensile tests.

Table 28: Elastic modulus and tensile strength of CCF/PA composites obtained by using CLT analysis. The relative error against the experimental data (%) is reported in brackets

Laminate layup	**Experimental**		**CLT analysis**	
	E (GPa)	**σ (MPa)**	**E (GPa)**	**σ (MPa)**
[0]	48.3	597.8	49.5 *(2.5%)*	651.1 *(8.1%)*
$[0/90]_s$	29.8	294.4	30.5 *(2.3%)*	271.8 *(-8.3%)*
$[0/\pm60]_s$	23.1	250.4	21.8 *(-5.9%)*	257.4 *(2.7%)*
$[0/45/90/-45]_s$	20.6	211.6	21.5 *(4.4%)*	211.3 *(-0.1%)*

A very good agreement was obtained between the predicted and experimental elastic modulus, as the modeling error is equal to 2.3% in the best case and 5.9% in the worst case, corresponding to the [0] and $[0/\pm60]_s$ respectively (Table 28). Similar predictive accuracy was achieved for strength at break, although slightly higher discrepancies can be seen for the longitudinal and cross-ply layups (Table 28). Nevertheless, the modeling error does not exceed 8.3%. Comparable results were found by Polyzos et al. [232]. The authors combine CLT analysis with common micro-mechanical and void models to predict the Young modulus of 3D printed PA/CCF laminates with cross-ply, quasi-isotropic and angled-ply layups with an error of 5-6%. The elastic modulus of the longitudinal layup was estimated with higher accuracy (0.4%) in [215] by performing CLT analysis

through the use of LAP software. However, it is worth noting that most of the published works reported to date [215,230–232] are focused on the elastic properties only.

The good predictive accuracy obtained by CLT analysis (Table 28) implies that the hypothesis of using the RoM to take account of the effect of the neat PA wall on the laminate properties is fairly accurate. The combination of CLT and RoM offers great flexibility because different internal layups and materials can be taken into consideration by the proposed model. As a result, it could be applied to complex layups designed for specific applications (e.g., parts including more than one perimeter wall or alternating layers of neat polymer, short and continuous fiber reinforced materials). Moreover, CLT has other significant advantages related to its formulation. Progressive ply failure analysis based on common failure theories (e.g., Maximum stress, Maximum strain, Tsai-Hill, Tsai-Wu, etc.) can be performed to determine the tensile strength and fracture mechanism of a fiber reinforced laminate. In fact, the mechanical response of the laminate can be evaluated after one or more plies have failed. Multi axial loads can also be applied to investigate how the composite will behave under complex stress conditions similar to those observed in real-life structural applications.

In conclusion, the overall results showed that CLT, which is commonly employed for evaluating a priori the stiffness and strength of traditional laminates, is an effective predictive method for PA/CCF composites produced via additive manufacturing too. Therefore, this model can be easily adopted by engineers to effectively design 3D printed carbon fibers reinforced laminates for specific loading conditions and exploit the design freedom and flexibility given by this technique. For example, the ratio between fiber reinforced and neat polymer filaments as well as the orientation and pattern of the fiber reinforced regions can be adjusted layer by layer.

4.4 Conclusions

It is worth noting that the comparison between the investigated AM techniques is not straightforward due to differences in polymer matrices' nature and carbon fiber content. However, some technological limitations related to the type of 3D printers used have limited the choice of materials. In fact, among polyamides, Sharebot SnowWhite SLS printer is able to process only PA12 and PA11 powders due to limitation in the maximum powder bed temperature achievable and the absence of an inert gas environment during printing. Moreover, MarkTwo CFF

printer is a closed system and only the materials supplied by the machine vendor can be processed (in this case a pure PA6 filament as matrix material and a pre-impregnated continuous carbon fiber filament made of a polyphthalamide matrix reinforced with a fixed amount of fibers). Nevertheless, typical features of the different additive technologies, such as the amount and distribution of voids, the orientation of the fibers, the effect of printing strategy on mechanical properties and the validity of predictive models for the estimation of the elastic modulus and tensile strength of the printed part can be effectively analyzed.

Chapter 5

Comparison between AM and traditional technologies

5.1 Microstructure

5.1.1 Short carbon fiber reinforced polymer composites

Figure 101 shows the typical microstructure of short carbon fiber reinforced polymer (SCFRP) composites produced by additive and traditional manufacturing techniques, including Fused Filament Fabrication (FFF), Selective Laser Sintering (SLS), injection molding (IM) and compression molding (CM). It can be noticed that FFF samples exhibit a high amount of porosity due to the inherent nature of material extrusion AM processes, that cannot guarantee an adequate bonding between the extruded filaments (Figure 101a). Differently, the void content in samples produced by SLS can be minimized through the optimization of laser process parameters (see Section 4.1.2), although some small pores resulting from incomplete particle coalescence can be detected in the optical micrograph (Figure 101b). By contrast, compression molded (Figure 101c) and injection molded (Figure 101d) samples shows no visible porosities as shear and compressive stresses applied during manufacturing inhibit voids formation (Figure 101d).

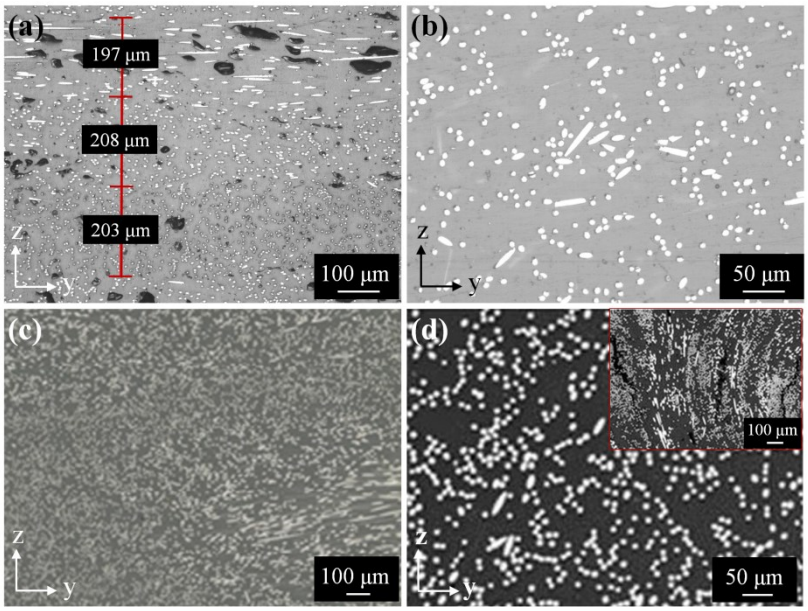

Figure 101: Microstructural differences between SCFRP composites produced by additive and conventional manufacturing techniques: (a) PA6/CF part printed by FFF, (b) PA12/CF part printed by SLS, (c) ABS/CF part produced by compression molding (CM) and (d) PA66/CF part produced by injection molding (IM). Optical cross sections of AM parts were obtained in this thesis, while CM and IM samples are reproduced from [314] and [176] respectively

Another significant difference between the adopted AM technologies and traditional processing techniques refers to the orientation of carbon fibers inside the polymer matrix. FFF process has the ability to produce SCFRP composites with highly oriented fibers as a result of both feedstock filament microstructure and AM processing characteristic (i.e., extrusion of filaments through a heated nozzle). Tekinalp et al. [176] demonstrated that 91.5% of fibers are oriented in the printing direction. Moreover, by changing the bead orientation layer by layer it is possible to obtain parts with fibers aligned in different directions according to simple or more complex layups resembling those obtained in conventional laminates reinforced with continuous fibers (Figure 101a). This feature is peculiar of material extrusion AM techniques [1,20,26]. In SLS-processed samples the fibers are mainly in-plane distributed inside a layer due to the mechanical action of the recoating system. In fact, very few fibers are oriented along the building direction (i.e., z-axis) because the blade/roller is capable of aligning the fibers in the plane of the powder bed of the SLS machine (i.e. x-y plane) during the deposition of a fresh layer of powders. Here, most fibers (57%) are aligned in parallel to the recoater movement or x-direction (i.e., circular cross sections in (Figure 101b) while others exhibit a random in-plane orientation (Figure 101b).

Therefore, in SCFRP composites produced by SLS the fibers are always arranged in a similar fashion (i.e., preferential orientation in the recoater moving direction) regardless of the printing parameters and scanning strategy adopted [35,147,271]. Therefore, higher stiffness and strength are expected along the recoating direction. Although it has been proved that layer thickness slightly affects the degree of fibers alignment [35], their orientation distribution and the consequent anisotropy in mechanical behaviour cannot be easily optimized as it happens in FFF.

For conventional technologies, it can be seen that the composite samples produced by CM display an almost random orientation of fibers in the polymer matrix (Figure 101c). However, a partial fiber alignment in the mold plane (i.e., x and y-axis) occurs (Figure 101c) because the material flows in these directions during processing due to application of the external pressure [176]. Similarly, in injection molded samples the fibers are mainly aligned along the flow direction due to the high shear stresses applied during mold cavity fillings (Figure 101d). However, the complex flow path generated during the filling stage usually results in preferential fiber orientation that differs from core and shell/skin regions of the mouldings (i.e., transversely and longitudinally aligned to the flow direction respectively) and sometimes vortexes with randomly oriented fibers can be created at the mold edges [314].

Table 29 reports the fiber orientation tensor components of different short fiber reinforced composites processed by AM and traditional technologies found in literature [35,147,176,271]**.** The reported data quantitatively validates the previous microstructural observations. A high ratio of fiber alignment can be obtained only by FFF, while in compression molded samples the fibers are randomly oriented in the three spatial directions. An intermediate behaviour was found for specimens manufactured using injection molding and SLS techniques, that offers a partial fiber orientation in the polymer flow and recoater moving direction respectively.

Table 29: Comparison between the components of the fiber orientation tensor of short fiber reinforced composite manufactured using different additive and conventional technologies (a_{11} , a_{22} and a_{33} correspond to the x, y and z direction respectively). The cited studies refer to carbon fiber filled ABS (ABS/CF), carbon fiber filled PA12 (PA12/CF), glass fiber filled PA6 (PA6/GF) and glass fiber filled polybutylene terephthalate (PBT/GF) composites

Technology	α_{11}	α_{22}	α_{33}	Ref.
FFF (ABS/CF)	0.91	0.03	0.06	[176]
IM (PBT/GF)	0.62	0.30	0.07	[271]
SLS (PBT/GF)	0.50	0.35	0.15	[271]
SLS (PA12/CF)	0.5-0.6	0.3-0.4	0.05-0.15	[147]
SLS (PA6/GF)	0.49-0.58	0.28	0.18	[35]
CM (ABS/CF)	0.38	0.39	0.22	[176]

5.1.2 Continuous carbon fiber reinforced polymer composites

Similar observations can be carried out by examining the microstructural defects of continuous carbon fiber reinforced polymer composites (CCFRP) composites prepared via additive manufacturing (AM), Automated Tape Placement (ATP) and more conventional methods like autoclave process or hot compression moulding (HCM). The differences between the microstructure as well as the void content and distribution in continuous carbon fibers reinforced thermoplastic laminates obtained by using these techniques are illustrated in Figure 102.

As already discussed in section 4.3.2, AM of continuous fiber composites leads to the formation of process-induced defects in the printed parts such large voids between layers and beads and poor interlayer bonding (Figure 102a). PEEK based laminates (e.g., AS4 carbon fibers/PEEK) processed by ATP also exhibit some voids in the interlaminar areas due to a partial consolidation between the laid prepreg tapes (Figure 102b). The same material processed using autoclave (pressure of 6.5 bar at 385 °C for 3h [305]) appears free of porosities (Figure 102c).

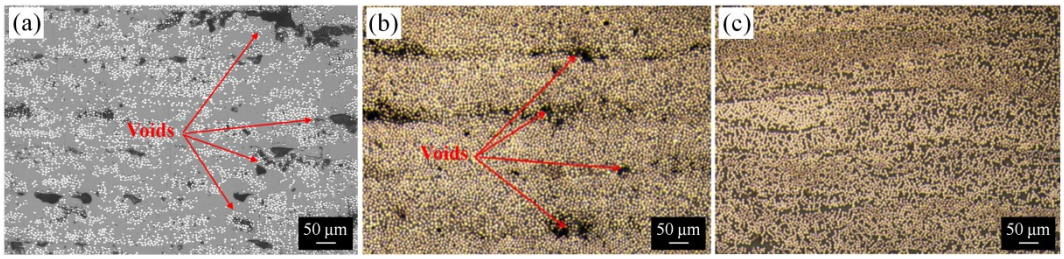

Figure 102: Typical microstructure and voids of unidirectional (a) PA/CCF laminates obtained by AM, (b) PEEK/CCF laminates prepared via Automated Tape Placement and (c) PEEK/CCF laminates manufactured by using autoclave technology. YZ cross sections, perpendicular to the fiber direction, are captured by optical microscopy for PA/CCF and reproduced from [305] for PEEK/CCF

These microstructural differences are related to the consolidation mechanism typical each technology. In material extrusion AM the absence of compaction forces and the temperature history (i.e., quick cooling below glass transition of the polymer matrix) inherent in the layer by layer printing process hinder the complete sintering and thermo-mechanical consolidation of the extruded beads, the both sides and the lower layer [201,206,208]. Therefore, the 3D printed laminates has high void content (11%) (Figure 102a). By contrast, in conventional processes, the consolidation of CCFRP composites occurs through the application of pressure and temperature cycles. In ATP the prepreg material is consolidated under the compressive action of the roller during tape laying. This leads to a lower void content (≃3.5%) [306] compared to the 3D printed part. Some voids at the ply interface are still present (Figure 102b) due to the surface roughness of the thermoplastic tape and the limited processing time above polymer T_m that hinder matrix flow between plies [305,306,315]. In autoclave prepreg technology high external pressure and temperatures (above polymer T_m for long times) and a vacuum environment are used to avoid the formation of defects and enhance the interlaminar bonding between plies. Apart from compression, other key mechanisms of void reduction like diffusion, coalescence and bubbles removing occurs in the autoclave oven [306]. Accordingly, the porosity is very low (<0.1%) [305,306] and laminates with the highest mechanical performances can be manufactured for primary load-bearing structures. However, it is worth noting that voids created by air bubbles entrapped in the polymer during the manufacturing process could still be found in laminates with complex geometries [308,316].

Differences in fibers distribution and fiber/matrix impregnation between additively manufactured and hot-pressed thermoplastic and thermosetting based laminates can also be evidenced (Figure 103).

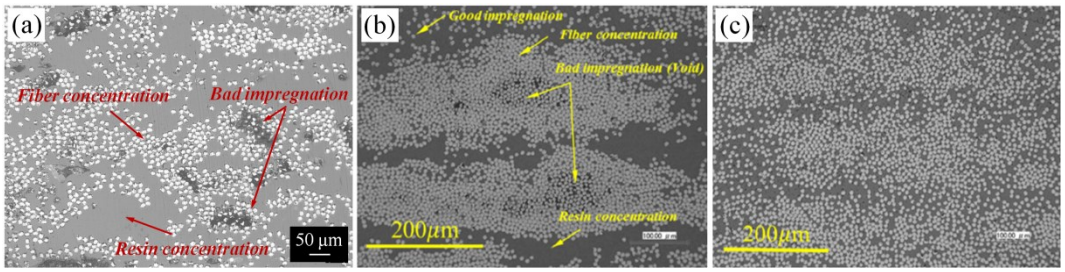

Figure 103: High magnification micrographs of the YZ cross-section of longitudinal (a) PA/CCF laminates prepared by AM and (b) PA6/CCF and (c) epoxy/CCF composites produced by hot compression moulding. Poor fiber impregnation and resin/fiber concentration regions are highlighted. The images of the hot-pressed samples are reproduced from [312]

PA/CCF composites produced by AM show a non homogeneous fiber distribution with large polymer dominated regions and few voids related to the incomplete impregnation of the feedstock filament (Figure 103a). Hot pressed PA6/CCF laminates exhibit an uneven reinforcement distribution too, with fiber agglomeration in a "bundle-like" shape alternated to regions with high resin concentration. Moreover, poor fiber/matrix impregnation can be observed in limited areas within the fiber bundles (Figure 103b). These defects fairly resemble those observed in additively manufactured parts, but in a much lesser amount due to the effect of pressure and temperature applied in HCM processing [200,201,206,315]. Differently, hot-pressed epoxy/CCF composites reveal a defect-free microstructure with uniform distribution of fibers (Figure 103c). This difference is likely due to the fact that epoxy resins have lower viscosity compared to polyamides and thus a better impregnation of the fiber bundles during prepreg and composite production is obtained [312].

5.2 Mechanical properties

Figure 104 provides a graphical overview of the tensile modulus and strength of short and continuous carbon fibers reinforced composites produced by additive and conventional technologies, based on data reported by various studies in literature (Table A1 and A2 in the Appendix section). A wide range of mechanical performances is illustrated in the Ashby plot as a result of different fiber type and content, microstructural characteristics as well as processing technique adopted. The results obtained in this thesis (outlined by fill symbols) are in-between those reported in literature for the same AM technology (Figure 104).

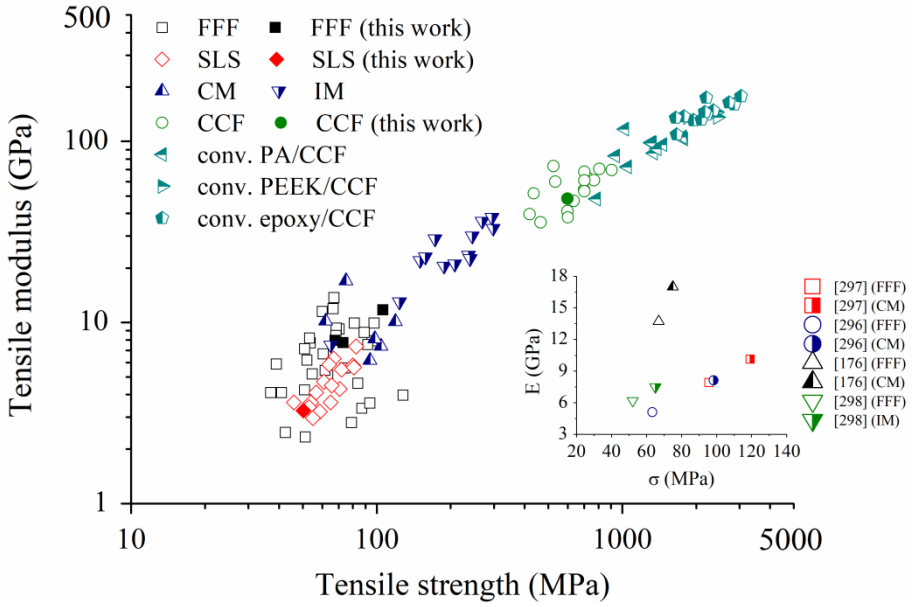

Figure 104: Tensile strength/stiffness plot for short and continuous carbon fibers reinforced polymers produced by additive and conventional technologies. Legend for SCFRP composites: FFF (Fused Filament Fabrication), SLS (Selective Laser Sintering), IM (injection molding) and CM (compression molding). For CCFRP composites the data include longitudinal PA/CCF composites processed by CFF (MarkForged® Continuous Filament Fabrication) and continuous carbon fibers/polyamide (PA/CCF), continuous carbon fibers/PEEK (PEEK/CCF) and continuous carbon fibers/epoxy (epoxy/CCF) laminates processed by conventional technologies such as Automated Fiber Placement, Hot Compression Moulding, autoclave (abbreviated as "conv."). The results obtained in this thesis are shown with solid fill symbols. See Table A1 and A2 for details about all data reported in the figure (E and σ value, author, matrix, fiber V_f). Inset: comparison between similar AM and compression / injection molded SCFRP composites

5.2.1 Short carbon fiber reinforced polymer composites

AM parts reinforced with short carbon fibers show good mechanical properties. It can be seen that the elastic modulus and tensile strength values obtained in this thesis for SLS and FFF composite parts are in good agreement with literature (Figure 104). Overall, values up to 10 GPa and 100 MPa for these properties respectively are reported when high fiber orientation is attained [26]. This observation highlights that FFF could have the potential to manufacture short carbon fiber composites for functional or structural (i.e., low or medium loading conditions) end-user applications. However, a closer look in the published works featuring a direct comparison between AM and compression / injection molded composites with identical composition [176,296–298] shows some differences in the tensile performances of the samples (inset of Figure 104). In fact, a 20%

average improvement of the mechanical properties for PA/CF composites by using conventional technologies can be found by examining these studies (inset of Figure 104). This is likely to be assigned to the higher void content and poorer interlayer and fiber/matrix interfacial bonding in AM parts, that prevails on the fiber orientation effect [176,296–298]. Comparable differences between injection molded and additively manufactured parts were also found for neat polymers [317]. Moreover, the benefits of using short fibers in AM parts (i.e., enhancement of mechanical properties without significantly changing material cost and processing methods) are limited by two other factors:

- fibers length in SLS and FFF materials is usually shorter than the critical length of a carbon fiber in a thermoplastic polymer due to processing constraints. The average lengths of the fibers in 3D printed PA/CF composites studied in this thesis fall below 100 µm (Figure 105), while the estimated critical lengths are 263 µm and 404 µm for FFF filament and SLS powders respectively;
- although composites with high fiber content have been studied [134,142,143,176,318], fibers volume fraction is usually lower than 20 wt.% due to poorer flowing and rheological properties of the material as well as nozzle clogging issues in FFF.

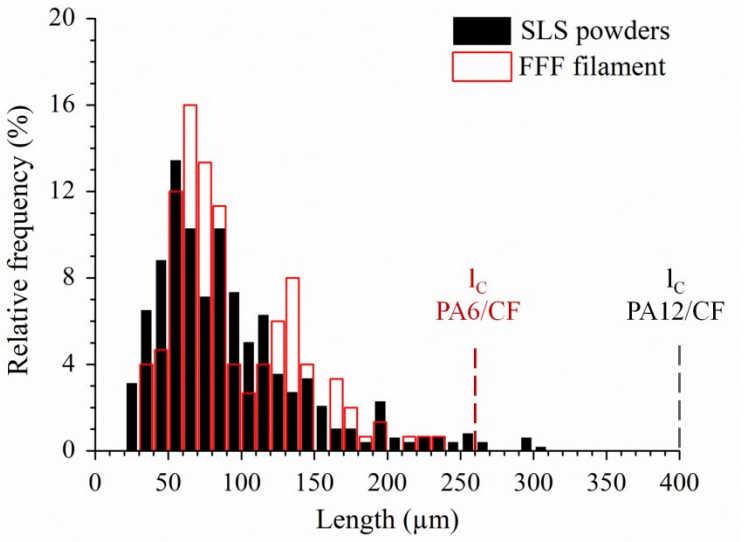

Figure 105: Length distribution histograms of the carbon fibers used in PA12/CF powders for SLS and PA6/CF filaments for FFF technologies. The respective critical lengths estimated using equation (25) are also evidenced

These limitations negatively affect the performances of SCFRP composites produced by AM techniques. In fact, the highest mechanical properties attainable are far inferior compared to injection-molded PA66/CF grades for automotive applications, where fiber length greater than 200 μm and fiber content up to 40 wt.% are commonly employed [314,319–321].

5.2.2 Continuous carbon fiber reinforced polymer composites

AM parts reinforced with continuous carbon fibers show a significant improvement (from 4 to 8 times) of tensile properties compared to short fiber composites (Figure 104). The values obtained in this thesis are similar to those found in literature [202–204,210,213,313] for CCFRP composites produced via MarkForged® printer by using a neat PA sandwich configuration (i.e., roof and floor layers and perimeter wall) and comparable fiber volume fraction (Figure 104). Higher tensile modulus and strength at break were obtained in other studies [195,206,208,209,214,215,322] by eliminating the PA shell before testing to evaluate the mechanical behaviour of 3D printed laminates composed by CCF filament only (Figure 104). In this way, laminates with higher fiber V_f (up to 35%) were obtained. Overall, stiffness and strength comparable to high strength aluminum alloys (E=70 GPa and σ>400 MPa [323]) can be reached, thus opening new possibilities for the adoption of this technology in high load bearing applications. However, the results clearly display that the tensile properties of PA/CCF composites produced by 3D printing remains still lower compared to conventional polyamide-based laminates (Figure 104). Moreover, it can be noticed that continuous fiber reinforced thermosetting composites based on epoxy matrices displays much higher performances (Figure 104). Elastic modulus and tensile strength as high as 160 GPa and 2860 MPa can be obtained by using commercial unidirectional prepregs, such as HexPly® M21/IM7 from Hexcel (Stamford, US) [324]. These materials, processed by autoclave curing techniques, are used as reference because they were specifically developed for load-bearing applications in the aerospace and space industry. Thermoplastic laminates based on high performance polymer matrices such as polyether ether ketone (PEEK) also exhibits higher stiffness and strength compared to the additive manufactured composites, as revelead by Figure 104 (E=140 GPa and σ>2000 Mpa in most cases [325–327]).

Different shortcomings of the MarkForged® CFF process for continuous fiber composites explain this behavior, as described below:

- fibers volume fraction (V_f) is lower compared to conventional laminates. Although the use pre-impregnated filaments with continuous fibers has improved the interfacial bonding between fibers and matrix, it does not provide the flexibility to modify the fiber content. For parts produced using Markforged® printers, V_f is limited by the Eiger™ software settings (i.e., the outer layers and at least one perimeter contour need to be printed with PA filament) and the amount of fibers in the pre-impregnated filament itself (≃36.5 vol.%). The tensile samples produced in this thesis show fiber volume fractions between 26.5% and 30% depending on their thickness (Table 26). The highest fiber V_f (34%) reported in was achieved by removing the PA outer shell after printing [206,208,209,214,215]. Nevertheless, additively manufactured parts show less amount of fibers with respect to traditional laminated made from prepregs (V_f > 50 vol.%). These values are not attainable in AM composites owing to processing constraints and current limitations in the fabrication of pre-impregnated filaments. This largely explain the discrepancies found in the mechanical properties of longitudinal composites, as shown in Figure 106. In the graph the tensile modulus (Figure 106a) and strength (Figure 106b) of additively manufactured and conventional laminates are plotted versus fiber volume fraction.

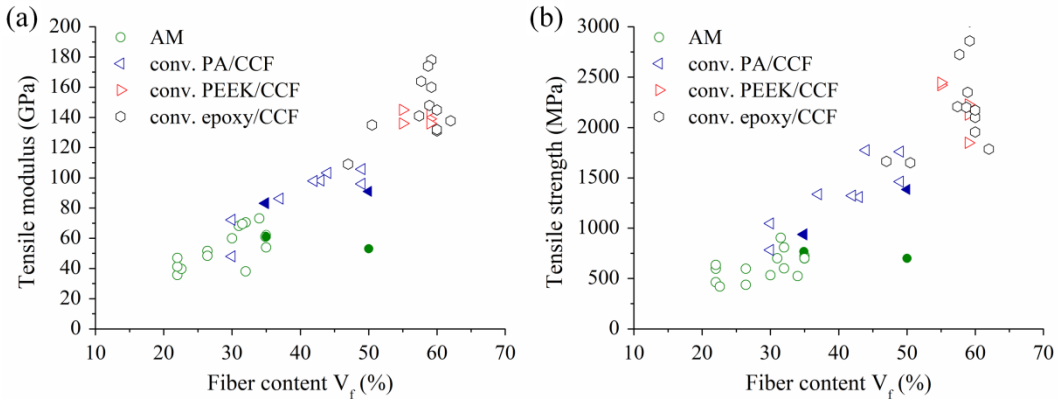

Figure 106: (a) Tensile modulus and (b) tensile strength versus fiber volume fraction of longitudinal continuous fibers reinforced composites manufactured via AM and various conventional techniques. A comparison between same AM and hot pressed PA/CCF composites is outlined in the graphs using solid fill symbols, with tensile properties being different

Although the data are not entirely complied with the rule of mixture due to different fiber type, polymer matrix and manufacturing processes considered, the tensile properties of CCFRP composites increase with

carbon fiber V_f irrespectively of the technology used. However, a detailed literature survey revealed that the stiffness and strength of 3D printed parts are still lower compared to traditional composites produced with the same matrix and fiber content (solid fill symbols in Figure 106) [206,328]. Yamanaki et al. [328] was able to additively manufactured continuous carbon fibers/PA6 composites with a high fiber content (50 vol.%) by using a novel 3D printing system, but the tensile modulus and strength of the 3D printed parts (53 GPa and 701 MPa respectively) remains lower than those obtained after a hot-pressing treatment (91 GPa and 1385 MPa respectively). Similarly, He et al. [206] reported a considerable enhancement of both properties (22% for Young modulus and 36% for strength) by using hot compression molding (HCM) after 3D printing (Figure 106);

- process-induced defects such as high amount of porosity and poor interlayer bonding are inherent in this technique due to the lack of compaction after filament deposition and the fast heating/cooling cycles involved in the printing process. In fact, the void content of additively manufactured parts (≃10%) is much higher with respect to that of laminates fabricated with conventional processing techniques (<1%). The aforementioned defects create stress concentration regions, leading the parts to fail at lower stresses. This observation is proved by the experimental datasets reported in Figure 106. In fact, several authors [206,328] found a significant improvement of the tensile properties by decreasing the void content through HCM (solid fill symbols in Figure 106). In addition, a recent study [329] reported a 145% increase of interlaminar shear strength and 87% reduction of porosity without affecting the dimensional accuracy of the parts using the same post-processing treatment with applied pressure and temperature equal to 1 MPa and 150 °C respectively. Process-induced defects also worsen matrix sensitive properties such as tranverse and in-plane shear strength. As a result, the elastic modulus (in most cases) and tensile strength of PA/CCF laminates with complex layups obtained in this thesis are lower compared to HCM counterparts (Table 30) [330–332]. In fact, delamination between layers and fiber/matrix debonding were observed in the fractured samples (Figure 99c and 99d);

Table 30: Mechanical properties of cross-ply and quasi-isotropic PA/CCF composites produced by CFF and hot compression moulding (HCM)

Laminate layup	Elastic modulus (GPa)	Tensile strength (MPa)	Fiber volume fractions (%)	Ref.
PA/CCF $[0/90]_s$	29.8	294.4	30	this work
	20.0	395.0	30	[330]
	35.4	408.0	40	[331]
PA/CCF $[0/45/90/-45]_s$	20.6	211.6	30	this work
	13.0	232.0	30	[330]
	34.6	540.0	42	[332]
	33.0	536.0	43	[332]

- mechanical properties of the polyamide matrix (PA6I/6T) used in the pre-impregnated CCF filament are inferior compared to those of PEEK and epoxies. Moreover, low or intermediate modulus carbon fibers are commonly used in AM parts [209,210];
- Eiger™ software does not allow to modify some important process parameters. The extrusion temperature (252 °C for the CCF filament) is too low to process high performance polymers such as PEI and PEEK and the layer thickness is fixed at 125 μm.

5.3 Conclusions and outlook

5.3.1 Short carbon fiber reinforced polymer composites

Short fiber composites fabricated by AM techniques exhibit peculiar microstructural and mechanical features that makes them different from conventional counterparts. Fused Filament Fabrication (FFF) grants high fiber alignment in the printing direction, thus maximizing the reinforcement effect of the fibers at the expense of isotropy. Also owing to simplicity of use and the

ability to fabricate highly complex geometries in a single processing step compared to traditional methods, this technique is considered very promising for the development of short fiber composites. Selective Laser Sintering (SLS) offers the possibility to manufacture lightweight composite structures with high geometrical complexity in a cost effective manner in terms of energy and material consumptions. The printed parts exhibit in-plane fiber alignment while the porosity content can be controlled by optimizing the process parameters, including laser power, scan speed and hatch distance as well as layer thickness. However, the mechanical properties of the 3D printed SCRFP composites are still lower compared to injection and compression molded materials (Figure 104) due to limitations in fiber length and volume fraction as well as void content (Figure 105 and Figure 101). The presence of pores notably affects the performance of FFF printed parts which suffer from the poor consolidation between the extruded beads. Moreover, 3D printed fiber reinforced composites usually show poorer impact damage and fatigue resistance compared to traditional parts [11] and anisotropic mechanical behaviour along the different building directions [26,179–183]. Therefore, improvements are needed to meet the stringent requirements for structural applications and metal replacement.

High performance polymer matrices such as polyether ether ketone (PEEK) [141,149,174,279,335], polyetherimide (PEI) [171,333,334] and polyphenylene sulfide (PPS) [171,173,336] has been utilized to enhance the performances of the printed parts due to their outstanding combination of mechanical properties and thermal stability. Although these composites could have the potential to replace low strength aluminum alloys for lightweight structures, the process conditions are more stringent. FFF printers with an enclosed heated chamber and SLS equipment capable of operating at high temperatures (up to 350 °C) are required to process these polymers [53]. Moreover, although FFF apparatus with heated chambers are targeted for high temperature polymers, it has been shown that such a high temperature environment during printing have also great benefits for other polymer grades, such as polyamide 12. In particular, environment temperature higher than the polymer T_g are responsible for a reduction in void content as well as an increase in interlayer bonding and transverse strength of the printed parts [225].

The use of aligned chopped fibers (few mm in length) instead of milled ones (only 100 μm long in most cases) has also been suggested to obtain superior mechanical performances due to a better packing efficiency and load transfer between fiber and polymer matrix [1]. In fact, previous studies found that SCFRP

composites containing fibers above their critical length (equation (25)) could reach mechanical properties up to 85% of continuous fiber counterparts [1]. However, fiber breakage always occurs during filament manufacturing by single or twin screw extrusion, thus leading to a significant reduction of the average fiber length from few mm to 150 μm [176,225]. Therefore, processing methods which preserve the initial fiber length are expected to overcome the limitations of current FFF technique. Processes capable of developing higher pressure (e.g., pultrusion), adding flow enhancing additives or redesigning the nozzle/feed system to decrease the pressure drop during extrusion were suggested as possible solutions [318]. In this context, Krajangsawasdi et al. [337] and Blok et al. [338] proposed an innovative filament manufacturing method, based on a combination between High Performance Discontinuous Fibre (HiPerDiF) technology, manual moulding and pultrusion, to produce round-shaped poly-lactic acid (PLA)/CF tows for 3D printing. Owing to this novel method, the raw filament and a full rectangular layer produced with a commercial FFF printer exhibit highly oriented fibers with sufficient length to result in mechanical properties comparable to continuous fiber reinforced PLA composites [337,338].

Finally, it is worth noting that AM techniques have peculiar advantages over injection and compression moulding when customized components with complex geometry are required. The design flexibility and the ability to produce end parts without using moulds and/or expensive equipments (such as moulding presses) outperform traditional processing methods in specific contexts or when small production batches are needed [13,186]. Prototypes, spare parts, small series production in the automotive, aerospace and customer goods industries as well as jigs, fixtures and manufacturing tools are just a few examples of the current applications of AM of short fiber reinforced polymers [20,23,26]. The unmatched manufacturing freedom and high geometrical complexity of the 3D printed parts can be more easily exploited by using SLS rather than FFF. In fact, SLS does not require support structures to fabricated thin walls and overhanging features because the unsintered powder functions as a support itself during the printing process. Therefore, SLS is particularly suitable for producing interlocking or moving parts, living hinges, lattice structures and other highly complex parts (Figure 107).

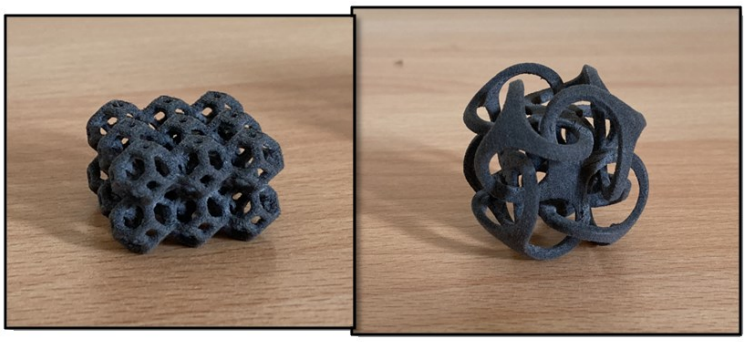

Figure 107: PA12/CF parts with complex geometries printed with Sharebot SnowWhite SLS machine

These overall advantages, coupled with system technology improvements in terms of productivity (e.g., multi-beam SLS machines), machine size (e.g., Big Area Additive Manufacturing for large format material extrusion) and process monitoring, may pave the way for an increased adoption of AM short fiber reinforced composites in different industrial applications. Moreover, an effective integration between these techniques and other fabrication and post-treatment methods could lead to the development of hybrid manufacturing systems able to solve current challenges in material selection, mechanical performances and defects. Zhu et al. [228] prepared high performance PA12/epoxy/carbon fiber ternary composites by using a combination of SLS technology (for making PA12/CF porous green parts) and infiltration in a vacuum drying oven (for curing the epoxy resin). This hybrid method yielded composites with high fiber content (33 vol.%) as well as better tensile (101 MPa) and flexural strength (153 MPa) with respect to other SLS materials [228]. Other hybrid processes based on the combination between laser powder bed fusion (LPBF) techniques for polymers and metals [339,340] or LPBF/Fused Filament Fabrication [341] has also been designed for multi-material objects fabrication. Finally, it has been proved that "Z-pinning" (i.e., inserting pins across multiple layers of the parts) [342], infrared heating during processing [343] and annealing post-treatments [344,345] helps to reduce void content and increase the z-direction properties of FFF parts.

5.3.2 Continuous carbon fiber reinforced polymer composites

The addition of continuous fiber reinforcements in 3D printed polymers allows to achieve mechanical properties far beyond that seen with short fiber counterparts (Figure 104). High stiffness and strength at break (up to 70 GPa and 600 MPa) can be obtained, implying the application of these composites for structural parts

and metal replacement (Figure 104). However, mechanical performances of conventional laminates (both thermoplastic and thermosetting based composites) are still superior compared to the AM counterparts. Lack of fiber impregnation, considerable void content and inhomogeneous fiber distribution due to the absence of compaction forces and the thermal cycles inherent in layer-by-layer fabrication processes have been acknowledged as the main reasons behind the lower tensile properties of 3D printed laminates [204,206,208–210]. These defects also lead to an appreciable drop in tranverse and interlaminar strength compared to conventional composites [203,204,206,208–210,216]. Therefore, it can be derived that additive manufacturing of CCFRP composites needs further improvements to reduce processing defects and achieve adequate mechanical properties for highly demanding applications.

According to the author, the efforts need to be focused on improving the fiber/matrix interfacial adhesion and the consolidation between layers. Some suggestions that will serve as guideline to enhance the mechanical behaviour of the printed parts are then proposed below:

- use of pre-impregnated filaments with higher quality and fiber volume fraction by using high-pressure impregnation methods [301–303]. In these methods, the fiber tow is pulled in tension over a series of convex shaped pins to improve the divergence between the individual fibers, while the impregnation is obtained by extruding the molten polymer through a slot-shaped die. Garofalo et al. [303] found that improved impregnation and distribution of the fibers within the filament as well as higher fiber content (up to 39%) can be achieved [303]. Other methods for improving pre-preg quality lay on decreasing the polymer melt viscosity by using rheology modifiers or nozzle geometries which induce turbulent melt flow. A proper surface functionalization (e.g., acid treatments or oxidation) or sizing treatment of the fibers could also help in improving wetting and interfacial adhesion between matrix and reinforcement [193];
- additional compaction steps after or during 3D printing to reduce the void percentage. Hot compression moulding (HCM) or hot isostatic pressing (HIP) has been proved really helpful in this regard. In fact, a decrease of porosity of 50% [200,206] and 87% [329] was reported by using these post-treatments on AM composites. In fact, the mechanical properties has been highly improved, as shown by the solid fill symbols in Figure 106. However, these post-processing methods increase the manufacturing time and require the use of specific molds, thus restricting the possibility to

fabricate near-net-shape structures with complex geometries. Therefore, other approaches are being investigated to enhance material consolidation. To mention a few, printing in a vacuum chamber [346], adding a material preheating system [347], a layer post-compaction step [348–351] or both [352,353] seems very promising. In fact, the integration between a heat source (laser or hot gas torch) and a compaction roller has been proved to enhance consolidation in Automated Fiber/Tape Placement (AFP/ATP) processes used for manufacturing thermoplastic laminates [201];

- use of high performance polymer matrices, such as PEI and PEEK. Van Der Werken et al. [200] reached tensile modulus and strength of 85.3 GPa and 1134.3 MPa respectively for longitudinal PEEK/CCF composites printed using CFF technique. These values correspond to a 25% increase in mechanical performances compared to the state-of-art AM polymer composites, mostly continuous fiber reinforced polyamide composites;
- development of five or six axis printing system able to place fiber reinforcement in all directions, thus surpassing the current limitation of poor off-axis properties [186].

Nevertheless, the mechanical properties of thermoplastic polymers and the difficulties in void suppression in out-of-autoclave processes for composite production, such as AM techniques and AFTP/ATP, complicated by the higher melt viscosity of these polymers, still represent a limitation for thermoplastic laminates compared to standard epoxy-based ones. However, material extrusion AM techniques can surpass traditional methods when parts with high geometrical complexity are required. Although the applications of 3D printed continuous fiber reinforced polymer composites are still rare because the technology is very recent, several examples have been proposed in literature. In fact, the feasibility of 3D printing continuous CCFRP composites lattice sandwich structures [354–357], bicycle lug [186], small unmanned aerial vehicle (UAV) frame [358], aircraft seat support [186], suspension plate with topological optimized design [359] and high performances UAV landing gear [322] was revelead (Figure 108). Moreover, this technology could bring great potential benefits in niche sector such as on-orbit manufacturing and space exploration. NASA have already proved the feasibility to additively manufacture neat thermoplastic polymer parts in a microgravity condition on the International Space Station using the Made In Space system [1]. The improved performances obtained by 3D printed CCFRP composites own the opportunity of enabling in-orbit manufacturing of spare parts and space structures (e.g., antennas, solar arrays, reflectors, etc.) for several applications [1].

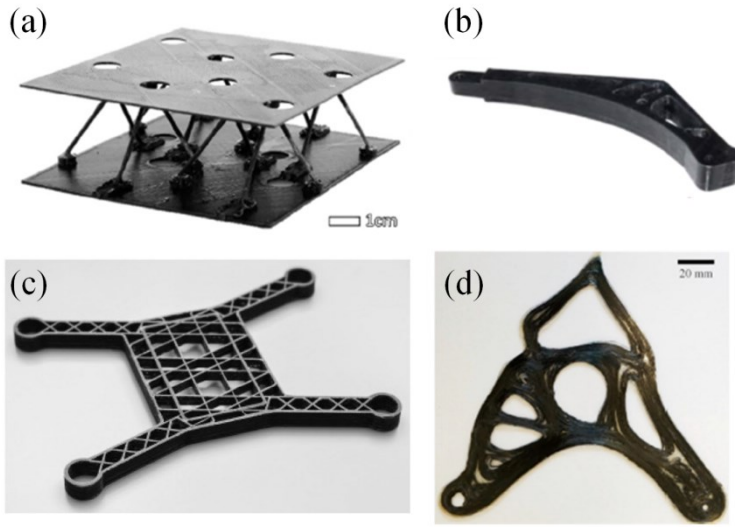

Figure 108: (a) Lattice truss sandwich structure [354], (b) aircraft seat support [186], (c) small size UAV frame [358] and (d) suspension plate [359] manufactured via material extrusion AM of continuous fibers composites

Chapter 6

Conclusions

The research covered in this thesis aims at foster the transition of AM carbon fiber reinforced polymer composites from laboratory and prototyping activities into industrial applications. For this purpose, the raw material properties as well as the microstructure and mechanical properties of carbon fiber reinforced polyamide composites produced by three complementary AM techniques (SLS. FFF and CFF) were investigated. The accuracy of different modeling approaches in the prediction of the elastic modulus and tensile strength of the printed composites was also evaluated. Lastly, a detailed comparison with traditional technologies was carried out to outline the advantages and current drawbacks of additive technologies for producing carbon fiber reinforced polymer composites. Therefore, some of the key barriers for the adoption of these materials in structural applications (e.g., process-induced defects, anisotropy, mechanical and failure behaviour) were identified. The conclusions are drawn in the following paragraphs.

Selective Laser Sintering (SLS)

PA12/CF powders can be easily processed by SLS although the addition of carbon fibers to the neat PA12 particles reduces their packing density and flowability as well as slightly accelerated polymer crystallization. The geometrical defects, microstructure and mechanical performance of the printed samples largely depends on the process parameters adopted. In particular, out of plane deformation of the part (also referred as curling) is sensitive to small variation of the powder bed temperature (T_b), while void content and tensile properties are

greatly affected by laser energy density. Since the traditional approach for optimizing the process parameters in SLS is largely empirical and relies on trial and error builds, an analytical design method was used. By analyzing both isothermal crystallization kinetics and stable sintering region, the intrinsic properties of the powders can be effectively correlated to processing defects and part performance. It was found that, to avoid part curling, T_b has to be set at 170 °C, at which the inverse of crystallization halftime approaches to zero. Moreover, although a wide range of laser energy density is theoretically applicable, Energy Melt Ratio values in the middle part of the stable sintering region are required to obtain low void content and high mechanical properties without sacrificing dimensional accuracy. The proposed approach is a more rational one and offers potential to limit processing defects, thus reducing cost and saving time in the material development phase,

The microstructure of PA12/CF parts printed with optimized energy density exhibits low void content and a uniform distribution of fibers in the matrix phase. The fibers are preferentially oriented in the build plane owing to the mechanical action of the recoating blade during powder layer spreading. The stiffness of PA12/CF parts is remarkably higher compared to the neat polymer at the expense of ductility. Although a strong interlayer bonding and a good interfacial adhesion between fiber and PA12 matrix was observed on the fractured surfaces, the increase in tensile strength was limited because fiber length is lower than a critical value thus not allowing an effective translation of the stresses from the matrix to the reinforcing phase.

Fused Filament Fabrication (FFF)

The microstructure of PA6/CF composites produced by FFF highly differs from that of PA12/CF parts produced by SLS. Different types of void (inter-layer, inter-beads and intra-beads voids) were identified in FFF samples. These voids are caused by the lack of pressure during bead deposition and the rapid heating/cooling cycle of the printing process itself. Moreover, it was found that FFF composites show high fiber alignment in the filament deposition direction and good fiber distribution due to the shear stresses applied in the extruder nozzle. These characteristics were also observed in the raw filament.

The preferential orientation of fibers is reflected on the different mechanical properties recorded for PA6/CF composites with [0], [±45] and [0/45/90/-45] architectures. Samples printed with 0° raster angle exhibit the highest values of

elastic modulus and strength at break because carbon fibers are well aligned in the direction of the applied load. Accordingly, this reinforcing effect decreases for the other printing layups. A remarkable enhancement of stiffness compared to the neat PA6 parts was achieved. Although a good interfacial bonding between fiber and PA6 matrix, the increase in tensile strength was lower than expected due to the presence of a considerable amount of voids (about 10%). In fact, these defects, along with the poor interlayer bonding typical of FFF parts, promote the formation of cracks and in some cases (e.g., [±45] and [0/45/90/-45] architecture) layer delamination

Continuous Filament Fabrication (CFF)

Fully dense PA6 filament (PA) and a pre-impregnated continuous carbon fiber reinforced filament (CCF) with 36 vol.% of fibers embedded in a semi aromatic polyamide matrix were used for producing PA/CCF composites. Few voids due to poor impregnation issues and regions with high fiber or resin concentration were found in the CCF filament. The microstructure of the laminates was characterized by high void percentage (11%), poor interlayer bonding and uneven fiber distribution. These defects were related to the filament morphology and intrinsic nature of the CFF technique. The morphology and amount of voids fairly resemble those described for short fiber composites produced by FFF as the processing conditions (i.e., absence of pressure and fast cooling rates) does not allow a complete consolidation of the material. It was also found that the laminate layup strongly affected the shape and distribution of voids, that changes from irregularly shaped inter-beads voids in longitudinal laminates to elongated inter-layer voids in cross-ply and quasi-isotropic ones.

Connections between the macroscopic mechanical response of the laminates and the typical microstructure induced by the additive process as well as the layup adopted were also identified. The longitudinal laminates displayed the highest stiffness and strength due to the fiber alignment along the load direction. These properties gradually got worse for [0/90], [0/60] and [0/45/90/-45] layups in reason of the lower number of 0° oriented plies. However, these layups are of great practical interest because they exhibit in-plane isotropic behaviour. Overall, the mechanical performances of PA/CCF laminates are much better compared to those of pure polyamides and SCFRP composites. The failure mechanism of the different composites largely depends on the microstructural defects and fiber orientation layup. Step-like failure with large fiber breakage and pull-out, transverse failure and interlaminar failure with debonding between layers were

identified for longitudinal, cross-ply and quasi-isotropic layups respectively. A good fiber/matrix interfacial adhesion was observed in most cases, although significant fiber debonding appears in low strength plies (90° layers of cross-ply laminates).

Modeling

AM of fiber reinforced composites is a new processing technique and little research has been focused on the prediction of their mechanical properties. In this study, it was proved that existing micro and macro mechanical models for fiber composites can be effectively applied to AM with slight changes to take into account the peculiar microstructure of the 3D printed parts. The modified rule of mixtures with the addition of a porosity correction factor estimates with good accuracy (error < 7%) the elastic modulus of short fiber composites produced by SLS and FFF. However, the tensile strength was significantly overestimated (error up to 20%) due to the presence of voids and the perfect fiber/matrix bonding assumed in the models. Classical Laminate Theory (CLT) coupled with the RoM was effective to predict the elastic modulus and tensile strength of AM composites with continuous carbon fibers. The predictions showed good agreement with the experimental data of elastic modulus and strength (error <10%). By exploiting this model, the mechanical properties of complex 3D printed structure (e.g., including more than one walls or alternating layers of neat polymer and reinforced materials) can be optimized according to the loading conditions by tailoring fiber orientation and material properties layer by layer. This will give engineers huge potential in design.

6.1 Future research prospects

AM of carbon fiber reinforced composites has demonstrated great potential owing to its unique advantages (cost-effectiveness, freedom of design, great performances compared to AM polymers). However, their properties are inferior with respect to conventionally manufactured composites and AM technologies are still in the development phase, particularly for continuous fiber parts. Further improvements are thus needed to achieve the performance of traditional composites. Some critical issues that appear relevant to the author and opportunities for advancement are outlined below, though this list is not comprehensive:

- various defects are created during AM, thus leading to a reduction of part performances. Understanding the formation mechanisms of these defects

can help to identify methods to reduce or eliminate them. Process monitoring techniques, such as thermal camera and sensors, can provide essential data for this purpose. The acquired knowledge will, in turn, enhance the 3D printed composite properties and simplify the quality certification of these materials;

- modeling the physical phenomena typical of AM technologies can assist the optimization of process parameters. Through this effort, it will be possible to change the paradigm of process optimization from an empirical approach to a more rational one. In this regard, there is still an insufficient comprehension of polymer rheology (e.g., viscosity changes with shear stress and temperature) and crystallization occurring during powder bed fusion and material extrusion AM of fiber reinforced polymer composites. These efforts can also facilitate the development of innovative polymeric composites as well as to improve the understanding of the link between AM processes and part microstructure and properties;
- this thesis and most published works so far are focused on the characterization of the quasi-static tensile properties. Therefore, it is necessary to extend the studies to non-tensile properties, such as fracture toughness, impact, fatigue and creep resistance, as well as functional properties (e.g., thermal, piezoelectric and magnetic properties). This will provide essential data for design and quality assessment of AM components;
- although the addition of carbon fibers greatly improves the mechanical properties of AM polymers, strategies to improve the composite performances are required. To this end, specific fiber sizing for thermoplastic matrices and post-processing treatments (e.g., annealing, hot isostatic pressing, vacuum infiltration, etc.) are advised to enhance fiber/matrix bonding and modify the crystalline fraction as well as the void content of the printed parts;
- AM materials with higher fiber content or longer fibers (greater than the critical length) are desired to obtain superior mechanical performances and high translation of fiber strength respectively;
- hybrid systems containing carbon fibers and one or more other fillers can provide a synergic effect on the composite properties as well as additional functionalities to AM parts. This could pave the way for the production of smart devices (e.g., sensors, actuators and energy storage modules) in one step, with less costs and higher structural integrity;

- the use of high-performance thermoplastics, including PPS, PEI and PEEK, can enable the fabrication of fiber reinforced composites with improved mechanical and thermal properties;
- since the microstructure of AM parts is different from conventional counterparts and the effect of voids is difficult to compute, there is a great demand for specific modeling approaches. Finite element (FE) models based on homogenization or unit cell methods are effective for analyzing composite structures. Using these approaches, the real features of voids and reinforcement can be included in the computational domain.

Apart from these points, the adoption of conventional processing technologies, such as injection and compression molding, to manufacture sample by using the same geometry and materials processed by AM in this thesis is foreseen. In this way, a more effective comparison of the microstructural and mechanical properties between additively and conventionally manufactured parts will be performed. For short fiber composites the scientific outcomes would greatly benefit from such a direct comparison because each processing technology has unique characteristics in terms of thermal history and consolidation mechanism. For example, high cooling rates and shear stresses are applied in injection moulding, while in SLS the polymer melt cools down very slowly and only viscous flow acts as driving force for material densification. As a result, the produced parts will exhibit high differences in terms of microstructure, crystallinity, fiber orientation and processing defects. For continuous fiber composites different studies on the comparison between additive and traditional methods using the same material processed in this thesis revealed that significant differences in mechanical performances and void content exist. However, a direct comparison between additive manufacturing and other automated processing technologies, such as Automated Fiber/Tape Placement and filament winding, could assume great importance for the manufacturing industry.

Appendix

Table A1: Summary of mechanical data for discontinuous fiber reinforced polymer composites reported in Figure 104. Legend: FFF (Fused Filament Fabrication), SLS (Selective Laser Sintering), IM (injection molding) and CM (compression molding), l (average fiber length), layup is indicated for FFF parts, orientation defines the spatial alignment of the SLS parts in the build chamber according to the sketch of Figure A1

Manufacturing technique	Material	E (GPa)	σ (MPa)	Layup / orientation	V_f (%)	Ref.
FFF	PLA/CF	7.7	53.7	[0]	15.0	[180]
FFF	PLA/CF	4.1	37.0	[±45]	15.0	[180]
FFF	PLA/CF	9.2	70.3	[0]	15.0	[360]
FFF	PLA/CF	6.7	60.6	[0/90]	15.0	[361]
FFF	PLA/CF	9.28	68.4	[0]	12.6	[179]
FFF	PLA/CF	5.2	54.6	[±45]	12.6	[179]
FFF	PETG/CF	8.47	68.3	[0]	17.7	[179]
FFF	PETG/CF	4.23	50.9	[±45]	17.7	[179]
FFF	ABS/CF	7.15	50.9	[0]	18.8	[179]
FFF	ABS/CF	2.46	42.5	[±45]	4.5	[182]
FFF	ABS/CF	8.18	53.3	[0]	13.0	[362]
FFF	ABS/CF	11.9	66.4	[0]	20.0	[362]

FFF	ABS/CF	4.1	41.0	[0]	15.0	[363]
FFF	ABS/CF	5.89	39.05	[0]	15.0	[181]
FFF	ABS/CF	11.5	60.0	[0]	20.0	[176]
FFF	ABS/CF	13.7	67.0	[0]	40.0	[176]
FFF	PP/CF	5.6	74.2	[0]	10.0	[183]
FFF	PA6/CF	1.85	33.5	[0]	6.0	[156]
FFF	PA6/CF	2.33	51.28	[±45]	15.0	this work
FFF	PA6/CF	3.15	56.2	[±45]	15.0	[364]
FFF	PA6/CF	3.96	128.0	[0]	10.0	[295]
FFF	PA6/CF	9.91	97.7	$[0]_{\text{on edge}}$	15.0	[146]
FFF	PA6/CF	9.93	81.1	$[0]_{\text{flat}}$	15.0	[146]
FFF	PA6/CF	7.89	95.7	[±45]	15.0	[297]
FFF	PA6/CF	6.19	52.0	[0]	20.0	[298]
FFF	PA6/CF	7.56	92.0	[0]	14.0	[296]
FFF	PA6/CF	5.1	63.3	[±45]	14.0	[296]
FFF	PA6/CF	11.71	105.8	[0]	15.5	this work
FFF	PA6/CF	7.48	72.9	[±45]	15.5	this work
FFF	PA6/CF	7.98	67.7	[0/±45/90]	15.5	this work

FFF	PA12/CF	2.79	79.0	[0]	6.0	[178]
FFF	PA12/CF	3.35	87.0	[0]	8.0	[178]
FFF	PA12/CF	3.58	93.8	[0]	10.0	[178]
FFF	PA12/CF	5.43	61.6	[0]	27.1	[225]
FFF	PA12/CF	8.80	89.0	[0]	23.1	[225]
SLS	PA12/CF	6.3	66.7	xy-0°	-	[145]
SLS	PA12/CF	3.6	54.0	xy-90°	-	[145]
SLS	PA12/CF	4.1	56.7	xy-45°	-	[145]
SLS	PA12/CF	5.5	72.0	xy-0°	30.0	[144]
SLS	PA12/CF $_{\text{dry mixed}}$	5.8	80.0	xy-0°	30.0	[144]
SLS	PA12/CF $_{\text{surface treated}}$	5.86	64.1	xy-0°	-	[140]
SLS	PA12/CF	3.61	46.0	xy-90°	-	[140]
SLS	PA12/CF	4.7	61.0	xy-0°	30.0	[148]
SLS	PA12/CF	3.4	53.0	xy-90°	30.0	[148]
SLS	PA12/CF	5.64	80.8	xy-0°	12.0	[147]
SLS	PA12/CF	4.29	70.7	xy-45°	12.0	[147]
SLS	PA12/CF	3.61	64.9	xy-90°	12.0	[147]
SLS	PA12/CF	7.37	82.56	xy-0°	28.0	[146]

SLS	PA12/CF	3.22	58.55	xz-0°	28.0	[146]
SLS	PA12/CF	3.25	50.3	xy-0°	19.0	this work
SLS	PA11/CF	4.48	65.6	xy-0°	19.0	[146]
SLS	PA11/CF	2.97	55.0	xz-0°	19.0	[146]
CM	PA6/CF $_{\text{EP sizing}}$	7.39	104		13.5	[365]
CM	PA6/CF $_{\text{PA sizing}}$	6.18	94.0		13.5	[365]
CM	PA6/CF	10.13	119.3		15.0	[297]
CM	ABS/CF	10.2	62.0		20.0	[176]
CM	ABS/CF	17.0	75.0		40.0	[176]
CM	PA6/CF	8.13	98.3		14.0	[296]
IM	PA66/CF $_{\text{virgin}}$	23.5	236.4		30.0	[314]
IM	PA66/CF $_{\text{recycled}}$	20.5	188.2		30.0	[314]
IM	PA6/CF	7.5	65.0		20.0	[298]
IM	PA66/CF $_{\text{l=200 µm}}$	13.0	124.0		21.0	[319]
IM	PA66/CF $_{\text{l=200 µm}}$	22.0	150.0		31.0	[319]
IM	PA66/CF $_{\text{l=400 µm}}$	23.0	158.0		20.0	[319]
IM	PA66/CF $_{\text{l=200 µm}}$	29.0	173.0		32.0	[319]
IM	PA6/T700	21.0	208.0		21.0	[320]

IM	PA66/CF	22.5	240.0	27.0	[321]
IM	PA66/CF	33.2	298.0	37.0	[321]
IM	PA66/CF $_{\text{Ultramid A3WC8}}$	36.3	269.0	37.0	[321]
IM	PA66/CF	30.0	245.0	40.0	[366]
IM	PA66/CF	38.1	295.0	40.0	[367]

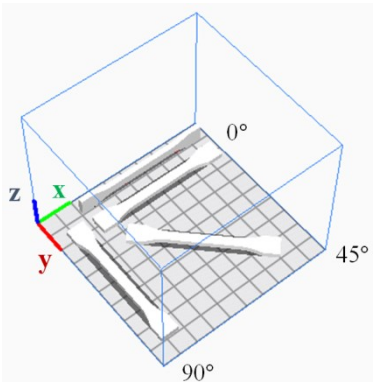

Figure A1: Graphical representation of the building orientation considered for SLS tensile dog-bones. The recoater spread the powders in the x-direction

Table A2: Summary of mechanical data for continuous fiber reinforced polymer composites reported in Figure 104. Legend: CFF (Continuous Filament Fabrication), HCM (Hot Compression Moulding), AFP (Automated Fiber Placement), UA-LOM (Ultrasonic Assisted Laminated Object Manufacturing), VBO (Vacuum Bag Only), PA (polyamide), PEEK (polyether ether ketone), EP (epoxy resin). The subscripts denote the commercial name of the composite prepregs

Manufacturing technique	**Material**	**E (GPa)**	**σ (MPa)**	**Layup**	**V_f (%)**	**Ref.**
CFF	PA/CCF	54.0	700.0	[0]	35.0	[195]
CFF	PA/CCF	35.7	464.4	[0]	22.0	[202]

CFF	PA/CCF	51.7	436.0	[0]	26.4	[210]
CFF	PA/CCF	62.5	726.0	[0]	35.0	[156]
CFF	PA/CCF	68.1	701.0	[0]	31.0	[209]
CFF	PA/CCF	60.0	534.0	[0]	30.0	[204]
CFF	PA/CCF	39.7	420.0	[0]	22.6	[204]
CFF	PA/CCF	70.5	808.0	[0]	32.0	[322]
CFF	PA/CCF	61.0	767.0	[0]	34.9	[206]
CFF	PA/CCF	69.4	905.3	[0]	31.5	[208]
CFF	PA/CCF	60.9	701.0	[0]	35.0	[214]
CFF	PA/CCF	73.2	524.6	[0]	34.0	[215]
CFF	PA/CCF	41.2	597.6	[0]	22.0	[313]
CFF	PA6/CCF	53.0	701.0	[0]	50.0	[328]
CFF	PA/CCF	38.1	600.0	[0]	32.0	[203]
CFF	PA/CCF	46.9	634.3	[0]	22.0	[213]
CFF	PA/CCF	48.3	597.6	[0]	26.4	this work
CCF + HCM	PA/CCF	83.2	939.0	[0]	34.9	[206]
HCM	PA6/CCF	72.2	1047.0	[0]	30.0	[312]
HCM	PA6/CCF	98.2	1308.0	[0]	43.0	[312]

HCM	PA/CCF	48.0	783.0	[0]	30.0	[330]
laser AFP	PA6/CCF	103.2	1774.2	[0]	44.0	[368]
HCM	PA6/CCF $_{8exe}$	86.3	1337.9	[0]	37.0	[368]
HCM	PA6/CCF Cetex-TC910	97.9	1322.6	[0]	42.0	[368]
AFP	PA/CCF	117.0	1022.0	[0]	-	[369]
UA-LOM	PA6/CCF	96.0	1461.7	[0]	49.0	[349]
HCM	PA6/CCF	105.7	1760.2	[0]	49.0	[349]
CCF + HCM	PA6/CCF	91.0	1385.0	[0]	50.0	[328]
VBO	PEEK/CCF APC2-AS4	139.0	2127.0	[0]	59.0	[325]
HCM	PEEK/CCF APC2-AS4	144.0	2228.0	[0]	59.0	[325]
laser AFP	PEEK/CCF	136.0	1847.0	[0]	59.0	[325]
AFP	PEEK/ CCF	145.0	2420.0	[0]	55.0	[326]
autoclave	PEEK/ CCF	136.0	2446.0	[0]	55.0	[326]
autoclave	EP/CCF HexPly M21/IM7	160.0	2860.0	[0]	59.2	[324]
autoclave	EP/CCF HexPly M21/IMA	178.0	3050.0	[0]	59.2	[370]
autoclave	EP/CCF HexPly M21/AS7	148.0	2350.0	[0]	58.9	[324]

autoclave	EP/CCF 85552/AS4	141.0	2207.0	[0]	57.4	[371]
autoclave	EP/CCF 85552/IM7	164.0	2724.0	[0]	57.7	[370]
autoclave	EP/CCF 3501-6/AS4	131.0	1954.0	[0]	60.0	[372]
autoclave	EP/CCF MTM45-1/IM7	174.0	2200.0	[0]	58.7	[372]
autoclave	EP/CCF 7901/T300	137.7	1784.9	[0]	62.0	[373]
autoclave	EP/CCF TDE85/T700	132.0	2100.0	[0]	60.0	[307]
HCM	EP/CCF MCP939/T700	109.1	1664.0	[0]	47.0	[312]
autoclave	EP/CCF Fibredux 914C/T300	135.0	1650.0	[0]	50.5	[374]
autoclave	EP/CCF HexPly 8551-7/AS4	145.0	2171.8	[0]	60.0	[375]

References

1. van de Werken, N.; Tekinalp, H.; Khanbolouki, P.; Ozcan, S.; Williams, A.; Tehrani, M. Additively manufactured carbon fiber-reinforced composites: State of the art and perspective. *Addit. Manuf.* **2020**, *31*, 100962.

2. Holmes, M. Global carbon fibre market remains on upward trend. *Reinf. Plast.* **2014**, *58*, 38–45.

3. Khurshid, M.F.; Hengstermann, M.; Hasan, M.M.B.; Abdkader, A.; Cherif, C. Recent developments in the processing of waste carbon fibre for thermoplastic composites – A review. *J. Compos. Mater.* **2020**, *54*, 1925–1944.

4. Yao, S.S.; Jin, F.L.; Rhee, K.Y.; Hui, D.; Park, S.J. Recent advances in carbon-fiber-reinforced thermoplastic composites: A review. *Compos. Part B Eng.* **2018**, *142*, 241–250.

5. Parmar, H.; Khan, T.; Tucci, F.; Umer, R.; Carlone, P. Advanced robotics and additive manufacturing of composites: towards a new era in Industry 4.0. *Mater. Manuf. Process.* **2021**, *00*, 1–35.

6. Frketic, J.; Dickens, T.; Ramakrishnan, S. Automated manufacturing and processing of fiber-reinforced polymer (FRP) composites: An additive review of contemporary and modern techniques for advanced materials manufacturing. *Addit. Manuf.* **2017**, *14*, 69–86.

7. Ford, S.; Despeisse, M. Additive manufacturing and sustainability: an exploratory study of the advantages and challenges. *J. Clean. Prod.* **2016**, *137*, 1573–1587.

8. Javaid, M.; Haleem, A.; Singh, R.P.; Suman, R.; Rab, S. Role of additive manufacturing applications towards environmental sustainability. *Adv. Ind. Eng. Polym. Res.* **2021**, *4*, 312–322.

9. Ashima, R.; Haleem, A.; Javaid, M.; Rab, S. Understanding the role and capabilities of Internet of Things-enabled Additive Manufacturing through its applications. *Adv. Ind. Eng. Polym. Res.* **2021**.

10. Ngo, T.D.; Kashani, A.; Imbalzano, G.; Nguyen, K.T.Q.; Hui, D. Additive

manufacturing (3D printing): A review of materials, methods, applications and challenges. *Compos. Part B Eng.* **2018**, *143*, 172–196.

11. Shanmugam, V.; Rajendran, D.J.J.; Babu, K.; Rajendran, S.; Veerasimman, A.; Marimuthu, U.; Singh, S.; Das, O.; Neisiany, R.E.; Hedenqvist, M.S.; et al. The mechanical testing and performance analysis of polymer-fibre composites prepared through the additive manufacturing. *Polym. Test.* **2021**, *93*, 106925.

12. K., P.; M., M.; P., S.P. Technologies in additive manufacturing for fiber reinforced composite materials: a review. *Curr. Opin. Chem. Eng.* **2020**, *28*, 51–59.

13. Schmidt, M.; Merklein, M.; Bourell, D.; Dimitrov, D.; Hausotte, T.; Wegener, K.; Overmeyer, L.; Vollertsen, F.; Levy, G.N. Laser based additive manufacturing in industry and academia. *CIRP Ann.* **2017**, *66*, 561–583.

14. Parandoush, P.; Lin, D. A review on additive manufacturing of polymer-fiber composites. *Compos. Struct.* **2017**, *182*, 36–53.

15. Gibson, I.; Rosen, D.; Stucker, B. *Additive Manufacturing Technologies - Rapid Prototyping*; 2010; ISBN 9781493921126.

16. Wang, Y.; Zhou, Y.; Lin, L.; Corker, J.; Fan, M. Overview of 3D additive manufacturing (AM) and corresponding AM composites. *Compos. Part A Appl. Sci. Manuf.* **2020**, *139*, 106114.

17. Ligon, S.C.; Liska, R.; Stampfl, J.; Gurr, M.; Mülhaupt, R. Polymers for 3D Printing and Customized Additive Manufacturing. *Chem. Rev.* **2017**, *117*, 10212–10290.

18. Wang, X.; Jiang, M.; Zhou, Z.; Gou, J.; Hui, D. 3D printing of polymer matrix composites: A review and prospective. *Compos. Part B Eng.* 2017, *110*, 442–458.

19. Dizon, J.R.C.; Espera, A.H.; Chen, Q.; Advincula, R.C. Mechanical characterization of 3D-printed polymers. *Addit. Manuf.* **2018**, *20*, 44–67.

20. Penumakala, P.K.; Santo, J.; Thomas, A. A critical review on the fused deposition modeling of thermoplastic polymer composites. *Compos. Part B Eng.* **2020**, *201*, 108336.

21. Kabir, S.M.F.; Mathur, K.; Seyam, A.F.M. A critical review on 3D printed continuous fiber-reinforced composites: History, mechanism, materials and

properties. *Compos. Struct.* **2020**, *232*, 111476.

22. Chatham, C.A.; Long, T.E.; Williams, C.B. A review of the process physics and material screening methods for polymer powder bed fusion additive manufacturing. *Prog. Polym. Sci.* 2019, *93*, 68–95.

23. Yuan, S.; Shen, F.; Chua, C.K.; Zhou, K. Polymeric composites for powder-based additive manufacturing: Materials and applications. *Prog. Polym. Sci.* 2019, *91*, 141–168.

24. Zindani, D.; Kumar, K. An insight into additive manufacturing of fiber reinforced polymer composite. *Int. J. Light. Mater. Manuf.* **2019**, *2*, 267–278.

25. Krajangsawasdi, N.; Blok, L.G.; Hamerton, I.; Longana, M.L.; Woods, B.K.S.; Ivanov, D.S. Fused deposition modelling of fibre reinforced polymer composites: A parametric review. *J. Compos. Sci.* **2021**, *5*.

26. Brenken, B.; Barocio, E.; Favaloro, A.; Kunc, V.; Pipes, R.B. Fused filament fabrication of fiber-reinforced polymers: A review. *Addit. Manuf.* 2018, *21*, 1–16.

27. Tian, X.; Peng, G.; Yan, M.; He, S.; Yao, R. Process prediction of selective laser sintering based on heat transfer analysis for polyamide composite powders. *Int. J. Heat Mass Transf.* **2018**, *120*, 379–386.

28. Drummer, D.; Greiner, S.; Zhao, M.; Wudy, K. A novel approach for understanding laser sintering of polymers. *Addit. Manuf.* **2019**, *27*, 379–388.

29. Goodridge, R.D.; Tuck, C.J.; Hague, R.J.M. Laser sintering of polyamides and other polymers. *Prog. Mater. Sci.* **2012**, *57*, 229–267.

30. Kusoglu, I.M.; Doñate-buendía, C.; Barcikowski, S.; Gökce, B. Laser powder bed fusion of polymers: Quantitative research direction indices. *Materials (Basel).* **2021**, *14*, 1–26.

31. Leigh, D.K. A comparison of polyamide 11 mechanical properties between laser sintering and traditional molding. In Proceedings of the 23rd Annual International Solid Freeform Fabrication Symposium - An Additive Manufacturing Conference, SFF 2012; 2012; pp. 574–605.

32. Qi, F.; Chen, N.; Wang, Q. Preparation of PA11/BaTiO3 nanocomposite powders with improved processability, dielectric and piezoelectric properties for use in selective laser sintering. *Mater. Des.* **2017**, *131*, 135–

143.

33. Esposito, G.R.; Dingemans, T.J.; Pearson, R.A. Changes in polyamide 11 microstructure and chemistry during selective laser sintering. *Addit. Manuf.* **2021**, *48*, 102445.

34. Chen, P.; Wu, H.; Zhu, W.; Yang, L.; Li, Z.; Yan, C.; Wen, S.; Shi, Y. Investigation into the processability, recyclability and crystalline structure of selective laser sintered Polyamide 6 in comparison with Polyamide 12. *Polym. Test.* **2018**, *69*, 366–374.

35. Heckner, T.; Seitz, M.; Raisch, S.R.; Huelder, G.; Middendorf, P. Selective laser sintering of pa6: Effect of powder recoating on fibre orientation. *J. Compos. Sci.* **2020**, *4*, 1–16.

36. Zhu, W.; Yan, C.; Shi, Y.; Wen, S.; Liu, J.; Shi, Y. Investigation into mechanical and microstructural properties of polypropylene manufactured by selective laser sintering in comparison with injection molding counterparts. *Mater. Des.* **2015**, *82*, 37–45.

37. Ituarte, I.F.; Wiikinkoski, O.; Jansson, A. Additive manufacturing of polypropylene: A screening design of experiment using laser-based powder bed fusion. *Polymers (Basel).* **2018**, *10*, 1293.

38. Tan, L.J.; Zhu, W.; Sagar, K.; Zhou, K. Comparative study on the selective laser sintering of polypropylene homopolymer and copolymer: processability, crystallization kinetics, crystal phases and mechanical properties. *Addit. Manuf.* **2021**, *37*, 101610.

39. Goodridge, R.D.; Hague, R.J.M.; Tuck, C.J. An empirical study into laser sintering of ultra-high molecular weight polyethylene (UHMWPE). *J. Mater. Process. Technol.* **2010**, *210*, 72–80.

40. Bai, J.; Zhang, B.; Song, J.; Bi, G.; Wang, P.; Wei, J. The effect of processing conditions on the mechanical properties of polyethylene produced by selective laser sintering. *Polym. Test.* **2016**, *52*, 89–93.

41. Gu, H.; Alfayez, F.; Ahmed, T.; Bashir, Z. Poly (ethylene terephthalate) Powder — A Versatile Material for Additive Manufacturing. *Polymers (Basel).* **2019**, *11*, 2041.

42. Gu, H.; Bashir, Z.; Yang, L. The re-usability of heat-exposed poly (ethylene terephthalate)powder for laser sintering. *Addit. Manuf.* **2019**, *28*, 194–204.

43. Dechet, M.A.; Gómez Bonilla, J.S.; Grünewald, M.; Popp, K.; Rudloff, J.; Lang, M.; Schmidt, J. A novel, precipitated polybutylene terephthalate feedstock material for powder bed fusion of polymers (PBF): Material development and initial PBF processability. *Mater. Des.* **2021**, *197*.

44. Arai, S.; Tsunoda, S.; Kawamura, R.; Kuboyama, K.; Ougizawa, T. Comparison of crystallization characteristics and mechanical properties of poly(butylene terephthalate) processed by laser sintering and injection molding. *Mater. Des.* **2017**, *113*, 214–222.

45. Schmidt, J.; Sachs, M.; Fanselow, S.; Zhao, M.; Romeis, S.; Drummer, D.; Wirth, K.E.; Peukert, W. Optimized polybutylene terephthalate powders for selective laser beam melting. *Chem. Eng. Sci.* **2016**, *156*, 1–10.

46. Dechet, M.A.; Baumeister, I.; Schmidt, J. Development of polyoxymethylene particles via the solution-dissolution process and application to the powder bed fusion of polymers. *Materials (Basel).* **2020**, *13*.

47. Chatham, C.A.; Das, A.; Long, T.E.; Bortner, M.J.; Williams, C.B. Ageing of PBF-Grade Poly(Phenylene Sulfide) Powder and its Effect on Critical Printability Properties. *Macromol. Mater. Eng.* **2021**, *306*, 1–14.

48. Chatham, C.A.; Long, T.E.; Williams, C.B. Powder bed fusion of poly(phenylene sulfide)at bed temperatures significantly below melting. *Addit. Manuf.* **2019**, *28*, 506–516.

49. Berretta, S.; Evans, K.E.; Ghita, O.R. Predicting processing parameters in high temperature laser sintering (HT-LS) from powder properties. *Mater. Des.* **2016**, *105*, 301–314.

50. Benedetti, L.; Brulé, B.; Decraemer, N.; Davies, R.; Evans, K.E.; Ghita, O. A route to improving elongation of high-temperature laser sintered PEKK. *Addit. Manuf.* **2020**, *36*, 101540.

51. Berretta, S.; Evans, K.E.; Ghita, O. Processability of PEEK, a new polymer for high temperature laser sintering (HT-LS). *Eur. Polym. J.* **2015**, *68*, 243–266.

52. Hoskins, T.J.; Dearn, K.D.; Kukureka, S.N. Mechanical performance of PEEK produced by additive manufacturing. *Polym. Test.* **2018**, *70*, 511–519.

53. Das, A.; Chatham, C.A.; Fallon, J.J.; Zawaski, C.E.; Gilmer, E.L.; Williams, C.B.; Bortner, M.J. Current understanding and challenges in high

temperature additive manufacturing of engineering thermoplastic polymers. *Addit. Manuf.* **2020**, *34*, 101218.

54. Dadbakhsh, S.; Verbelen, L.; Vandeputte, T.; Strobbe, D.; Van Puyvelde, P.; Kruth, J.P. Effect of powder size and shape on the SLS processability and mechanical properties of a TPU elastomer. *Phys. Procedia* **2016**, *83*, 971–980.

55. Vasquez, G.M.; Majewski, C.E.; Haworth, B.; Hopkinson, N. A targeted material selection process for polymers in laser sintering. *Addit. Manuf.* **2014**, *1*, 127–138.

56. Yuan, S.; Shen, F.; Bai, J.; Chua, C.K.; Wei, J.; Zhou, K. 3D soft auxetic lattice structures fabricated by selective laser sintering: TPU powder evaluation and process optimization. *Mater. Des.* **2017**, *120*, 317–327.

57. Verbelen, L.; Dadbakhsh, S.; Van den Eynde, M.; Strobbe, D.; Kruth, J.P.; Goderis, B.; Van Puyvelde, P. Analysis of the material properties involved in laser sintering of thermoplastic polyurethane. *Addit. Manuf.* **2017**, *15*, 12–19.

58. Adams, R.; Soe, S.P.; Santiago, R.; Robinson, M.; Hanna, B.; McShane, G.; Alves, M.; Burek, R.; Theobald, P. A novel pathway for efficient characterisation of additively manufactured thermoplastic elastomers. *Mater. Des.* **2019**, *180*, 107917.

59. Berzins, M.; Childs, T.H.C.; Ryder, G.R. The Selective Laser Sintering of Polycarbonate. *CIRP Ann. - Manuf. Technol.* **1996**, *45*, 187–190.

60. Shi, Y.; Chen, J.; Wang, Y.; Li, Z.; Huang, S. Study of the selective laser sintering of polycarbonate and postprocess for parts reinforcement. *Proc. Inst. Mech. Eng. Part L J. Mater. Des. Appl.* **2007**, *221*, 37–42.

61. Ho, H.C.H.; Cheung, W.L.; Gibson, I. Morphology and properties of selective laser sintered bisphenol a polycarbonate. *Ind. Eng. Chem. Res.* **2003**, *42*, 1850–1862.

62. Yang, J.; Shi, Y.; Shen, Q.; Yan, C. Selective laser sintering of HIPS and investment casting technology. *J. Mater. Process. Technol.* **2009**, *209*, 1901–1908.

63. Zeng, Z.; Deng, X.; Cui, J.; Jiang, H.; Yan, S.; Peng, B. Improvement on selective laser sintering and post-processing of polystyrene. *Polymers (Basel).* **2019**, *11*, 956.

64. Yan, C.; Shi, Y.; Hao, L. Investigation into the differences in the selective laser sintering between amorphous and semi-crystalline polymers. *Int. Polym. Process.* **2011**, *26*, 416–423.

65. Tan, L.J.; Zhu, W.; Zhou, K. Recent Progress on Polymer Materials for Additive Manufacturing. *Adv. Funct. Mater.* **2020**, *30*, 1–54.

66. Schmid, M.; Amado, A.; Wegener, K. Materials perspective of polymers for additive manufacturing with selective laser sintering. *J. Mater. Res.* **2014**, *29*, 1824–1832.

67. Niino, T.; Sato, K. Effect of Powder Compaction in Plastic Laser Sintering Fabrication Toshiki. In Proceedings of the 2009 International Solid Freeform Fabrication Symposium; 2009; Vol. 12, pp. 193–205.

68. Dupin, S.; Lame, O.; Barrès, C.; Charmeau, J.Y. Microstructural origin of physical and mechanical properties of polyamide 12 processed by laser sintering. *Eur. Polym. J.* **2012**, *48*, 1611–1621.

69. Van den Eynde, M.; Verbelen, L.; Van Puyvelde, P. Assessing polymer powder flow for the application of laser sintering. *Powder Technol.* **2015**, *286*, 151–155.

70. Amado Becker, A.F. Characterization and prediction of SLS processability of polymer powders with respect to powder flow and part warpage, ETH Zurich, 2016.

71. Özer, G.; Özbay, B.; Öter, Z.Ç.; Tarakçi, G.; Yılmaz, M.S.; Bulduk, M.E.; Koç, E.; Acar, S.; Güler, K.A. Investigation of the surface quality and dimensional accuracy of polymer patterns produced by selective laser sintering (SLS) method for investment casting (IC). *Int. J. Cast Met. Res.* **2020**, *33*, 146–152.

72. Schmid, M.; Wegener, K. Additive Manufacturing: Polymers applicable for laser sintering (LS). In Proceedings of the Procedia Engineering; Elsevier Ltd, 2016; Vol. 149, pp. 457–464.

73. Meyer, K.-R.; Hornung, K.-H.; Feldmann, R.; Smigerski, H.-J. Method for Polytropically Precipitating Polyamide Powder Coating Compositions where the Polyamide Have at least 10 Aliphatically Bound Carbon Atoms per Carbonamide Group.

74. Evonik Industries AG Vestosint® Polyamide 12 Powders from Evonik Available online: https://www.vestosint.com/en (accessed on Feb 2, 2022).

75. Schmid, M.; Kleijnen, R.; Vetterli, M.; Wegener, K. Influence of the origin of polyamide 12 powder on the laser sintering process and laser sintered parts. *Appl. Sci.* **2017**, *7*, 462.

76. Loyen, K.; Senff, H.; Pauly, F.-X. Patent Application Publication Pub . No .: US 2005 / 0197446 A1. **2005**, *1*, 6–9.

77. Arkema Orgasol® Invent PA12 (Nylon 12) for powder bed fusion Available online: https://www.extrememateriales-arkema.com/en/markets-and-applications/3d-printing/powder-bed-fusion/#pa12 (accessed on Feb 2, 2022).

78. Lexow, M.M.; Drummer, D. New Materials for SLS: The Use of Antistatic and Flow Agents. *J. Powder Technol.* **2016**, *2016*, 1–9.

79. Laumer, T.; Stichel, T.; Raths, M.; Schmidt, M. Analysis of the influence of different flowability on part characteristics regarding the simultaneous laser beam melting of polymers. In Proceedings of the Physics Procedia; Elsevier B.V., 2016; Vol. 83, pp. 937–946.

80. Blümel, C.; Sachs, M.; Laumer, T.; Winzer, B.; Schmidt, J.; Schmidt, M.; Peukert, W.; Wirth, K.E. Increasing flowability and bulk density of PE-HD powders by a dry particle coating process and impact on LBM processes. *Rapid Prototyp. J.* **2015**, *21*, 697–704.

81. Berretta, S.; Ghita, O.; Evans, K.E. Morphology of polymeric powders in Laser Sintering (LS): From Polyamide to new PEEK powders. *Eur. Polym. J.* **2014**, *59*, 218–229.

82. Xi, S.; Zhang, P.; Huang, Y.; Kong, M.; Yang, Q.; Li, G. Laser sintering of cryogenically ground polymer powders into high-performance parts: The role of dry particle coating with a conductive flow agent. *Polymer (Guildf).* **2020**, *186*, 122044.

83. Kruth, J.P.; Levy, G.; Klocke, F.; Childs, T.H.C. Consolidation phenomena in laser and powder-bed based layered manufacturing. *CIRP Ann. - Manuf. Technol.* **2007**, *56*, 730–759.

84. Schmachtenberg, E.; Seul, T. Model of isothermic laser sintering. In Proceedings of the 60th Anual Technical Conference of the Society of Plastic Engineers (ANTEC); San Francisco, California, 2002.

85. Drummer, D.; Rietzel, D.; Kühnlein, F. Development of a characterization approach for the sintering behavior of new thermoplastics for selective laser sintering. *Phys. Procedia* **2010**, *5*, 533–542.

86. Chen, P.; Cai, H.; Li, Z.; Li, M.; Wu, H.; Su, J.; Wen, S.; Zhou, Y.; Liu, J.; Wang, C.; et al. Crystallization kinetics of polyetheretherketone during high temperature-selective laser sintering. *Addit. Manuf.* **2020**, *36*, 101615.

87. Zhao, M.; Wudy, K.; Drummer, D. Crystallization kinetics of polyamide 12 during Selective laser sintering. *Polymers (Basel).* **2018**, *10*.

88. Soldner, D.; Greiner, S.; Burkhardt, C.; Drummer, D.; Steinmann, P.; Mergheim, J. Numerical and experimental investigation of the isothermal assumption in selective laser sintering of PA12. *Addit. Manuf.* **2021**, *37*, 101676.

89. Greiner, S.; Jaksch, A.; Cholewa, S.; Drummer, D. Development of material-adapted processing strategies for laser sintering of polyamide 12. *Adv. Ind. Eng. Polym. Res.* **2021**.

90. Bourell, D.L.; Watt, T.J.; Leigh, D.K.; Fulcher, B. Performance limitations in polymer laser sintering. *Phys. Procedia* **2014**, *56*, 147–156.

91. Pilipović, A.; Brajlih, T.; Drstvenšek, I. Influence of processing parameters on tensile properties of SLS polymer product. *Polymers (Basel).* **2018**, *10*, 1208.

92. Franco, A.; Lanzetta, M.; Romoli, L. Experimental analysis of selective laser sintering of polyamide powders: An energy perspective. *J. Clean. Prod.* **2010**, *18*, 1722–1730.

93. Kruth, J.P.; Wang, X.; Laoui, T.; Froyen, L. Lasers and materials in selective laser sintering. *Assem. Autom.* **2003**, *23*, 357–371.

94. Bierwisch, C.; Mohseni-Mofidi, S.; Dietemann, B.; Grünewald, M.; Rudloff, J.; Lang, M. Universal process diagrams for laser sintering of polymers. *Mater. Des.* **2021**, *199*.

95. Xin, L.; Boutaous, M.; Xin, S.; Siginer, D.A. Numerical modeling of the heating phase of the selective laser sintering process. *Int. J. Therm. Sci.* **2017**, *120*, 50–62.

96. Gusarov, A. V.; Yadroitsev, I.; Bertrand, P.; Smurov, I. Model of radiation and heat transfer in laser-powder interaction zone at selective laser melting. *J. Heat Transfer* **2009**, *131*, 1–10.

97. Foroozmehr, A.; Badrossamay, M.; Foroozmehr, E.; Golabi, S. Finite Element Simulation of Selective Laser Melting process considering Optical Penetration Depth of laser in powder bed. *Mater. Des.* **2016**, *89*, 255–263.

98. Laumer, T.; Stichel, T.; Nagulin, K.; Schmidt, M. Optical analysis of polymer powder materials for Selective Laser Sintering. *Polym. Test.* **2016**, *56*, 207–213.

99. Osmanlic, F.; Wudy, K.; Laumer, T.; Schmidt, M.; Drummer, D.; Körner, C. Modeling of laser beam absorption in a polymer powder bed. *Polymers (Basel).* **2018**, *10*, 1–11.

100. Xin, L.; Boutaous, M.; Xin, S.; Siginer, D.A. Multiphysical modeling of the heating phase in the polymer powder bed fusion process. *Addit. Manuf.* **2017**, *18*, 121–135.

101. Peyre, P.; Rouchausse, Y.; Defauchy, D.; Régnier, G. Experimental and numerical analysis of the selective laser sintering (SLS) of PA12 and PEKK semi-crystalline polymers. *J. Mater. Process. Technol.* **2015**, *225*, 326–336.

102. Dong, L.; Makradi, A.; Ahzi, S.; Remond, Y. Three-dimensional transient finite element analysis of the selective laser sintering process. *J. Mater. Process. Technol.* **2009**, *209*, 700–706.

103. Riedlbauer, D.; Drexler, M.; Drummer, D.; Steinmann, P.; Mergheim, J. Modelling, simulation and experimental validation of heat transfer in selective laser melting of the polymeric material PA12. *Comput. Mater. Sci.* **2014**, *93*, 239–248.

104. Shen, F.; Yuan, S.; Chua, C.K.; Zhou, K. Development of process efficiency maps for selective laser sintering of polymeric composite powders: Modeling and experimental testing. *J. Mater. Process. Technol.* **2018**, *254*, 52–59.

105. Mokrane, A.; Boutaous, M.; Xin, S. Process of selective laser sintering of polymer powders: Modeling, simulation, and validation. *Comptes Rendus - Mec.* **2018**, *346*, 1087–1103.

106. Li, M.; Han, Y.; Zhou, M.; Chen, P.; Gao, H.; Zhang, Y.; Zhou, H. Experimental investigating and numerical simulations of the thermal behavior and process optimization for selective laser sintering of PA6. *J. Manuf. Process.* **2020**, *56*, 271–279.

107. Yuan, S.; Li, J.; Yao, X.; Zhu, J.; Gu, X.; Gao, T.; Xu, Y.; Zhang, W. Intelligent optimization system for powder bed fusion of processable thermoplastics. *Addit. Manuf.* **2020**, *34*, 101182.

108. Vasquez, M.; Haworth, B.; Hopkinson, N. Optimum sintering region for

laser sintered Nylon-12. In Proceedings of the Proceedings of the Institution of Mechanical Engineers, Part B: Journal of Engineering Manufacture; 2011; Vol. 225, pp. 2240–2248.

109. Gibson, I.; Shi, D. Material properties and fabrication parameters in selective laser sintering process. *Rapid Prototyp. J.* **1997**, *3*, 129–136.

110. Williams, J.D.; Deckard, C.R. Advances in modeling the effects of selected parameters on the SLS process Advances in modeling the effects of selected parameters on the SLS process. *Rapid Prototyp. J.* **1998**, *4*, 90–100.

111. Caulfield, B.; McHugh, P.E.; Lohfeld, S. Dependence of mechanical properties of polyamide components on build parameters in the SLS process. *J. Mater. Process. Technol.* **2007**, *182*, 477–488.

112. Hopkinson, N.; Majewski, C.E.; Zarringhalam, H. Quantifying the degree of particle melt in Selective Laser Sintering®. *CIRP Ann. - Manuf. Technol.* **2009**, *58*, 197–200.

113. Starr, T.L.; Gornet, T.J.; Usher, J.S. The effect of process conditions on mechanical properties of laser-sintered nylon. *Rapid Prototyp. J.* **2011**, *17*, 418–423.

114. Usher, J.S.; Gornet, T.J.; Starr, T.L. Weibull growth modeling of laser-sintered nylon 12. *Rapid Prototyp. J.* **2013**, *19*, 300–306.

115. Beal, V.E.; Paggi, R.A.; Salmoria, G. V.; Lago, A. Statistical Evaluation of Laser Energy Density Effect on Mechanical Properties of Polyamide Parts Manufactured by Selective Laser Sintering. *J. Appl. Polym. Sci.* **2009**, *113*, 2910–2919.

116. Hofland, E.C.; Baran, I.; Wismeijer, D.A. Correlation of Process Parameters with Mechanical Properties of Laser Sintered PA12 Parts. *Adv. Mater. Sci. Eng.* **2017**, *2017*, 1–11.

117. Stoia, D.I.; Marsavina, L.; Linul, E. Correlations between process parameters and outcome properties of laser-sintered polyamide. *Polymers (Basel).* **2019**, *11*, 1850.

118. Zhu, W.; Yan, C.; Shi, Y.; Wen, S.; Han, C.; Cai, C.; Liu, J.; Shi, Y. Study on the selective laser sintering of a low-isotacticity polypropylene powder. *Rapid Prototyp. J.* **2016**, *22*, 621–629.

119. Singh, A.K.; Prakash, R.S. Response surface-based simulation modeling

for selective laser sintering process. *Rapid Prototyp. J.* **2010**, *16*, 441–449.

120. Negi, S.; Dhiman, S.; Sharma, R.K. Determining the effect of sintering conditions on mechanical properties of laser sintered glass filled polyamide parts using RSM. *Meas. J. Int. Meas. Confed.* **2015**, *68*, 205–218.

121. Pilipović, A.; Drstvenšek, I.; Šercer, M. Mathematical model for the selection of processing parameters in selective laser sintering of polymer products. *Adv. Mech. Eng.* **2014**, *2014*.

122. Vasquez, M.; Haworth, B.; Hopkinson, N. Methods for quantifying the stable sintering region in laser sintered polyamide-12. *Polym. Eng. Sci.* **2013**, *53*, 1230–1240.

123. Yuan, S.; Bai, J.; Chua, C.K.; Wei, J.; Zhou, K. Material evaluation and process optimization of CNT-coated polymer powders for selective laser sintering. *Polymers (Basel).* **2016**, *8*, 370.

124. Frenkel, J. Viscous flow of crystalline bodies under the action of surface tension. *J. Phys.* **1945**, *9*, 385–391.

125. Bellehumeur, C.T.; Kontopoulou, M.; Vlachopoulos, J. The role of viscoelasticity in polymer sintering. *Rheol. Acta* **1998**, *37*, 270–278.

126. Zhao, M.; Drummer, D.; Wudy, K.; Drexler, M. Sintering Study of Polyamide 12 Particles for Selective Laser Melting. *Int. J. Recent Contrib. from Eng. Sci. IT* **2015**, *3*, 28.

127. Verbelen, L.; Dadbakhsh, S.; Van Den Eynde, M.; Kruth, J.P.; Goderis, B.; Van Puyvelde, P. Characterization of polyamide powders for determination of laser sintering processability. *Eur. Polym. J.* **2016**, *75*, 163–174.

128. Dadbakhsh, S.; Verbelen, L.; Verkinderen, O.; Strobbe, D.; Van Puyvelde, P.; Kruth, J.P. Effect of PA12 powder reuse on coalescence behaviour and microstructure of SLS parts. *Eur. Polym. J.* **2017**, *92*, 250–262.

129. Benedetti, L.; Brulé, B.; Decraemer, N.; Evans, K.E.; Ghita, O. Evaluation of particle coalescence and its implications in laser sintering. *Powder Technol.* **2019**, *342*, 917–928.

130. Berretta, S.; Wang, Y.; Davies, R.; Ghita, O.R. Polymer viscosity, particle coalescence and mechanical performance in high-temperature laser sintering. *J. Mater. Sci.* **2016**, *51*, 4778–4794.

131. Papadatos, A.L.; Ahzi, S.; Deckard, C.R.; Paul, F.W. On dimensional

stabilities : Modeling of the Bonus-Z during the SLS Process. *1997 Int. Solid Free. Fabr. Symp.* **1997**, 709–716.

132. Goodridge, R.D.; Shofner, M.L.; Hague, R.J.M.; McClelland, M.; Schlea, M.R.; Johnson, R.B.; Tuck, C.J. Processing of a Polyamide-12/carbon nanofibre composite by laser sintering. *Polym. Test.* **2011**, *30*, 94–100.

133. Wang, Y.; Rouholamin, D.; Davies, R.; Ghita, O.R. Powder characteristics, microstructure and properties of graphite platelet reinforced Poly Ether Ether Ketone composites in High Temperature Laser Sintering (HT-LS). *Mater. Des.* **2015**, *88*, 1310–1320.

134. Yan, C.; Hao, L.; Xu, L.; Shi, Y. Preparation, characterisation and processing of carbon fibre/polyamide-12 composites for selective laser sintering. *Compos. Sci. Technol.* **2011**, *71*, 1834–1841.

135. Chen, B.; Berretta, S.; Davies, R.; Ghita, O. Characterisation of carbon fibre (Cf) - Poly Ether Ketone (PEK) composite powders for laser sintering. *Polym. Test.* **2019**, *76*, 65–72.

136. Takahashi, K.; Tsukamoto, M.; Masuno, S.; Sato, Y. Heat conduction analysis of laser CFRP processing with IR and UV laser light. *Compos. Part A Appl. Sci. Manuf.* **2016**, *84*, 114–122.

137. Laumer, T.; Stichel, T.; Sachs, M.; Amend, P.; Schmidt, M. Qualification and modification of new polymer powders for laser beam melting using Ulbricht spheres. *High Value Manuf. Adv. Res. Virtual Rapid Prototyp. - Proc. 6th Int. Conf. Adv. Res. Rapid Prototyping, VR@P 2013* **2014**, 255–260.

138. Athreya, S.R.; Kalaitzidou, K.; Das, S. Processing and characterization of a carbon black-filled electrically conductive Nylon-12 nanocomposite produced by selective laser sintering. *Mater. Sci. Eng. A* **2010**, *527*, 2637–2642.

139. Bai, J.; Goodridge, R.D.; Yuan, S.; Zhou, K.; Chua, C.K.; Wei, J. Thermal influence of CNT on the polyamide 12 nanocomposite for selective laser sintering. *Molecules* **2015**, *20*, 19041–19050.

140. Flodberg, G.; Pettersson, H.; Yang, L. Pore analysis and mechanical performance of selective laser sintered objects. *Addit. Manuf.* **2018**, *24*, 307–315.

141. Yan, M.; Tian, X.; Peng, G.; Li, D.; Zhang, X. High temperature rheological behavior and sintering kinetics of CF/PEEK composites during

selective laser sintering. *Compos. Sci. Technol.* **2018**, *165*, 140–147.

142. Lanzl, L.; Wudy, K.; Drummer, D. The effect of short glass fibers on the process behavior of polyamide 12 during selective laser beam melting. *Polym. Test.* **2020**, *83*, 106313.

143. Arai, S.; Tsunoda, S.; Yamaguchi, A.; Ougizawa, T. Effects of short-glass-fiber content on material and part properties of poly(butylene terephthalate) processed by selective laser sintering. *Addit. Manuf.* **2018**, *21*, 683–693.

144. Jing, W.; Hui, C.; Qiong, W.; Hongbo, L.; Zhanjun, L. Surface modification of carbon fibers and the selective laser sintering of modified carbon fiber/nylon 12 composite powder. *Mater. Des.* **2017**, *116*, 253–260.

145. Jansson, A.; Pejryd, L. Characterisation of carbon fibre-reinforced polyamide manufactured by selective laser sintering. *Addit. Manuf.* **2016**, *9*, 7–13.

146. Badini, C.; Padovano, E.; Lambertini, V.G. Preferred orientation of chopped fibers in polymer-based composites processed by selective laser sintering and fused deposition modeling : Effects on mechanical properties. **2020**, 1–12.

147. Khudiakova, A.; Berer, M.; Niedermair, S.; Plank, B.; Truszkiewicz, E.; Meier, G.; Stepanovsky, H.; Wolfahrt, M.; Pinter, G.; Lackner, J. Systematic analysis of the mechanical anisotropy of fibre-reinforced polymer specimens produced by laser sintering. *Addit. Manuf.* **2020**, *36*, 101671.

148. Tang, H.; Chen, H.; Sun, Q.; Chen, Z.; Yan, W. Experimental and computational analysis of structure-property relationship in carbon fiber reinforced polymer composites fabricated by selective laser sintering. *Compos. Part B Eng.* **2021**, *204*, 108499.

149. Fischer, S.; Pfister, A.; Galitz, V.; Lyons, B.; Robinson, C.; Rupel, K.; Booth, R.; Kubiak, S. A High-performance Material for Aerospace Applications: Development of carbon fiber filled PEKK for laser sintering. *Solid Free. Fabr. 2016 Proc. 27th Annu. Int. Solid Free. Fabr. Symp. - An Addit. Manuf. Conf. SFF 2016* **2016**, 808–813.

150. Chen, B.; Wang, Y.; Berretta, S.; Ghita, O. Poly Aryl Ether Ketones (PAEKs) and carbon-reinforced PAEK powders for laser sintering. *J. Mater. Sci.* **2017**, *52*, 6004–6019.

151. Czelusniak, T.; Amorim, F.L. Selective laser sintering of carbon fiber–

reinforced PA12: Gaussian process modeling and stochastic optimization of process variables. *Int. J. Adv. Manuf. Technol.* **2020**, *110*, 2049–2066.

152. Wickramasinghe, S.; Do, T.; Tran, P. FDM-Based 3D printing of polymer and associated composite: A review on mechanical properties, defects and treatments. *Polymers (Basel).* **2020**, *12*, 1–42.

153. Bertolino, M.; Battegazzore, D.; Arrigo, R.; Frache, A. Designing 3D printable polypropylene: Material and process optimisation through rheology. *Addit. Manuf.* **2021**, *40*, 101944.

154. Duty, C.; Ajinjeru, C.; Kishore, V.; Compton, B.; Hmeidat, N.; Chen, X.; Liu, P.; Hassen, A.A.; Lindahl, J.; Kunc, V. What makes a material printable? A viscoelastic model for extrusion-based 3D printing of polymers. *J. Manuf. Process.* **2018**, *35*, 526–537.

155. Elbadawi, M. Polymeric Additive Manufacturing: The Necessity and Utility of Rheology. In *Polymer Rheology*; Rivera-Armenta, J.L., Salazar Cruz, B.A., Eds.; IntechOpen: London, United Kingdom, 2018; pp. 1–63.

156. Blok, L.G.; Longana, M.L.; Yu, H.; Woods, B.K.S. An investigation into 3D printing of fibre reinforced thermoplastic composites. *Addit. Manuf.* **2018**, *22*, 176–186.

157. Bellehumeur, C.; Li, L.; Sun, Q.; Gu, P. Modeling of bond formation between polymer filaments in the fused deposition modeling process. *J. Manuf. Process.* **2004**, *6*, 170–178.

158. Sun, Q.; Rizvi, G.M.; Bellehumeur, C.T.; Gu, P. Effect of processing conditions on the bonding quality of FDM polymer filaments. *Rapid Prototyp. J.* **2008**, *14*, 72–80.

159. Faes, M.; Ferraris, E.; Moens, D. Influence of Inter-layer Cooling time on the Quasi-static Properties of ABS Components Produced via Fused Deposition Modelling. In Proceedings of the Procedia CIRP; Elsevier B.V., 2016; Vol. 42, pp. 748–753.

160. Aliheidari, N.; Tripuraneni, R.; Ameli, A.; Nadimpalli, S. Fracture resistance measurement of fused deposition modeling 3D printed polymers. *Polym. Test.* **2017**, *60*, 94–101.

161. Abbott, A.C.; Tandon, G.P.; Bradford, R.L.; Koerner, H.; Baur, J.W. Process-structure-property effects on ABS bond strength in fused filament fabrication. *Addit. Manuf.* **2018**, *19*, 29–38.

162. Coogan, T.J.; Kazmer, D.O. Prediction of interlayer strength in material extrusion additive manufacturing. *Addit. Manuf.* **2020**, *35*, 101368.

163. Wang, T.M.; Xi, J.T.; Jin, Y. A model research for prototype warp deformation in the FDM process. *Int. J. Adv. Manuf. Technol.* **2007**, *33*, 1087–1096.

164. Stoof, D.; Pickering, K. Sustainable composite fused deposition modelling filament using recycled pre-consumer polypropylene. *Compos. Part B Eng.* **2018**, *135*, 110–118.

165. Carneiro, O.S.; Silva, A.F.; Gomes, R. Fused deposition modeling with polypropylene. *Mater. Des.* **2015**, *83*, 768–776.

166. Spoerk, M.; Holzer, C.; Gonzalez-Gutierrez, J. Material extrusion-based additive manufacturing of polypropylene: A review on how to improve dimensional inaccuracy and warpage. *J. Appl. Polym. Sci.* **2020**, *137*, 1–16.

167. Ahn, S.H.; Montero, M.; Odell, D.; Roundy, S.; Wright, P.K. Anisotropic material properties of fused deposition modeling ABS. *Rapid Prototyp. J.* **2002**, *8*, 248–257.

168. Ferreira, I.; Machado, M.; Alves, F.; Torres Marques, A. A review on fibre reinforced composite printing via FFF. *Rapid Prototyp. J.* **2019**, *25*, 972–988.

169. Yasa, E.; Ersoy, K. Additive Manufacturing of Polymer Matrix Composites. In *Aircraft Technology*; Kushar, M.C., Ed.; IntechOpen: London, 2018; pp. 147–169 ISBN 978-1-78923-645-3.

170. Shofner, M.L.; Lozano, K.; Rodríguez-Macías, F.J.; Barrera, E. V Nanofiber-Reinforced Polymers Prepared by Fused Deposition Modeling. *J. Appl. Polym. Sci.* **2003**, *89*, 3081–3090.

171. Duty, C.; Kunc, V.; Compton, B.; Post, B.; Erdman, D.; Smith, R.; Lind, R.; Lloyd, P.; Love, L. Structure and mechanical behavior of Big Area Additive Manufacturing (BAAM) materials. *Rapid Prototyp. J.* **2017**, *23*, 181–189.

172. Compton, B.G.; Post, B.K.; Duty, C.E.; Love, L.; Kunc, V. Thermal analysis of additive manufacturing of large-scale thermoplastic polymer composites. *Addit. Manuf.* **2017**, *17*, 77–86.

173. DeNardo, N.M. Additive manufacturing of carbon-fiber-reinforced thermoplastic composites, 2016.

174. Yang, C.; Tian, X.; Li, D.; Cao, Y.; Zhao, F.; Shi, C. Influence of thermal processing conditions in 3D printing on the crystallinity and mechanical properties of PEEK material. *J. Mater. Process. Technol.* **2017**, *248*, 1–7.

175. Ning, F.; Cong, W.; Qiu, J.; Wei, J.; Wang, S. Additive manufacturing of carbon fiber reinforced thermoplastic composites using fused deposition modeling. *Compos. Part B Eng.* **2015**, *80*, 369–378.

176. Tekinalp, H.L.; Kunc, V.; Velez-Garcia, G.M.; Duty, C.E.; Love, L.J.; Naskar, A.K.; Blue, C.A.; Ozcan, S. Highly oriented carbon fiber-polymer composites via additive manufacturing. *Compos. Sci. Technol.* **2014**, *105*, 144–150.

177. Hofstätter, T.; Gutmann, I.W.; Koch, T.; Pedersen, D.B.; Tosello, G.; Heinz, G.; Hansen, H.N. Distribution and orientation of carbon fibers in polylactic acid parts produced by fused deposition modeling. In Proceedings of the Proceedings - ASPE/euspen 2016 Summer Topical Meeting: Dimensional Accuracy and Surface Finish in Additive Manufacturing; 2016; pp. 44–49.

178. Liao, G.; Li, Z.; Cheng, Y.; Xu, D.; Zhu, D.; Jiang, S.; Guo, J.; Chen, X.; Xu, G.; Zhu, Y. Properties of oriented carbon fiber/polyamide 12 composite parts fabricated by fused deposition modeling. *Mater. Des.* **2018**, *139*, 283–292.

179. Jiang, D.; Smith, D.E. Anisotropic mechanical properties of oriented carbon fiber filled polymer composites produced with fused filament fabrication. *Addit. Manuf.* **2017**, *18*, 84–94.

180. Ferreira, R.T.L.; Amatte, I.C.; Dutra, T.A.; Bürger, D. Experimental characterization and micrography of 3D printed PLA and PLA reinforced with short carbon fibers. *Compos. Part B Eng.* **2017**, *124*, 88–100.

181. Zhang, W.; Cotton, C.; Sun, J.; Heider, D.; Gu, B.; Sun, B.; Chou, T.W. Interfacial bonding strength of short carbon fiber/acrylonitrile-butadiene-styrene composites fabricated by fused deposition modeling. *Compos. Part B Eng.* **2018**, *137*, 51–59.

182. Ning, F.; Cong, W.; Hu, Y.; Wang, H. Additive manufacturing of carbon fiber-reinforced plastic composites using fused deposition modeling: Effects of process parameters on tensile properties. *J. Compos. Mater.* **2017**, *51*, 451–462.

183. Spoerk, M.; Savandaiah, C.; Arbeiter, F.; Traxler, G.; Cardon, L.; Holzer, C.; Sapkota, J. Anisotropic properties of oriented short carbon fibre filled

polypropylene parts fabricated by extrusion-based additive manufacturing. *Compos. Part A Appl. Sci. Manuf.* **2018**, *113*, 95–104.

184. Das, A.; Gilmer, E.L.; Biria, S.; Bortner, M.J. Importance of Polymer Rheology on Material Extrusion Additive Manufacturing: Correlating Process Physics to Print Properties. *ACS Appl. Polym. Mater.* **2021**, *3*, 1218–1249.

185. Ajinjeru, C.; Kishore, V.; Liu, P.; Lindahl, J.; Hassen, A.A.; Kunc, V.; Post, B.; Love, L.; Duty, C. Determination of melt processing conditions for high performance amorphous thermoplastics for large format additive manufacturing. *Addit. Manuf.* **2018**, *21*, 125–132.

186. Zhuo, P.; Li, S.; Ashcroft, I.A.; Jones, A.I. Material extrusion additive manufacturing of continuous fibre reinforced polymer matrix composites: A review and outlook. *Compos. Part B Eng.* **2021**, *224*, 109143.

187. Zhong, W.; Li, F.; Zhang, Z.; Song, L.; Li, Z. Research on rapid-prototyping/part manufacturing (RP&M) for the continuous fiber reinforced composite. *Mater. Manuf. Process.* **2001**, *16*, 17–26.

188. Dickson, A.; Abourayana, H.; Dowling, D. Composites Using Fused Filament Fabrication — A Review. *Polymers (Basel).* **2020**, *12*, 1–18.

189. Matsuzaki, R.; Ueda, M.; Namiki, M.; Jeong, T.K.; Asahara, H.; Horiguchi, K.; Nakamura, T.; Todoroki, A.; Hirano, Y. Three-dimensional printing of continuous-fiber composites by in-nozzle impregnation. *Sci. Rep.* **2016**, *6*, 1–7.

190. Yang, C.; Tian, X.; Liu, T.; Cao, Y.; Li, D. 3D printing for continuous fiber reinforced thermoplastic composites: Mechanism and performance. *Rapid Prototyp. J.* **2017**, *23*.

191. Tian, X.; Liu, T.; Yang, C.; Wang, Q.; Li, D. Interface and performance of 3D printed continuous carbon fiber reinforced PLA composites. *Compos. Part A Appl. Sci. Manuf.* **2016**, *88*, 198–205.

192. Liu, T.; Tian, X.; Zhang, M.; Abliz, D.; Li, D.; Ziegmann, G. Interfacial performance and fracture patterns of 3D printed continuous carbon fiber with sizing reinforced PA6 composites. *Compos. Part A Appl. Sci. Manuf.* **2018**, *114*, 368–376.

193. Mark, T.G.; Gozdz, A.S. Three dimensional printer with composite filament fabrication 2015, 1–46.

194. Caminero, M.A.; Chacón, J.M.; García-Moreno, I.; Rodríguez, G.P. Impact damage resistance of 3D printed continuous fibre reinforced thermoplastic composites using fused deposition modelling. *Compos. Part B Eng.* **2018**, *148*, 93–103.

195. Markforged *Material datasheet Composites Rev 3.1*; Watertown, Massachusetts, 2019;

196. Anisoprint Anisoprint Industrial Solutions Available online: https://anisoprint.com/solutions/industrial/ (accessed on Feb 4, 2022).

197. AZAROV, A.V.; VASILIEV, V.V.; RAZIN, A.F.; SALOV, V.A. Composite Reinforcing Thread, Prepreg, Tape for 3D Printing and Installation for Preparing Same 2017, 1–13.

198. CEAD Group CFAM (Continuous Fiber Additive Manufacturing) Prime Available online: https://ceadgroup.com/solutions/gantry-based-solutions/cfam-prime/ (accessed on Feb 4, 2022).

199. Hu, Q.; Duan, Y.; Zhang, H.; Liu, D.; Yan, B.; Peng, F. Manufacturing and 3D printing of continuous carbon fiber prepreg filament. *J. Mater. Sci.* **2018**, *53*, 1887–1898.

200. van de Werken, N.; Koirala, P.; Ghorbani, J.; Doyle, D.; Tehrani, M. Investigating the hot isostatic pressing of an additively manufactured continuous carbon fiber reinforced PEEK composite. *Addit. Manuf.* **2021**, *37*, 101634.

201. Struzziero, G.; Barbezat, M.; Skordos, A.A. Consolidation of continuous fibre reinforced composites in additive processes: A review. *Addit. Manuf.* **2021**, *48*, 102458.

202. Der Klift, F. Van; Koga, Y.; Todoroki, A.; Ueda, M.; Hirano, Y.; Matsuzaki, R. 3D Printing of Continuous Carbon Fibre Reinforced Thermo-Plastic (CFRTP) Tensile Test Specimens. *Open J. Compos. Mater.* **2016**, *06*, 18–27.

203. Goh, G.D.; Dikshit, V.; Nagalingam, A.P.; Goh, G.L.; Agarwala, S.; Sing, S.L.; Wei, J.; Yeong, W.Y. Characterization of mechanical properties and fracture mode of additively manufactured carbon fiber and glass fiber reinforced thermoplastics. *Mater. Des.* **2018**, *137*, 79–89.

204. Chabaud, G.; Castro, M.; Denoual, C.; Le Duigou, A. Hygromechanical properties of 3D printed continuous carbon and glass fibre reinforced polyamide composite for outdoor structural applications. *Addit. Manuf.*

2019, *26*, 94–105.

205. Pascual-González, C.; Iragi, M.; Fernández, A.; Fernández-Blázquez, J.P.; Aretxabaleta, L.; Lopes, C.S. An approach to analyse the factors behind the micromechanical response of 3D-printed composites. *Compos. Part B Eng.* **2020**, *186*, 107820.

206. He, Q.; Wang, H.; Fu, K.; Ye, L. 3D printed continuous CF/PA6 composites: Effect of microscopic voids on mechanical performance. *Compos. Sci. Technol.* **2020**, *191*, 108077.

207. Dickson, A.N.; Barry, J.N.; McDonnell, K.A.; Dowling, D.P. Fabrication of continuous carbon, glass and Kevlar fibre reinforced polymer composites using additive manufacturing. *Addit. Manuf.* **2017**, *16*, 146–152.

208. Iragi, M.; Pascual-González, C.; Esnaola, A.; Lopes, C.S.; Aretxabaleta, L. Ply and interlaminar behaviours of 3D printed continuous carbon fibre-reinforced thermoplastic laminates; effects of processing conditions and microstructure. *Addit. Manuf.* **2019**, *30*, 100884.

209. Justo, J.; Távara, L.; García-Guzmán, L.; París, F. Characterization of 3D printed long fibre reinforced composites. *Compos. Struct.* **2018**, *185*, 537–548.

210. Chacón, J.M.; Caminero, M.A.; Núñez, P.J.; García-Plaza, E.; García-Moreno, I.; Reverte, J.M. Additive manufacturing of continuous fibre reinforced thermoplastic composites using fused deposition modelling: Effect of process parameters on mechanical properties. *Compos. Sci. Technol.* **2019**, *181*, 107688.

211. Naranjo-Lozada, J.; Ahuett-Garza, H.; Orta-Castañón, P.; Verbeeten, W.M.H.; Sáiz-González, D. Tensile properties and failure behavior of chopped and continuous carbon fiber composites produced by additive manufacturing. *Addit. Manuf.* **2019**, *26*, 227–241.

212. van de Werken, N.; Hurley, J.; Khanbolouki, P.; Sarvestani, A.N.; Tamijani, A.Y.; Tehrani, M. Design considerations and modeling of fiber reinforced 3D printed parts. *Compos. Part B Eng.* **2019**, *160*, 684–692.

213. Dutra, T.A.; Ferreira, R.T.L.; Resende, B.H.; Guimaraes, A. Mechanical characterization and asymptotic homogenization of 3D-printed continuous carbon fiber-reinforced thermoplastic. *J. Brazilian Soc. Mech. Sci. Eng.* **2019**, *41*.

214. Todoroki, A.; Oasada, T.; Mizutani, Y.; Suzuki, Y.; Ueda, M.; Matsuzaki, R.; Hirano, Y. Tensile property evaluations of 3D printed continuous carbon fiber reinforced thermoplastic composites. *Adv. Compos. Mater.* **2020**, *29*, 147–162.

215. Saeed, K.; McIlhagger, A.; Harkin-Jones, E.; Kelly, J.; Archer, E. Predication of the in-plane mechanical properties of continuous carbon fibre reinforced 3D printed polymer composites using classical laminated-plate theory. *Compos. Struct.* **2021**, *259*, 113226.

216. Caminero, M.A.; Chacón, J.M.; García-Moreno, I.; Reverte, J.M. Interlaminar bonding performance of 3D printed continuous fibre reinforced thermoplastic composites using fused deposition modelling. *Polym. Test.* **2018**, *68*, 415–423.

217. Mei, H.; Ali, Z.; Yan, Y.; Ali, I.; Cheng, L. Influence of mixed isotropic fiber angles and hot press on the mechanical properties of 3D printed composites. *Addit. Manuf.* **2019**, *27*, 150–158.

218. Ibrahim, Y.; Elkholy, A.; Schofield, J.S.; Melenka, G.W.; Kempers, R. Effective thermal conductivity of 3D-printed continuous fiber polymer composites. *Adv. Manuf. Polym. Compos. Sci.* **2020**, *6*, 17–28.

219. Kousiatza, C.; Tzetzis, D.; Karalekas, D. In-situ characterization of 3D printed continuous fiber reinforced composites: A methodological study using fiber Bragg grating sensors. *Compos. Sci. Technol.* **2019**, *174*, 134–141.

220. Peng, Y.; Wu, Y.; Wang, K.; Gao, G.; Ahzi, S. Synergistic reinforcement of polyamide-based composites by combination of short and continuous carbon fibers via fused filament fabrication. *Compos. Struct.* **2019**, *207*, 232–239.

221. Peng, Y.; Wu, Y.; Li, S.; Wang, K.; Yao, S.; Liu, Z.; Garmestani, H. Tailorable rigidity and energy-absorption capability of 3D printed continuous carbon fiber reinforced polyamide composites. *Compos. Sci. Technol.* **2020**, *199*, 108337.

222. 9T Labs Additive Fusion Solution Available online: https://www.9tlabs.com/solutions/additive-fusion-solution (accessed on Feb 4, 2022).

223. Madsen, B.; Lilholt, H. Physical and mechanical properties of unidirectional plant fibre composites-an evaluation of the influence of porosity. *Compos. Sci. Technol.* **2003**, *63*, 1265–1272.

224. Rodríguez, J.F.; Thomas, J.P.; Renaud, J.E. Mechanical behavior of acrylonitrile butadiene styrene fused deposition materials modeling. *Rapid Prototyp. J.* **2003**, *9*, 219–230.

225. Abderrafai, Y.; Hadi Mahdavi, M.; Sosa-Rey, F.; Hérard, C.; Otero Navas, I.; Piccirelli, N.; Lévesque, M.; Therriault, D. Additive manufacturing of short carbon fiber-reinforced polyamide composites by fused filament fabrication: Formulation, manufacturing and characterization. *Mater. Des.* **2022**, *214*, 110358.

226. Choi, J.Y.; Kortschot, M.T. Stiffness prediction of 3D printed fiber-reinforced thermoplastic composites. *Rapid Prototyp. J.* **2020**, *26*, 549–555.

227. Somireddy, M.; Singh, C. V.; Czekanski, A. Mechanical behaviour of 3D printed composite parts with short carbon fiber reinforcements. *Eng. Fail. Anal.* **2020**, *107*, 104232.

228. Zhu, W.; Yan, C.; Shi, Y.; Wen, S.; Liu, J.; Wei, Q.; Shi, Y. A novel method based on selective laser sintering for preparing high-performance carbon fibres/polyamide12/epoxy ternary composites. *Sci. Rep.* **2016**, *6*, 1–10.

229. Melenka, G.W.; Cheung, B.K.O.; Schofield, J.S.; Dawson, M.R.; Carey, J.P. Evaluation and prediction of the tensile properties of continuous fiber-reinforced 3D printed structures. *Compos. Struct.* **2016**, *153*, 866–875.

230. Al Abadi, H.; Thai, H.T.; Paton-Cole, V.; Patel, V.I. Elastic properties of 3D printed fibre-reinforced structures. *Compos. Struct.* **2018**, *193*, 8–18.

231. Yu, T.; Zhang, Z.; Song, S.; Bai, Y.; Wu, D. Tensile and flexural behaviors of additively manufactured continuous carbon fiber-reinforced polymer composites. *Compos. Struct.* **2019**, *225*, 111147.

232. Polyzos, E.; Katalagarianakis, A.; Polyzos, D.; Van Hemelrijck, D.; Pyl, L. A multi-scale analytical methodology for the prediction of mechanical properties of 3D-printed materials with continuous fibres. *Addit. Manuf.* **2020**, *36*, 101394.

233. Sharebot Sharebot SnowWhite Available online: https://www.sharebot.it/sharebot-snowwhite/ (accessed on Feb 4, 2022).

234. Berzins, M.; Childs, T.H.C.; Dalgarno, K.W.; Ryder, G.R.; Stein, G. Densification and distortion in selective laser sintering of polycarbonate. *Proc. ...* **1995**, 196–203.

235. Mousa, A.A. Experimental investigations of curling phenomenon in selective laser sintering process. *Rapid Prototyp. J.* **2016**, *22*, 405–415.

236. Ahmadi Dastjerdi, A.; Movahhedy, M.R.; Akbari, J. Optimization of process parameters for reducing warpage in selected laser sintering of polymer parts. *Addit. Manuf.* **2017**, *18*, 285–294.

237. Manshoori Yeganeh, A.; Movahhedy, M.R.; Khodaygan, S. An efficient scanning algorithm for improving accuracy based on minimising part warping in selected laser sintering process. *Virtual Phys. Prototyp.* **2019**, *14*, 59–78.

238. Soe, S.P. Quantitative analysis on SLS part curling using EOS P700 machine. *J. Mater. Process. Technol.* **2012**, *212*, 2433–2442.

239. Roboze *Roboze One brochure*; 2018;

240. Fornes, T.D.; Paul, D.R. Crystallization behavior of nylon 6 nanocomposites. *Polymer (Guildf).* **2003**, *44*, 3945–3961.

241. Vyazovkin, S.; Burnham, A.K.; Criado, J.M.; Pérez-Maqueda, L.A.; Popescu, C.; Sbirrazzuoli, N. ICTAC Kinetics Committee recommendations for performing kinetic computations on thermal analysis data. *Thermochim. Acta* 2011, *520*, 1–19.

242. Schmid, M.; Amado, F.; Levy, G.; Wegener, K. Flowability of powders for selective laser sintering (SLS) investigated by round robin test. In Proceedings of the High Value Manufacturing : Proceedings of the 6th International Conference on Advanced Research in Virtual and Rapid Prototyping; Taylor & Francis, 2013; pp. 95–99.

243. Matthews, F.L.; Rawlings, R.D. *Composite Materials: Engineering and Science*; Chapman & Hall: London, 1994; ISBN 041255976.

244. Cox, H.L. The elasticity and strength of paper and other fibrous materials. *Br. J. Appl. Phys.* **1952**, *3*, 72–79.

245. Tucker, C.L.; Liang, E. Stiffness predictions for unidirectional short-fiber composites.pdf. *Compos. Sci. Technol.* **1999**, *59*, 655–671.

246. Kelly, A.; Tyson, W.R. Tensile properties of fibre-reinforced metals: Copper/tungsten and copper/molybdenum. *J. Mech. Phys. Solids* **1965**, *13*.

247. Ogi, K.; Nishikawa, T.; Okano, Y.; Taketa, I. Mechanical properties of ABS resin reinforced with recycled CFRP. *Adv. Compos. Mater. Off. J.*

Japan Soc. Compos. Mater. **2007**, *16*, 181–194.

248. Favaloro, A. Laminate Failure Analysis (Progressive and Envelopes) Available online: https://cdmhub.org/resources/progfail (accessed on Sep 11, 2021).

249. Loukil, M.S.; Hussain, W.; Kirti, A.; Pupurs, A.; Varna, J. Thermoelastic constants of symmetric laminates with cracks in 90-layer: Application of simple models. *Plast. Rubber Compos.* **2013**, *42*, 157–166.

250. Whitney, J.M. On the ‘ ply discount method ’ for determining effective thermo-elastic constants of laminates containing transverse cracks. **2005**, *36*, 1347–1354.

251. Qian, X.; Zou, R.; OuYang, Q.; Wang, X.; Zhang, Y. Surface structural evolvement in the conversion of polyacrylonitrile precursors to carbon fibers. *Appl. Surf. Sci.* **2015**, *327*, 246–252.

252. Wu, S.; Liu, Y.; Ge, Y.; Ran, L.; Peng, K.; Yi, M. Surface structures of PAN-based carbon fibers and their influences on the interface formation and mechanical properties of carbon-carbon composites. *Compos. Part A Appl. Sci. Manuf.* **2016**, *90*, 480–488.

253. Sutton, A.T.; Kriewall, C.S.; Leu, M.C.; Newkirk, J.W. Powder characterisation techniques and effects of powder characteristics on part properties in powder-bed fusion processes. *Virtual Phys. Prototyp.* **2017**, *12*, 3–29.

254. Karsli, N.G.; Aytac, A. Tensile and thermomechanical properties of short carbon fiber reinforced polyamide 6 composites. *Compos. Part B Eng.* **2013**, *51*, 270–275.

255. Liang, J.; Xu, Y.; Wei, Z.; Song, P.; Chen, G.; Zhang, W. Mechanical properties, crystallization and melting behaviors of carbon fiber-reinforced PA6 composites. *J. Therm. Anal. Calorim.* **2014**, *115*, 209–218.

256. Lorenzo, A.T.; Arnal, M.L.; Albuerne, J.; Müller, A.J. DSC isothermal polymer crystallization kinetics measurements and the use of the Avrami equation to fit the data: Guidelines to avoid common problems. *Polym. Test.* **2007**, *26*, 222–231.

257. Neugebauer, F.; Ploshikhin, V.; Ambrosy, J.; Witt, G. Isothermal and non-isothermal crystallization kinetics of polyamide 12 used in laser sintering. *J. Therm. Anal. Calorim.* **2016**, *124*, 925–933.

258. Benedetti, L.; Brulé, B.; Decreamer, N.; Evans, K.E.; Ghita, O. Shrinkage behaviour of semi-crystalline polymers in laser sintering: PEKK and PA12. *Mater. Des.* **2019**, *181*.

259. Advanc3D Materials *Technical Data Sheet AdSint PA12 CF*; 2018;

260. Ruggi, D.; Barrès, C.; Charmeau, J.Y.; Fulchiron, R.; Barletta, D.; Poletto, M. A quantitative approach to assess high temperature flow properties of a PA 12 powder for laser sintering. *Addit. Manuf.* **2020**, *33*, 101143.

261. Amado, A.; Schmid, M.; Wegener, K. Flowability of SLS powders at elevated temperature. *Rapid.Tech* **2014**, *2*, 1–7.

262. Erdal, M.; Dag, S.; Jande, Y.; Tekin, C.M. Manufacturing of functionally graded porous products by selective laser sintering. *Mater. Sci. Forum* **2010**, *631–632*, 253–258.

263. Yuan, S.; Strobbe, D.; Kruth, J.P.; Van Puyvelde, P.; Van der Bruggen, B. Production of polyamide-12 membranes for microfiltration through selective laser sintering. *J. Memb. Sci.* **2017**, *525*, 157–162.

264. Singh, J.P.; Pandey, P.M.; Verma, A.K. Fabrication of three dimensional open porous regular structure of PA-2200 for enhanced strength of scaffold using selective laser sintering. *Rapid Prototyp. J.* **2016**, *22*, 752–765.

265. Saenz Del Burgo, L.; Ciriza, J.; Espona-Noguera, A.; Illa, X.; Cabruja, E.; Orive, G.; Hernández, R.M.; Villa, R.; Pedraz, J.L.; Alvarez, M. 3D Printed porous polyamide macrocapsule combined with alginate microcapsules for safer cell-based therapies. *Sci. Rep.* **2018**, *8*, 1–14.

266. Du, Y.; Liu, H.; Shuang, J.; Wang, J.; Ma, J.; Zhang, S. Microsphere-based selective laser sintering for building macroporous bone scaffolds with controlled microstructure and excellent biocompatibility. *Colloids Surfaces B Biointerfaces* **2015**, *135*, 81–89.

267. Heinl, M.; Laumer, T.; Bayer, F.; Hausotte, T. Temperature-dependent optical material properties of polymer powders regarding in-situ measurement techniques in additive manufacturing. *Polym. Test.* **2018**, *71*, 378–383.

268. Schuffenhauer, T.; Stichel, T.; Schmidt, M. Experimental determination of scattering processes in the interaction of laser radiation with polyamide 12 powder. *Procedia CIRP* **2020**, *94*, 85–88.

269. Wegner, A.; Witt, G. Understanding the decisive thermal procebes in laser

sintering of polyamide 12. *AIP Conf. Proc.* **2015**, *1664*, 1–6.

270. Drexler, M.; Lexow, M.; Drummer, D. Selective Laser Melting of Polymer Powder - Part Mechanics as Function of Exposure Speed. *Phys. Procedia* **2015**, *78*, 328–336.

271. Arai, S.; Tsunoda, S.; Yamaguchi, A.; Ougizawa, T. Effect of anisotropy in the build direction and laser-scanning conditions on characterization of short-glass-fiber-reinforced PBT for laser sintering. *Opt. Laser Technol.* **2019**, *113*, 345–356.

272. Chatham, C.A.; Bortner, M.J.; Johnson, B.N.; Long, T.E.; Williams, C.B. Predicting mechanical property plateau in laser polymer powder bed fusion additive manufacturing via the critical coalescence ratio. *Mater. Des.* **2021**, *201*, 109474.

273. Scherer, G.W. Viscous Sintering of a Bimodal Pore-Size Distribution. *J. Am. Ceram. Soc.* **1984**, *67*, 709–715.

274. Chen, P.; Tang, M.; Zhu, W.; Yang, L.; Wen, S.; Yan, C.; Ji, Z.; Nan, H.; Shi, Y. Systematical mechanism of Polyamide-12 aging and its micro-structural evolution during laser sintering. *Polym. Test.* **2018**, *67*, 370–379.

275. Drummer, D.; Greiner, S.; Zhao, M.; Wudy, K. A novel approach for understanding laser sintering of polymers. *Addit. Manuf.* **2019**, *27*, 379–388.

276. Toray Composite Materials America *T300 Standard Modulus Carbon Fibers*; 2018;

277. Wang, W.; Dai, Y.; Zhang, C.; Gao, X.; Zhao, M. Micromechanical Modeling of Fiber-Reinforced Composites with Statistically Equivalent Random Fiber Distribution. *Materials (Basel).* **2016**, *9*, 1–14.

278. TANAKA, K.; HOSOO, N.; KATAYAMA, T.; NOGUCHI, Y.; IZUI, K. Effect of temperature on the fiber/matrix interfacial strength of carbon fiber reinforced polyamide model composites. *Mech. Eng. J.* **2016**, *3*, 16-00158-16–00158.

279. Li, Q.; Zhao, W.; Li, Y.; Yang, W.; Wang, G. Flexural properties and fracture behavior of CF/PEEK in orthogonal building orientation by FDM: Microstructure and mechanism. *Polymers (Basel).* **2019**, *11*, 656.

280. Duifhuis, P.L. Magnetite functional filler: a compounding study in polypropylene and polyamide. *Plast. Addit. Compd.* **2001**, 14–17.

281. Weidenfeller, B.; Höfer, M.; Schilling, F. Thermal and electrical properties of magnetite filled polymers. *Compos. Part A Appl. Sci. Manuf.* **2002**, *33*, 1041–1053.

282. Dearmitt, C. Magnetite. In *Encyclopedia of Polymers and Composites*; Kar, K.K., Ed.; Springer Berlin Heidelberg, 2014 ISBN 9783642371790.

283. Krause, B.; Kroschwald, L.; Pötschke, P. The influence of the blend ratio in PA6/PA66/MWCNT blend composites on the electrical and thermal properties. *Polymers (Basel).* **2019**, *11*, 122.

284. Wypich, G. *Handbook of Polymers*; 2nd Editio.; ChemTec Publishing: Ontario, Canada, 2016; ISBN 9781895198928.

285. Rebenfeld, L.; Desio, G.P.; Wu, J.C. Effects of fibers on the glass transition temperature of polyphenylene sulfide composites. *J. Appl. Polym. Sci.* **1991**, *42*, 801–805.

286. Schick, C. Differential scanning calorimetry (DSC) of semicrystalline polymers. *Anal. Bioanal. Chem.* **2009**, *395*, 1589–1611.

287. Ois Dabrowski, F.; Bourbigot, S.; Delobel, R.; Le Bras, M. Kinetic modelling of the thermal degradation of polyamide-6 nanocomposite. *Eur. Polym. J.* **2000**, *36*, 273–284.

288. Li, J.; Tong, L.; Fang, Z.; Gu, A.; Xu, Z. Thermal degradation behavior of multi-walled carbon nanotubes/polyamide 6 composites. *Polym. Degrad. Stab.* **2006**, *91*, 2046–2052.

289. Tao, Y.; Kong, F.; Li, Z.; Zhang, J.; Zhao, X.; Yin, Q.; Xing, D.; Li, P. A review on voids of 3D printed parts by fused filament fabrication. *J. Mater. Res. Technol.* **2021**, *15*, 4860–4879.

290. Alaimo, G.; Marconi, S.; Costato, L.; Auricchio, F. Influence of meso-structure and chemical composition on FDM 3D-printed parts. *Compos. Part B Eng.* **2017**, *113*, 371–380.

291. Papon, E.A.; Haque, A. Tensile properties, void contents, dispersion and fracture behaviour of 3D printed carbon nanofiber reinforced composites. *J. Reinf. Plast. Compos.* **2018**, *37*, 381–395.

292. Guild, F.J.; Summerscales, J. Microstructural image analysis applied to fibre composite materials: a review. *Composites* **1993**, *24*, 383–393.

293. Vélez-García, G.M.; Wapperom, P.; Kunc, V.; Baird, D.G.; Zink-Sharp, A.

Sample preparation and image acquisition using optical-reflective microscopy in the measurement of fiber orientation in thermoplastic composites. *J. Microsc.* **2012**, *248*, 23–33.

294. Sharma, B.N.; Naragani, D.; Nguyen, B.N.; Tucker, C.L.; Sangid, M.D. Uncertainty quantification of fiber orientation distribution measurements for long-fiber-reinforced thermoplastic composites. *J. Compos. Mater.* **2018**, *52*, 1781–1797.

295. Peng, X.; Zhang, M.; Guo, Z.; Sang, L.; Hou, W. Investigation of processing parameters on tensile performance for FDM-printed carbon fiber reinforced polyamide 6 composites. *Compos. Commun.* **2020**, *22*, 100478.

296. Hendlmeier, A.; Simon, Ž.; Wickramasingha, Y.A.; Henderson, L.C. A comparison of compression molded and additively manufactured short carbon fiber reinforced polyamide-6 samples and the effect of different infill printing patterns. *Polym. Compos.* **2021**, *42*, 4728–4735.

297. Dul, S.; Fambri, L.; Pegoretti, A. High-Performance Polyamide/Carbon Fiber Composites for Fused Filament Fabrication: Mechanical and Functional Performances. *J. Mater. Eng. Perform.* **2021**, *30*, 5066–5085.

298. de Toro, E.V.; Sobrino, J.C.; Martínez, A.M.; Eguía, V.M.; Pérez, J.A. Investigation of a short carbon fibre-reinforced polyamide and comparison of two manufacturing processes: Fused Deposition Modelling (FDM) and polymer injection moulding (PIM). *Materials (Basel).* **2020**, *13*, 672.

299. Chicot, D.; Mendoza, J.; Zaoui, A.; Louis, G.; Lepingle, V.; Roudet, F.; Lesage, J. Mechanical properties of magnetite (Fe3O4), hematite (α-Fe2O3) and goethite (α-FeO·OH) by instrumented indentation and molecular dynamics analysis. *Mater. Chem. Phys.* **2011**, *129*, 862–870.

300. Hidaka, Y.; Anraku, T.; Otsuka, N. Deformation of iron oxides upon tensile tests at 600-1250°C. *Oxid. Met.* **2003**, *59*, 97–113.

301. Van De Steene, W.; Verstockt, J.; Degrieck, J.; Ragaert, K.; Cardon, L. An evaluation of three different techniques for melt impregnation of glass fiber bundles with polyamide 12. *Polym. Eng. Sci.* **2018**, *58*, 601–608.

302. Liu, T.; Tian, X.; Zhang, Y.; Cao, Y.; Li, D. High-pressure interfacial impregnation by micro-screw in-situ extrusion for 3D printed continuous carbon fiber reinforced nylon composites. *Compos. Part A Appl. Sci. Manuf.* **2020**, *130*, 105770.

303. Garofalo, J.; Walczyk, D. In situ impregnation of continuous thermoplastic composite prepreg for additive manufacturing and automated fiber placement. *Compos. Part A Appl. Sci. Manuf.* **2021**, *147*, 106446.

304. EMS-GRIVORY Grivory G 21 PA6I/6T TDS Available online: https://www.emsgrivory.com/en/ems-material-database/ (accessed on Nov 19, 2021).

305. Qureshi, Z.; Swait, T.; Scaife, R.; El-Dessouky, H.M. In situ consolidation of thermoplastic prepreg tape using automated tape placement technology: Potential and possibilities. *Compos. Part B Eng.* **2014**, *66*, 255–267.

306. Comer, A.J.; Ray, D.; Obande, W.O.; Jones, D.; Lyons, J.; Rosca, I.; O'Higgins, R.M.; McCarthy, M.A. Mechanical characterisation of carbon fibre-PEEK manufactured by laser-assisted automated-tape-placement and autoclave. *Compos. Part A Appl. Sci. Manuf.* **2015**, *69*, 10–20.

307. Liu, L.; Zhang, B.M.; Wang, D.F.; Wu, Z.J. Effects of cure cycles on void content and mechanical properties of composite laminates. *Compos. Struct.* **2006**, *73*, 303–309.

308. Netzel, C.; Hoffmann, D.; Battley, M.; Hubert, P.; Bickerton, S. Effects of environmental conditions on uncured prepreg characteristics and their effects on defect generation during autoclave processing. *Compos. Part A Appl. Sci. Manuf.* **2021**, *151*, 106636.

309. Rodrigo, O.; Bertrand, G. Radial thermal conductivity of a PAN type carbon fiber using the 3 omega method. *Int. J. Therm. Sci.* **2022**, *172*, 107321.

310. Whetsell, J.A.; Liang, J.; Saha, M.C.; Altan, M.C. Effects of sizing on thermal conductivity of single carbon fibers in longitudinal and radial directions. *Proc. Am. Soc. Compos. - 29th Tech. Conf. ASC 2014; 16th US-Japan Conf. Compos. Mater. ASTM-D30 Meet.* **2014**.

311. Zheng, X.; Kim, S.; Park, C.W. Enhancement of thermal conductivity of carbon fiber-reinforced polymer composite with copper and boron nitride particles. *Compos. Part A Appl. Sci. Manuf.* **2019**, *121*, 449–456.

312. Ma, Y.; Ueda, M.; Yokozeki, T.; Sugahara, T.; Yang, Y.; Hamada, H. A comparative study of the mechanical properties and failure behavior of carbon fiber/epoxy and carbon fiber/polyamide 6 unidirectional composites. *Compos. Struct.* **2017**, *160*, 89–99.

313. Kikuchi, B.C.; Bussamra, F.L. de S.; Donadon, M.V.; Ferreira, R.T.L.;

Sales, R. de C.M. Moisture effect on the mechanical properties of additively manufactured continuous carbon fiber-reinforced Nylon-based thermoplastic. *Polym. Compos.* **2020**, *41*, 5227–5245.

314. Colucci, G.; Ostrovskaya, O.; Frache, A.; Martorana, B.; Badini, C. The effect of mechanical recycling on the microstructure and properties of PA66 composites reinforced with carbon fibers. *J. Appl. Polym. Sci.* **2015**, *132*, 1–9.

315. Sebaey, T.A.; Bouhrara, M.; O'dowd, N. Fibre alignment and void assessment in thermoplastic carbon fibre reinforced polymers manufactured by automated tape placement. *Polymers (Basel).* **2021**, *13*, 1–12.

316. Mehdikhani, M.; Gorbatikh, L.; Verpoest, I.; Lomov, S. V. Voids in fiber-reinforced polymer composites: A review on their formation, characteristics, and effects on mechanical performance. *J. Compos. Mater.* **2019**, *53*, 1579–1669.

317. Lay, M.; Thajudin, N.L.N.; Hamid, Z.A.A.; Rusli, A.; Abdullah, M.K.; Shuib, R.K. Comparison of physical and mechanical properties of PLA, ABS and nylon 6 fabricated using fused deposition modeling and injection molding. *Compos. Part B Eng.* **2019**, *176*, 107341.

318. Fallon, J.J.; McKnight, S.H.; Bortner, M.J. Highly loaded fiber filled polymers for material extrusion: A review of current understanding. *Addit. Manuf.* **2019**, *30*, 100810.

319. Hassan, A.; Hornsby, P.R.; Folkes, M.J. Structure-property relationship of injection-molded carbon fibre-reinforced polyamide 6,6 composites: The effect of compounding routes. *Polym. Test.* **2003**, *22*, 185–189.

320. Nishikawa, M.; Fukuzo, A.; Matsuda, N.; Hojo, M. Evaluation of elastic-plastic response of discontinuous carbon fiber-reinforced thermoplastics: Experiments and considerations based on load-transfer-based micromechanical simulation. *Compos. Sci. Technol.* **2018**, *155*, 117–125.

321. Caltagirone, P.E.; Ginder, R.S.; Ozcan, S.; Li, K.; Gay, A.M.; Stonecash, J.; Steirer, K.X.; Cousins, D.; Kline, S.P.; Maxey, A.T.; et al. Substitution of virgin carbon fiber with low-cost recycled fiber in automotive grade injection molding polyamide 66 for equivalent composite mechanical performance with improved sustainability. *Compos. Part B Eng.* **2021**, *221*, 109007.

322. Goh, G.D.; Toh, W.; Yap, Y.L.; Ng, T.Y.; Yeong, W.Y. Additively manufactured continuous carbon fiber-reinforced thermoplastic for

topology optimized unmanned aerial vehicle structures. *Compos. Part B Eng.* **2021**, *216*.

323. Aversa, A.; Marchese, G.; Saboori, A.; Bassini, E.; Manfredi, D.; Biamino, S.; Ugues, D.; Fino, P.; Lombardi, M. New aluminum alloys specifically designed for laser powder bed fusion: A review. *Materials (Basel).* **2019**, *12*.

324. HEXCEL Corporation *HexPly ® M21 180C Curing Epoxy Matrix Report*; 2020;

325. Saenz-Castillo, D.; Martín, M.I.; García-Martínez, V.; Ramesh, A.; Battley, M.; Güemes, A. A comparison of mechanical properties and X-ray tomography analysis of different out-of-autoclave manufactured thermoplastic composites. *J. Reinf. Plast. Compos.* **2020**, *39*, 703–720.

326. Van Hoa, S.; Duc Hoang, M.; Simpson, J. Manufacturing procedure to make flat thermoplastic composite laminates by automated fibre placement and their mechanical properties. *J. Thermoplast. Compos. Mater.* **2017**, *30*, 1693–1712.

327. Cytec Engineered Materials *Technical Data Sheet APC-2-PEEK Thermoplastic Polymer*; Tempe. Arizona, 2016;

328. Yamawaki, M.; Kouno, Y. Fabrication and mechanical characterization of continuous carbon fiber-reinforced thermoplastic using a preform by three-dimensional printing and via hot-press molding. *Adv. Compos. Mater.* **2018**, *27*, 209–219.

329. Pascual-González, C.; San Martín, P.; Lizarralde, I.; Fernández, A.; León, A.; Lopes, C.S.; Fernández-Blázquez, J.P. Post-processing effects on microstructure, interlaminar and thermal properties of 3D printed continuous carbon fibre composites. *Compos. Part B Eng.* **2021**, *210*, 108652.

330. Zhang, Y.; Sun, L.; Li, L.; Wei, J. Effects of strain rate and high temperature environment on the mechanical performance of carbon fiber reinforced thermoplastic composites fabricated by hot press molding. *Compos. Part A Appl. Sci. Manuf.* **2020**, *134*, 105905.

331. Botelho, E.C.; Figiel; Rezende, M.C.; Lauke, B. Mechanical behavior of carbon fiber reinforced polyamide composites. *Compos. Sci. Technol.* **2003**, *63*, 1843–1855.

332. Mohd Tahir, M.; Wang, W.X.; Matsubara, T. Failure behavior of quasi-

isotropic carbon fiber-reinforced polyamide composites under tension. *Adv. Compos. Mater.* **2018**, *27*, 483–497.

333. Chuang, K.C.; Grady, J.E.; Draper, R.D.; Shin, E.S.E.; Patterson, C.; Santelle, T.D. Additive manufacturing and characterization of ultem polymers and composites. *CAMX 2015 - Compos. Adv. Mater. Expo* **2015**, 448–463.

334. Slonov, A.; Musov, I.; Zhansitov, A.; Rzhevskaya, E.; Khakulova, D.; Khashirova, S. The effect of modification on the properties of polyetherimide and its carbon-filled composite. *Polymers (Basel).* **2020**, *12*.

335. Stepashkin; Chukov, D.I.; Senatov, F.S.; Salimon, A.I.; Korsunsky, A.M.; Kaloshkin, S.D. 3D-printed PEEK-carbon fiber (CF) composites: Structure and thermal properties. *Compos. Sci. Technol.* **2018**, *164*, 319–326.

336. Fitzharris, E.R.; Watt, I.; Rosen, D.W.; Shofner, M.L. Interlayer bonding improvement of material extrusion parts with polyphenylene sulfide using the Taguchi method. *Addit. Manuf.* **2018**, *24*, 287–297.

337. Krajangsawasdi, N.; Longana, M.L.; Hamerton, I.; Woods, B.K.S.; Ivanov, D.S. Batch production and fused filament fabrication of highly aligned discontinuous fibre thermoplastic filaments. *Addit. Manuf.* **2021**, *48*, 102359.

338. Blok, L.G.; Longana, M.L.; Woods, B.K.S. Fabrication and characterisation of aligned discontinuous carbon fibre reinforced thermoplastics as feedstock material for fused filament fabrication. *Materials (Basel).* **2020**, *13*, 1–26.

339. Goetzendorfer, B.; Mohr, T.; Hellmann, R. Hybrid approaches for selective laser sintering by building on dissimilar materials. *Materials (Basel).* **2020**, *13*, 1–11.

340. Chueh, Y.H.; Zhang, X.; Ke, J.C.R.; Li, Q.; Wei, C.; Li, L. Additive manufacturing of hybrid metal/polymer objects via multiple-material laser powder bed fusion. *Addit. Manuf.* **2020**, *36*, 101465.

341. Chueh, Y.H.; Wei, C.; Zhang, X.; Li, L. Integrated laser-based powder bed fusion and fused filament fabrication for three-dimensional printing of hybrid metal/polymer objects. *Addit. Manuf.* **2020**, *31*, 100928.

342. Duty, C.; Failla, J.; Kim, S.; Smith, T.; Lindahl, J.; Kunc, V. Z-Pinning approach for 3D printing mechanically isotropic materials. *Addit. Manuf.* **2019**, *27*, 175–184.

343. Kishore, V.; Ajinjeru, C.; Nycz, A.; Post, B.; Lindahl, J.; Kunc, V.; Duty, C. Infrared preheating to improve interlayer strength of big area additive manufacturing (BAAM) components. *Addit. Manuf.* **2017**, *14*, 7–12.

344. Bhandari, S.; Lopez-Anido, R.A.; Gardner, D.J. Enhancing the interlayer tensile strength of 3D printed short carbon fiber reinforced PETG and PLA composites via annealing. *Addit. Manuf.* **2019**, *30*, 100922.

345. Handwerker, M.; Wellnitz, J.; Marzbani, H.; Tetzlaff, U. Annealing of chopped and continuous fibre reinforced polyamide 6 produced by fused filament fabrication. *Compos. Part B Eng.* **2021**, *223*.

346. O'Connor, H.J.; Dowling, D.P. Low-pressure additive manufacturing of continuous fiber-reinforced polymer composites. *Polym. Compos.* **2019**, *40*, 4329–4339.

347. Luo, M.; Tian, X.; Shang, J.; Zhu, W.; Li, D.; Qin, Y. Impregnation and interlayer bonding behaviours of 3D-printed continuous carbon-fiber-reinforced poly-ether-ether-ketone composites. *Compos. Part A Appl. Sci. Manuf.* **2019**, *121*, 130–138.

348. Ranabhat, B.; Kirmse, S.; Hsiao, K.T. Feasibility study of novel magnetic compaction force assisted additive manufacturing (MCFA-AM) methodology for continuous carbon fiber reinforced polymer (C-CFRP) composites. *Int. SAMPE Tech. Conf.* **2019**, *2019-May*.

349. Chang, B.; Parandoush, P.; Li, X.; Ruan, S.; Shen, C.; Behnagh, R.A.; Liu, Y.; Lin, D. Ultrafast printing of continuous fiber-reinforced thermoplastic composites with ultrahigh mechanical performance by ultrasonic-assisted laminated object manufacturing. *Polym. Compos.* **2020**, *41*, 4706–4715.

350. Zhang, J.; Zhou, Z.; Zhang, F.; Tan, Y.; Tu, Y.; Yang, B. Performance of 3D-printed continuous-carbon-fiber-reinforced plastics with pressure. *Materials (Basel).* **2020**, *13*.

351. Ueda, M.; Kishimoto, S.; Yamawaki, M.; Matsuzaki, R.; Todoroki, A.; Hirano, Y.; Le Duigou, A. 3D compaction printing of a continuous carbon fiber reinforced thermoplastic. *Compos. Part A Appl. Sci. Manuf.* **2020**, *137*, 105985.

352. Zhang, D.; Rudolph, N.; Woytowitz, P. Reliable optimized structures with high performance continuous fiber thermoplastic composites from additive manufacturing (AM). *Int. SAMPE Tech. Conf.* **2019**, *2019-May*, 1–21.

353. Parandoush, P.; Zhou, C.; Lin, D. 3D Printing of Ultrahigh Strength

Continuous Carbon Fiber Composites. *Adv. Eng. Mater.* **2019**, *21*, 1–8.

354. Eichenhofer, M.; Wong, J.C.H.; Ermanni, P. Continuous lattice fabrication of ultra-lightweight composite structures. *Addit. Manuf.* **2017**, *18*, 48–57.

355. Liu, S.; Li, Y.; Li, N. A novel free-hanging 3D printing method for continuous carbon fiber reinforced thermoplastic lattice truss core structures. *Mater. Des.* **2018**, *137*, 235–244.

356. Wang, Z.; Luan, C.; Liao, G.; Yao, X.; Fu, J. Mechanical and self-monitoring behaviors of 3D printing smart continuous carbon fiber-thermoplastic lattice truss sandwich structure. *Compos. Part B Eng.* **2019**, *176*, 107215.

357. Quan, C.; Han, B.; Hou, Z.; Zhang, Q.; Tian, X.; Lu, T.J. 3D Printed Continuous Fiber Reinforced Composite Auxetic Honeycomb Structures. *Compos. Part B Eng.* **2020**, *187*, 107858.

358. Azarov, A. V.; Antonov, F.K.; Golubev, M. V.; Khaziev, A.R.; Ushanov, S.A. Composite 3D printing for the small size unmanned aerial vehicle structure. *Compos. Part B Eng.* **2019**, *169*, 157–163.

359. Li, N.; Link, G.; Wang, T.; Ramopoulos, V.; Neumaier, D.; Hofele, J.; Walter, M.; Jelonnek, J. Path-designed 3D printing for topological optimized continuous carbon fibre reinforced composite structures. *Compos. Part B Eng.* **2020**, *182*, 107612.

360. Reverte, J.M.; Caminero, M. ángel; Chacón, J.M.; García-Plaza, E.; Núñez, P.J.; Becar, J.P. Mechanical and geometric performance of PLA-based polymer composites processed by the fused filament fabrication additive manufacturing technique. *Materials (Basel).* **2020**, *13*.

361. Ivey, M.; Melenka, G.W.; Carey, J.P.; Ayranci, C. Characterizing short-fiber-reinforced composites produced using additive manufacturing. *Adv. Manuf. Polym. Compos. Sci.* **2017**, *3*, 81–91.

362. Duty, C.E.; Kunc, V.; Compton, B.; Post, B.; Erdman, D.; Smith, R.; Lind, R.; Lloyd, P.; Love, L. Structure and mechanical behavior of Big Area Additive Manufacturing (BAAM) materials. *Rapid Prototyp. J.* **2017**, *23*, 181–189.

363. Young, D.; Wetmore, N.; Czabaj, M. Interlayer fracture toughness of additively manufactured unreinforced and carbon-fiber-reinforced acrylonitrile butadiene styrene. *Addit. Manuf.* **2018**, *22*, 508–515.

364. Yasa, E.; Ersoy, K. Dimensional Accuracy and Mechanical Properties of Chopped Carbon Reinforced Polymers Produced by Material Extrusion Additive Manufacturing. *Materials (Basel).* **2019**, *12*, 3885.

365. Hendlmeier, A.; Simon, Ž.; Chutani, A.; Henderson, L.C. Generating short carbon fiber polyamide-6 composites from continuous carbon fiber – A preliminary examination of surface treatment and sizing effects. *Compos. Part A Appl. Sci. Manuf.* **2020**, *138*.

366. FORD Motor Company *Ford WRS-M4D1062-A1 - polyamide (PA66), heat stabilized, 40% short carbon fiber filled, molding compound, 40% recycled material by*; 2019;

367. BASF *Ultramid ® A3WC8 Polyamide 66 Technical datasheet*; 2020;

368. Tahir, M.M.; Wang, W.X.; Matsubara, T. A novel tab for tensile testing of unidirectional thermoplastic composites. *J. Thermoplast. Compos. Mater.* **2019**, *32*, 37–51.

369. Rakhshbahar, M.; Sinapius, M. A novel approach: Combination of automated fiber placement (afp) and additive layer manufacturing (alm). *J. Compos. Sci.* **2018**, *2*.

370. Nixon-Pearson, O.J.; Belnoue, J.P.H.; Ivanov, D.S.; Potter, K.D.; Hallett, S.R. An experimental investigation of the consolidation behaviour of uncured prepregs under processing conditions. *J. Compos. Mater.* **2017**, *51*, 1911–1924.

371. HEXCEL Corporation *HexPly 8552 ® Epoxy matrix (180°C/356°F curing matrix). Epoxy Matrix Product Datasheet*; Stamford, Connecticut, 2020;

372. Bertorello, C.; Viña, J.; Viña, I.; Argüelles, A. Study of the influence of the type of matrix used in carbon-epoxy composites on fatigue delamination under mode III fracture. *Mater. Des.* **2020**, *186*, 108345.

373. Zhao, Y.Q.; Zhou, Y.; Huang, Z.M.; Batra, R.C. Experimental and micromechanical investigation of T300/7901 unidirectional composite strength. *Polym. Compos.* **2019**, *40*, 2639–2652.

374. Ciba-Geisy Plastics *Fibredux 914 (Information sheet No. FTA 490)*; 1989;

375. Ming, Y.; Duan, Y.; Wang, B.; Xiao, H.; Zhang, X. A novel route to fabricate high-performance 3D printed continuous fiber-reinforced thermosetting polymer composites. *Materials (Basel).* **2019**, *12*.